State of Oregon
Oregon Department of Geology and Mineral Industries
Ian P. Madin, Interim State Geologist

OPEN-FILE REPORT O-15-07

COASTAL FLOOD HAZARD STUDY, CURRY COUNTY, OREGON

By Jonathan C. Allan[1], Peter Ruggiero[2], Nick Cohn[2], Fletcher E. O'Brien[3], Katherine Serafin[2], Jed T. Roberts[3], and Laura L. Stimely[1]

2015

[1] Oregon Department of Geology and Mineral Industries, Coastal Field Office, P.O. Box 1033, Newport, OR 97365
[2] College of Earth, Ocean and Atmospheric Sciences, Oregon State University, Corvallis, OR 97331
[3] Oregon Department of Geology and Mineral Industries, 800 NE Oregon St., Ste. 965, Portland, OR 97232

DISCLAIMER

Cover photograph: Photo of the mouth of Hunter Creek, looking north toward Gold Beach. Photo taken by J. Allan, December 7, 2012.

Oregon Department of Geology and Mineral Industries Open-File Report O-15-07
Published in conformance with ORS 516.030

For additional information:
Administrative Offices
800 NE Oregon Street #28, Suite 965
Portland, OR 97232
Telephone (971) 673-1555
Fax (971) 673-1562
http://www.oregongeology.org
http://www.oregon.gov/DOGAMI/

TABLE OF CONTENTS

LIST OF FIGURES

LIST OF TABLES

1.0 INTRODUCTION

The objective of the Curry County Flood Hazard Project is to develop updated Digital Flood Insurance Rate Maps (DFIRM) and a Flood Insurance Study (FIS) report for Curry County, Oregon (**Figure 1-1**). For this effort, DOGAMI will be using newly acquired (2008) light detection and ranging data (lidar) to redelineate coastal and riverine flood hazards within Curry County, produce revised DFIRMs and a revised FIS report, and produce other mapping products useable at the local, state, and federal level for mitigation planning, risk analysis, and disaster response.

As part of the redelineation, DOGAMI has been contracted to perform detailed coastal flood hazard studies for several stretches of beach along the Curry County shoreline of the Pacific Ocean. These analyses are to include assessments of the 1%, or 100-year, extreme storm wave event and the associated calculated wave setup, runup, and total water level (i.e., the wave runup superimposed on the tidal level) to help guide the determination of Special Flood Hazard Areas (SFHAs), the most significant being regions subject to high coastal flood risk (Zone VE), characterized with base flood elevations (BFEs) that are used to guide building practices. Additional modeling of the 0.2%, or 500-year, event will also be undertaken.

Detailed coastal flood analyses will be limited to the following key areas:

- Port Orford, in the vicinity of the port facilities to Battle Rock, and from the Port Orford Heads north to Paradise Point Road;
- Nesika Beach, from approximately Otter Point north to Three Sisters;
- Rouge Shores, from the Rogue River north to Otter Point;
- Gold Beach, from Cape Sebastian to the Rogue River; and
- Brookings, from the Oregon-California border to Longacre Loop road at the north end of town.

Aside from these areas, DOGAMI will develop revised V-zones for the remainder of the county shoreline. While a few sections of the coastline have previously been mapped as VE, the bulk of the coastline have either not been mapped, or are mapped approximate “A.” After consulting with FEMA and State government representatives, the decision has been made to revise these latter zones to better reflect the geomorphology of the coast, and in addition redefine these zones as V-zones.

The development of coastal flood maps is complicated, due to its dependence on a myriad of data sources required to perform the wave transformations, runup, and overtopping calculations. These challenges are further compounded by an equally wide range of potential settings in which the data and methods can be applied, which range from dune to bluff-backed beaches, sites that may be backed by coastal engineering structures such as sea walls, rip rap revetments, or wooden bulkheads, to gravel and hard rock shorelines. **Figure 1-2** broadly summarizes the various steps described in the ensuing sections in order to help understand conceptually the process that leads to the completed coastal flood hazard zones.

This report first examines the coastal geology and geomorphology of the Curry County shoreline, including a discussion of the erosion history of the coast. The results presented in this section will ultimately form the basis for defining the flood zones along the Curry County coastline. Section 3 presents the results of Real-Time Kinematic Differential Global Positioning Surveys (RTK-DGPS) of the detailed study sites established along the length of Curry County, undertaken at the peak of the 2013-14 winter. These surveys are also compared with recent historical data derived from lidar data, which are used to help define the most eroded winter profile used in the runup calculations described in Section 6. Section 3 also documents various parameters associated with the measured beach profile data, including the beach-dune junction elevation, the beach slope, and dune/bluff crest/top elevations.

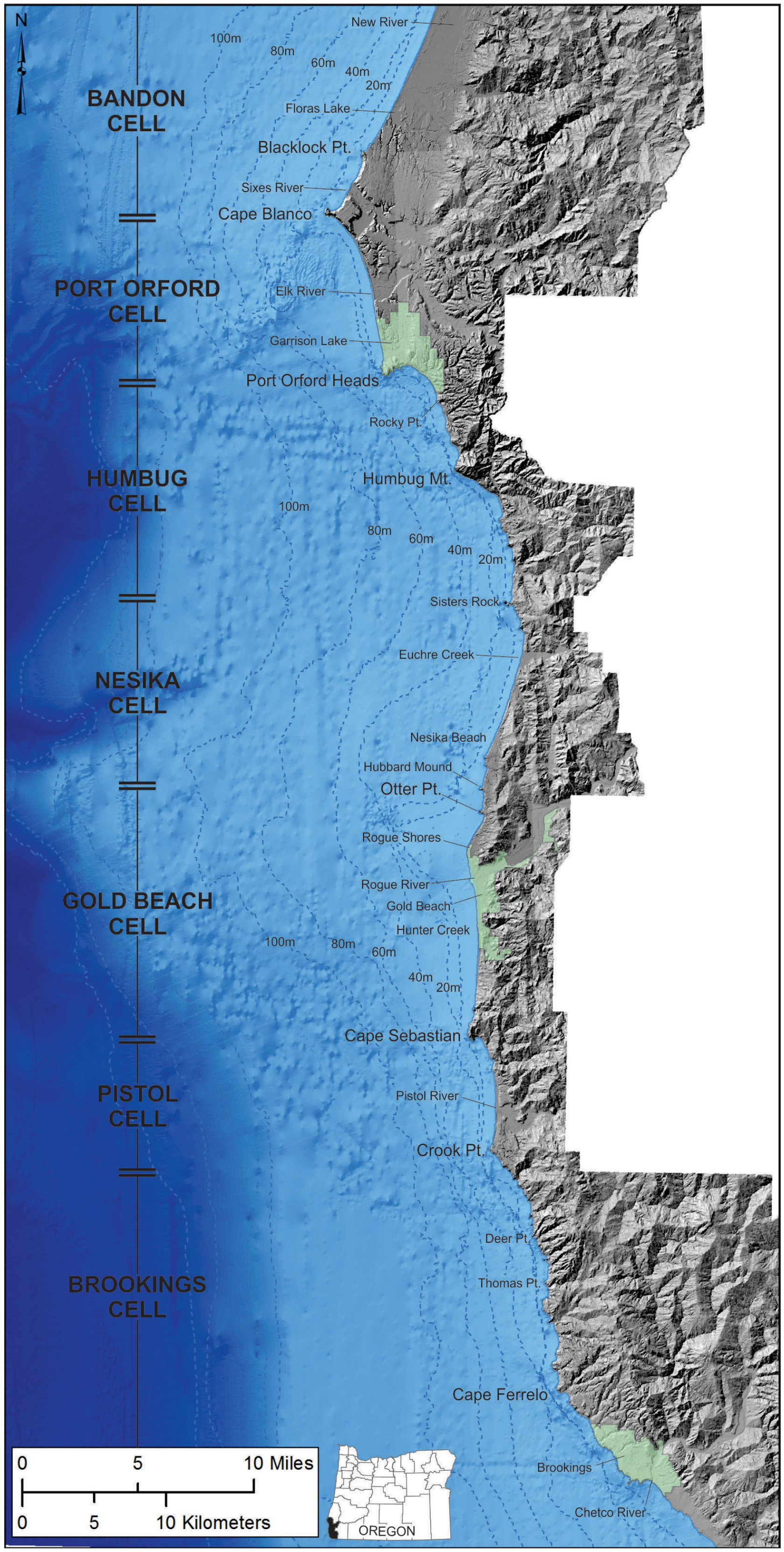

Figure 1-1. Location map of Curry County coastline.

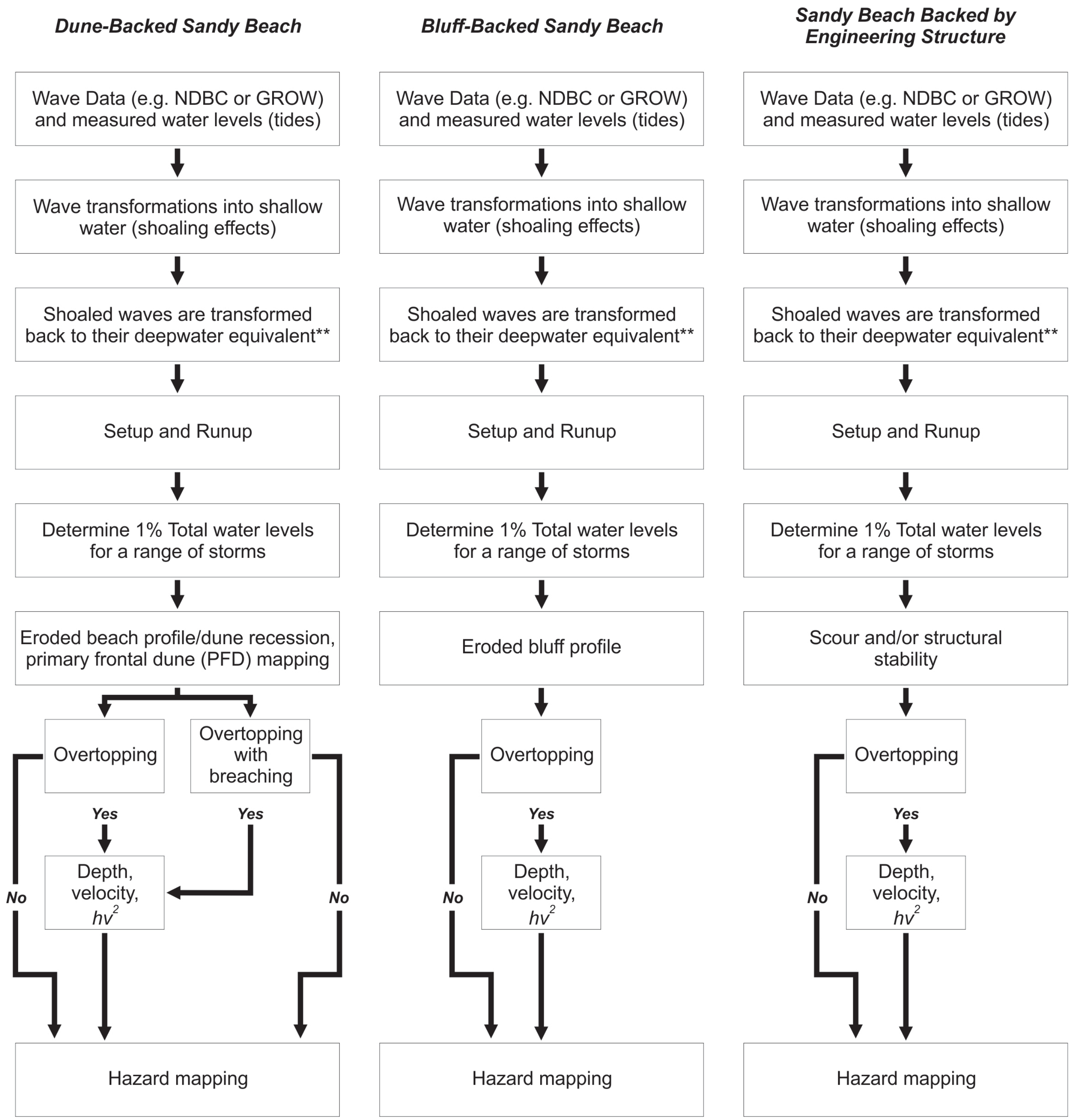

Figure 1-2. Three representative examples of the steps that may be taken to derive coastal flood hazard maps on the Pacific Northwest coast. **Note: The waves are first shoaled using numerical models in order to account for the effect of wave changes (refraction/diffraction) that take place across the shelf and in the nearshore. Because many coastal engineering equations (e.g. wave runup) require deepwater inputs, the "shoaled" waves are then converted back to their deepwater equivalence.

An examination of tide data measured by the National Ocean Service (NOS) at multiple stations, including South Beach (Yaquina Bay), Charleston (Coos Bay), Port Orford and Crescent City is presented in Section 4, including an analysis of the 1% and 0.2% *still water levels* (SWL). Section 5 describes the steps undertaken to develop a synthesized wave climate, critical for developing the input wave statistics used in calculating the wave runup. Section 5 also examines the procedures used to refract the waves from deep water into the nearshore using the SWAN (Simulating Waves Nearshore) wave model. Analyses of the wave runup, including the calculation of the 1% and 0.2% total water levels (TWL) as well as any overtopping calculations is presented and discussed in Section 6.

Section 7 discusses the steps used to determine the degree of erosion that might occur on the dune-backed beaches, including the approach used to define the duration-reduced erosion factor, important for further establishing the initial conditions on which the runup and overtopping calculations are ultimately performed. Similar discussions are provided describing observations of bluff erosion, characteristic of a few discrete sections of the Curry County shoreline. Finally, Section 8 synthesizes all of the information and describes the steps taken to draft new flood maps along the Curry County shoreline.

2.0 COASTAL GEOLOGY AND GEOMORPHOLOGY OF CURRY COUNTY

Curry County is located on the southwest Oregon coast, between latitudes 41°59′53.0″N (Oregon/California border) and 42°57′16.0″N (just south of New Lake), and longitudes 124°34′12″W (Cape Blanco) and 123°42′57.6″W (near Nine Mile Spring Road). The terrain varies from low elevation sandy beaches and dunes on the coast, to elevations over 1,000 m (e.g., Brandy Peak reaches 1,615 m [5,298 ft]) farther inland. The coastal strip is approximately 166 km (~103 mi) in length and varies in its geomorphology from broad, low-sloping sandy beaches backed by dunes, cobble and boulder beaches adjacent to the headlands, and cliff shorelines (**Figure 2-1**). Coastal bluffs fronted by sandy beaches and/or cobbles and boulders make up the bulk of the coastline (49.2%), while barrier beaches and dunes (24.5%) and plunging cliffs (24.2%) make up the remainder of the coastline; approximately 2% of the shoreline consists of jetties. Prominent headlands formed of moderately resistant sandstone/mudstone units (e.g., Cape Ferrelo, Cape Sebastian, Otter Point, Humbug Mountain, and Cape Blanco) provide natural barriers to alongshore sediment transport (Komar, 1997), effectively dividing the county coastline into a number of littoral cells (**Figure 1-1**). These include:

- The Smith River littoral cell (~25 km [15.5 mi]), which extends from Point St. George in northern California to the Chetco River;
- The Brookings cell (41.3 km [25.7 mi]), from the Chetco River north to Crook Point;
- Pistol river cell (~9.2 km [5.7 mi]), from Crook Point to Cape Sebastian;
- Gold beach cell (~18.8 km [11.7 mi]), from Cape Sebastian to Otter Point;
- The Nesika littoral cell (~12.1 km [7.5 mi]), from Hubbard Mound to Sisters Rock;
- Humbug cell (11.6 km [7.2 mi]), from Sisters Rock to Humbug Mountain;
- Humbug (9.3 km [5.8 mi]), from Humbug Mountain to Port Orford;
- Port Orford (11.7 km [7.2 mi}), from the Port Orford heads to Cape Blanco (**Figure 2-1**); and
- The Bandon littoral cell (54.4 km {33.8 mi]), which extends from Cape Blanco to Cape Arago.

Each of these cells is further broken up into a series of smaller subcells due to the presence of several rivers (Winchuck, Chetco, Pistol, Rogue, Elk, Sixes, and New River) that terminate at the ocean. Due to their generally low flows and the terrain they are down cutting into, most of these rivers carry little (>4×10^3 to <10×10^4 m^3/yr) sediment to the open coast today (**Figure 2-2**). The one exception to this is the Rogue River, which is estimated to carry some 2×10^5 to 3×10^5 m^3/yr of sediment to the coast (Clemens and Komar, 1988). Hence, the beaches of Curry County receive very little sediment along the coast today other than from erosion of the backshore.

Figure 2-1. Looking north along the Blanco littoral cell. In the foreground is the Port Orford Heads (Otter Point Formation) with Garrison Lake located at mid-photo. North of Garrison Lake is a Quaternary middle marine terrace that is actively being eroded, supplying coarse sand and gravel to the beach. Farther north, is the barrier beach that separates the Elk River from the ocean, and beyond that is another sequence of marine terraces that abut against Cape Blanco (photo: J. Allan, DOGAMI, 2011).

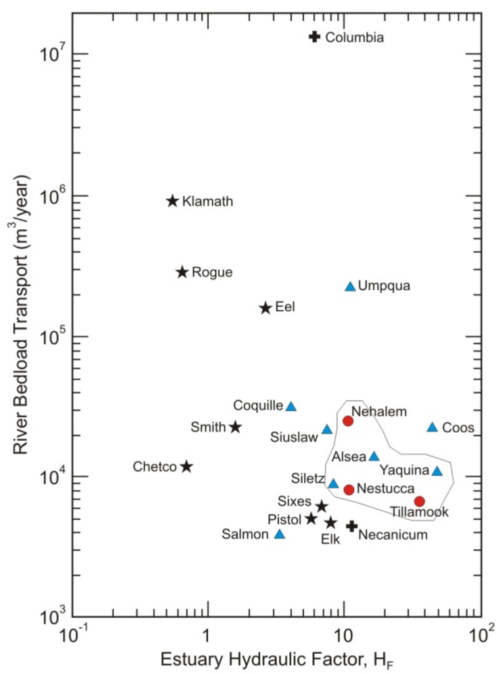

Figure 2-2. Estimated annual bedload transport for Oregon coastal rivers, including the Smith River in northern California, and the hydraulic factors (ratio of tidal prism to river-water input, H_F) for their estuaries as an indication of their ability to bypass sediment to the beaches. As H_F decreases, river discharge increasingly dominates over the tidal prism, allowing sand to bypass the estuary. Plus symbols indicate rivers from the Columbia south to Tillamook Head, red circles indicate rivers from Tillamook Head to Cascade Head, blue triangles indicate rivers south of Cascade Head) (after Clemens and Komar, 1988).

2.1 Local Geology

Approximately 73% of the Curry County coastline consists of prominent bluffs and cliffs that have eroded into sandstone/siltstone units of various formations. These units are considered to be mostly early Cretaceous in age. Interspersed among these units are various formations defined as metamorphic (late Jurassic in age) that reflect a variety of rock units including sandstone, siltstone, marine basalt, and conglomerates. These include the Otter Point (**Figure 2-3**) and Dothan Formations (**Figure 2-4**) (Beaulieu and Hughes, 1976). The former is exposed in discrete sections along the Curry County coastline, but is particularly abundant near Sisters Rock, at Otter Point and near Nesika Beach, and on the very south coast north of Cape Ferrelo. The Otter Point Formation is commonly referred to as a mélange due to the fact that it is characterized by significant shearing and lack of structural integrity (Beaulieu and Hughes, 1976). The Dothan Formation is particularly prominent near Brookings (**Figure 2-4**) and to its north (~ Cape Ferrelo). In many respects, the Dothan Formation resembles rocks in the Otter Point Formation though the Dothan is not as pervasively sheared as the Otter Point Formation. North of Sisters Rock, the predominant Formations include the Humbug Mountain (**Figure 2-5**) and Rocky Point Formations. The former is described as a thick-bedded fine-grained conglomerate consisting of coarse to pebbly sandstone, while the latter overlies the Humbug Mountain Conglomerate and consists of alternating beds of hard sandstone and moderately hard siltstone.

North of Port Orford, the beaches are typically backed by a suite of marine terraces of varying elevations that were formed during the Quaternary and reflect previous sea level high stands, and subsequent tectonic uplift (**Figure 2-1**). The lowest terrace thought to have formed around 35,000 years ago, dominates much of the northern County (e.g., north of Floras Lake) and contain abundant sand, silt and basal gravels. South of Blacklock Point and north of Port Orford, a series of middle terraces dominate much of the coastline. Radiocarbon dating of material on the terrace suggest ages of >45,000 years. These latter terraces consist of basal gravel and overlying sand. Erosion of the terraces is contributing significant amounts of sand and gravel to the beach system in both the Blanco and Bandon littoral cells, evident by the northward extension of the both the Elk and New River spits over the past century (**Figure 2-6**).

Farther south in the Gold Beach littoral cell, construction of jetties at the mouth of the Rogue River (completed in 1960) has resulted in significant changes to the beach, with the shoreline having prograded seaward on both sides of the jetties (**Figure 2-7**). Landward of the beach is a series of middle marine terraces of Quaternary age. The terrace is particularly prominent on the north side of the Rogue River, while south of Hunter Creek, the backshore transitions to rocks of the Otter Point and Hunter Cove Formations. The latter makes up the much of the area surrounding Cape Sebastian.

Figure 2-3. Looking east toward Otter Point. The headland likely presents a significant barrier to longshore sediment transport, separating the Gold Beach (right) from the Nesika (left) littoral cells. The bluffs to the left have eroded into rocks of the Otter Point Formation, while broad sand beaches abut against a series of middle marine terraces near Rogue Shores. Within the Gold Beach cell, sand and gravel are actively being supplied to the beach system via the Rogue River (photo: J. Allan, DOGAMI, 2011).

Figure 2-4. Exposed rocks of the Dothan Formation make up much of the coastal bluffs near Brookings (photo: J. Allan, DOGAMI, 2011).

Figure 2-5. Looking east at Humbug Mountain. An extensive rockfall is present near mid photo (photo: R. Witter, DOGAMI, 2010).

Figure 2-6. Looking south along the Elk River spit toward the Port Orford Heads in the distance. Erosion of the terrace south of the river is actively contributing sand and gravel to the beach system (photo: J. Allan, DOGAMI, 2011).

Figure 2-7. Overlooking the mouth of the Rogue River and Gold Beach. Construction of the jetties was completed in 1960 and resulted in the beach and shoreline prograding rapidly seaward. However, recent patterns of shoreline movement suggest a reversal toward erosion (photo: J. Allan, DOGAMI, 2011).

2.2 Tsunami Hazards Associated with the Cascadia Subduction Zone and from Distant Earthquake Sources

There is considerable geologic evidence from estuaries and coastal lakes along the Cascadia subduction zone that provides evidence for episodic occurrences of abrupt coastal subsidence immediately followed by significant ocean flooding associated with major tsunamis that swept across the ocean beaches and also traveled well inland through the bays and estuaries. Coastal paleoseismic records document the impacts of as many as 13 major subduction zone earthquakes and associated tsunamis over the past ~7,000 years (Witter and others, 2003; Kelsey and others, 2005; Witter and others, 2010), while recent studies of turbidite records within sediment cores collected in deep water at the heads of Cascadia submarine canyons provide evidence for at least 41 distinct tsunami events over the past ~10,000 years (Goldfinger and others, 2003; Goldfinger, 2009; Goldfinger and others, 2009). The length of time between these events varies from as short as a century to as long as 1200 years, with the average recurrence interval for major Cascadia earthquakes (magnitude [M_W] > 9) estimated to be ~530 years (Witter and others, 2010).

The most recent Cascadia subduction zone earthquake occurred on January 26, 1700 (Satake and others, 1996; Atwater and others, 2005) and is estimated to have been a magnitude (M_W) 9 or greater based on the size of the tsunami documented along the coast of Japan. This event probably ruptured the full length (~1,200 km) of the subduction zone, based on correlations between tsunami deposits identified at multiple sites along the length of the PNW coast.

There is now increasing recognition that great earthquakes do not necessarily result in a complete rupture of the Cascadia subduction zone (i.e., rupture along the full 1,200 km fault zone), such that partial ruptures of the plate boundary have occurred in the paleo-records due to smaller earthquakes with magnitudes (M_W) < 9 (Witter and others, 2003; Kelsey and others, 2005). These partial segment ruptures appear to occur more frequently on the southern Oregon coast, determined from paleotsunami studies (stratigraphic coring, radiocarbon dating and marine diatom analyses) undertaken at several locations on the southern Oregon coast, including Bradley Lake located just south of Bandon, the Sixes River and the Coquille estuary. According to Kelsey and others (2005), initial estimates of the recurrence intervals of Bradley Lake tsunami incursion is typically shorter (~380–400 years) than the average recurrence intervals inferred for great earthquakes (~530 years). Furthermore, they have documented from those records that local tsunamis from Cascadia earthquakes recur in clusters (~250–400 years) followed by gaps of 700–1,300 years, with the highest tsunamis associated with earthquakes occurring at the beginning and end of a cluster.

Recent analyses of the turbidite records (Goldfinger, 2009; Goldfinger and others, 2009) suggest that of the 41 events in the geologic past:

- 20 events were probably associated with a rupture of the full Cascadia subduction zone, characterized by a magnitude (M_W) ~9 or greater earthquake;
- 2-3 events reflected a partial rupture (~75%) of the length of the subduction zone, characterized by an estimated earthquake magnitude (M_W) of ~8.5–8.8 earthquake;
- 10-11 events were associated with a partial rupture (~50%), characterized by an estimated earthquake magnitude (M_W) of ~8.3–8.5 earthquake; and
- 8 events reflected a partial rupture (~25%), with an estimated earthquake magnitude (M_W) of ~7.6–8.4.

The last 19 shorter ruptures are concentrated in the southern part of the margin and have estimated recurrence intervals of ~240–320 years. Goldfinger (2009) estimated that time-independent probabilities for segmented ruptures range from 7–9% for full margin ruptures, to ~18% in 50 years for a southern segment rupture; time dependent rupture analyses indicate that the probability increases to ~25% in 50 years for the northern zone.

Aside from local tsunamis associated with the Cascadia Subduction Zone, the Oregon coast is also susceptible from tsunamis generated by distant events, particularly along the coast of Japan, along the Aleutian Island chain, and from the Gulf of Alaska. The most recent distant tsunami event occurred on March 11, 2011, when a magnitude (M_W) 9.0 earthquake occurred 129 km (80 mi) offshore from the coast of Sendai, northeast Honshu, Japan (Allan and others, 2012a). This earthquake triggered a catastrophic tsunami that within minutes inundated the northeast coast of Japan, sweeping far inland; most recent reports indicate 15,854 dead and another 3,155 missing. Measurements derived from a tide gauge on the impacted shore (Ayukawa, Ishinomaki, Miyagi Prefecture) recorded a tsunami amplitude of 7.6 m, before the gauge was destroyed by the initial tsunami wave (Yamamoto, 2011), while post-tsunami surveys indicate that the tsunami water levels within the inundation zone reached as high as 19.5 m (Mori and others, 2011). The tsunami also propagated eastward across the Pacific Ocean, impacting coastal communities in Hawaii and along the west coast of the continental United States — Washington, Oregon, and California.

Damage in Oregon, Washington, and northern California from the tsunami was almost entirely confined to harbors, including Depoe Bay, Coos Bay, Brookings in Oregon, and in Crescent City, California, having been moderated by the arrival of the tsunami's highest waves during a relatively low tide (Allan and others, 2012a). At Crescent City, an open-coast breakwater, the to-and-fro surge of the water associated with the tsunami waves overturned and sank 15 vessels and damaged 47, while several boats were swept offshore. Flood damage also occurred during the early hours of March 12; for example, an RV park near the mouth of Elk Creek was flooded when a 1.05 m (3.4 ft) tsunami wave arrived, coinciding with high tide. The total damage to the Crescent City harbor and from the effects of the flooding has been placed at $12.5 million. At Brookings on the southern Oregon coast, 12 fishing vessels put to sea at about 6 am, prior to the arrival of the tsunami waves. However, the *Hilda*, a 220-ton fishing boat and the largest in the harbor, broke loose under the forces of the wave-induced currents, washing around the harbor and smashing into and sinking several other boats. Much of the commercial part of the harbor and about one third of the sports basin were destroyed; the total damage has been estimated at about $10 million.

Prior to the Tōhoku tsunami, the previous most significant distant tsunami occurred on March 27, 1964, when a magnitude (M_W) 9.2 earthquake occurred near Prince William Sound in Alaska, which generated a catastrophic local tsunami in Alaska, while the effects of the tsunami was also felt around the Pacific Basin. The tsunami caused significant damage to infrastructure in the coastal communities of Seaside and Cannon Beach and killed four people camping along Beverly Beach in Lincoln County.

In 2009, the Oregon Department of Geology and Mineral Industries (DOGAMI) initiated a multi-year study to accelerate remapping of the Oregon coast for tsunami inundation using state of the art computer modeling and laser-based terrain mapping (lidar). The outcome of this effort was the creation of new and more accurate tsunami evacuation maps for the entire length of the coast. DOGAMI, in collaboration with researchers (Zhang and Baptista) at the Oregon Health and Science University (OHSU), Oregon State University (Goldfinger) and the Geological Survey of Canada (Wang), developed a new approach to produce a suite of next-generation tsunami hazard maps for Oregon (Priest and others, 2010; Witter and others, 2010). Modeling tsunami inundation on the southern Oregon coast was initiated late in 2009 and consisted of a range of scenarios, including 15 Cascadia events and two distant earthquake source events (e.g., 1964 Prince William Sound earthquake magnitude [M_W] 9.2 earthquake [Witter, 2008]). The last of the suite of new evacuation maps (TIM series) was released in 2013; the maps are also available in an online tsunami hazard portal (http://nvs.nanoos.org/TsunamiEvac).

Associated with great Cascadia earthquakes is a near instantaneous lowering (subsidence) of the coast by ~0.4 m (1.3 ft) to as much as 3 m (9.8 ft) (Witter and others, 2003). This process equates to raising sea level by the same amount along the entire Pacific Northwest coastline. Following the earthquake, coastal erosion is expected to accelerate everywhere as the beaches and shorelines adjusted to a new equilibrium condition that, over time, would likely decrease asymptotically (Komar and others, 1991). On the southern Oregon coast, Komar and others have suggested that the extensive development of sea stacks offshore from Bandon may be evidence for that erosion response following the last major subduction zone earthquake in 1700. Over the past century, the erosion appears to have stabilized, as there is little evidence for any progressive erosion trend. This suggests that the south coast is now being uplifted (estimated to be ~0.6 to 1.1 m) due to the Cascadia subduction zone having become locked again, such that strain is now building toward the next major earthquake. With the release of that energy and land subsidence, cliff erosion along the Bandon shore (and elsewhere on the Oregon coast) would be expected to begin again.

2.3 Coastal Geomorphology

On the basis of geology and geomorphology, the Curry County shoreline can be broadly divided into three morphological beach types. These are depicted in **Figure 2-8** to **Figure 2-12** and include:

1. ***Dune-backed beaches:*** Barrier beaches and beaches backed by dunes make up approximately one quarter (24.5%) of the Curry County shoreline (**Figure 2-8** to **Figure 2-12**). These beach types are located in selected regions along the coast, including Crissey Field (south of the Winchuck River), adjacent to the Pistol River, from Hunter Creek north to Otter Point [**Figure 2-7**]), along the Garrison Lake barrier beach (**Figure 2-1**), and along the Elk and New River Spits (**Figure 2-6**). The geomorphology of these beaches reflect two broad types:
    a. Wide, dissipative surf zones with low sloping foreshores are located almost exclusively north of the Rogue River and south of Otter Point **(Figure 2-10**). The average beach slope (tan β) for these beaches is 0.050 (σ = 0.012), slightly steeper than those observed on the north coast, where the beaches have slopes that range from tan β = 0.03-0.04;
    b. The remainder of the dune-backed beaches in Curry County are characterized as steep sloping, reflective beaches, containing abundant coarse sand to pebble size sediments. These latter beaches are characterized by a narrow surf zone, and due to their steep nature, wave breaking typically occurs close to the shore over a plunge step. The average beach slope for these beaches is tan β = 0.074 (σ = 0.021).
2. ***Cliffed shore:*** Cliffed shores comprise approximately 24% of the Curry County coastline (**Figure 2-5**). Examples of this type of shore predominate around the major headlands and along much of the shore north of Brookings. This particular shore type invariably consists of near-vertical cliffs that plunge into the ocean. In some cases, the cliffs may be fronted by rock platforms and/or talus.
3. ***Bluff-backed beaches:*** Bluff-backed beaches are the most prominent geomorphic type in Curry County comprising approximately 49.2% of the shore (**Figure 2-4**). This particular geomorphic type dominates the shoreline from Port Orford to Otter Point and from Cape Sebastian to the Winchuck River. Bluff back beaches are also present from the Elk River mouth to Flora's Lake. The bluffs that back the beaches vary in height from low scarps to heights greater than 50 m (164 ft) in height. Beach slopes (tan β) seaward of the bluffs are similar to those observed throughout Curry County, averaging about 0.082 (σ = 0.022). Geomorphically, these beaches may be characterized as "composite" using the terminology of Jennings and Shulmeister (2002), such that the beaches consist of a dissipative sand beach, backed by a steeper upper foreshore composed of gravels and boulders.

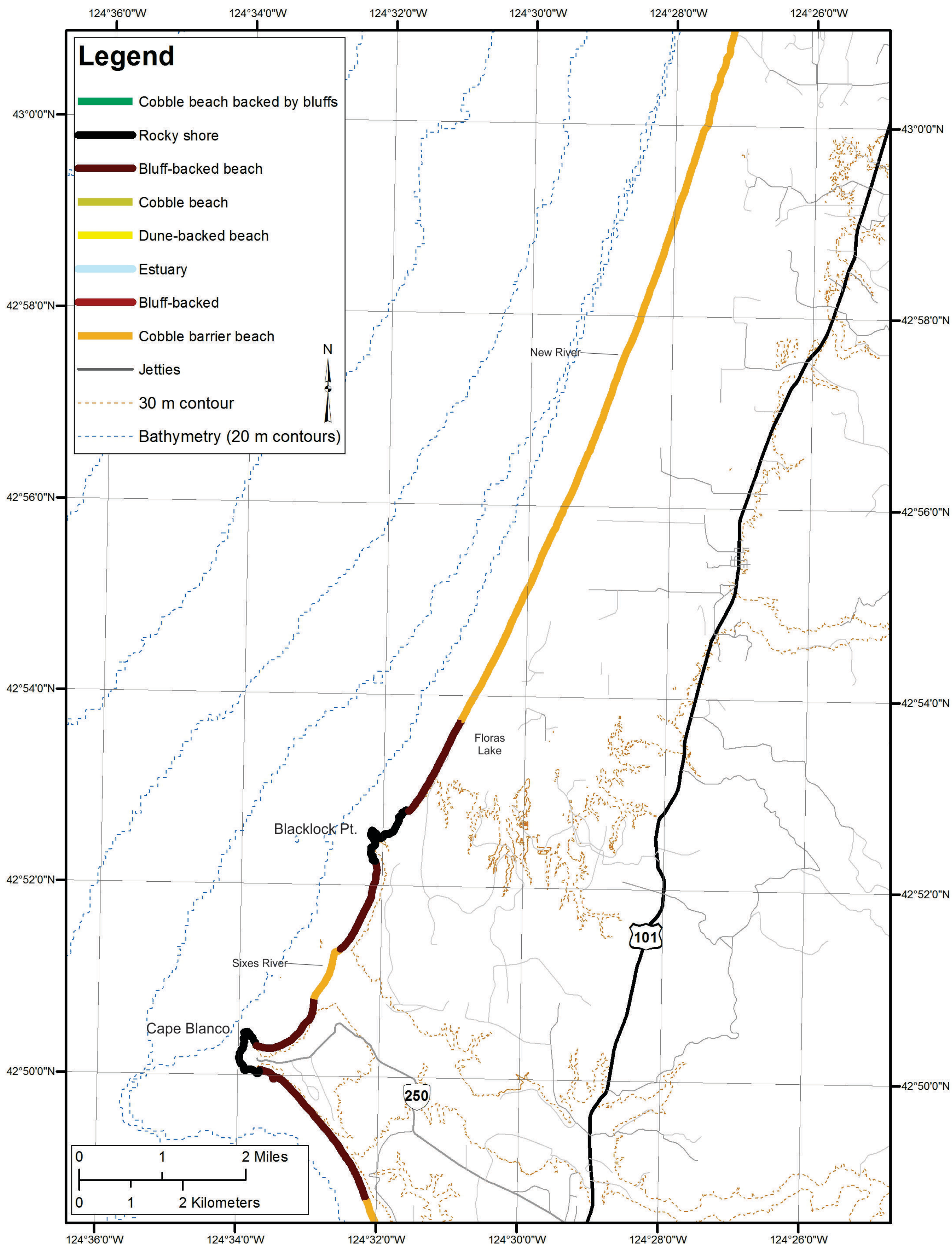

Figure 2-8. Geomorphic classification of the Cape Blanco region (Cape Blanco to the New River).

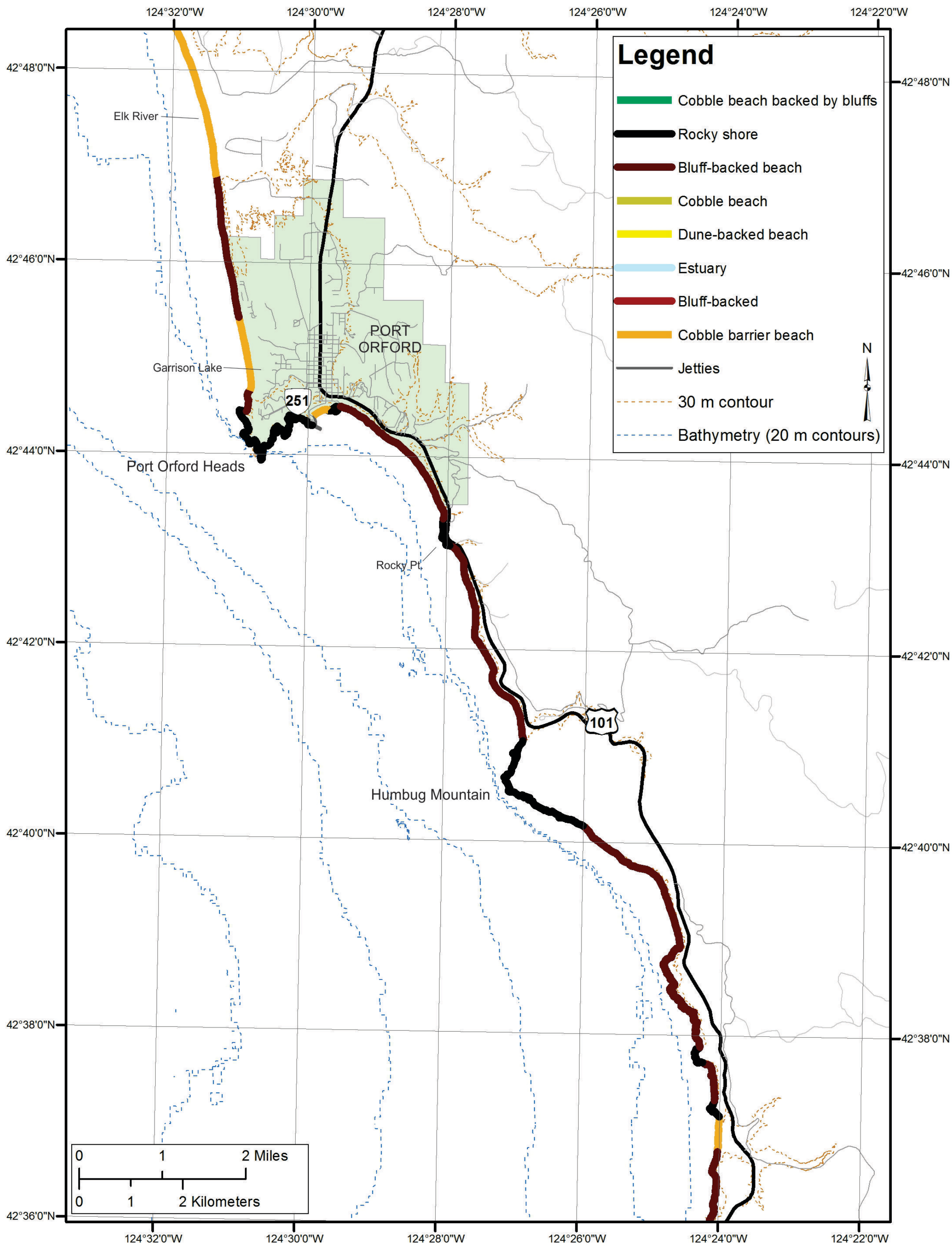

Figure 2-9. Geomorphic classification of the Port Orford–Humbug Mountain region (Sisters Rock to the Elk River).

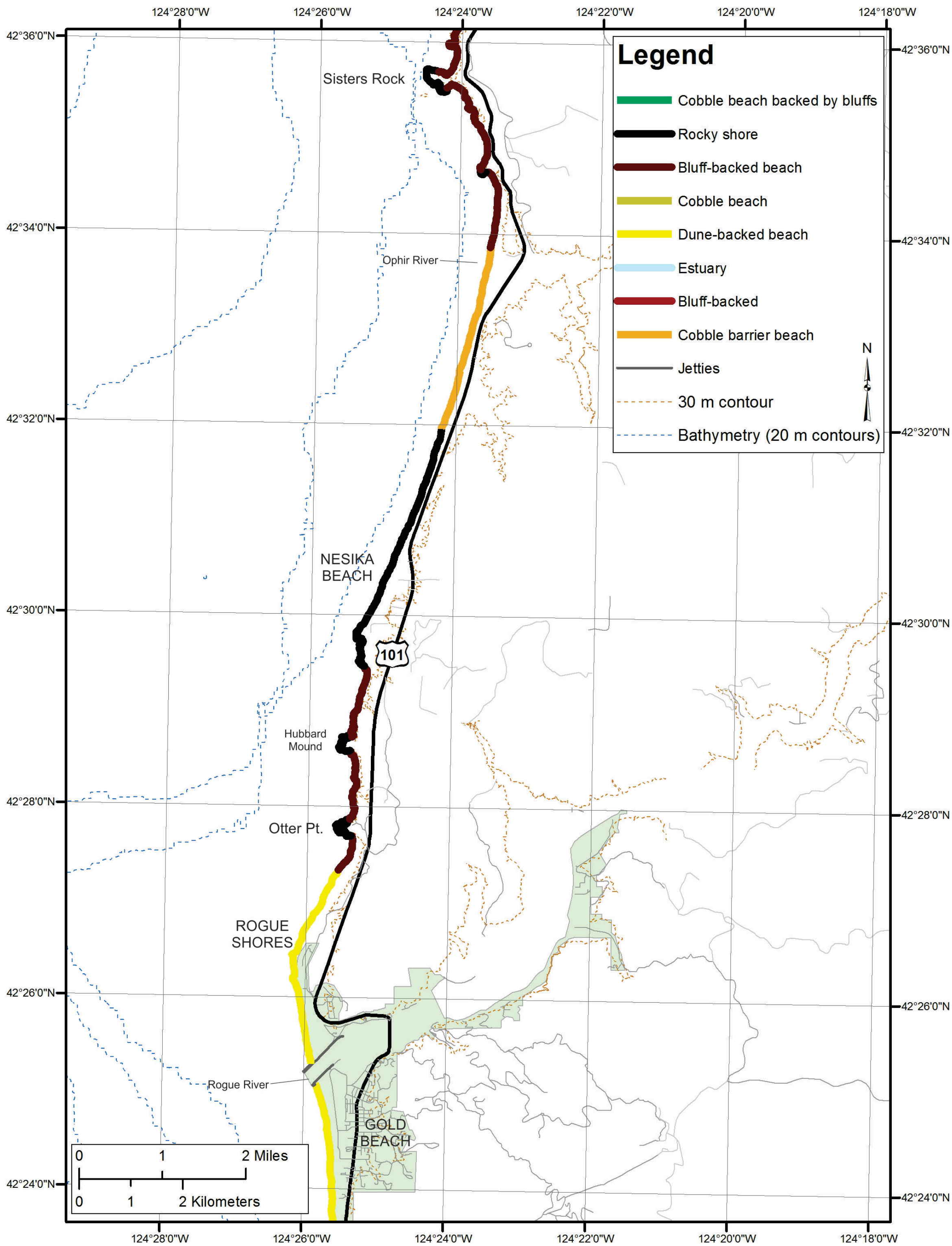

Figure 2-10. Geomorphic classification of Gold Beach–Nesika Beach region (Gold Beach to Sisters Rock).

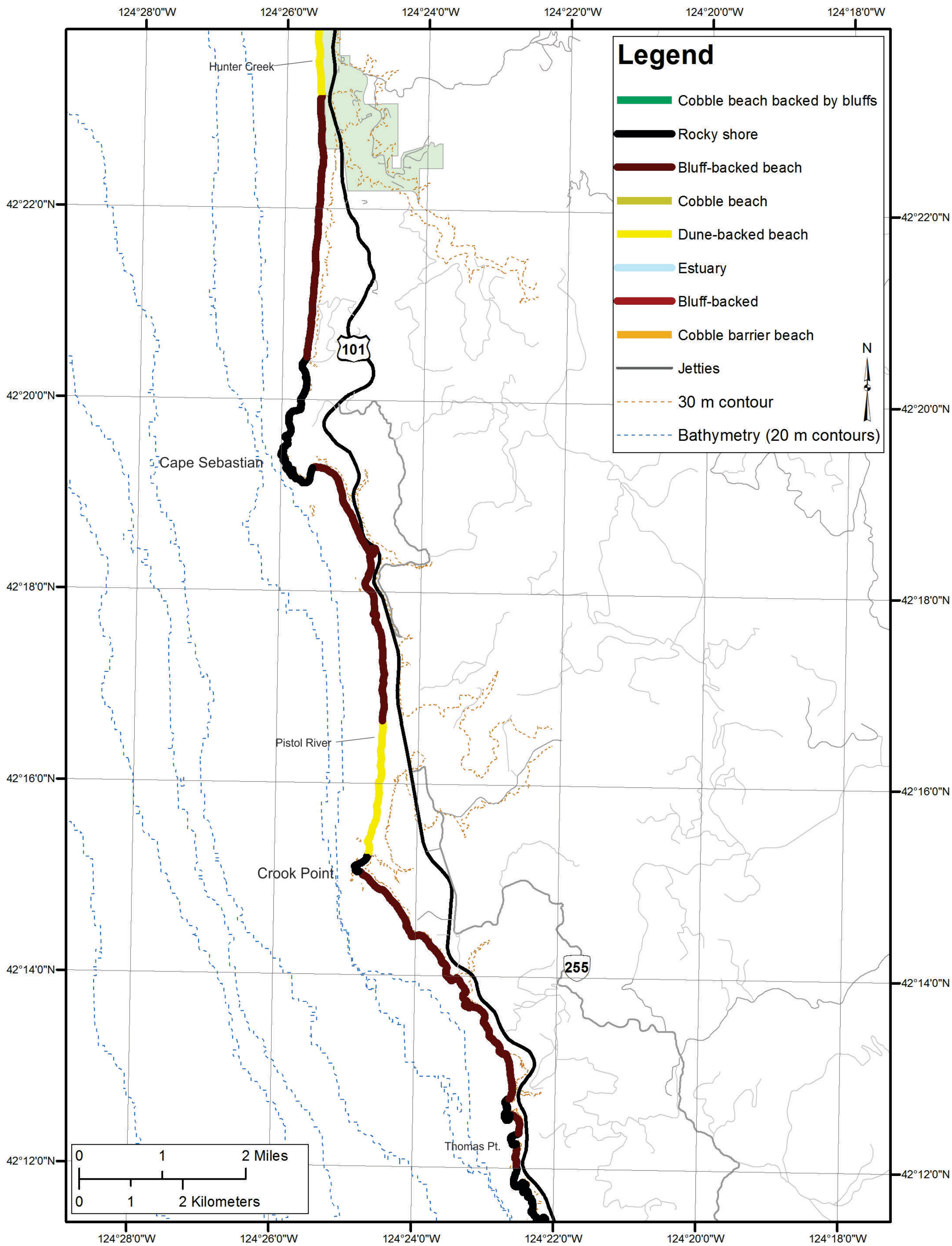

Figure 2-11. Geomorphic classification of the Cape Sebastian–Crook Point region (Thomas Point to Hunter Creek).

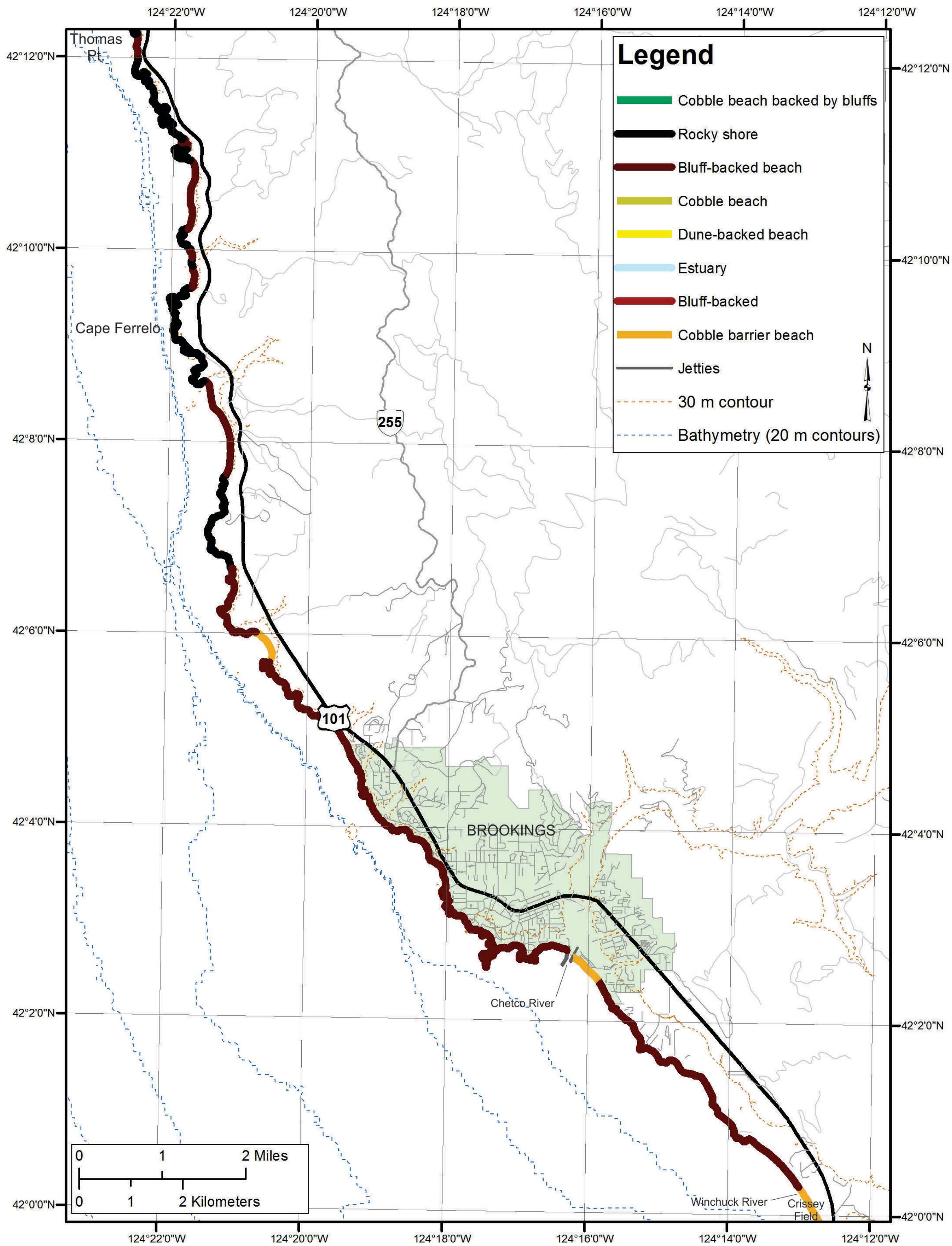

Figure 2-12. Geomorphic classification of the Brookings region (Crissey Field to Thomas Point).

2.4 Coastal Erosion and Flood History

2.4.1 Curry County historical shoreline positions

This section presents a qualitative discussion of large-scale morphological changes derived from analyses of historical and contemporary shorelines derived for the Curry County coastline. This summary stems from work undertaken by researchers at DOGAMI and OSU over the past decade (Allan, 2005; Allan and Stimely, 2013; Ruggiero and others, 2013).

National Ocean Service (NOS) Topographic (T)-sheet shoreline positions covering the 1920s and 1950s were previously obtained from NOAA (Allan and Priest, 2001). These lines reflect the Mean High Water (MHW) line mapped by early NOS surveyors, on an average tide typically in mid- to late summer. Additional shorelines were derived from a variety of other sources including: 1967 digital orthophotos (Ruggiero and others, 2013), 1980s era U.S. Geological Survey topographic maps, 1994 digital orthophotos, and from 1998, and 2002 lidar data (Allan and Stimely, 2013). Pre-lidar historical shorelines use the High Water Line (HWL) as a shoreline proxy. The HWL has been used by researchers for more than 150 years because it could be visually identified in the field or from aerial photographs. In contrast, shorelines derived from lidar data are datum-based and can be extracted objectively using a tidal datum, such as Mean High Water (MHW) or Mean Higher High Water (MHHW). Studies by Moore [2000] and Ruggiero and others [2003] note that HWL-type shoreline proxy are virtually never coincident with datum-based MHW-type shorelines. In fact, they are almost universally estimated to be higher (landward) on the beach profile when compared to MHW shorelines [Ruggiero and others, 2013]. According to Ruggiero and others, the average absolute horizontal offset between the HWL and MHW range from ~6 m (~19 ft) to as much as 50 m (164 ft), while the average is typically less than 20 m (65 ft). Offsets are typically greatest on flat, dissipative beaches where the wave runup may be large and smallest where beaches are steep (e.g., gravel beaches).

Estimates of the uncertainty of HWL shoreline measurements have been assessed in a number of studies [e.g., Moore, 2000; Ruggiero and others, 2013]. These uncertainties reflect the following errors: 1) mapping methods and materials for historical shorelines (including the offset between the HWL and MHW shoreline), 2) the registration of shoreline positions relative to Cartesian coordinates, and 3) shoreline digitizing, and have been summarized in **Table 2-1**.

Table 2-1. Average uncertainties for Pacific Northwest shorelines (Ruggiero and others, 2013).

	NOS T-Sheets (1800s to 1950s)		DRGs (1940s to 1990s)		Aerial Photography (1960s to 1990s)		Lidar	
Total shoreline position uncertainty	18.3 m	60 ft	21.4 m	70 ft	15.1 m	50 ft	4.1 m	14 ft

Shorelines measured by DOGAMI staff using Real-Time Kinematic Differential Global Positioning System (RTK-DGPS) surveys of the beach are also available for a few select areas (Allan and Stimely, 2013). These latter data sets provide the most up-to-date assessments of the changes taking place along the coastline and have been collected since 2008 in order to document the seasonal to interannual variability in shoreline positions along the County. In all cases, the GPS shorelines reflect measurements of the Mean Higher High Water (MHHW) line located at an elevation of 2.07 m (6.8 ft). We have relied on the latter as opposed to the MHW line, because previous studies indicate that MHHW most closely approximates the MHW line surveyed by early NOS surveyors. Errors associated with these products are described by Moore (2000). GPS shoreline positioning errors, a function of the orientation of the GPS receiver relative to the slope of the beach, are estimated to be ~±0.1 to ±0.2 m (±0.3 to ±0.6 ft).

The approach adopted here is to describe the broad morphological changes identified along the coast, beginning in the south at Crissey Field and progressing northward toward Port Orford.

2.4.1.1 Crissey Field

The Crissey field subcell makes up the northern portion of the larger Smith River littoral cell, located in northern California. The beach is bounded in the north by the Winchuck River and in the south by Crissey Point. Although the south end of this beach system is characterized by a small headland that may limit the alongshore movement of beach sand, it is extremely unlikely that this occurs. Instead, sand is probably transported just offshore of the headland, where the water is not too deep, enabling the sand to be freely exchanged both to the north and south of this boundary.

Figure 2-13 and **Figure 2-14** present the historical and contemporary shoreline positions for the area between Crissey Point and the Winchuck River. As can be seen in **Figure 2-13**, the overall configuration of the shore did not appear to change greatly between 1928 and 1967, a period of some 39 years, with both shorelines having followed very similar tracts along the entire length of this beach. However, of interest in the north is the southward inflexion of the Winchuck River channel in 1928, placing the channel in close proximity (i.e., to the immediate north) to the existing Oregon Parks and Recreation Department (OPRD) Welcome Center. This region has likely remained susceptible to periodic river flooding. For example, it is apparent in **Figure 2-14** that there is a significant amount of woody debris distributed along the banks of the river and around the river mouth. Furthermore, portions of this area continue to exist as a wetland, further emphasizing its low-lying nature and its close association to the Winchuck River.

Between 1967 and the 1980s the beach foredune advanced seaward by some 70 m (230 ft) in the north around the mouth of the river, while eroding in the southern half of the cell. This response may be associated with the earlier 1982/83 El Niño, which could have resulted in "hotspot" erosion at the south end of the subcell, with the removal of these sediments to the north causing the shore to advance seaward. It is also possible that accretion in the north is linked to the movement of sand from south of Crissey Point, around the point where it has been subsequently redistributed to the north. Although not included in **Figure 2-13** and **Figure 2-14**, the beach did erode slightly in the north between 1980s and the early 1990s, but by 2002 had again shifted seaward again. Since 2002, the entire shoreline has maintained its present configuration as measured by the 2008 lidar and our subsequent survey of the beach using GPS in August 2013.

The response of the beach over the past two decades highlights the dynamic nature of such beaches as they respond to variations in the incident wave energy and nearshore currents. However, of interest is the period of beach advance that occurred between 1967 and the early 1980s; the advance suggests either an extended period of relatively quiet wave conditions (i.e., lower wave energy levels) in which the waves were arriving out of the southwest creating a northward transport of sand along the coast, and/or above average sediment supply to the beach system from the Smith River to the south. The latter is likely, given the accumulation of sand to the south of Crissey Point, which has resulted in the development of a well-vegetated backshore and dune system in front of a terrace that previously must have been subject to wave erosion.

Finally, much of the foredune that was originally active (i.e., subject to wave erosion) in the 1960s has since been stabilized both by European beach grass and with low stands of Sitka spruce (dashed red line in **Figure 2-14**). Under today's wave climate regime, the original 1967 shoreline is now characterized by the location of the beach-dune junction.

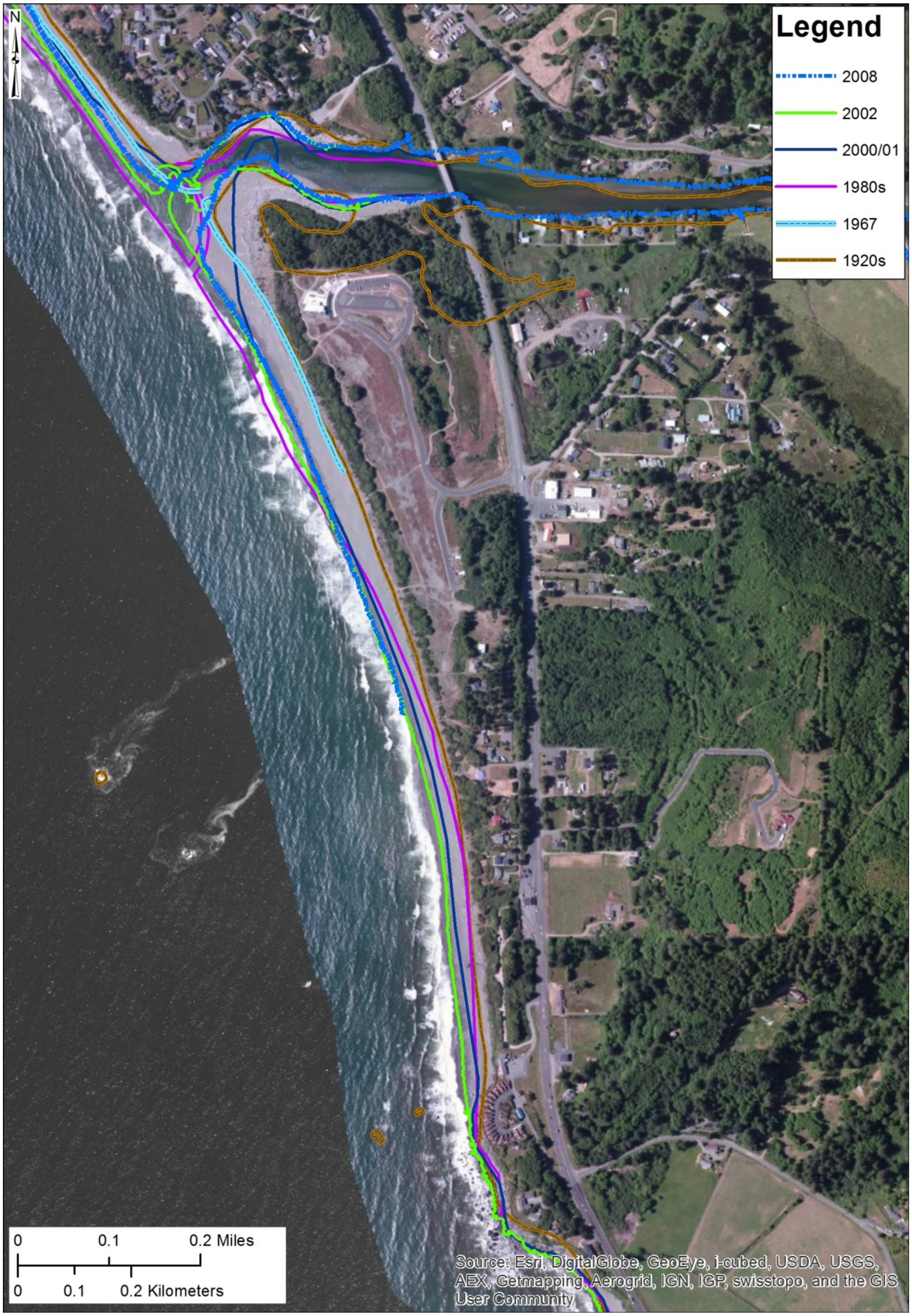

Figure 2-13. Historical and contemporary shoreline changes identified at Crissey Field and overlaid on a 2014 digital orthophoto.

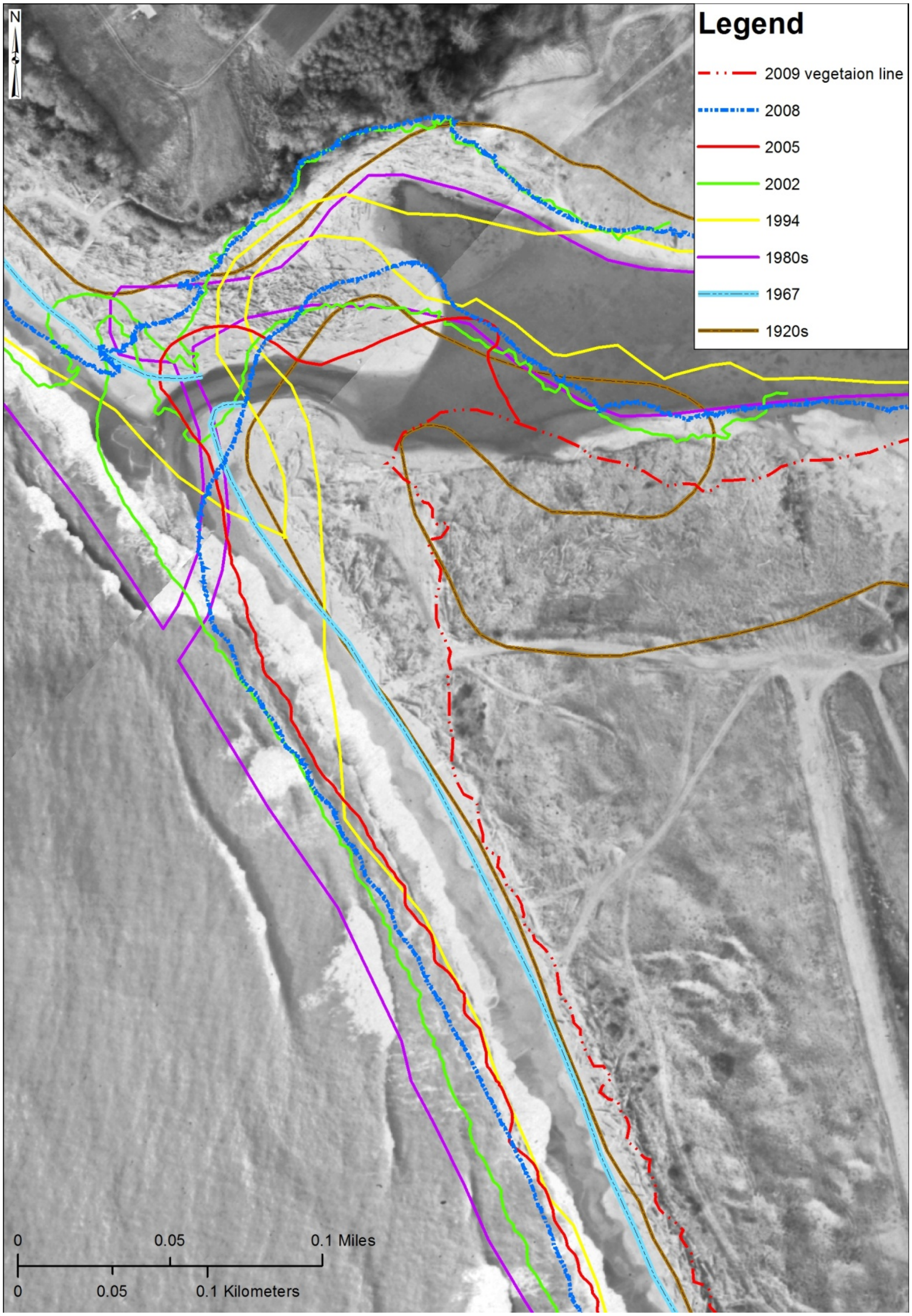

Figure 2-14. Detailed perspective of historical and contemporary shoreline changes identified adjacent to the Winchuck River at Crissey Field. These data have been overlaid on a 1967 digital orthophoto. Note the significant changes that have occurred in the beach and foredune between 1967 and 2008.

2.4.1.2 Brookings

As described previously, the bulk of the Brookings shoreline consists of high bluffs composed of mostly resistant sandstones. Erosion is considered to be relatively low throughout the study area, with the most significant shoreline changes having occurred near the Chetco River mouth (**Figure 2-15**). As with other areas on the Oregon coast, jetty construction (completed in 1957), and subsequent extension of an additional 137 m (450 ft) in 1969, resulted in the shoreline prograding seaward on both sides of the jetties. From these data we estimate that between the 1920s and 2008 the shoreline advanced a net distance of ~30–35 m (98–115 ft) south of the river and about 20 m (66 ft) north side of the river. Overtopping and flooding have been identified to occur along the road south of the jetty and to some degree in the south near a Best Western Inn resort.

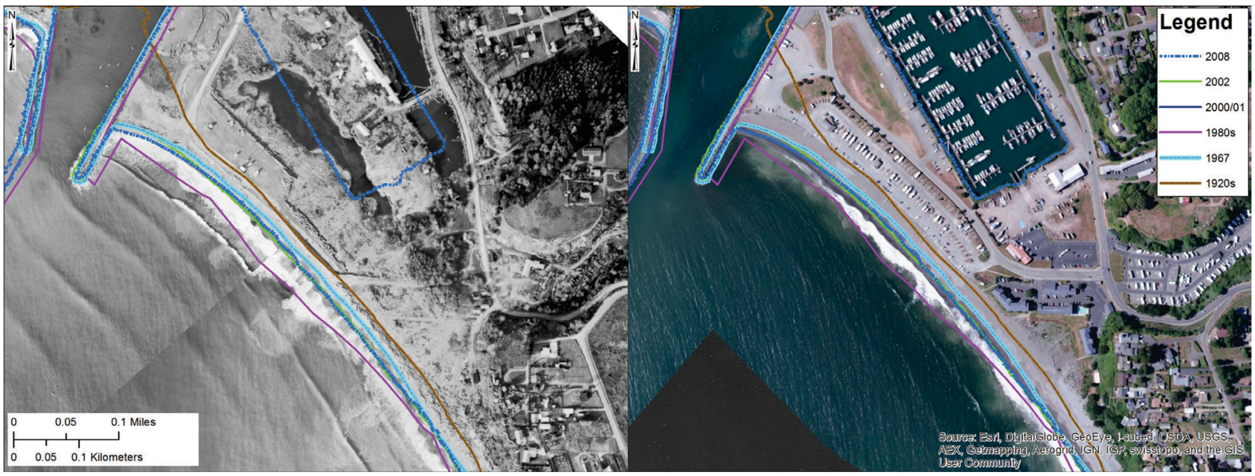

Figure 2-15. Left) Shoreline change adjacent to the Chetco River overlaid on a 1967 orthorectified image, and Right) on a modern aerial image highlighting the degree of change in the boat basin.

2.4.1.3 Gold Beach

South of the Rogue River the beaches highlight two contrasting states (**Figure 2-16**). Immediately north of Cape Sebastian the beaches are gaining sand and are actively prograding seaward (**Figure 2-16A**), while in the north nearest to the jetty the beaches are in an erosional phase (**Figure 2-16B**). **Figure 2-17** depicts the various historical shoreline positions derived from aerial photos, lidar, and beach surveys. From these data we can identify the following shoreline changes:

1. The beach immediately north (up to ~2 km [1.2 mi]) of Cape Sebastian (**Figure 2-17A**) has gained sand and over time has resulted in the shoreline advancing seaward by some 50–80 m (164–262 ft);
2. Immediately south of Hunter Creek (**Figure 2-17B**), the beach initially eroded (retreated) landward between 1928 and 1967. However, since the 1960s, the beach and shoreline has been aggrading, while the shoreline has prograded (advanced) seaward by ~60 m (197 ft), such that today the shoreline follows closely its original location as defined in 1928;
3. North of Hunter Creek (**Figure 2-17C**), a similar response can be seen with the beach having initially eroded landward between 1928 and 1967. Since 1967 the shoreline advanced seaward and by 1985 had reached its most accreted state ~100–130 m (328–426 ft) west of the 1967 shoreline. However, since 1985 the shoreline has eroded landward by some 60 m (197 ft) and is presently located either near its original 1928 location or is just seaward of the 1928 shoreline; and
4. Adjacent to the south Rogue River jetty (**Figure 2-17D**), the shoreline appears to have reached its most accreted state in the mid-1980s with considerable sand having built up against the south jetty. Since the 1980s, the beach has been in a predominantly erosional phase, with the shoreline having retreated landward by ~60–90 m (197–295 ft). Today, the shoreline is close to its original 1967 location.

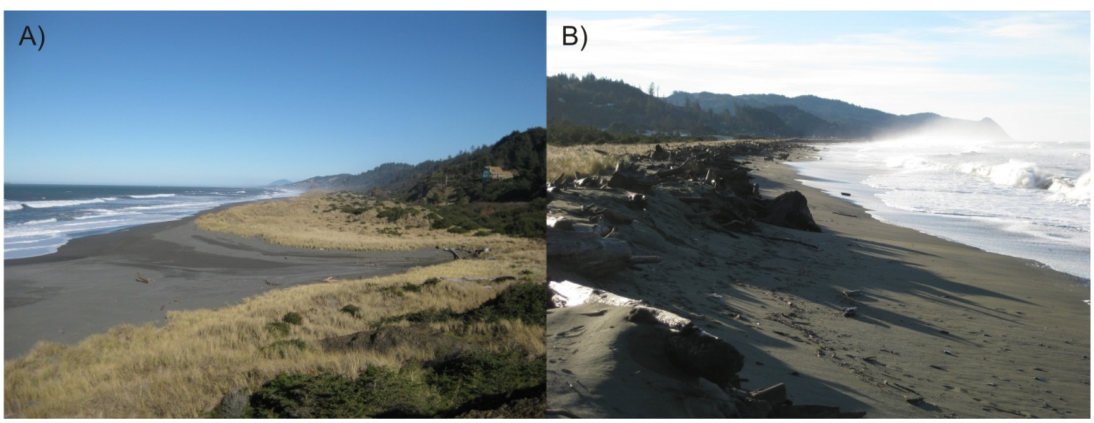

Figure 2-16. Contrasting beach and dune morphologies in the southern portion of the Gold Beach littoral cell. A) Development of a well-vegetated dune. The original 1967 shoreline position is probably depicted by the transition from the darker green brush line to the region dominated by dune grasses, while the low dune elevations west of the brush line indicate that the beach advanced (prograded) seaward rapidly. B) Erosion now appears to dominate beach response immediately south of the Rogue jetty (photo: J. Allan, DOGAMI, 2012).

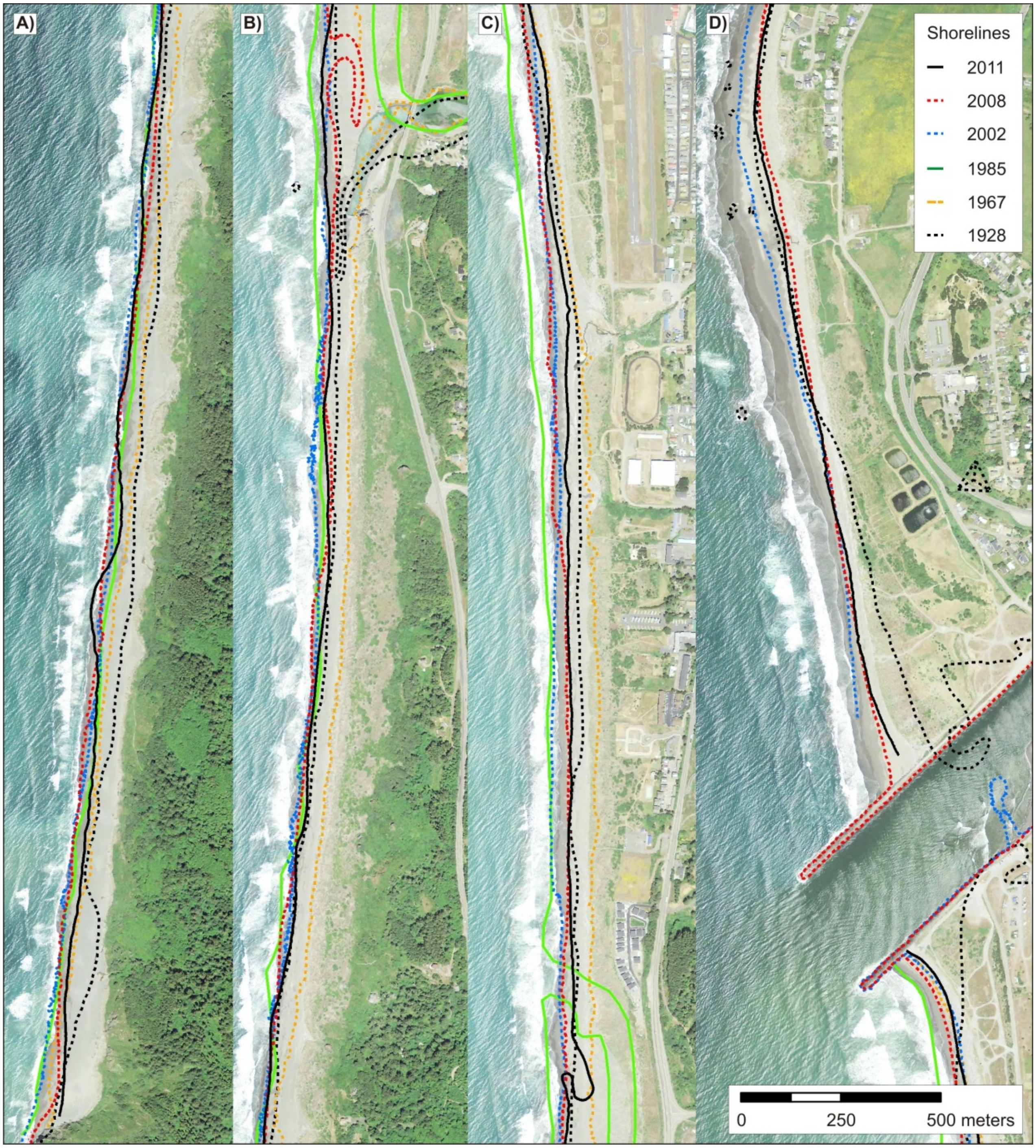

Figure 2-17. Shoreline changes south of the Rogue River. The images progress left to right from Cape Sebastian in the south to Hunter Creek (top of B) to the Rogue River.

Erosion has been particularly acute in recent years near the mouth of Hunter Creek (**Figure 1-1**). **Figure 2-18** documents river channel changes adjacent to Hunter Creek, just south of the town of Gold Beach. As can be seen in the figure, Hunter Creek periodically experiences large shoreline excursions that may vary spatially by as much as ~1 km from its most northern position defined in a 1985 aerial image, to its southern most position which typically abuts against Kissing Rock. These variations are driven to a large degree by a combination of riverine discharge versus the accumulation and migration of sand at the mouth of the creek due to variations in wave approach angles that drive longshore currents and ultimately alongshore sediment transport. The latter process serves to cause sand build-up around the creek mouth and as these sediments build and shift about it deflects the creek channel accordingly. Although it is not immediately clear from the 1985 aerial photo why the channel was so far north, it is interesting to note that the northern position of the creek occurred two years after the major 1982-83 El Niño. It is well documented that El Niños result in significant alongshore shifts in sediment, with the southern ends of littoral cells typically experiencing greater erosion, while the northern ends of the cell tend to gain sand causing the shoreline to advance seaward. Associated with this migration of sand, El Niños also tend to produce a northward shift in the position of the mouths of estuaries and rivers (e.g., Komar, 1986, 1998; Allan and others, 2003), responses that are entirely consistent with the observed changes at Hunter Creek. In addition, it is interesting to note that the analyses of the 1985 shoreline described above, indicates that the beach north of Hunter Creek was located some 30–55 m west of the shores present position. This would suggest that the 1982-83 El Niño probably contributed to a substantial alongshore shift in the beach sediments that likely contributed to its overall 1985 migration to the north.

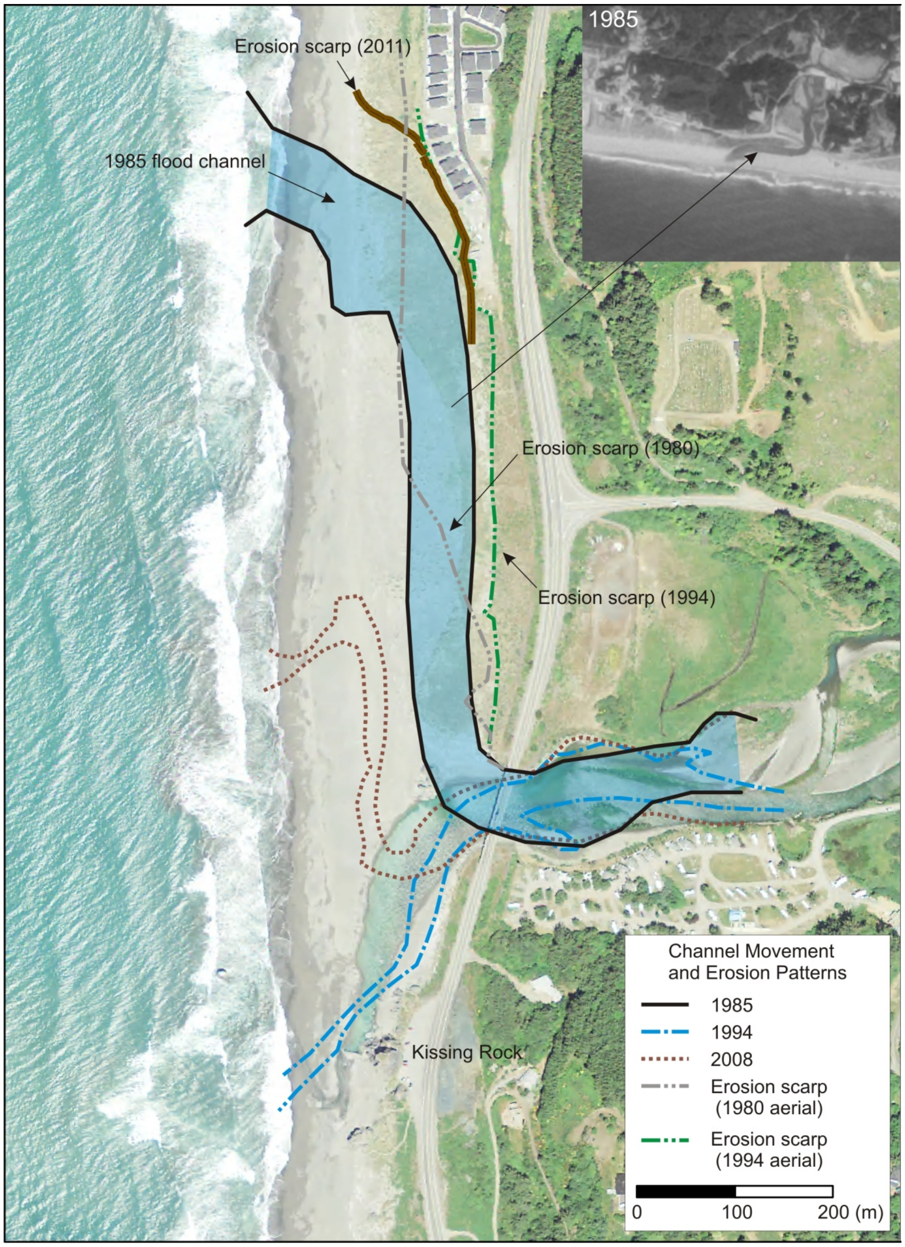

Figure 2-18. Hunter Creek channel migration patterns in 1985, 1994, and 2008.

Due to its northern position and high flows, the river eroded landward into a bank located immediately west of Highway 101, where the river formed an erosion scarp that can be clearly identified in aerial imagery (e.g., 1994 aerials) of the coast (**Figure 2-18**); this feature is also captured in the 2008 lidar data flown by DOGAMI and matches perfectly the location of the scarp in 1994. Examination of earlier aerial imagery obtained in 1951, 1977, and 1980 tends to reinforce the perception that the erosion scarp was indeed caused by the 1985 northward migration of Hunter Creek. Although we do not have any additional photos between 1985 and 1994, given the proximity of the erosion scarp to the flood channel in 1985, we can speculate that erosion of the bank continued for some time after the 1985 event due to ongoing influences associated with the river and from erosion from waves, which were now able to swash across the eroded channel and attack the back of the beach. As can be seen in **Figure 2-18**, by 1994 Hunter Creek had shifted back to the south, where it continued to fluctuate between its southern limit and a few hundred meters north of the bridge.

Recently, however, in early spring 2010, the creek once again shifted back to the north (**Figure 2-19**) exposing a series of groynes constructed by ODOT. These groynes were installed sometime in the late 1980s, presumably to protect U.S. Highway 101 by deflecting the creek away from the road, and having been installed in response to the 1985 erosion event. As can be seen in **Figure 2-18**, the northern most position of the creek channel (brown line) was measured in January 2011 with the aid of RTK-DGPS. As can be seen in **Figure 2-19** and **Figure 2-20**, migration of Hunter Creek this time resulted in the river shifting farther north and eroding landward, eventually reaching several homes that had been constructed close to the beach and immediately adjacent to the original erosion scarp documented in the 1994 orthophoto. As a result of this recent phase of erosion, home owners mobilized rapidly to mitigate the problem by constructing a riprap revetment in front of their properties. While the problem stemmed originally from the movement of the channel, the lowering of the elevation of the beach throughout this area enabled waves to easily crest the beach and erode the bank, on top of which the homes had been built.

Coastal shoreline changes for the northern Gold Beach subcell (Rogue River to Otter Point) is presented in **Figure 2-21**. Based on these patterns three broad responses are apparent:

1. The beach and shoreline north of the Rogue River is presently eroding and has been retreating since at least the mid 1960s. The erosion extends at least 1.6 km (1 mile) north of the Rogue, with the greatest shoreline retreat (~85 m [279 ft]) occurring adjacent to the jetty.
2. Adjacent to the community of Rogue shores, the beach appears to be a hinge point, separating the erosion in the south from accretion to its north.
3. North of Rogue Shores, the beach is actively accreting and prograding, with the shoreline having advanced seaward by about 50–80 m (164–262 ft).

Figure 2-19. In early spring 2010, Hunter Creek once again migrated northward to such an extent that it began to erode the toe of several homes constructed immediately adjacent to the creek and beach. Note the locations of at least two of the groynes, which are depicted by the two prominent horns at the back of the beach around mid-photo (photo: Ron Sonneville, Geotechnical Consultant, TerraFirma, April 9, 2011).

Figure 2-20. Homeowners attempt to mitigate the erosion caused by a combination of riverine channel erosion and wave runup and overtopping of the barrier beach. Photo shows DOGAMI geologist Laura Stimely surveying the toe of the erosion scarp (photo: J. Allan, DOGAMI, 2012).

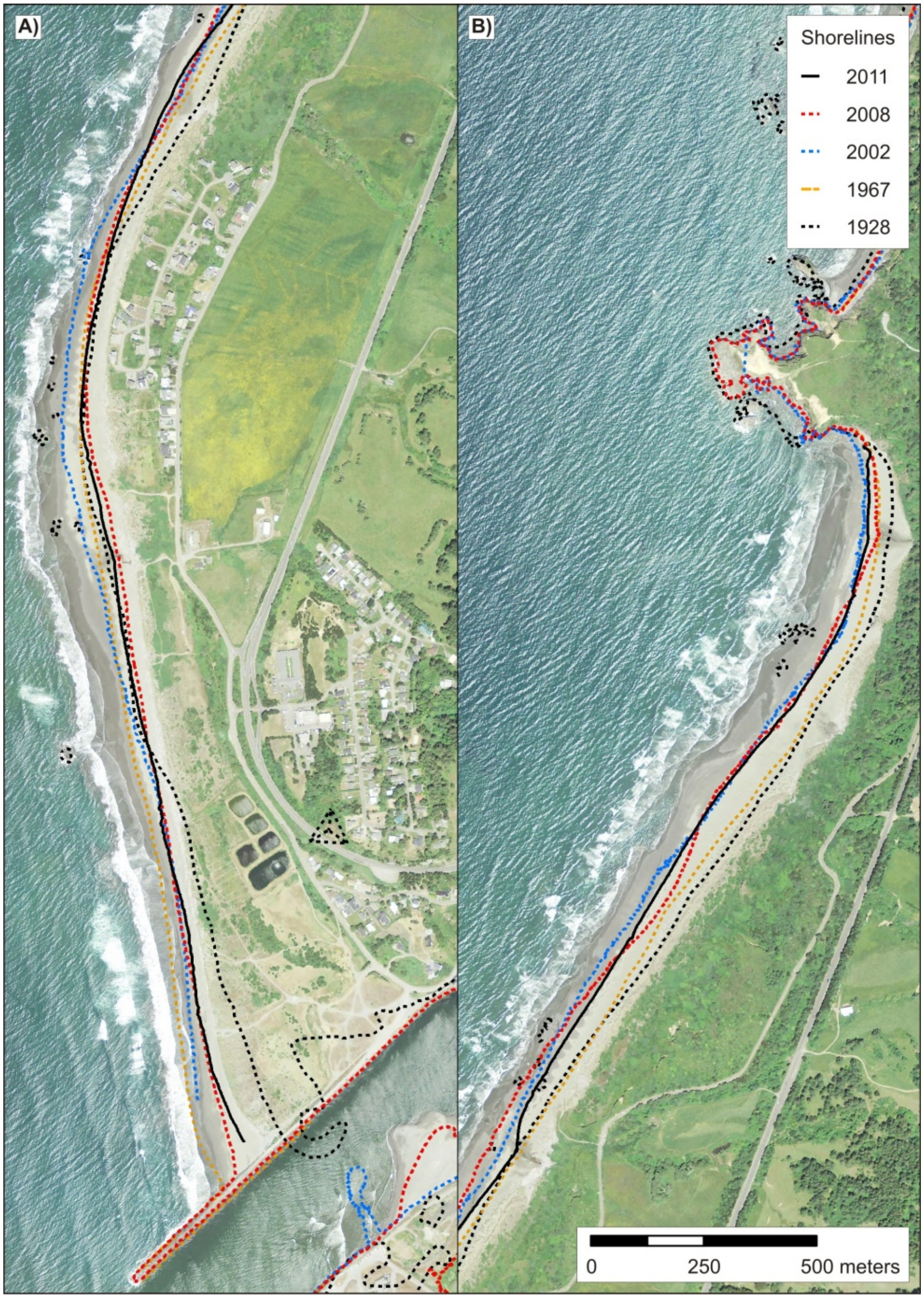

Figure 2-21. Shoreline changes in the northern Gold Beach subcell (Rogue River to Otter Point), including the community of Rogue Shores. The images progress left to right from the Rogue River in the south to Otter Point in the north.

2.4.1.4 Nesika Beach

Coastal shoreline changes for the Nesika Beach littoral cell (Nesika to Sisters Rocks) is presented in **Figure 2-22**. Based on these patterns three broad responses are apparent:

1. The beach and shoreline in front of the community of Nesika beach is presently eroding and has been retreating since at least the late 1920s (**Figure 2-22A**). The area of greatest erosion extends at least 1.4 km (0.9 mile) from the southern end of the cell, with the shoreline having retreated by as much as ~50 m [160 ft]) since the late 1920s. Erosion of the bluffs extends at least another 1 km (0.6 mi) to the north for a total of 2.4 km (1.5 mi) north of the south end of the cell.
2. North of the community of Nesika and about 1.2 km (0.75 mi) south of the Ophir Creek, the shorelines fluctuate considerably, with little to no evidence of a prevailing trend (**Figure 2-22B**). However, as can be seen from the 2011 recently surveyed shoreline, this portion of the coast is strongly influenced by rip embayments. For example, the break in the 2011 shoreline depicted in **Figure 2-22B** reflects the formation of a large rip (**Figure 2-23**) that extended to the base of the riprap that presently protects U.S. Highway 101, enabling waves at the time to directly attack the toe of the revetment.
3. Just south of the Ophir Creek to Sisters Rocks, the shoreline is presently in an accreted state, with the mean shoreline located some 50 to as much as 100 m seaward of the 1967 shoreline (**Figure 2-22C,D**) suggesting that this portion of the cell is actively prograding seaward.

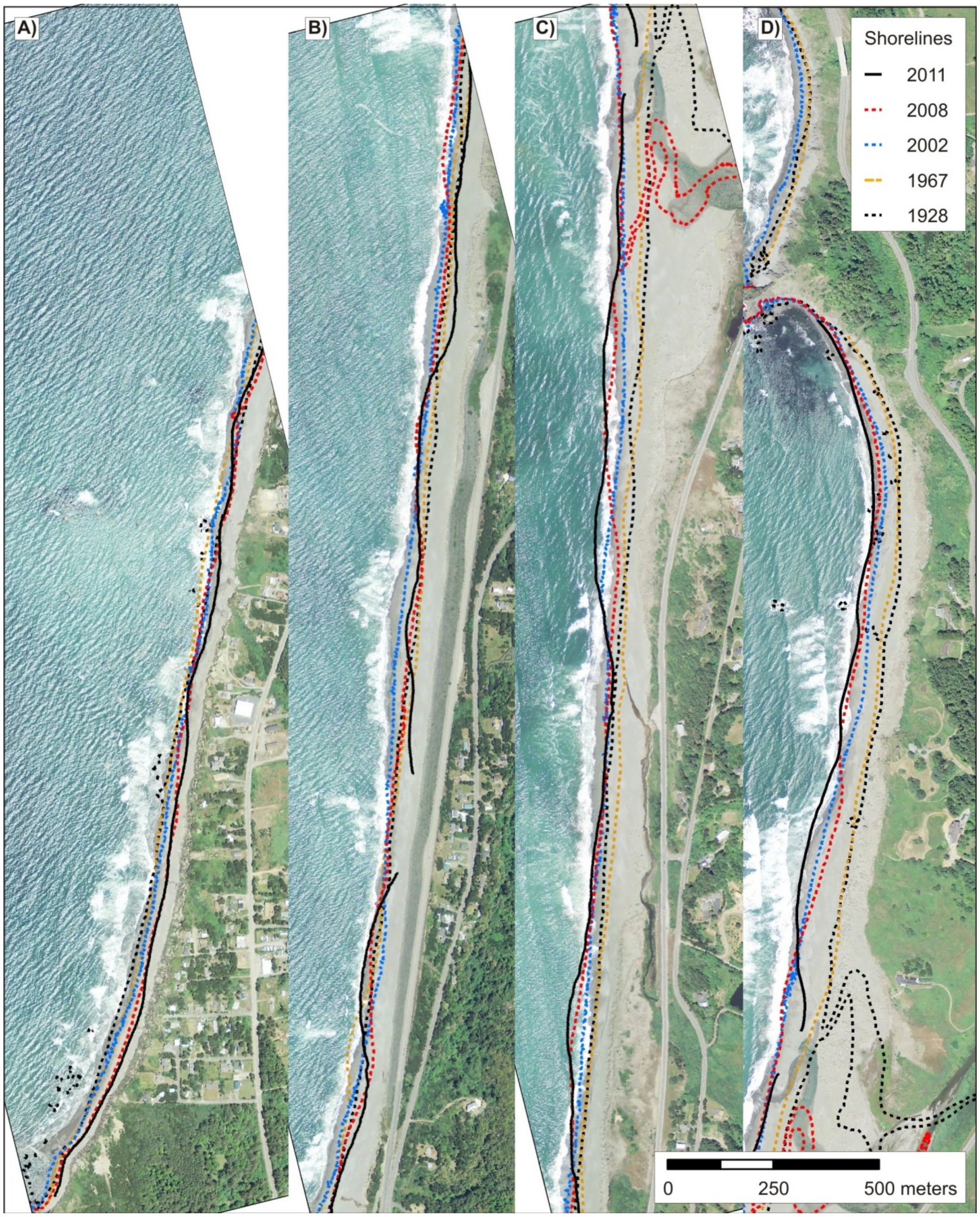

Figure 2-22. Shoreline changes in the Nesika Beach littoral cell. The plates progress left to right from Nesika Beach in the south to Sisters Rock in the north (top of D).

Figure 2-23. Development of a rip embayment adjacent to U.S. Highway 101 is allowing waves to directly attack the toe of the revetment. The photo was taken on February 16, 2011, at low tide (photo: J. Allan, DOGAMI, 2012).

Figure 2-24 and **Figure 2-25** provide more detailed views of the erosion of the coastal bluffs along the Nesika Beach shore in order to derive more detailed estimates of the erosion rates along this shore (**Figure 2-26**). Mapping was undertaken for two distinct areas.

1. The toe of the bluff was mapped using 1967 orthorectified aerial imagery. The mapping was accomplished by identifying distinct breaks between the top of the beach and the active vegetation line. A similar approach was carried out using 2009 orthorectified aerial images, coupled with high-resolution lidar data flown by DOGAMI in 2008. Additional measurements were carried out using detailed RTK-DGPS mapping of the toe of the bluff in February 2011, which was achieved by mapping the toe of the bluff with the GPS mounted on a backpack; and
2. The top of the bluff was mapped using the 2008 lidar data and field-based mapping of selected sites carried out with the GPS equipment. The former was accomplished in GIS by looking for distinct (sharp) breaks in the slope contours (i.e., the bluff and backslope geomorphology). In contrast, the latter was achieved by carefully locating the GPS along the edge of the bluff top. No attempt was made to map the top of the bluff from the 1967 aerial imagery due to the difficulties associated with this process.

Figure 2-24. Bluff toe changes at Nesika Beach, Oregon, between 1967 and 2008.

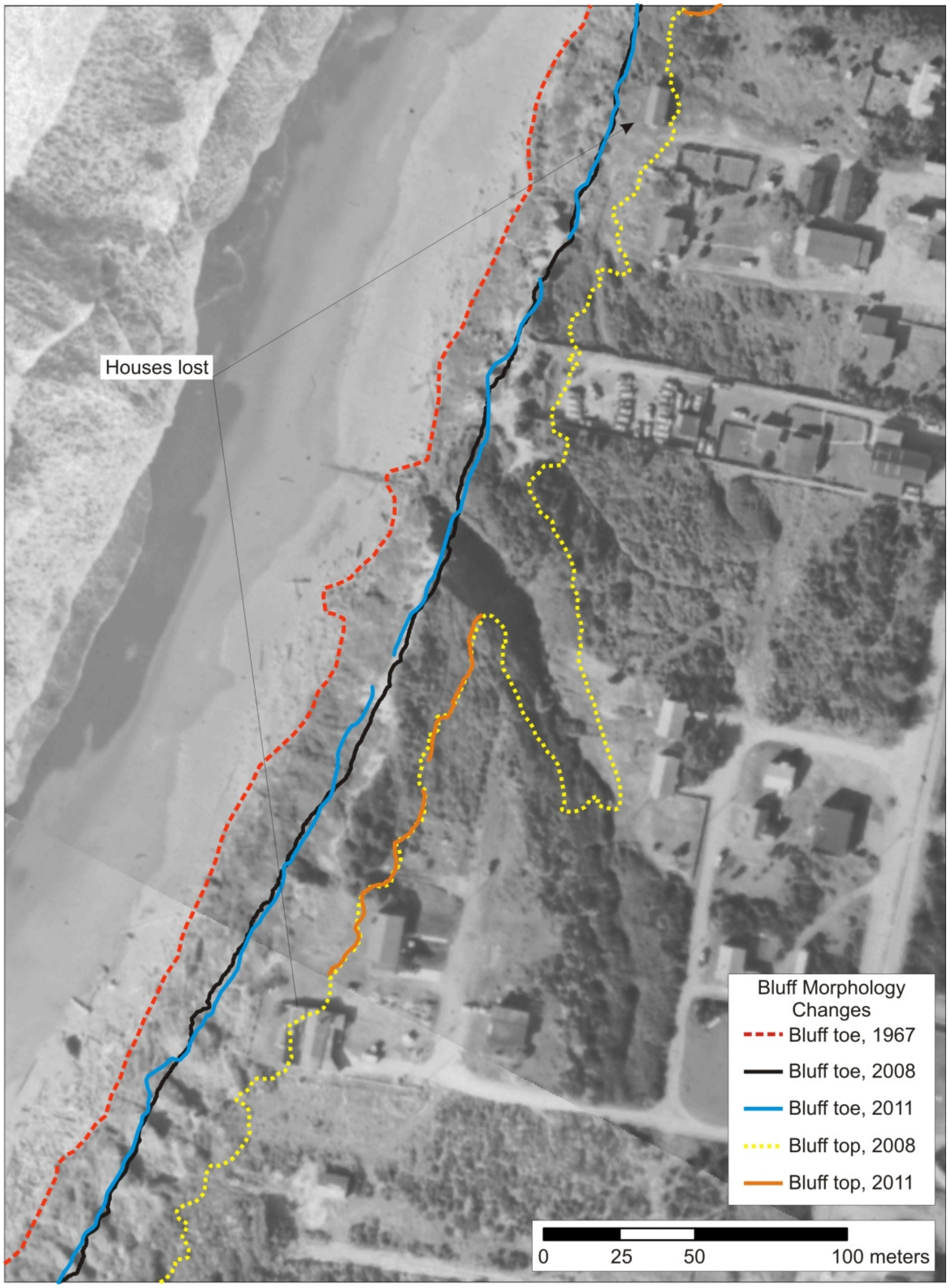

Figure 2-25. Close-up view of geomorphic changes (bluff toe and top) along a portion of the Nesika Beach shore depicted on a 1967 orthorectified image. Note the two homes identified in the 1967 aerial images that have subsequently been lost due to retreat of the bluffs.

As depicted in **Figure 2-26** (left plot), the mean change in the toe of the bluffs between 1967 and 2008 was determined to be −15.4 m (−50.5 ft), with a standard deviation (σ) of ±7.1 m; ±1σ about the mean gives an erosion range of −8.3 to −22.5 m (−27.2 to −73.8 ft), while the total range was found to vary from +2.4 m to −30 m (+7.9 to −98.4 ft). (±1σ equates to 68.2% of all measured values and provides a good measure of the typical range of responses along a given shore) This equates to an average bluff-retreat rate of -0.38 m/yr (−1.25 ft/yr), while ±1σ about the mean gives a range of -0.20 to −0.55 m/yr (−0.66 to −1.8 ft/yr). These values are slightly lower than the erosion rates determined by Priest and others (2004), who identified an average erosion rate of ~0.58 m/yr (−1.9 ft/yr) based on discrete measurements of the shore. As can be seen from **Figure 2-25**, our recent mapping of the bluff toe and (bluff top) reveal that the erosion along the bluff top has changed little since the lidar was flown in 2008. Nevertheless, a few discrete sections of shore have experienced some 2–3 m (6.6–9.8 ft) of additional retreat, causing the bluffs to become over-steepened in those areas. The absence of significant shorewide changes along the Nesika bluffs is probably not surprising given the relatively mild winters observed during the past few years, with generally nominal wave activity (particularly when compared to storm wave runup during the late 1990s) and hence generally lower wave runup and wave impact at the toe of the bluffs. Despite this, it is very clear that this section of coast remains highly vulnerable to wave attack, such that the next period of heightened storm wave activity will almost certainly re-invigorate bluff toe erosion, which will lead to over-steepening of the bluffs and their eventual collapse and subsequent retreat. As Priest and others (2004) concluded, the Nesika Beach shore continues to be characterized by some of the highest bluff toe erosion rates measured thus far on the Oregon coast and care must be taken when sitting new development along the bluffs, providing appropriate set-back from the edge of the bluffs.

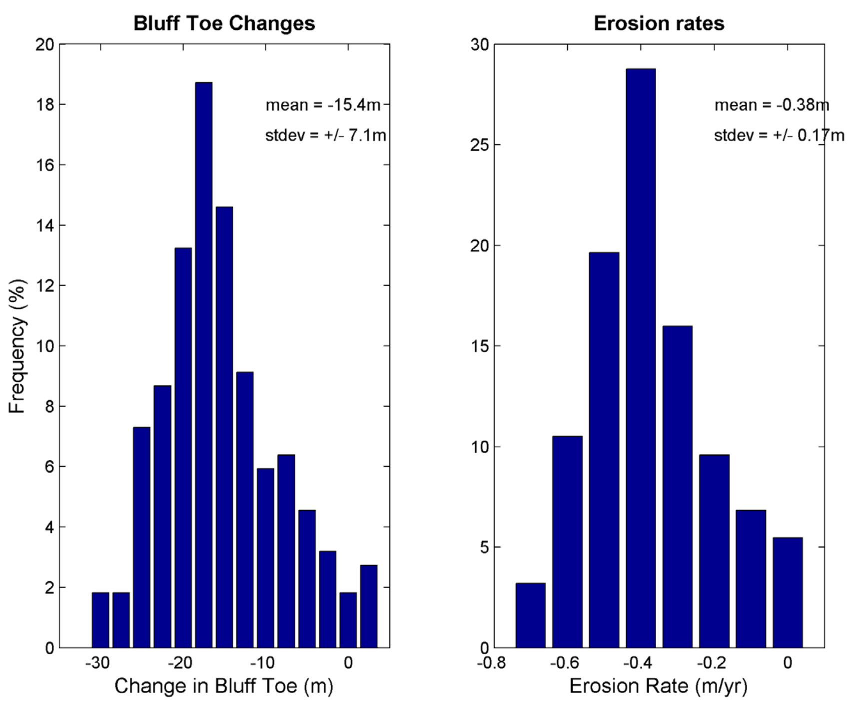

Figure 2-26. Left) Histogram showing the net change in the position of the toe between 1967 and 2008 and Right) the calculated erosion rates.

2.4.1.5 Port Orford

Garrison Lake is located within the Blanco littoral cell (**Figure 1-1**). The cell is bounded in the south by the Port Orford headland—"The Heads"—and Cape Blanco in the north. The beaches in this cell are characterized by mixed sand and gravel that results in steep beaches and narrow surf zones, which contributes to a highly dynamic system with rapid shoreline changes. Of particular interest are the shoreline changes that have occurred in the community of Port Orford itself, at the south end of the cell, the ocean shore opposite Garrison Lake. This area experienced very significant erosion during the late 1990s, being a classic example of El Niño hotspot erosion (Komar, 1998b). The erosion losses became critical during the El Niño winter of 1997-98, with the rapid retreat of the fronting beach and then the erosion of a dune field that contained the drainage system for the city's sewage treatment facility. The major storms of the following winter broke through into Garrison Lake, draining it of fresh water, one of two sources of water for the community.

Figure 2-27 presents a range of shorelines overlaid on a 2014 aerial photograph, illustrating the extent of change since the 1920s. As can be seen in the figure, the 1976 shoreline tracks just seaward of its position in the 1920s, and reflects an accreted beach state. This would imply that during those 50 years this area was either relatively stable or that the beach and shoreline is capable of returning to its original position following major storms as defined by its initial position in the 1920s. This argument is further reinforced by the position of the 1967 and 2008 shorelines, which also track close to the 1920s shoreline position. The overall stability of the barrier beach between the 1920s until the 1982-83 El Niño is suggested also by the community's decision to place its sewage treatment drain field in the foredunes.

With the change in regional climate to one dominated by the occurrence of strong El Niños, the beach entered an erosional phase. Over the 10-year period between 1976 and 1986, the shoreline analyses in **Figure 2-27** show that the south end of the Blanco cell experienced rapid erosion, with the shoreline retreating ~80–100 m (262–328 ft). Part of this retreat occurred prior to the major 1982-83 El Niño, possibly under the action of the more moderate El Niños during the late 1970s. Very significant erosion occurred between 1982 and 1986, especially at the south end of Garrison Lake where the shoreline retreated 98 m (321 ft), undoubtedly a response to the hotspot erosion of the 1982-83 El Niño. While the shoreline experienced considerable erosion at that time, it did not result in the loss of foredunes to the extent that it threatened the sewage drainage field.

Following 1986, the beach accreted, and by 1994 it had regained much of the sand that had been eroded during the previous 18 years. This is typical of hotspot erosion zones, having been eroded by the northward transport of sand at the time of the El Niño, but with the slow return of the sand to the south during non-El Niño years the beaches rebuild. However, with the occurrence of the 1997-98 El Niño, the Port Orford shoreline again experienced considerable erosion. Consistent with the 1982-83 El Niño, the south end of the beach suffered hotspot erosion, cutting back the MHHW shoreline by a similar amount (~80–100 m [262–328 ft]) (**Figure 2-27**). This time the erosion cut back the foredunes to the extent that the sewage drainage field was undermined and partially lost. Additional erosion occurred during the following 1998-99 winter in response to a series of major storms. Due to the steeply sloping beach and narrow surf zone, the strong runup of the storm waves was able to overtop the crest of the 5 to 7 m high dunes, carrying salt water into Garrison Lake. With water added to the lake, together with water entering the lake from the heavy winter rains, the level of the lake rose to the extent that shoreline properties were flooded. Subsequent monitoring of the area, including the collection of lidar data in 2002 and 2008 indicate that the shoreline has once again prograded seaward in response to a return of sand to the south.

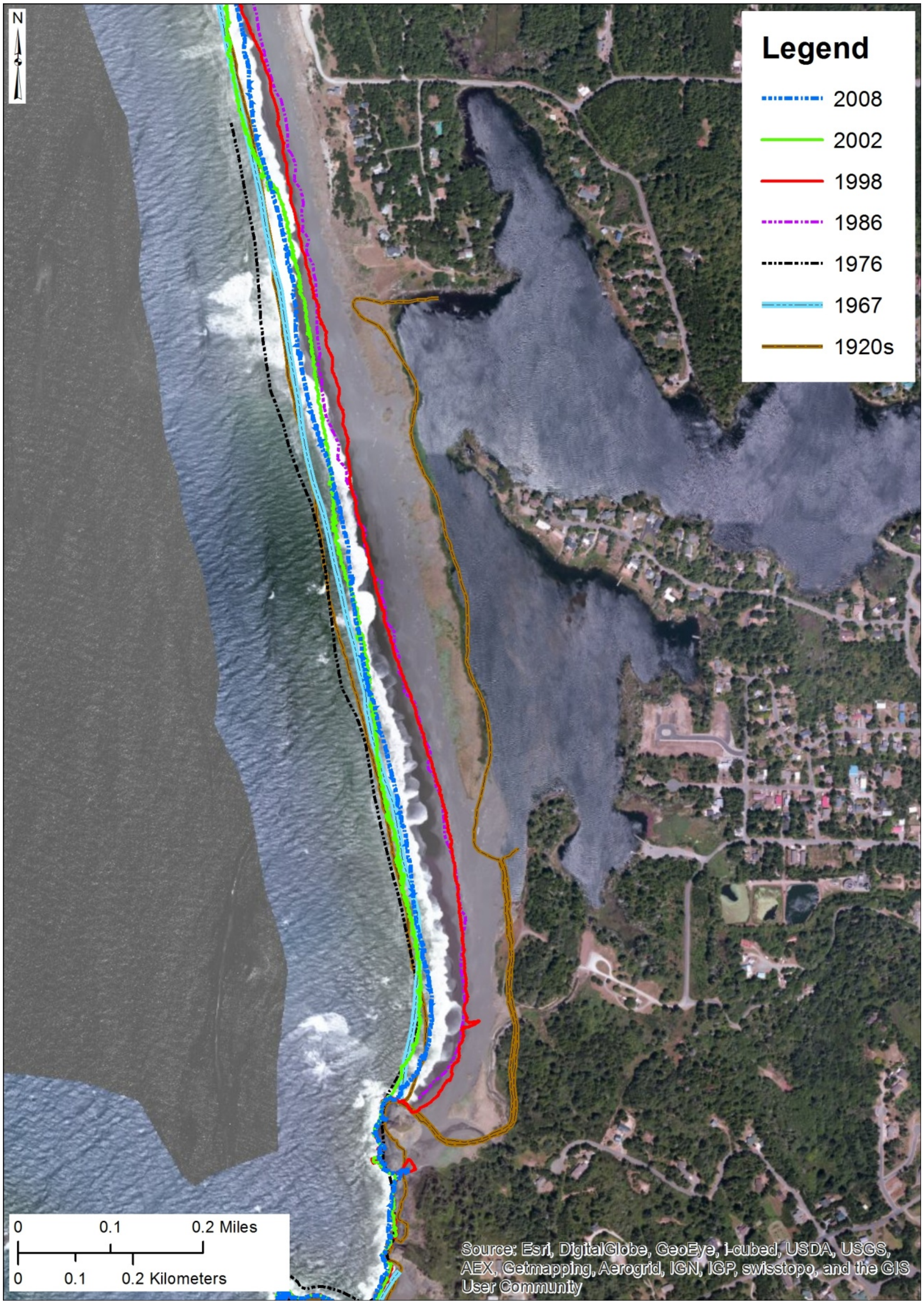

Figure 2-27. Hotspot erosion effects and shoreline variability at the south end of the Blanco cell, overlain on a 2014 aerial photograph.

3.0 BEACH AND BLUFF MORPHOLOGY ASSESSMENTS

Field surveys were undertaken throughout Curry County in both the winter and summer of 2013. These surveys serve two important objectives:

1. To establish beach profile transects along discrete but representative sections of the shoreline's geomorphology/geology, including sections of coast where coastal engineering structures have been constructed, for the purposes of coastal hydraulic analyses.
2. To provide representative measurements of the beach in its winter state whether it be derived from lidar or GPS data, in order to define the morphology, elevations, and slope of the beach face for use in subsequent wave runup and overtopping computations.

Surveying along the Curry County coast was initially carried out in early April 2013 at the end of the 2012-13 winter and again in late August 2013. The surveys were completed late in the winter season when Oregon beaches are typically in their most eroded state (Aguilar-Tunon and Komar, 1978; Komar, 1997; Allan and Komar, 2002; Allan and Hart, 2008). A total of 110 beach profile transects were established along the length of Curry County (**Figure 3-1** to **Figure 3-5**) and can be subdivided according to the following littoral cells:

- Brookings: 48 sites (includes the addition of one supplemental transect (7_13401) derived from lidar data);
- Gold Beach: 14 sites;
- Rogue Shores: 13 sites;
- Nesika Beach: 19 sites; and
- Port Orford: 16 sites.

Appendix B provides a table that describes the naming conventions used by DOGAMI, which may be linked to the final accepted DFIRM.

3.1 Survey Methodology

Beach profiles that are oriented perpendicular to the shoreline can be surveyed using a variety of approaches, including a simple graduated rod and chain, surveying level and staff, Total Station theodolite and reflective prism, light detection and ranging (lidar) airborne altimetry, and Real-Time Kinematic Differential Global Positioning System (RTK-DGPS) technology. Traditional techniques such as leveling instruments and Total Stations are capable of providing accurate representations of the morphology of a beach but are demanding in terms of time and effort. At the other end of the spectrum, high-resolution topographic surveys of the beach derived from lidar are ideal for capturing the three-dimensional state of the beach over an extended length of coast within a matter of hours; other forms of lidar technology are now being used to measure nearshore bathymetry out to moderate depths but are dependent on water clarity. However, the lidar technology remains expensive and is impractical along small segments of shore; more importantly, the high cost effectively limits the temporal resolution of the surveys and hence the ability of the end-user to understand short-term changes in the beach morphology (Bernstein and others, 2003).

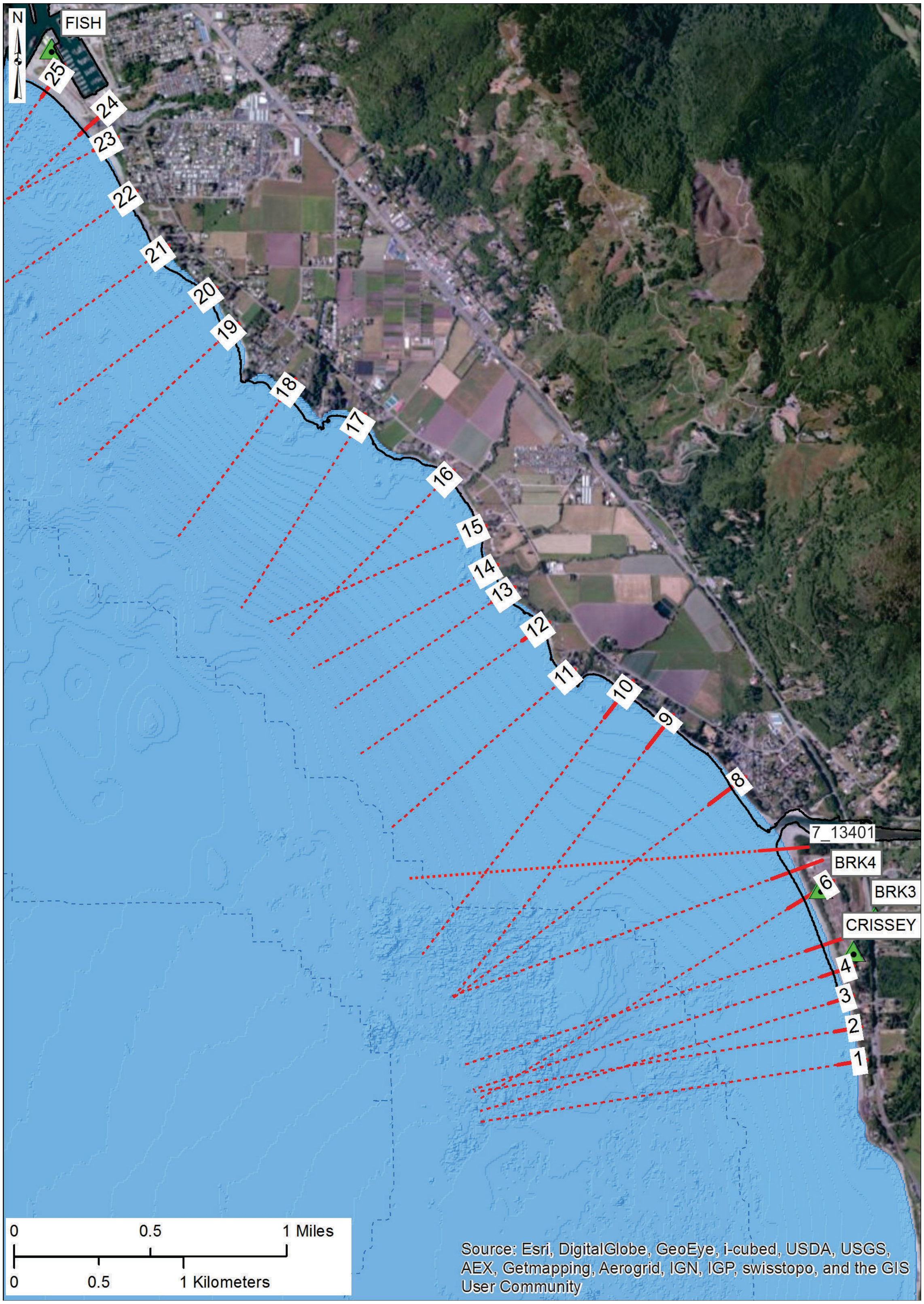

Figure 3-1. Location map of beach profiles measured south of the Chetco River in Brookings to the Oregon/California border. Solid and dashed red lines denote transect locations. Green triangles denote the locations of benchmarks used in local site calibrations.

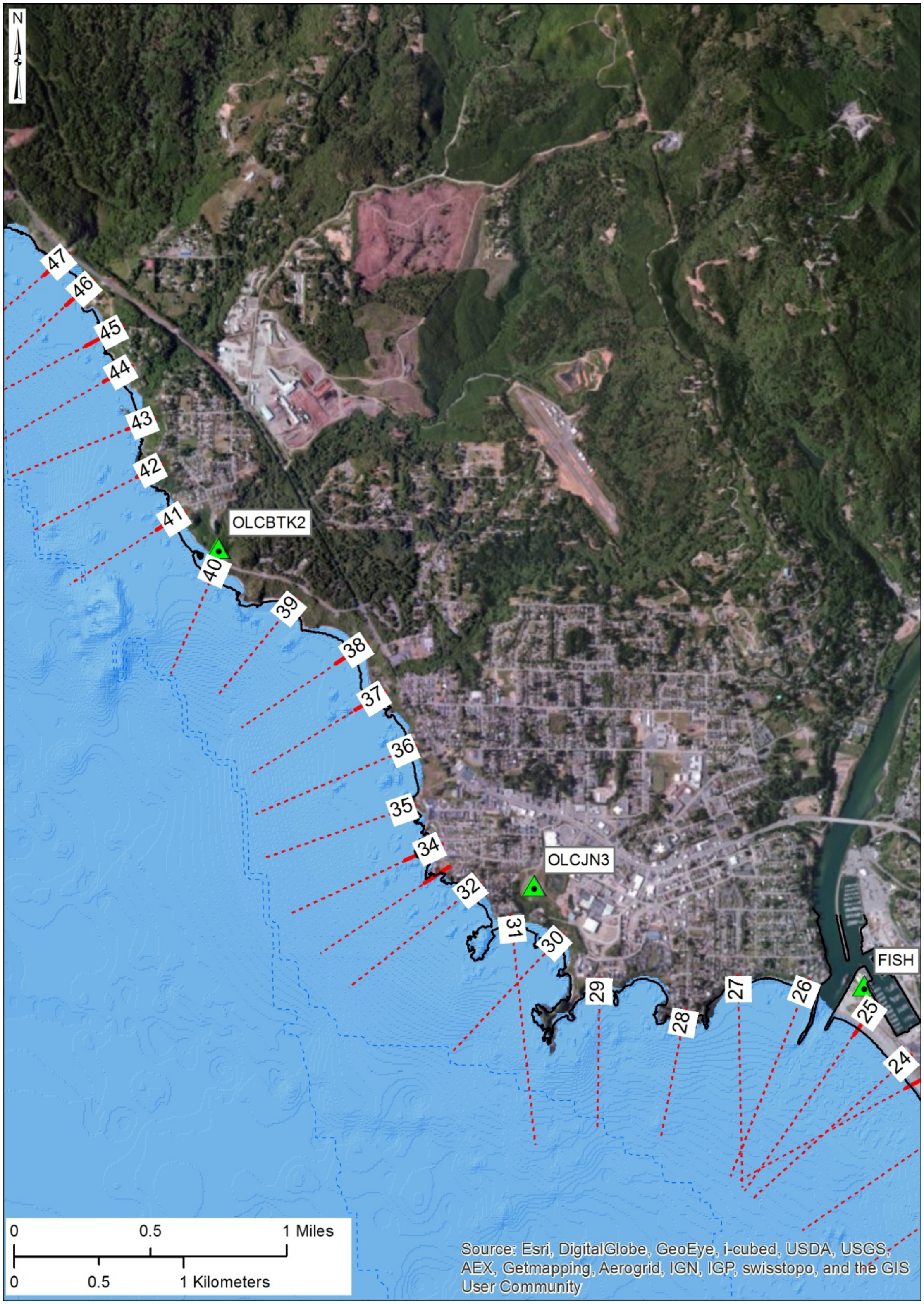

Figure 3-2. Location map of beach profiles measured north of the Chetco River in Brookings. Solid and dashed red lines denote transect locations. Green triangles denote the locations of benchmarks used in local site calibrations.

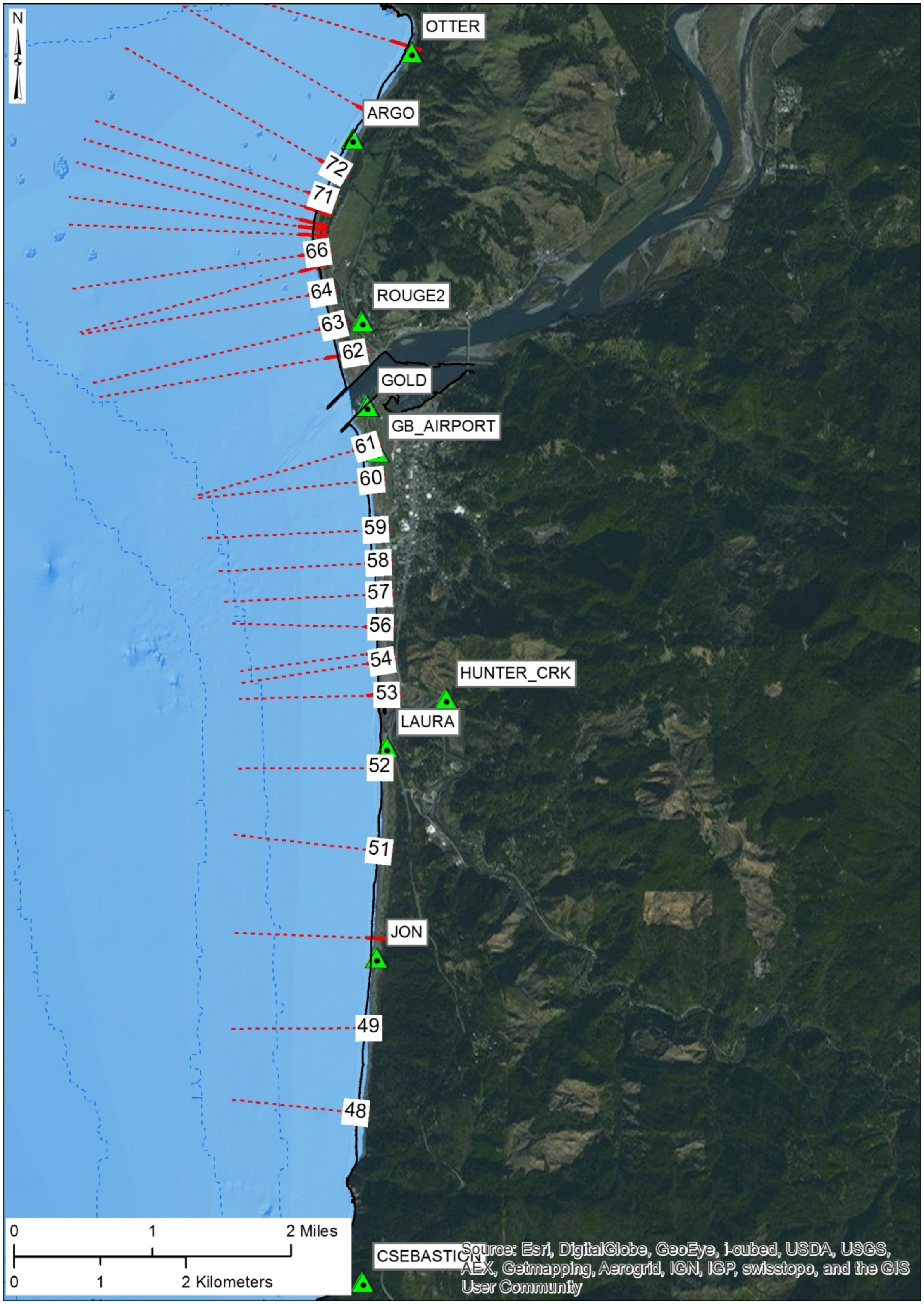

Figure 3-3. Location map of beach profiles measured in the Gold Beach littoral cell (north of Cape Sebastian and south of Otter Point). Solid and dashed red lines denote transect locations. Green triangles denote the locations of benchmarks used in local site calibrations.

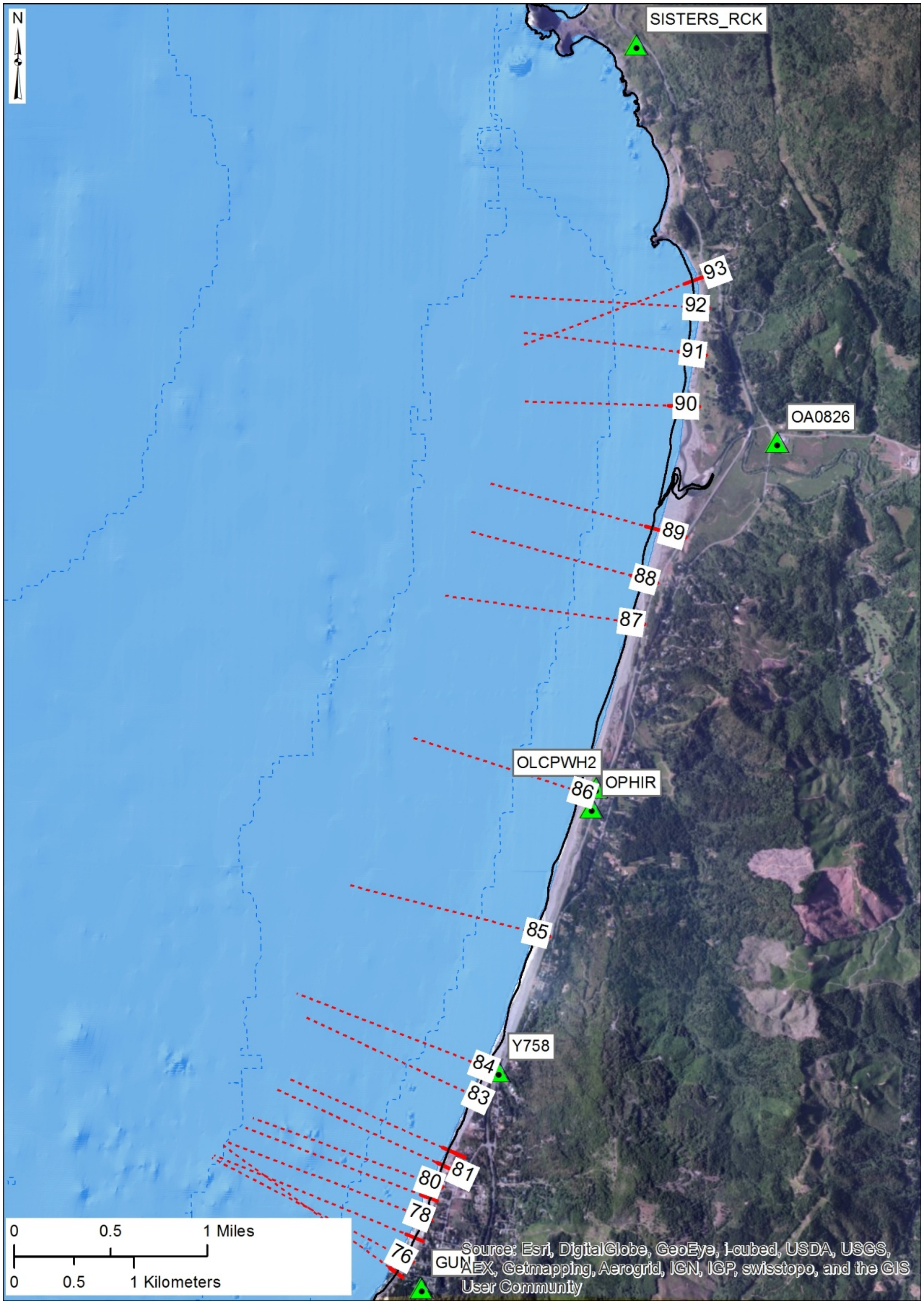

Figure 3-4. Location map of beach profiles measured in the Nesika Beach littoral cell (north of Hubbard Mound and south of Sisters Rock). Solid and dashed red lines denote transect locations. Green triangles denote the locations of benchmarks used in local site calibrations.

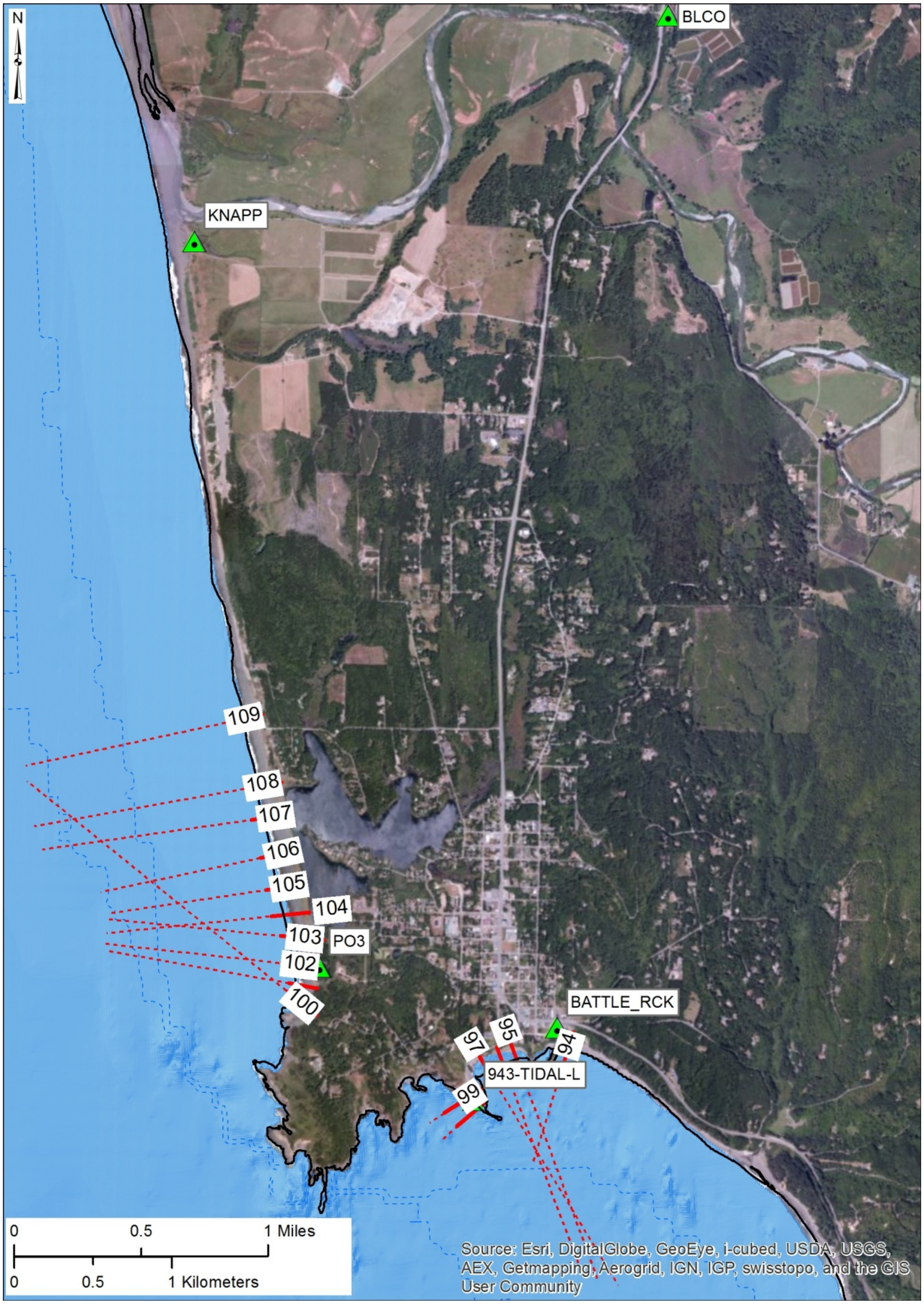

Figure 3-5. Location map of beach profiles measured in the vicinity of Port Orford and in the Blanco littoral cell (north of the Port Orford Heads and south of Cape Blanco). Solid and dashed red lines denote transect locations. Green triangles denote the locations of benchmarks used in local site calibrations.

Within this range of technologies, the application of RTK-DGPS for surveying the morphology of both the subaerial and subaqueous portions of the beach has effectively become the accepted standard (Morton and others, 1993; Ruggiero and Voigt, 2000; Bernstein and others, 2003; Ruggiero and others, 2005), and has been the surveying technique used in this study. The Global Positioning System (GPS) is a worldwide radio-navigation system formed from a constellation of 24 satellites and their ground stations, originally developed by the U.S. Department of Defense; in 2007 the Russian Government made their GLONASS satellite network available increasing the number of satellites to ~46 (as of February 2011). In its simplest form, GPS can be thought of as triangulation with the GPS satellites acting as reference points, enabling users to calculate their position to within several meters (e.g., using inexpensive off the shelf hand-held units), while survey grade GPS units are capable of providing positional and elevation measurements that are accurate to a centimeter. At least four satellites are needed mathematically to determine an exact position, although more satellites are generally available. The process is complicated because all GPS receivers are subject to error, which can significantly degrade the accuracy of the derived position. These errors include the GPS satellite orbit and clock drift plus signal delays caused by the atmosphere and ionosphere and multipath effects (where the signals bounce off features and create a poor signal). For example, hand-held autonomous receivers have positional accuracies that are typically less than about 10 m (<~30 ft), but can be improved to less than 5 m (<~15 ft) using the Wide Area Augmentation System (WAAS). This latter system is essentially a form of differential correction that accounts for the above errors, which is then broadcast through one of two geostationary satellites to WAAS-enabled GPS receivers.

Greater survey accuracies are achieved with differential GPS (DGPS) using two or more GPS receivers to simultaneously track the same satellites enabling comparisons to be made between two sets of observations. One receiver is typically located over a known reference point and the position of an unknown point is determined relative to that reference point. With the more sophisticated 24-channel dual-frequency RTK-DGPS receivers, positional accuracies can be improved to the sub-centimeter level when operating in static mode and to within a few centimeters when in RTK mode (i.e., as the rover GPS is moved about). In this study we used Trimble® 24-channel dual-frequency R7/R8 and 5700/5800 GPS receivers. This system consists of a GPS base station (R7 and/or 5700 unit), Zephyr Geodetic™ antenna (model 2), HPB450 radio modem, and R8 (and/or 5800) "rover" GPS (**Figure 3-6**). Trimble reports that both the R7/R8 and 5700/5800 GPS systems have horizontal errors of approximately ±1 cm + 1 ppm (parts per million × the baseline length) and ±2 cm in the vertical (Trimble, 2005).

To convert a space-based positioning system to a ground-based local grid coordinate system, a precise mathematical transformation is necessary. While some of these adjustments are accomplished by specifying the map projection, datum and geoid model prior to commencing a field survey, an additional transformation is necessary whereby the GPS measurements are tied to known ground control points (**Figure 3-7**). This latter step is called a GPS site calibration, such that the GPS measurements are calibrated to ground control points with known vertical and horizontal coordinates using a rigorous least-squares adjustments procedure. Performing the calibration is initially undertaken in the field by using the Trimble TSC2 GPS controller and then is re-evaluated in the office using Trimble's Business Office software (v2.5).

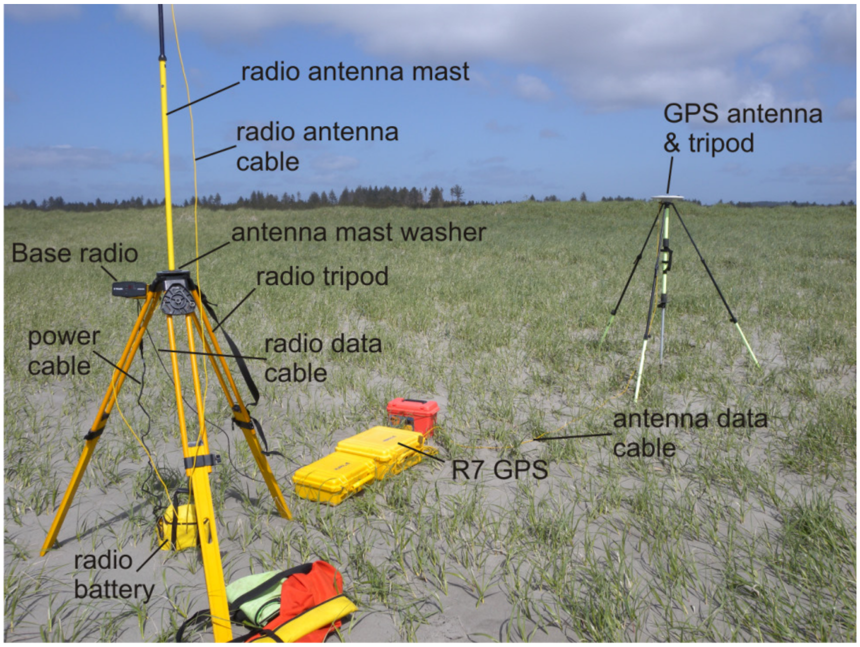

Figure 3-6. The Trimble R7 base station antenna in operation on the Clatsop Plains. Corrected GPS position and elevation information is then transmitted by an HPB450 Pacific Crest radio to the R8 GPS rover unit.

Figure 3-7. A 180-epoch calibration check is performed on a survey monument (ROUGE2) established in the Gold Beach littoral cell in Curry County. This procedure is important for bringing the survey into a local coordinate system and for reducing errors associated with the GPS survey (photo: J. Allan, DOGAMI, 2012).

3.1.1 Curry County survey control procedures

Survey control (**Table 3-1**) along the Curry County shore was provided by occupying multiple benchmarks established by the Coastal Field Office of DOGAMI. The approaches used to establish the benchmarks are fully described in the reports by Allan and Stimely (2013).

Coordinates assigned to the benchmarks (**Table 3-1**), were derived by occupying a Trimble R8 GPS receiver over the established benchmark, which then receives real-time kinematic corrections via the Oregon Real Time GPS Network (ORGN, http://www.theorgn.net/). The ORGN is a network of permanently installed, continuously operating GPS reference stations established and maintained by ODOT and partners (essentially a CORS network similar to those operated and maintained by the National Geodetic Survey [NGS]) that provide real-time kinematic (RTK) correctors to field GPS users over the internet via cellular phone networks. As a result, GPS users that are properly equipped to take advantage of these correctors, such as the Trimble system used in this study, can survey in the field to the one centimeter horizontal accuracy level in real time. Each benchmark was observed on a single occasion. Additional checking was undertaken for each of the GPS base station sites (**Table 3-1**), by comparing the multi-hour (and multi-day) GPS measurements to coordinates and elevations derived using the Online Positioning User Service (OPUS) maintained by the NGS (http://www.ngs.noaa.gov/OPUS/ [Soler and others, 2011]). OPUS provides a simplified way to access high-accuracy National Spatial Reference System (NSRS) coordinates using a network of continuously operating GPS reference stations (CORS, http://www.ngs.noaa.gov/CORS/). In order to use OPUS, static GPS measurements are typically made using a fixed height tripod for periods of 2 hours or greater. OPUS returns a solution report with positional accuracy confidence intervals for adjusted coordinates and elevations for the observed point. In all cases we used the Oregon State Plane coordinate system (NAD83 [2011]), northern zone (meters), while the vertical datum is relative to the North American Vertical Datum of 1988 (NAVD88). For each of the discrete shore reaches, the R7 GPS base station was located on the prescribed base station monument (e.g., RON, OPHIR, BRK4, OLCJN3, KNAPP; **Table 3-1**), using a 2.0 m fixed height tripod. Survey control was provided by undertaking 180 GPS epoch measurements (~3 minutes of measurement per calibration site) using the calibration sites indicated in **Table 3-1**, enabling us to perform a GPS site calibration which brought the survey into a local coordinate system. This step is critical in order to eliminate various survey errors that may be compounded by factors such as poor satellite geometry, multipath, and poor atmospheric conditions, combining to increase the total error to several centimeters. **Table 3-2** shows the relative variability identified when comparing the mean derived benchmark coordinate and the original ORGN/OPUS derivations. As can be seen from **Table 3-2**, differences in the horizontal and vertical values at the various benchmarks were typically less than 2 cm (i.e., within one standard deviation [σ]).

Table 3-1. Survey benchmarks used to calibrate GPS surveys of the beach along the Curry County coastline. Asterisk signifies the location of the GPS base station during each respective survey. NGS denotes National Geodetic survey monument, WSI denotes Watershed Sciences, Inc. monument, ORGN signifies ORGN derivation solution.

Study Area	Primary Identification (PID) Name[1]	Easting (m)	Northing (m)	Elevation (m)
Brookings	CRISSEY - NGS/ORGN	1192699.723	43701.808	5.495
	BRK3 - NGS/ORGN	1192834.682	43893.928	12.255
	BRK4 - DOGAMI/ORGN*	1192519.215	44077.108	8.752
	FISH - DOGAMI/ORGN	1188120.122	49176.816	5.622
	OLCJN3 – WSI/ORGN*	1186186.887	49829.289	29.989
	OLCBTK2 – WSI/ORGN	1184382.094	51880.860	12.197
Gold Beach	OLCPWH1 – WSI/ORGN	1176522.146	81138.749	205.638
	LAURA - DOGAMI/ORGN	1176983.097	87355.353	9.262
	OA0244 - NGS/ORGN	1177694.558	87900.671	8.991
	RON - DOGAMI/ORGN*	1176979.804	90802.058	7.103
	GOLD - NGS/ORGN	1176877.072	91339.942	7.067
Rogue Shores	GOLD - NGS/ORGN	1176877.072	91339.942	7.067
	RON - DOGAMI/ORGN*	1176979.804	90802.058	7.103
	ROUGE2 - NGS/ORGN	1176851.529	92325.700	48.584
	ARGO - DOGAMI/ORGN	1176804.244	94456.177	4.188
	OTTER - DOGAMI/ORGN	1177520.565	95447.215	5.845
	GUN - DOGAMI/ORGN	1178168.787	99944.671	28.308
Nesika Beach	GUN - DOGAMI/ORGN	1178168.787	99944.671	28.308
	OPHIR - DOGAMI/ORGN*	1179707.240	103909.554	12.101
	OLCPWH2 – WSI/ORGN	1179749.434	104074.688	14.064
	SISTERS - DOGAMI/ORGN	1180272.194	110264.686	70.212
Port Orford	943-TIDAL-L - NGS/ORGN	1172671.014	126929.076	5.898
	BATTLE_RCK - DOGAMI/ORGN	1173207.775	127371.357	20.373
	KNAPP - DOGAMI/ORGN*	1171058.002	132431.014	4.280
	BLCO - NGS/ORGN	1174105.213	133772.311	53.099

Notes: Coordinates are expressed in the Oregon State Plane Coordinate System (2011), northern zone (meters) and the vertical datum is NAVD88.

[1]Control provided using the Oregon Reference Geodetic Network (ORGN).

Table 3-2. Comparison of horizontal and vertical coordinates (expressed as a standard deviation) at the primary base station benchmark locations, compared to the final coordinates referenced in Table 3-1.

Study Area	Primary Identification (PID) Name	Northing (m) σ	Easting (m) σ	Elevation (m) σ
Brookings	BRK4	0.000	0.006	0.010
Goldbeach	RON	0.003	0.003	0.005
Rogue Shore	RON	0.003	0.003	0.005
Nesika Beach	OPHIR	0.017	0.011	0.017
Port Orford	KNAPP	0.003	0.004	0.006

Having completed a local site calibration, cross-shore beach profiles were surveyed with the R8 GPS rover unit mounted on a backpack, worn by a surveyor (**Figure 3-8**). This was undertaken during periods of low tide, enabling more of the beach to be surveyed. The approach was to generally walk from the landward edge of the primary dune or bluff edge, down the beach face and out into the ocean to approximately wading depth. A straight line, perpendicular to the shore was achieved by navigating along a predetermined line displayed on a hand-held Trimble TSC2 computer controller, connected to the R8 receiver. The computer shows the position of the operator relative to the survey line and indicates the deviation of the GPS operator from the line. The horizontal variability during the survey is generally minor, being typically less than about ±0.25 m either side of the line (**Figure 3-9**), which results in negligible vertical uncertainties due to the relatively uniform nature of beaches characteristic of much of the Oregon coast (Ruggiero and others, 2005). From our previous research at numerous sites along the Oregon coast, this method of surveying can reliably detect elevation changes on the order of 4-5 cm, that is well below normal seasonal changes in beach elevation, which typically varies by 1-2 m (3–6 ft) (Ruggiero and others, 2005; Allan and Hart, 2007, 2008).

Analysis of the beach survey data involved a number of stages. The data were first imported into the MathWorks® MATLAB® environment (a suite of computer programming languages) using a customized script. A least-squares linear regression was then fit to the profile data. The purpose of this script is to examine the reduced data and eliminate data point residuals (e.g., **Figure 3-9**) that exceed a ±0.75-m threshold (i.e., the outliers) on either side of the predetermined profile line. The data are then exported into a Microsoft® Excel® database for archiving purposes. A second MATLAB script uses the Excel profile database to plot the survey data (relative to the earlier surveys) and outputs the generated figure as a Portable Network Graphics (png) file. Appendix B shows the reduced beach profile plots for the Curry County transects.

Figure 3-8. Surveying the morphology of the beach at Bandon using a Trimble 5800 "rover" GPS.

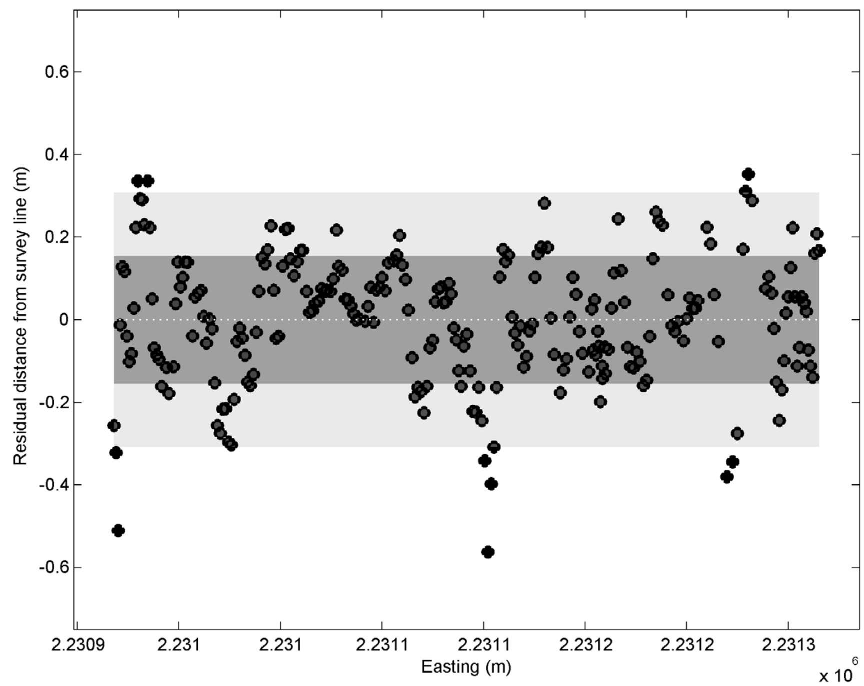

Figure 3-9. Residuals of GPS survey points relative to zero (transect) line. Example reflects the Cannon Beach 10 profile line. Dark grey shading indicates 68.3% of measurements located ±0.15 m (1σ) from the transect line, while 95.5% (2σ) of the measurements are located within ±0.30 m of the profile line (grey shading).

To supplement the GPS beach and bluff data, high-resolution lidar data measured by Watershed Sciences, Inc. (WSI) in 2008 for DOGAMI were also analyzed and integrated into the beach profile data set. This was especially important for backshore areas where it was not possible to easily survey with the GPS gear. In addition, lidar data flown by the USGS/NASA/NOAA in 1998 and 2002, and by the USACE in 2010 were used to extend the time series of the beach and bluff profile data. (1997 lidar data were not available for Curry County, while 1998 lidar data are available only north of and including Port Orford.) In particular, the 1998 lidar data measured at the end of the major 1997-98 El Niño were analyzed, providing additional measurements of the beach in an eroded state that can be compared with more recent winter surveys of the beach. The 1998 and 2002 lidar data were downloaded from NOAA's Coastal Service Center (http://coast.noaa.gov/dataregistry/search/collection/info/coastallidar) and were gridded in Esri® ArcGIS® by using a triangulated irregular network (TIN) algorithm; distance and elevation data were extracted from the grid lidar digital elevation models (DEMs).

3.2 Beach Characterization

Analyses of the beach profile data were undertaken using additional scripts developed in MATLAB. These scripts require the user to interactively locate the positions of the seaward edge and crest of the Primary Frontal Dune (PFD) backing the beach, and then evaluate the beach-dune juncture (E_j) elevations and beach slopes (tan β) for the 1998, 2002, 2008, 2010, and 2013 surveys along each of the profile sites. Beach slope was determined by fitting a linear regression through the measured profile data. In all cases, the slope of the beach face was determined to be the region of the beach located between Mean Sea Level (~1.4 m, MLLW) and the highest observed tide (~3.8 m, MLLW), an approach that is consistent with methodologies adopted by Ruggiero and others, 2005; Stockdon and others (2006). Determination of the location of the beach-dune junctures (E_j) was accomplished interactively using the MATLAB scripts and from local knowledge of the area. In general, the beach-dune juncture (E_j) reflects a major break in slope between the active part of the beach face and the toe location of the primary dune or bluff. For most sites along the Oregon coast, the beach-dune junctures (E_j) typically occurs at elevations between about 4-6 m (NAVD88). **Figure 3-10** provides an example of the identified beach-dune juncture (E_j) for one site, CURRY 5, after it has been eroded (described in Section 7), and is located just south of the Winchuck River near the Oregon/California border (**Figure 3-1**). In this example, it is apparent that the dune has experienced little change during the past 15 years, with the dune face having remained essentially where it is when compared with the 1998 survey of the beach. Examination of the profile data indicates that the beach-dune juncture (E_j) has varied in elevation, a function of repeated phases of both erosion and accretion events. As of August 2013, a small dune had developed seaward of the primary dune reinforcing the view that this site has been stable for some time. After having eroded the dune, the beach-dune juncture can be seen located near the 6m (20ft) contour. **Figure 3-10** also includes the derived beach slope ($\tan \beta = 0.073$), the crest of the primary dune, as well as the landward boundary of the primary frontal dune. These latter data are used later to develop new VE flood zones along the Curry County coast.

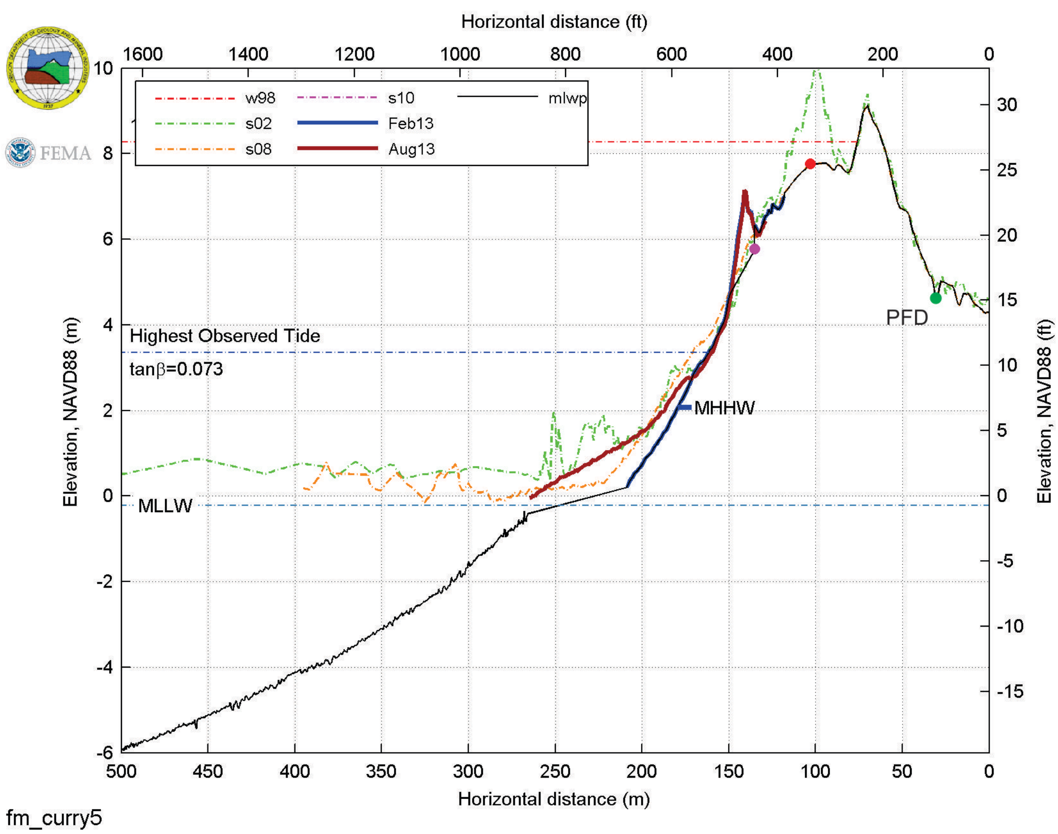

Figure 3-10. Plot showing various cross-sections at the CURRY 5 profile site, located at Crissey Field. In this example, the MLWP is depicted as the solid black line, the *eroded* beach-dune juncture location, dune crest and primary frontal dune location (PFD) is characterized respectively by the magenta, red, and green circles.

To estimate beach erosion and profile changes for a specific coastal setting that occurs during a particular storm, it is essential to first define the initial conditions of the morphology of the beach prior to the actual event of interest (Northwest Hydraulic Consultants, 2005). This initial beach profile is referred to as the most likely winter profile (MLWP) condition for that particular coastal setting and is depicted in **Figure 3-10** by the solid black line. The MLWP was assessed based on an examination of the combined surveyed profiles and lidar data. In the **Figure 3-10** example, the 2008 lidar survey of the primary dune and backshore was found to best characterizes the landward component of the MLWP, while our February 2013 survey best captured the state of the active beach and seaward edge of the foredune. Landward of the dune crest, information on the backshore topography was derived by incorporating the actual measured GPS data because those data provided the best representation of the actual ground surface. Where GPS survey data were not available, we used topographic data derived from the 2008 lidar flown for DOGAMI.

Table 3-3 summarizes the various morphological parameters identified for each transect site along the Curry County coastline, including their geomorphic classification. **Figure 3-11** provides a plot of the alongshore changes in beach slopes (tan β), mean sediment grain sizes (M_z), beach-dune juncture (E_j) elevations, and the dune/bluff/structure crest heights. In general, the steepest slopes are confined to those beaches with coarse sediments on the foreshore (**Figure 3-12**), while sites containing finer sediments are characterized by generally lower beach slopes (**Figure 3-13**). As can be seen in **Figure 3-11**, mean grain-sizes are coarsest (~M_z = 0Ø [1 mm (Peterson and others, 1994)]) adjacent to the Chetco River in Brookings and at Garrison Lake near Port Orford, while the finest sediments (~M_z = 2.5Ø [0.18 mm]) are located north of the Rogue River, and on the south side of Cape Blanco. Also apparent in **Figure 3-11** is that a few of the cells appear to show a progressive change in grain-size in the alongshore direction, which may be indicative of longshore sediment transport and lateral sorting. For example, in the Gold Beach cell sediments progressively decrease in size from Cape Sebastian at the south end of the cell (~M_z = 1.2Ø [0.43 mm]) toward Otter Point where they become fine sand (M_z = 2.5Ø [0.18 mm]); a similar pattern is apparent in the Blanco cell. In general, the steepest beach slopes are typically identified adjacent to the headlands, where the composition of the beach is comprised predominantly of gravels and boulders and the sediment is locally sourced from the headlands as a result of landslides. At several of the beach study sites, sediment grain-sizes vary both in the alongshore and cross-shore directions. For example, beaches south of the Chetco River in Brookings may be characterized as “composite” using the nomenclature of Jennings and Shulmeister (2002), consisting of a wide dissipative sandy beach composed of fine to medium sand, backed by an extensive gravel beach on the upper foreshore. North of the Chetco, much of the Brookings shoreline is characterized by a wide dissipative sand beach in the inter-tidal zone, which is often backed by a substantial cobble/boulder berm (**Figure 2-4**). The latter provides significant protection to the backshore (Allan and others, 2005).

Figure 3-11 also plots the beach-dune and beach-bluff juncture elevations (Ej) for the various study sites. Values for Ej vary significantly along the length of the Curry County coast. The lowest Ej values tend to occur along the toe of coastal bluffs, such as much of the Brookings shoreline and at Nesika Beach. In general, the highest beach-dune juncture elevations are found to the south of Gold Beach, north of Neskia beach, and along the barrier beach at Garrison Lake, areas that are actively aggrading. In addition, **Figure 3-11** (bottom) indicates the dune/bluff/structure crest elevations. Because these heights are indicative of the potential for flooding, with higher crests generally limiting flood overtopping, it can be seen that the risk from coastal flooding and inundation is likely to be potentially highest in the areas of Crissey Field, Gold Beach, Rogue Shore, and at Port Orford. Along the remainder of the shore, the beaches are protected by prominent bluffs (e.g., much of the Brookings shoreline and at Nesika Beach) with crest elevations that range from 15 to 40 m (49–131 ft) that effectively preclude wave overtopping and hence inundation in those areas. Nevertheless, some of these sites are subject to erosion hazards that likely will influence the extent of the flood zones in those areas, after factoring the potential for erosion from storms.

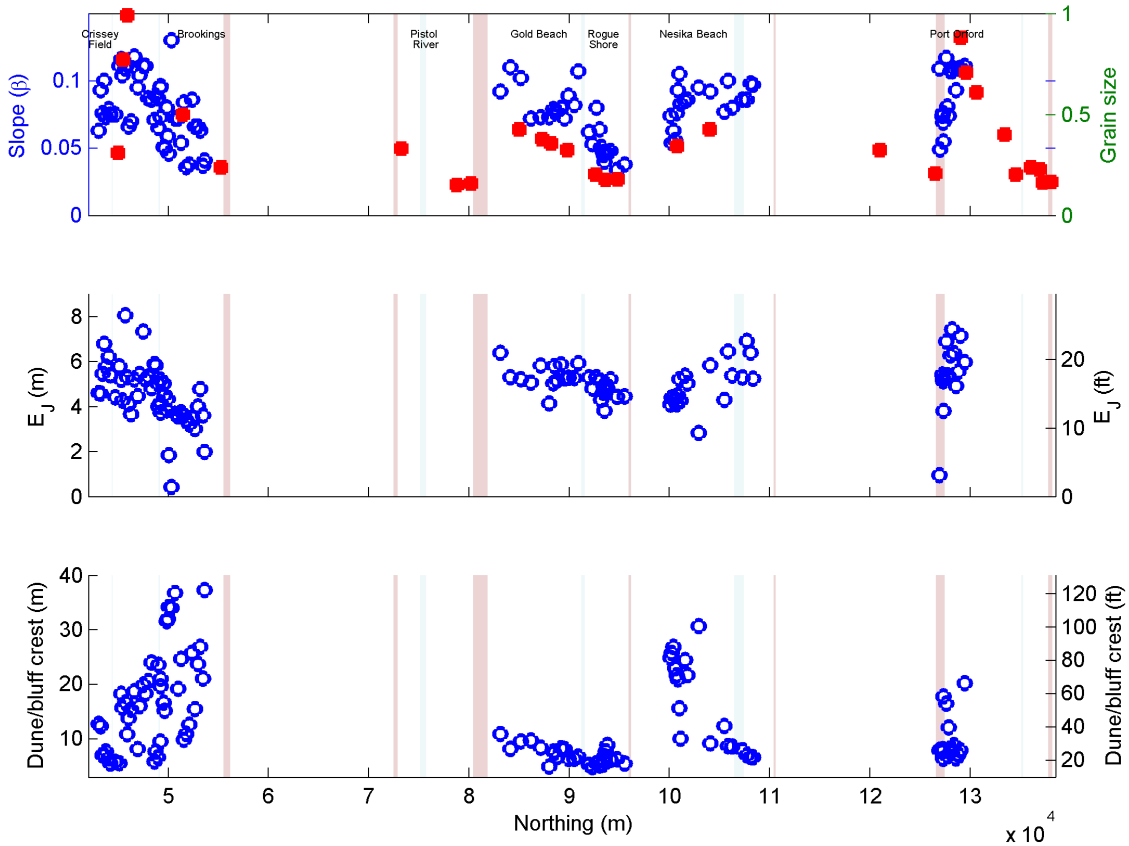

Figure 3-11. Alongshore changes in beach slopes (tan β), beach-dune juncture (Ej) elevations, and dune/bluff crest/tops along Curry County. Red squares indicate mean sediment grain-sizes measured by Peterson and others (1994). Vertical blue shading denotes the location of estuary mouths, while the red shading denotes the location of headlands.

Figure 3-12. Mixed sand and gravel beach located seaward of Garrison Lake in Port Orford. Note the steep beach face with waves breaking directly on the beach face (photo: J. Allan, DOGAMI, 2003).

Figure 3-13. North of the Rogue River. Jetty construction has enabled the beach and dunes to prograde seaward, where the material now forms a wide, gently sloping dissipative beach. The beach contains mostly fine to medium sand, as well as gravels (photo: J. Allan, DOGAMI, 2011).

Table 3-3. Identified beach morphological parameters from the most likely winter profile *(*MLWP*)* along the Curry County shoreline. Parameters include the beach-dune junction elevation (E_j*_MLWP*), beach slope (tan *θ*) and a site description.

Reach	Transect	Dune Crest/ Bluff Top (m)	*Ej_MLWP* (m)	Beach Slope (tan *θ*)	Description
Brookings	CURRY 1	12.787	4.603	0.063	coarse sand beach backed by moderately high cliffs
	CURRY 2	12.35	4.579	0.093	coarse sand beach backed by moderately high cliffs
	CURRY 3	7.068	5.458	0.076	coarse sand beach backed by low cliffs
	CURRY 4	7.056	6.786	0.1	coarse sand beach backed by dune
	CURRY 5	7.763	5.775	0.073	coarse sand beach backed by dune
	CURRY 6	6.524	6.216	0.079	coarse sand beach backed by dune
	CURRY 7	5.539	5.388	0.075	coarse sand beach backed by dune
	CURRY 8	5.833	4.414	0.075	coarse sand beach backed by moderately high cliffs
	CURRY 9	5.604	5.788	0.111	coarse sand beach backed by moderately high cliffs
	CURRY 10	18.288	5.189	0.116	coarse sand beach backed by moderately high cliffs
	CURRY 11	15.733	4.273	0.104	coarse sand beach backed by moderately high cliffs
	CURRY 12	16.687	8.049	0.109	coarse sand beach backed by moderately high cliffs
	CURRY 13	10.896	5.298	0.112	coarse sand beach backed by low cliffs
	CURRY 14	13.796	4.115	0.066	coarse sand beach backed by moderately high cliffs
	CURRY 15	15.389	3.664	0.07	coarse sand beach backed by moderately high cliffs
	CURRY 16	18.755	5.202	0.118	coarse sand beach backed by moderately high cliffs
	CURRY 17	8.195	4.465	0.095	coarse sand beach backed by moderately high cliffs
	CURRY 18	16.013	5.443	0.104	coarse sand beach backed by moderately high cliffs
	CURRY 19	19.918	7.33	0.111	coarse sand beach backed by moderately high cliffs
	CURRY 20	18.321	5.206	0.111	coarse sand beach backed by moderately high cliffs
	CURRY 21	20.634	5.332	0.087	coarse sand beach backed by moderately high cliffs
	CURRY 22	24.004	4.821	0.086	coarse sand beach backed by moderately high cliffs
	CURRY 23	5.895	5.895	0.071	coarse sand beach backed by moderately high cliffs
	CURRY 24	7.734	5.823	0.089	coarse sand beach backed by riprap
	CURRY 25	6.674	5.007	0.087	coarse sand beach backed by riprap
	CURRY 26	9.569	5.198	0.095	coarse sand beach backed by moderately high cliffs
	CURRY 27	19.643	3.735	0.096	coarse sand beach backed by moderately high cliffs
	CURRY 28	23.601	4.009	0.065	rocky beach backed by high cliffs
	CURRY 29	21.048	4.181	0.073	rocky beach backed by high cliffs
	CURRY 30	16.663	5.023	0.051	sand beach backed by moderately high cliffs
	CURRY 31	15.179	4.519	0.05	sand beach backed by low bluff
	CURRY 32	31.548	3.839	0.08	rocky beach backed by moderately high cliffs
	CURRY 33	31.948	4.329	0.059	rocky beach backed by moderately high cliffs
	CURRY 34	34.153	1.853	0.046	rocky beach backed by moderately high cliffs
	CURRY 35	33.985	0.432	0.13	rocky beach backed by high cliffs
	CURRY 36	36.718	3.684	0.072	rocky beach backed by high cliffs
	CURRY 37	19.206	3.567	0.072	coarse sand beach backed by high cliffs
	CURRY 38	24.669	3.749	0.054	coarse sand beach backed by high cliffs
	CURRY 39	9.885	3.6	0.084	coarse sand beach backed by moderately high cliffs
	CURRY 40	10.97	3.394	0.036	coarse sand beach backed by sloping wall
	CURRY 41	12.655	3.219	0.038	coarse sand beach backed by moderately high cliffs
	CURRY 42	25.783	3.511	0.086	coarse sand beach backed by high cliffs
	CURRY 43	15.497	3.011	0.066	coarse sand beach backed by moderately high cliffs
	CURRY 44	23.73	4.008	0.066	coarse sand beach backed by high cliffs
	CURRY 45	26.866	4.783	0.063	coarse sand beach backed by high cliffs
	CURRY 46	21.069	3.61	0.037	coarse sand beach backed by high cliffs
	CURRY 47	37.239	1.995	0.041	rocky beach backed by high cliffs

Reach	Transect	Dune Crest/ Bluff Top (m)	*Ej_MLWP* (m)	Beach Slope (tan *θ*)	Description
Gold Beach	CURRY 48	10.938	6.384	0.092	coarse sand beach backed by dune and high bluffs
	CURRY 49	8.217	5.304	0.11	coarse sand beach backed by dune and high bluffs
	CURRY 50	9.597	5.215	0.102	coarse sand beach backed by dune and high bluffs
	CURRY 51	9.759	5.063	0.072	coarse sand beach backed by dune
	CURRY 52	8.451	5.822	0.073	coarse sand beach backed by dune
	CURRY 53	4.987	4.141	0.073	coarse sand beach backed by dune
	CURRY 54	7.73	5.037	0.079	coarse sand beach backed by dune
	CURRY 55	7.488	5.802	0.077	coarse sand beach backed by dune
	CURRY 56	6.727	5.16	0.077	coarse sand beach backed by dune
	CURRY 57	8.342	5.873	0.08	coarse sand beach backed by dune
	CURRY 58	8.191	5.251	0.072	coarse sand beach backed by dune
	CURRY 59	6.405	5.278	0.089	coarse sand beach backed by dune
	CURRY 60	6.414	5.27	0.082	coarse sand beach backed by dune
	CURRY 61	6.817	5.929	0.107	coarse sand beach backed by dune
Rogue Shores	CURRY 62	5.3	5.3	0.062	coarse sand beach backed by dune
	CURRY 63	4.894	4.8	0.053	coarse sand beach backed by dune
	CURRY 64	5.584	5.308	0.08	coarse sand beach backed by dune
	CURRY 65	5.211	5.143	0.064	coarse sand beach backed by dune
	CURRY 66	5.277	4.299	0.051	coarse sand beach backed by dune
	CURRY 67	5.333	4.621	0.047	coarse sand beach backed by dune
	CURRY 68	6.106	4.792	0.045	coarse sand beach backed by dune
	CURRY 69	6.871	3.818	0.04	sand beach backed by poor riprap
	CURRY 70	7.797	4.996	0.047	coarse sand beach backed by dune
	CURRY 71	8.944	4.8	0.047	coarse sand beach backed by dune
	CURRY 72	6.214	5.215	0.048	coarse sand beach backed by dune
	CURRY 73	6.355	4.438	0.034	coarse sand beach backed by dune
	CURRY 74	5.547	4.453	0.038	coarse sand beach backed by dune and high cliff
Nesika Beach	CURRY 75	24.855	4.094	0.074	coarse sand beach backed by moderately high bluff
	CURRY 76	25.739	4.403	0.054	coarse sand beach backed by moderately high bluff
	CURRY 77	26.867	4.305	0.063	coarse sand beach backed by moderately high bluff
	CURRY 78	22.964	4.334	0.056	coarse sand beach backed by moderately high bluff
	CURRY 79	21.675	4.105	0.076	coarse sand beach backed by moderately high bluff
	CURRY 80	20.923	4.502	0.093	coarse sand beach backed by moderately high bluff
	CURRY 81	15.649	5.22	0.105	coarse sand beach backed by moderately high bluff
	CURRY 82	10.082	4.264	0.083	coarse sand beach backed by moderately high bluff
	CURRY 83	24.455	5.373	0.085	coarse sand beach backed by moderately high bluff
	CURRY 84	21.697	5.025	0.086	coarse sand beach backed by moderately high bluff
	CURRY 85	30.639	2.831	0.095	coarse sand beach backed by riprap wall
	CURRY 86	9.227	5.834	0.092	coarse sand beach backed by dune and bluff
	CURRY 87	12.406	4.299	0.077	coarse sand beach backed by low bluff
	CURRY 88	8.737	6.446	0.1	coarse sand beach backed by dune
	CURRY 89	8.661	5.377	0.08	coarse sand beach backed by dune
	CURRY 90	7.983	5.293	0.086	coarse sand beach backed by dune and bluff
	CURRY 91	7.071	6.915	0.086	coarse sand beach backed by dune and bluff
	CURRY 92	6.749	6.387	0.098	coarse sand beach backed by dune and bluff
	CURRY 93	6.683	5.238	0.097	coarse sand beach backed by dune and bluff

Reach	Transect	Dune Crest/ Bluff Top (m)	*Ej_MLWP* (m)	Beach Slope (tan *β*)	Description
Port Orford	CURRY 94	17.803	3.81	0.055	coarse sand beach backed by moderately high cliffs
	CURRY 95	6.416	5.127	0.069	coarse sand beach backed by dune and moderately high cliffs
	CURRY 96	8.189	5.257	0.076	coarse sand beach backed by dune and moderately high cliffs
	CURRY 97	7.718	5.418	0.074	coarse sand beach backed by dune and low cliffs
	CURRY 98	7.913	0.388	0.106	Steep rock platform and seawall at port
	CURRY 99	8.083	0.533	0.078	Steep rock platform and seawall at port
	CURRY 100	16.495	6.888	0.117	coarse sand beach backed by dune
	CURRY 101	6.854	5.389	0.081	coarse sand beach backed by low bluff
	CURRY 102	12.147	5.327	0.074	coarse sand beach backed by moderately high bluff
	CURRY 103	7.589	6.272	0.107	coarse sand beach backed by moderately high bluff
	CURRY 104	8.235	7.427	0.107	barrier beach
	CURRY 105	8.903	6.375	0.109	barrier beach
	CURRY 106	6.466	4.916	0.093	barrier beach
	CURRY 107	7.179	5.555	0.109	barrier beach
	CURRY 108	7.957	7.141	0.11	barrier beach
	CURRY 109	20.22	5.971	0.111	coarse sand beach backed by moderately high bluff
Brookings Supplemental	7_13401	4.582	4.23	0.056	coarse sand beach backed by dune

3.3 Recent Coastal Changes in Curry County

This section briefly reviews beach profile changes that have occurred during the past decade, having been documented by lidar and recent GPS surveys of the shore.

The overall approach used to define the morphology of the beach and dune system, including the location of the PFD along the length of county shoreline, and shoreline changes over the past decade, was based on detailed analyses of lidar data measured by the USGS/NASA/NOAA in1998 and 2002, the USACE in 2010, and by DOGAMI in 2008. However, because lidar data flown by the USGS/NASA/NOAA is of relatively poor resolution (~1 point/m^2) and reflects a single return (i.e., includes vegetation where present), while the lidar data flown by DOGAMI has a higher resolution (8 points/m^2) and was characterized by multiple returns enabling the development of a bare-earth digital elevation model (DEM), determination of the most critical beach/dune morphological features was based entirely on analysis of the 2008 lidar data.

Lidar data flown in 1998, 2002, and 2010 were downloaded from NOAA's Coastal Service Center and gridded in ArcGIS using a TIN algorithm (Allan and Harris, 2012); a similar approach was undertaken with the 2008 lidar data flown by DOGAMI. Transects spaced 10 m apart were cast for the full length of the county coastline using the Digital Shoreline Analysis System (DSAS) developed by the USGS (Thieler and others, 2009). For each transect, xyz values for the 1998, 2002, 2008, and 2010 lidar data were extracted at 1 m interval along each transect line and saved as a text file using a customized ArcGIS script.

Processing of the lidar data was undertaken in MATLAB using a custom beach profile analysis script developed by DOGAMI. This script requires the user to interactively define various morphological features including the dune/bluff crest/top, bluff slope (where applicable), landward edge of the PFD, beach-dune juncture elevations for each year, and the slope of the beach foreshore.

3.3.1 Brookings

Figure 3-14 presents profile changes measured for selected transects in the Brookings area. Curry 6 is located at Crissey Field on the Oregon/California border and crosses a barrier beach, with dune heights reaching ~10 m (33 ft). Overall, the beach shows very little change over the past decade, with the most significant changes occurring low on the profile (~MHHW) where it is appears to be responding largely in response to seasonal changes in waves. As noted previously in Section 2.3.1.1, the beach advanced seaward by some 70 m (230 ft) between 1967 and the 1980s and is depicted in **Figure 3-14** by the generally flat area located between the 6 and 8 m contours, west of the primary dune crest. Midway between the Winchuck and Chetco Rivers, the Curry 15 transect site crosses a bluff that is eroding slowly. Although the profile data suggests the bluff eroded between 2002 and 2008, these data probably reflect vegetation effects (characteristic of the 2002 lidar) that have subsequently been removed in the 2008 bare earth lidar. Curry 24 is located about 500 m (1,640 ft) south of the mouth of the Chetco River. The beach consists of a mixture of coarse sand and gravel (mostly shingle) and is steep. Crest elevations in this area are relatively low (~7.7 m [25.3 ft]), while the backshore is protected by riprap. As with the Curry 6 transect, there is no obvious pattern of change with the beach responding largely to variations in waves. Finally, the Curry 40 transect site is located at Harris Beach State Park. The beach contains fine sand and is largely dissipative of waves. The site is backed by a structure, built to enable wheelchair access to the beach. As can be seen from the transect data, in its most accreted state (August 2013), the beach can build seaward by some 50 m (164 ft).

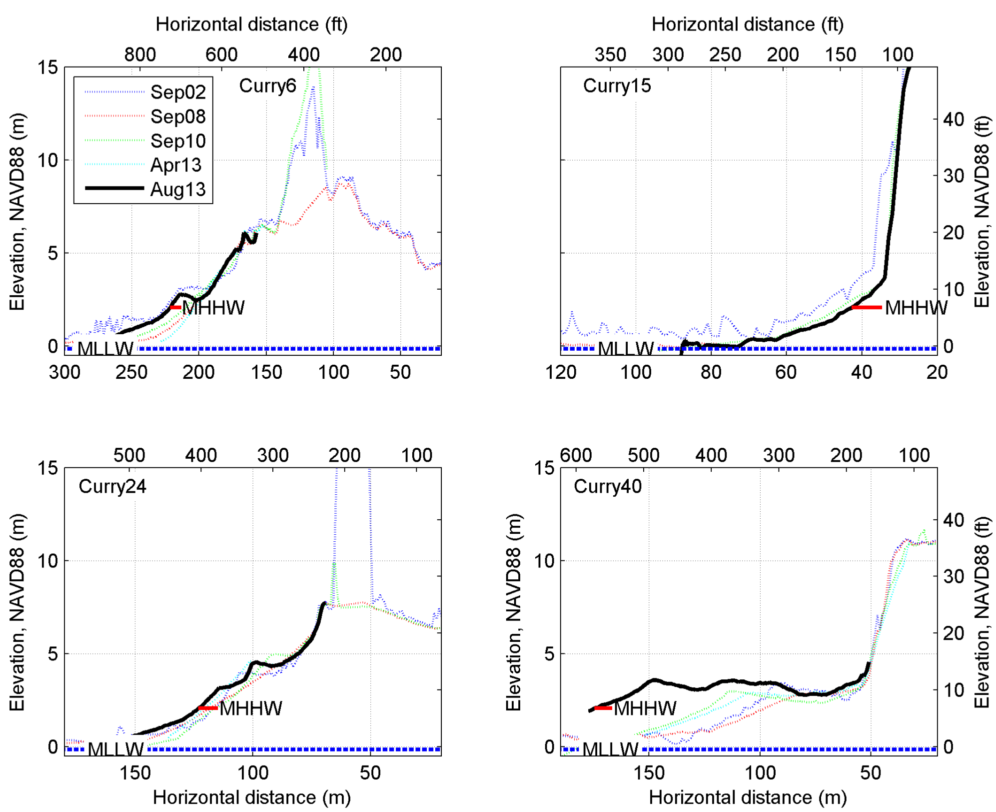

Figure 3-14. Measured beach morphological changes carried out between 2002 and 2013 for selected sites in the Brookings region.

3.3.2 Gold Beach

Figure 3-15 presents profile changes measured for selected transects in the Gold Beach area, north of Cape Sebastian and south of the Rogue River. South of Hunter Creek the beach appears to be actively gaining sand and is advancing seaward, while north of the creek the beach is mostly stable to erosional. At the Curry 48 transect site, a new primary dune is building having now attained a height of ~11 m (36 ft), while the beach has advanced seaward by ~8 m (26 ft) since 2002. Low (< 5 m [16 ft]) on the beach face, large fluctuations in the morphology of the beach are apparent that reflect winter erosion and summer beach building. Similar changes can be seen at the Curry 50 transect.

North of Hunter Creek, the beach has fluctuated between erosion and accretion. At the Curry 55 transect site, the dune face has eroded landward by 64 m (210 ft) since 2002, most of which having occurred between February 2011 and April 2013. As noted previously in section 2.3.1.3, these changes are due to the northward shift in the mouth of Hunter Creek. Because of low beach elevations seaward of the creek channel, storm waves were able to easily overtop the beach berm and erode the back of the beach creating a major hazard for several homes built adjacent to the beach (**Figure 2-19** and **Figure 2-20**). Emergency riprap was placed along the toe of the erosion scarp but is poorly constructed and is unlikely to survive a major storm. Finally, beach erosion is also occurring immediately adjacent to the south Rogue jetty (Curry 61). There, the back of the beach eroded 7 m between February 2011 and April 2013.

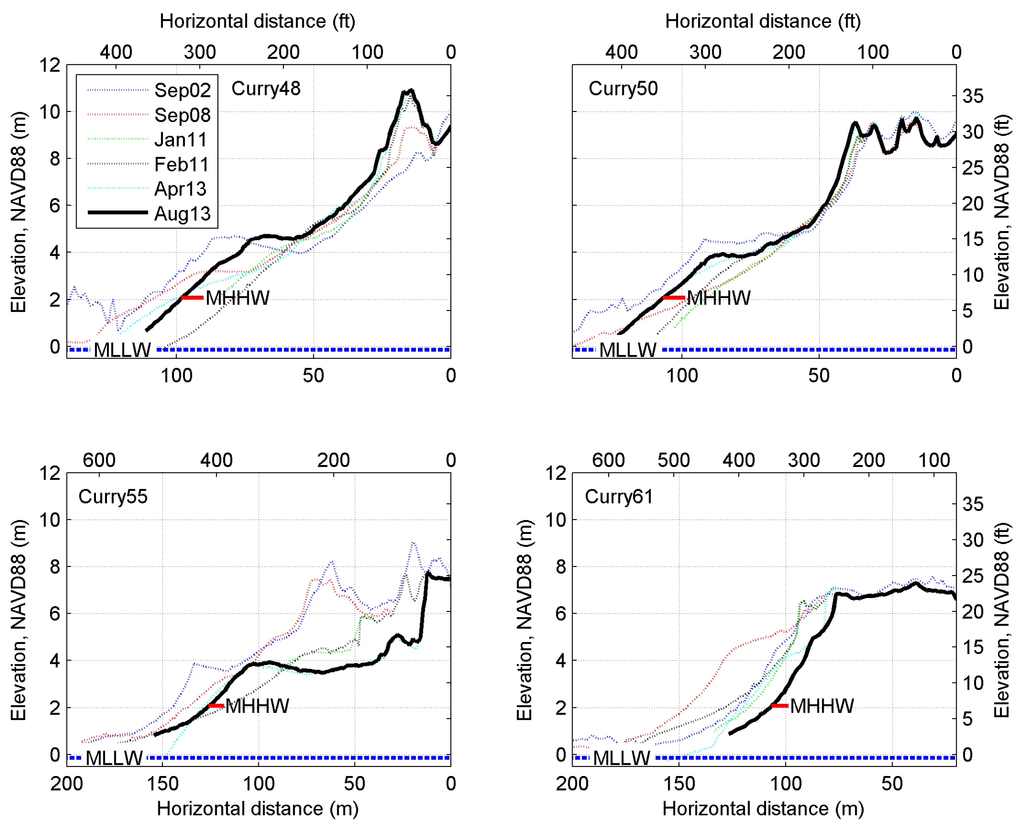

Figure 3-15. Measured beach morphological changes carried out between 2002 and 2013 for selected sites in the Gold Beach region.

3.3.3 *Rogue Shores*

Figure 3-16 presents profile changes measured for selected transects north of the Rogue River and south of Otter Point. As described in section 2.3.1.4, the beach immediately north of the Rogue River is presently eroding and has been retreating landward since at least the mid 1960s. The erosion extends approximately 1.6 km (1 mile) north of the Rogue, with the greatest shoreline retreat (~85 m [279 ft]) occurring immediately adjacent to the jetty. Recent surveys of the beach confirm that the site continues to retreat, with the beach having cut back an additional 9 m (30 ft) since 2002.

With progress north, the beach is considered to be mostly stable to accreting. At the Curry 66 transect site (**Figure 3-16**), the vertical range (~1.4 m [4.7 ft]) in the beach profile provides a good measure of the typical summer/winter beach profile changes characteristic of fine grained sand beaches of the southern Oregon coast. Crest elevation of the dunes in this area are low (~5.2 m [17 ft]), while the primary dune (poorly developed) fronts a low lying marshy region that eventually transitions to a marine terrace located at the back of the beach. In contrast, a prominent dune system characterizes the area between transects 69 to 73. Here, the beach is actively aggrading, enabling the primary dune to grow vertically. Finally, beach progradation is also occurring near the Curry 74 transect site, immediately south of Otter Point. Little dune development has occurred here, possibly due to topographical shielding by Otter Point. As can be seen in **Figure 3-16**, landward of the primary dune, the backshore is low lying and is backed by a prominent marine terrace.

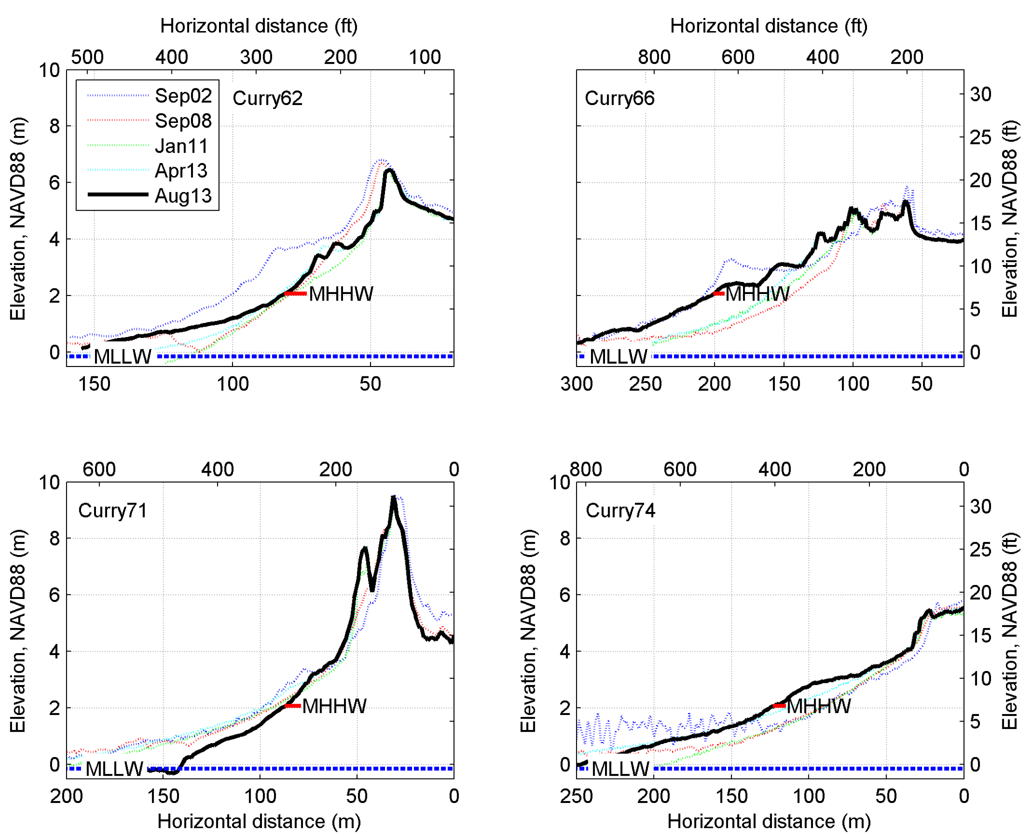

Figure 3-16. Measured beach morphological changes carried out between 2002 and 2013 for selected sites in the Rogue Shores region.

3.3.4 Nesika Beach

Figure 3-17 presents profile changes measured for selected transects in the Nesika Beach littoral cell, north of the Hubbard Mound and south of Sisters Rock. Much of this cell is backed by coastal bluffs that reach as high as 25 m (82 ft). The bluffs dominated the southern half of the cell, while the northern half is characterized by a broad sandy beach backed by dunes, transitioning to a marine terrace. In the south central portion of the cell (north of Curry 84 and south 86), an extensive riprap structure is present along the seaward edge of Highway 101 (**Figure 2-23**). In the south, the bluffs are actively eroding. For example, the Curry76 and 81 transects indicate that the bluff face has eroded landward by ~7 m (23 ft) since 2002. Farther north at the Curry86 transect site, the beach is essentially stable. Much of this section of the cell is characterized with coarse beach sand. As a result, the beach is steep, with waves breaking directly on the beach face and the shoreline oscillates over large (~60 m [197 ft]) horizontal distances as the beach responds to storms and subsequent beach rebuilding. In the far north at the Curry93 transect site, the beach is actively prograding seaward.

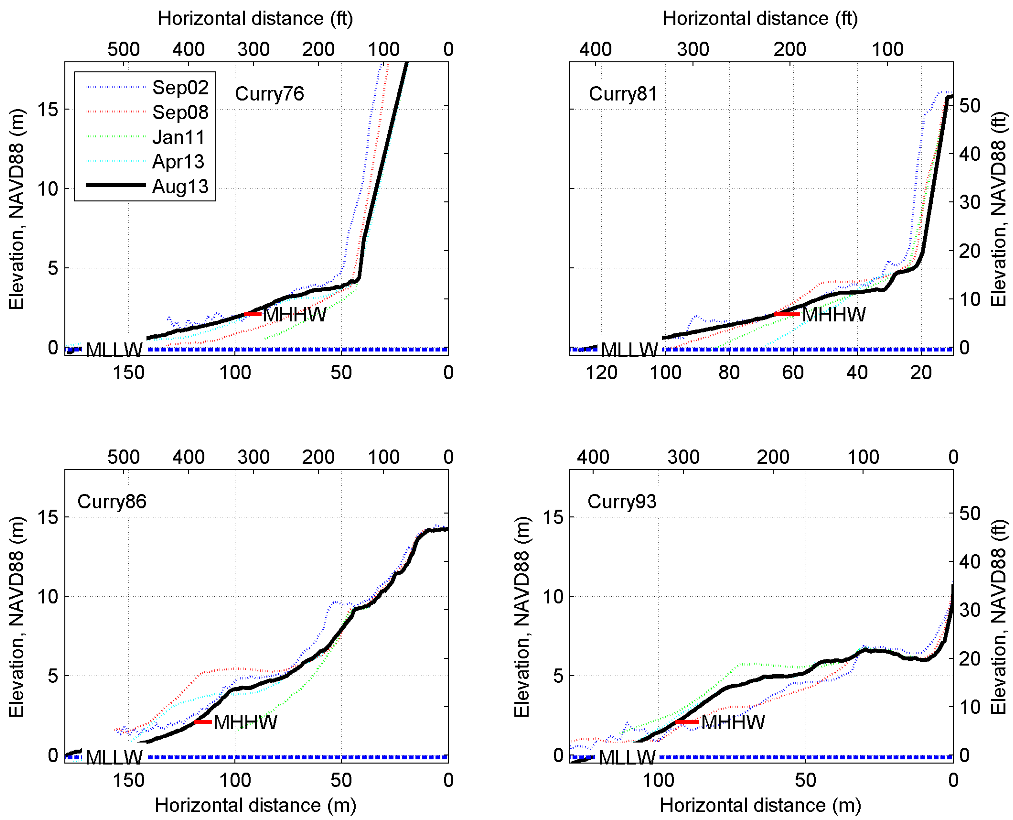

Figure 3-17. Measured beach morphological changes carried out between 2002 and 2013 for selected sites in the Nesika Beach region.

3.3.5 Port Orford

Figure 3-18 presents profile changes measured for selected transects in the Blanco littoral cell, north of the Port Orford Heads and south of Cape Blanco. Similar to the Curry86 transect site, the Garrison Lake beach undergoes large shoreline excursions that is due to it being a coarse beach (sand to granules), making it intermediate to reflective using the classification of Wright and Short (1984). Because waves are effectively breaking directly on the beach face, the beach responds rapidly to variations in the incident waves and particularly in response to changes in the predominant direction of wave approach as occurred during the 1997-98 El Niño winter. As can be seen in **Figure 3-18**, all four transects have experienced large shoreline excursions (measured at the 6 m (19.6 ft) contour), which range from 40 m (131 ft) in the north at the Curry109 site, to as much as 74 m (246 ft) farther south at the Curry107 transect. In response to the 1997-98 El Niño, the beach eroded significantly with waves overtopping the barrier beach along essentially its entire length (**Figure 3-19**). At the time (April 1998), the barrier beach had a crest elevation of ~6.9 to 8.9 m (23 to 29 ft); the crest of the barrier at the Curry107 (**Figure 3-19**) transect site was ~7.2 m (23.6 ft). However, since April 1998 the beach has essentially regained much of the sand it had originally lost. On average, the beach has advanced seaward by 65 m (213 ft), while the crest of the barrier has also aggraded significantly reaching elevations of 8 to 11.9 m (26–39 ft).

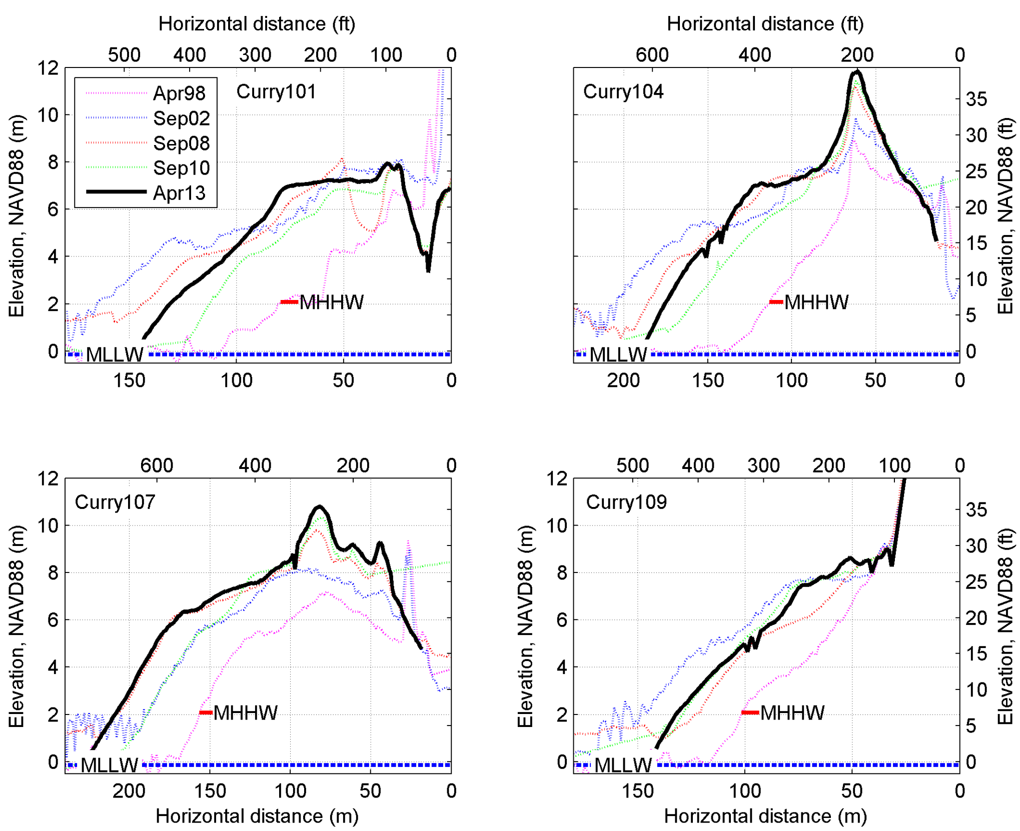

Figure 3-18. Measured beach morphological changes carried out between 1998 and 2013 for selected sites in the Port Orford region.

Figure 3-19. Overtopping of the Garrison Lake barrier beach near the Curry107 transect site during a major storm on February 16, 1999 (photo courtesy of a resident at Port Orford).

3.4 Bathymetry

Important for calculating wave transformations and determining nearshore beach slopes is information on the local bathymetry seaward from the Curry County coast. For the purposes of this study we have adopted two approaches:

1. For the purposes of SWAN numerical wave modeling, we used bathymetric data compiled by the National Geophysical Data Center (NGDC), an office of the National Oceanic and Atmospheric Administration (NOAA) for the purposes of developing an integrated bathymetric-topographic digital elevation model (DEM) for tsunami inundation modeling.
2. For erosion assessments and wave runup calculations, we used bathymetric data collected in late summer 2013 with the aid of personal watercrafts (Ozkan-Haller and others, 2009).

For the purposes of developing an integrated bathymetric-topographic digital elevation model (DEM) that can be used for tsunami inundation modeling, the National Geophysical Data Center (NGDC), an office of the National Oceanic and Atmospheric Administration (NOAA) has compiled detailed bathymetric data across the continental shelf from multiple agencies. The synthesized bathymetric-topographic DEM (Port Orford http://www.ngdc.noaa.gov/dem/squareCellGrid/download/410, and Crescent City http://www.ngdc.noaa.gov/dem/squareCellGrid/download/724) is a 1/3 arc-second (approximately 10 m [~33 ft]) DEM of the southern Oregon coast and northern California coast that spans all of Curry County, and includes the offshore rocks, small islands, and reefs that would affect wave shoaling.. The DEM was generated from a diverse suite of digital data sets that span the region (Carignan and others, 2009; Grothe and others, 2011). A summary of the data sources and methods used to synthesize the data to develop the Port Orford and Crescent City DEMs is described in the reports by Carignan and others (2009) and Grothe and others (2011). In general, the best available data were obtained by the NGDC and shifted to common horizontal and vertical datums: North America Datum 1983 (NAD 83) and Mean High Water (MHW).

NGDC used shoreline, bathymetric, and topographic digital data sets (**Figure 3-20**) from several U.S. federal, state and local agencies (e.g., NOAA's National Ocean Service (NOS), Office of Coast Survey (OCS) and Coastal Services Center (CSC); the U.S. Geological Survey (USGS); the U.S. Army Corps of Engineers (USACE); and the Oregon Department of Fish and Wildlife/Marine Resource Program (ODFW). After all the data had been converted to a common coordinate system and vertical datum, the grid data were checked for anomalous data and corrected accordingly. Because the data sets, particularly in deep water and near to the coast, were relatively sparse, further manipulation and smoothing was required to create a uniform grid. These products were then compared with the original surveys to ensure grid accuracy. According to Grothe and others (2011) the final DEM is estimated to have an accuracy of up to 10 m (~33 ft), while some portions of the grid are more accurate (e.g., the coastal strip where high-resolution lidar data were available). The bathymetric portion of the data set is estimated to have an accuracy of between 0.1 m (0.33 ft) and 5% of the water depth, again depending on the type of survey data that was used to calibrate the final grid development.

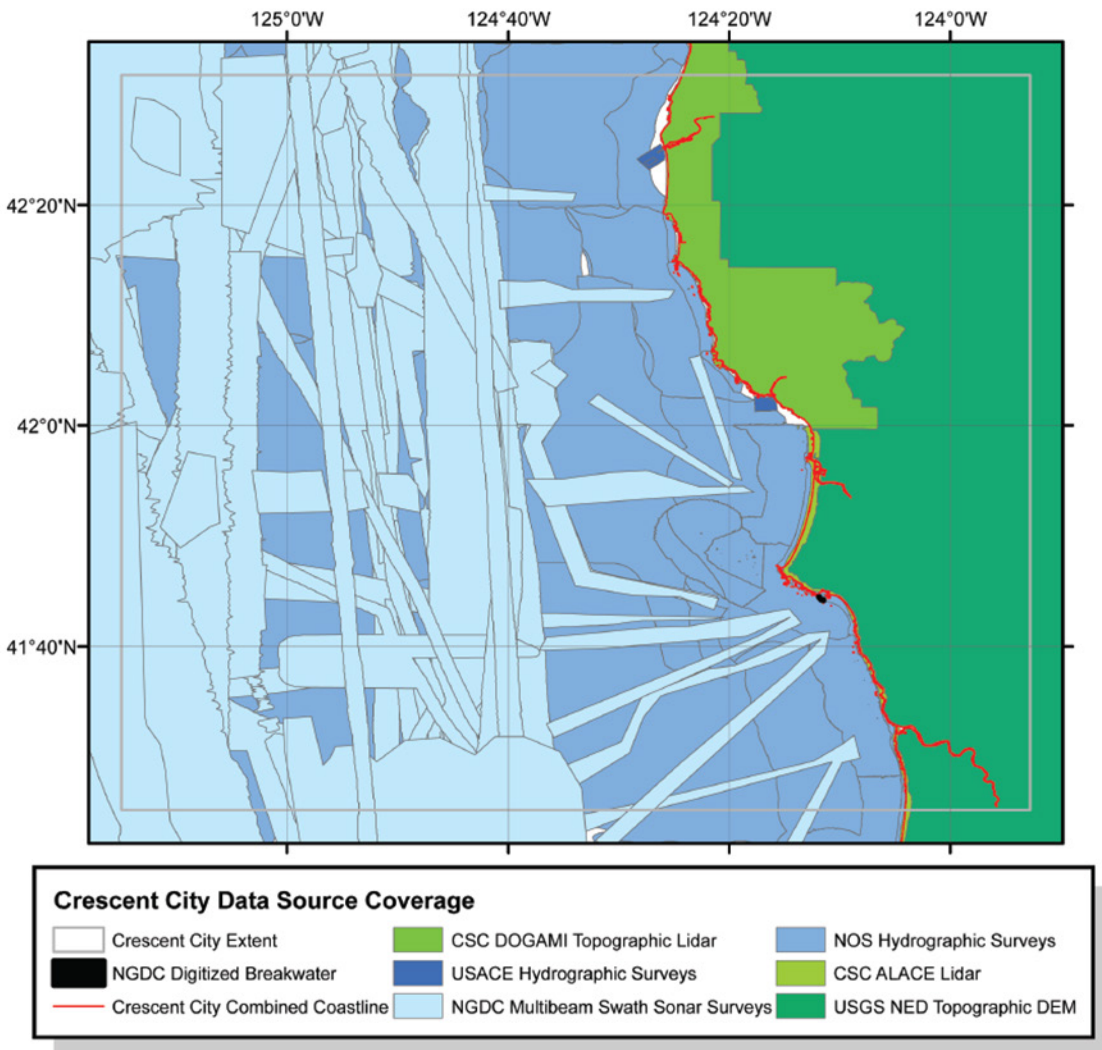

Figure 3-20. U.S. federal, state, and local agency bathymetric data sets used to compile the Crescent City DEM (Grothe and others, 2011).

Finally, despite all these efforts it is important to note that a limitation of the DEMs being developed by NGDC is the virtual absence of suitable bathymetric data in the nearshore (effectively landward of the 10 m [33 ft] bathymetry contour), because few survey boats are able to venture into this highly turbulent and dangerous portion of the surf zone. The exception to this is where surveys have been undertaken by the USACE in the entrance channels to estuaries and harbors where navigable water depths need to be maintained. Thus, there is some uncertainty about estimating nearshore slopes for the surf zone due to the absence of sufficient data for this region, with the user having to make some assumptions based on the best available data that is present outside the surf zone and information at the shoreface. This is a recognized problem with all coastal flood analyses. To resolve this problem, we used a Coastal Profiling System (CPS) that has been developed for nearshore bathymetric surveys by Dr. Peter Ruggiero, Department of Geosciences, Oregon State University (Ruggiero and others, 2005). The CPS consists of a highly maneuverable personal watercraft that is equipped with a survey grade GPS receiver and antenna, an echo sounder and an on board computer. Repeatability tests undertaken by Ruggiero and colleagues indicate sub-decimeter accuracy on the order of 0.15 m (0.5 ft) (Ozkan-Haller and others, 2009). **Figure 3-21** provides an example of the CPS system, while **Figure 3-22** to **Figure 3-25** present the mapped coverage of our bathymetric surveys undertaken in the 2013 summer. An example of two of the bathymetric transects undertaken in Curry County is presented in **Figure 3-26**.

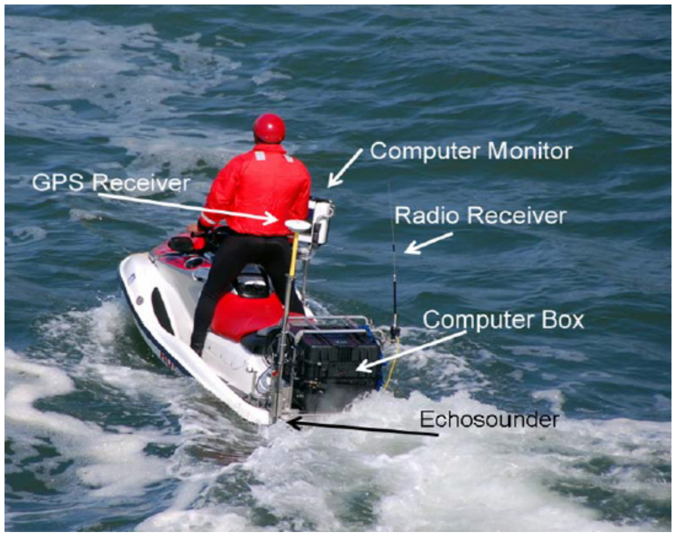

Figure 3-21. Data acquisition boat and onboard equipment(photo: P. Ruggiero, OSU).

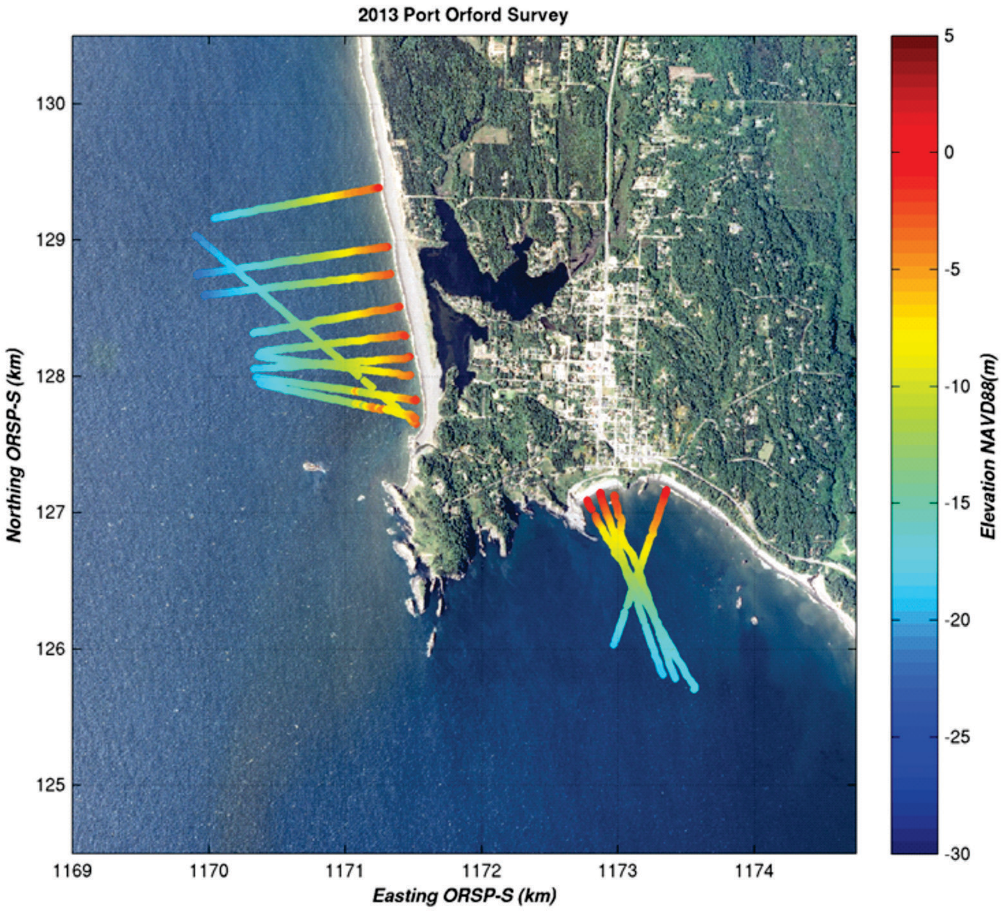

Figure 3-22. Processed elevation data collected during the 2013 Curry County Survey for the Port Orford region, Curry County, Oregon. Elevations are reported in meters and the vertical datum is NAVD88. The horizontal datum is NAD83, m, with coordinates shown in Oregon State Plane North.

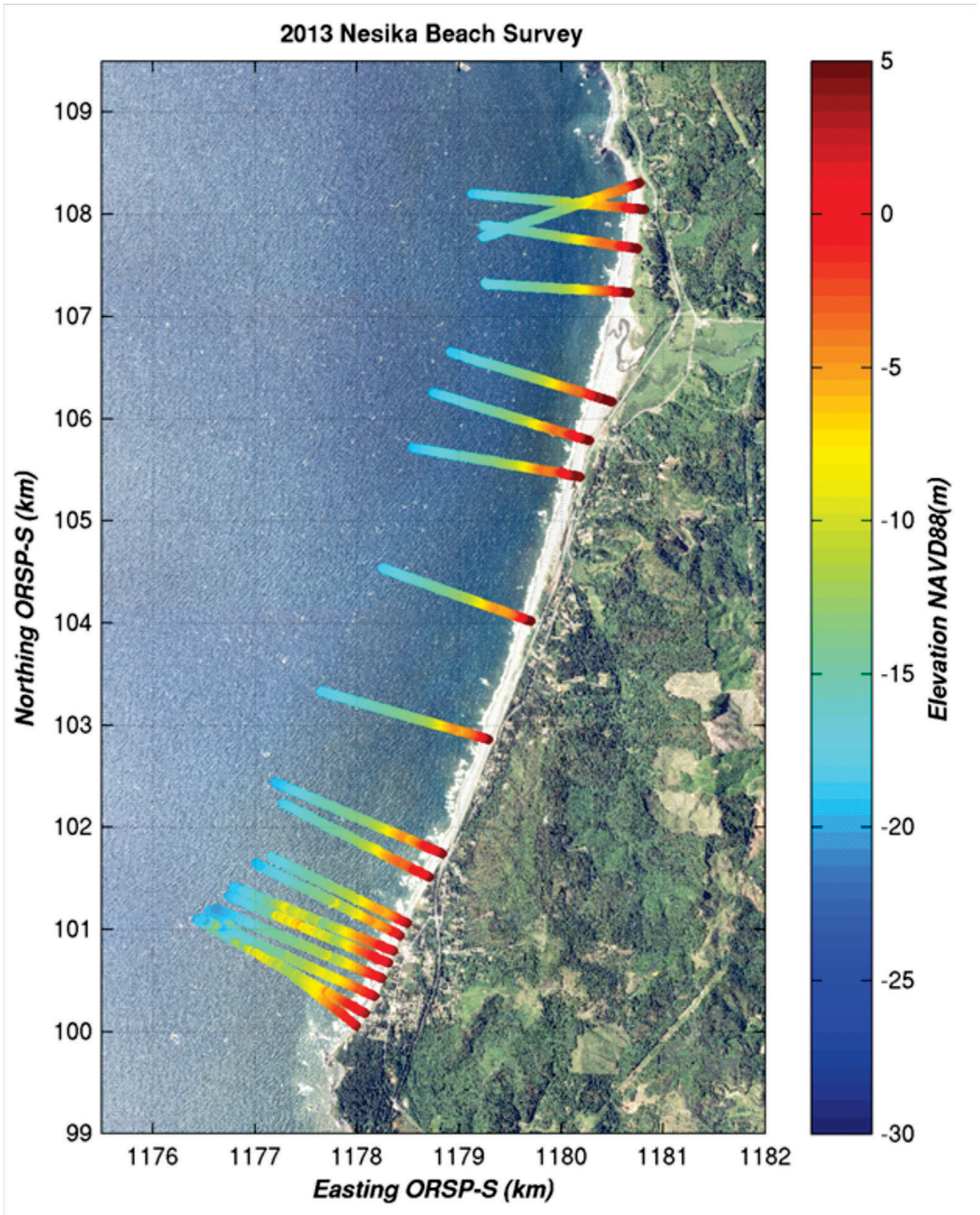

Figure 3-23. Processed elevation data collected during the 2013 Curry County Survey for the Nesika Beach littoral cell, Curry County, Oregon. Elevations are reported in meters and the vertical datum is NAVD88. The horizontal datum is NAD83, m, with coordinates shown in Oregon State Plane North.

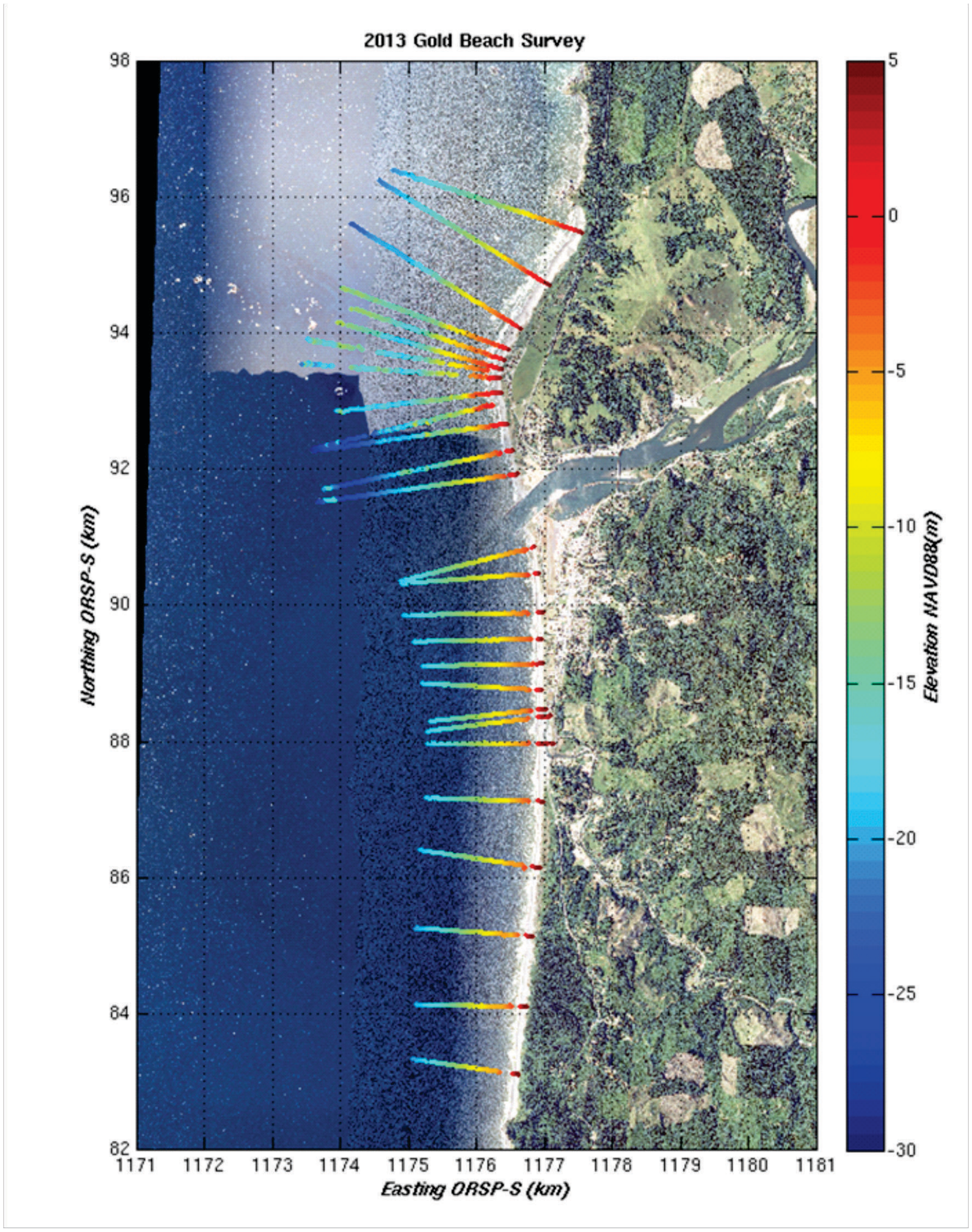

Figure 3-24. Processed elevation data collected during the 2013 Curry County Survey for the Gold Beach littoral cell, Curry County, Oregon. Elevations are reported in meters and the vertical datum is NAVD88. The horizontal datum is NAD83, m, with coordinates shown in Oregon State Plane North.

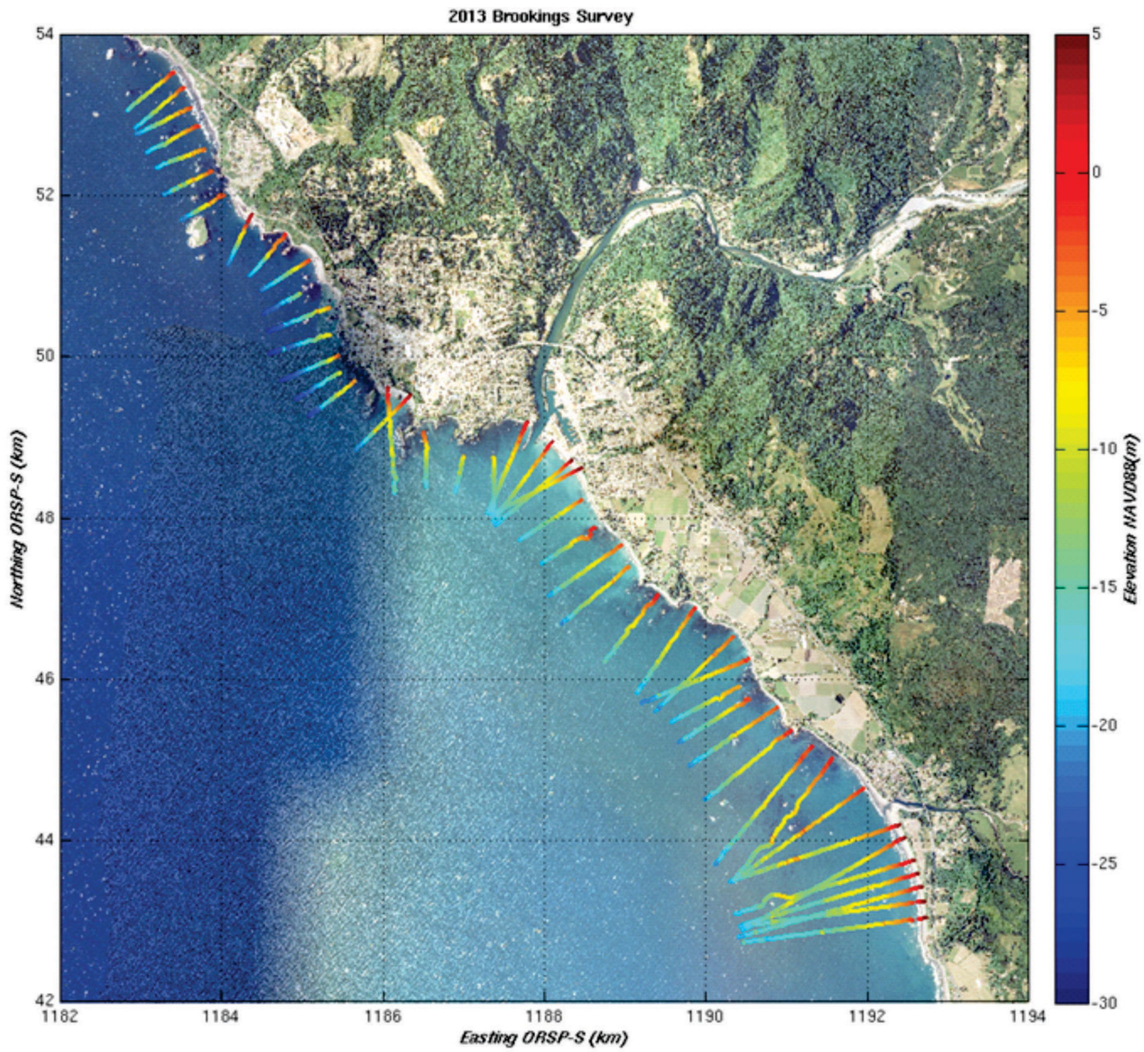

Figure 3-25. Processed elevation data collected during the 2013 Curry County Survey for the Brookings region, Curry County, Oregon. Elevations are reported in meters and the vertical datum is NAVD88. The horizontal datum is NAD83, m, with coordinates shown in Oregon State Plane North.

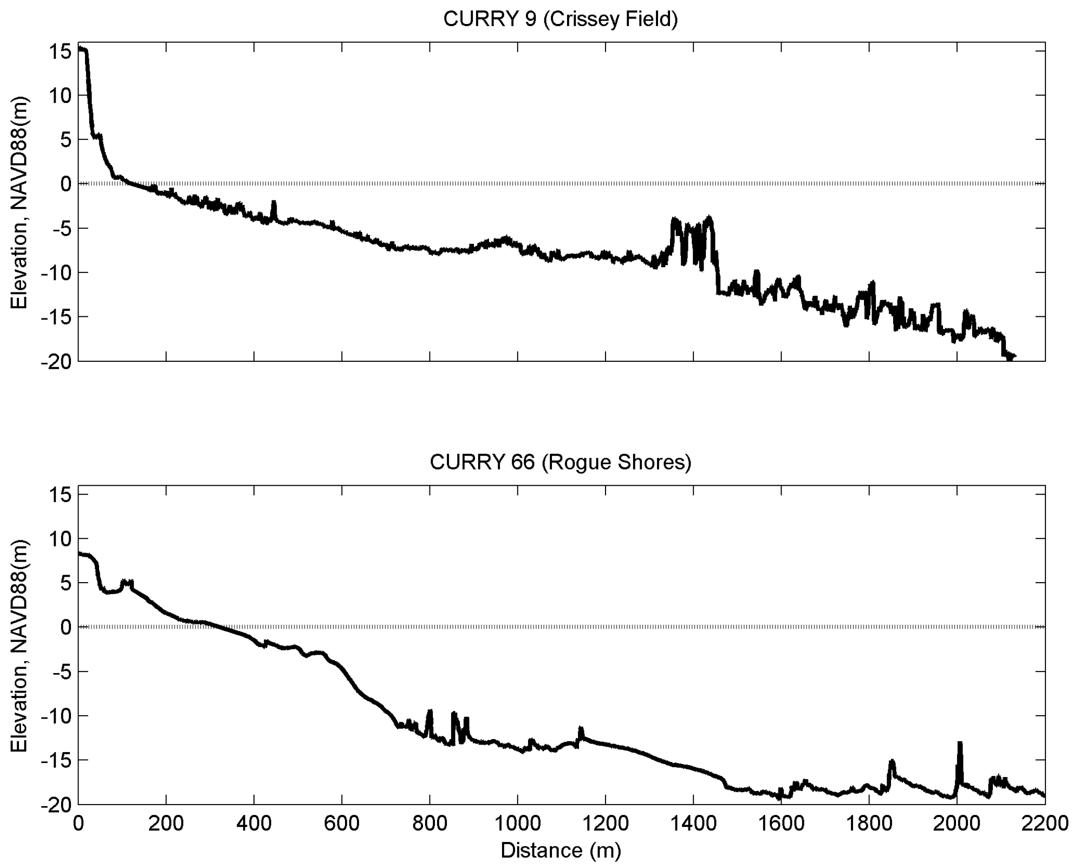

Figure 3-26. Combined topographic and bathymetric cross-shore transects measured offshore from Crissey Field and Rogue Shores (respectively, southern and central Curry County) showing the presence of significant reef structure (both) as well sand bars (Curry 66). Note the contrasting nearshore slopes between the two sites, with steeper topography observed at Rogue Shores and wider shallower topography offshore from Crissey Field.

4.0 TIDES

Measurements of tides on the Oregon coast are available from various tide gauges operated by the National Ocean Service (NOS; http://tidesandcurrents.noaa.gov/stations.html?type=Water+Levels#Oregon). Hourly tidal records are available from the following coastal sites (**Table 4-1**): Newport (South Beach, #9435380), Coos Bay (Charleston, #9432780) and at Port Orford (#9431647) on the southern Oregon coast. Long-term tidal records are also available from the Crescent City tide gauge (#9419750), located in northern California. The objective of this section is to establish which tide gauge would be most appropriate in applications directed toward FEMA wave and total water level analyses for the Curry County Coast.

The four tide gauges in this region are listed in **Table 4-1**, including their available records. **Figure 4-1** maps the locations of the most pertinent tide gauges present on the central to southern Oregon coast, along with the locations of various wave buoys operated by the National Data Buoy Center (NDBC) and the Coastal Data Information Program (CDIP), and Global Reanalysis of Ocean Waves (GROW) Fine Northeast Pacific wave hindcast data. These latter stations are pertinent to discussions of the wave climate and modeling described in Section 5, and ultimately in calculations of wave runup and overtopping.

As can be seen in **Table 4-1**, all the gauges have long records (30+ years) suitable for coastal flood analyses. The longest tide-gauge record (79 years) is located at Crescent City (CC) in northern California. The South Beach (SB) and Charleston (CH) gauges have moderately long records on the order of 45 and 42 years respectively (**Table 4-1**); the SB gauge is located within Yaquina Bay, ~2 km from the open coast, and the CH gauge is in close proximity to the mouth of Coos Bay. All hourly tide data were purchased from the NOS and were processed using various scripts developed in MATLAB. In addition to the measured tides, hourly tide predictions were calculated for all years using the NOS tide prediction program, NTP4.

4.1 Tide Characteristics on the Central to Southern Oregon Coast

Tides along the Oregon coast are classified as moderate, with a maximum range of up to 4.3 m (14 ft) and an average range of about 1.8 m (6 ft) (Komar, 1997). There are two highs and two lows each day, with successive highs (or lows) usually having markedly different levels. Tidal elevations are given in reference to the mean of the lower low water levels (MLLW), and can be easily adjusted to the NAVD88 vertical datum. (MLLW to NAVD88 conversions may be performed using values provided for a specific tide gauge by the NOS, or using the VDATUM (http://vdatum.noaa.gov/) tool developed by NOAA.) As a result, most tidal elevations are positive numbers with only the most extreme lower lows having negative values.

Table 4-1. Pacific Northwest NOAA tide gauges.

Gauge Site	Gauge Location	Record Interval	Years
Oregon			
South Beach (SB)	Yaquina Bay, near the inlet mouth	Feb. 1967 – present	45.6
Charleston (CH)	Coos Bay, near the inlet mouth	Apr. 1970 – present	42.4
Port Orford (PO)	Port Orford, open coast harbor	Oct. 1977 – present	35.0
California			
Crescent City (CC)	Crescent City, open coast harbor	Sep. 1933 – present	79.1

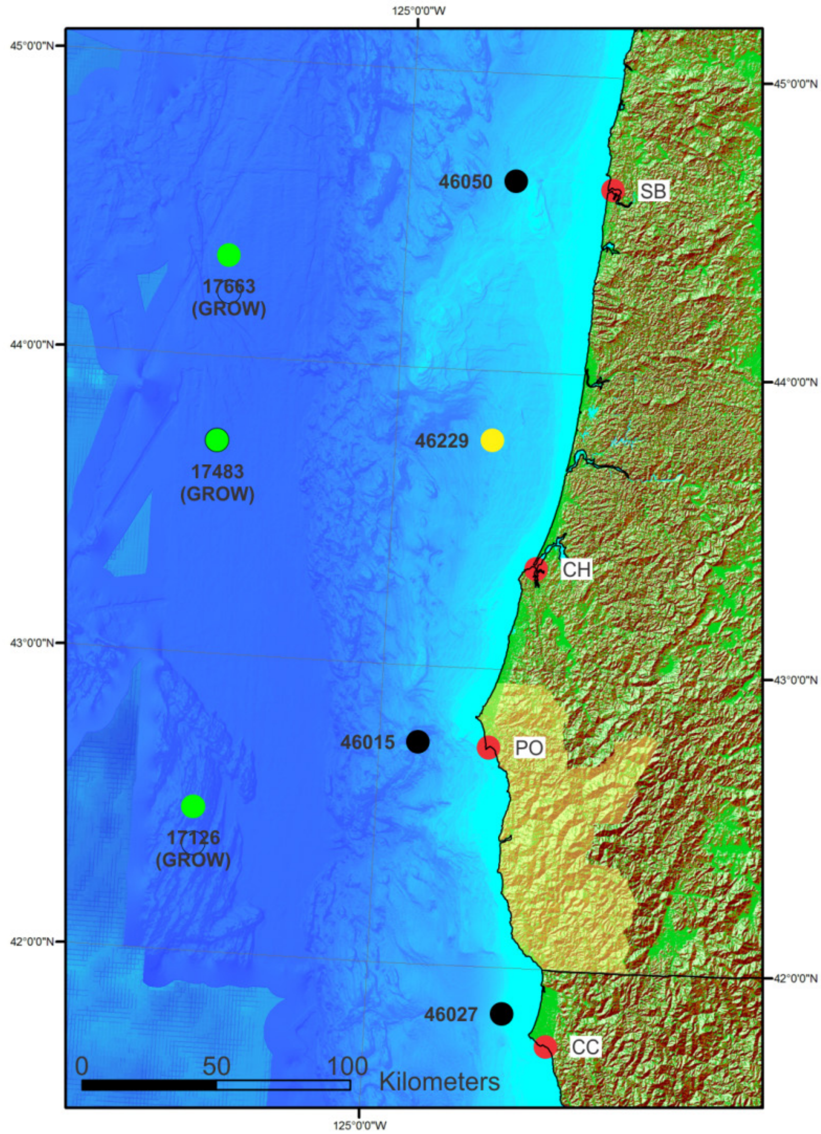

Figure 4-1. Location map of NDBC (black) and CDIP (yellow) wave buoys, tide gauges (red) and GROW wave hindcast stations (green).

Initial analyses of the measured tides focused on developing empirical Probability density function (PDF) plots of the measured tidal elevations for each of the tide gauges located between Newport, Oregon and Crescent City, California. The objective here is to assess the measured tides along the Oregon/northwest California coast in order to identify any significant characteristics (including differences) between the gauges. **Figure 4-2** presents a series of PDF plots from each of the gauges. Because the gauges are characterized by varying record lengths, we have truncated the analyzed data to the period 1978 to 2013, when measurements were available from all four gauges.

As seen in the top plot of **Figure 4-2**, the gauges can be broadly characterized into three regions. In general, the SB gauge on the central Oregon coast indicates a slightly higher incidence of water levels between ~2.0 m and 3.1 m (6.9-10.2 ft). This contrasts with the measured water levels down at Crescent City, which indicate generally lower water levels and in particular a lower incidence of water levels in the same range as at SB. Water levels on the south central Oregon coast (CH and PO) exhibit essentially the same distribution and range, suggesting these two sites are most compatible. These differences are probably related to a combination of effects associated with the regional oceanography (upwelling, shelf currents, and Coriolis effects that deflect the currents toward the coast). The lower plot in **Figure 4-2**shows the same PDF, but now clipped to span tidal elevations between 2 and 4 m (6.5-13 ft). Based on this latter plot, the higher water levels characteristic of SB stand out, being approximately ~0.2 m higher when compared to PO and CH, and significantly higher (~0.4 m) when compared to the CC gauge.

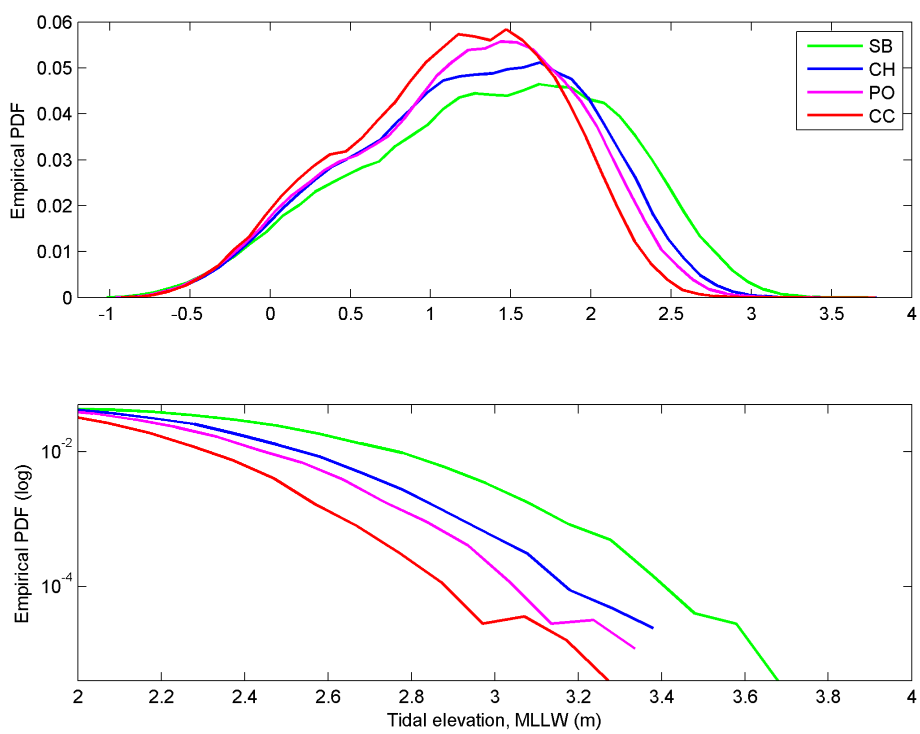

Figure 4-2. Empirical PDF plots for various tide gauges for overlapping years of data (1978–2013). Top) PDF plots showing the full range of tidal elevations, Bottom) truncated to higher water levels.

Figure 4-3 is broadly similar to **Figure 4-2**, with the exception that the PDFs now include the complete time series of data measured by the respective tide gauges. As previously noted, the SB gauge is characterized by a higher incidence of water levels above 2.0 m (>6.9 ft), and a lower incidence of water levels between about 0 and 1.0 m (-0.6–3.3 ft). This clearly contrasts with the CH and PO gauges, which show a higher incidence of water levels between ~1.0 and 1.8 m (3.3-5.9 ft). Detailed examination of the hourly tides indicate that the higher incidence of SB water levels in the wings of the PDF reflect the fact that the Higher Highs are generally larger at SB when compared with CH and PO, while the Higher Lows are generally more frequent at CH and PO compared with the SB gauge.

At the extreme high end of the PDF plots (**Figure 4-3**), the highest water levels measured at SB, CH, PO and CC (when not constrained to the same time period) are respectively 3.64, 3.39, 3.34 and 3.28 m (11.9, 11.1, 11.0, and 10.8 ft). These results equate to a difference of ~0.25 m (~0.8 ft) between SB and CH/PO and 0.36 m (1.2 ft) between SB and CC. Overall, the relative consistency in the PDF plots generated for each gauge, is indicative of the areal impact of major North Pacific extratropical storms, which can affect stretches of coast up to 1,500 km (932 mi, i.e., 3 times the length of the Oregon coast) in length (Davis and Dolan, 1993; Allan and Komar, 2002).

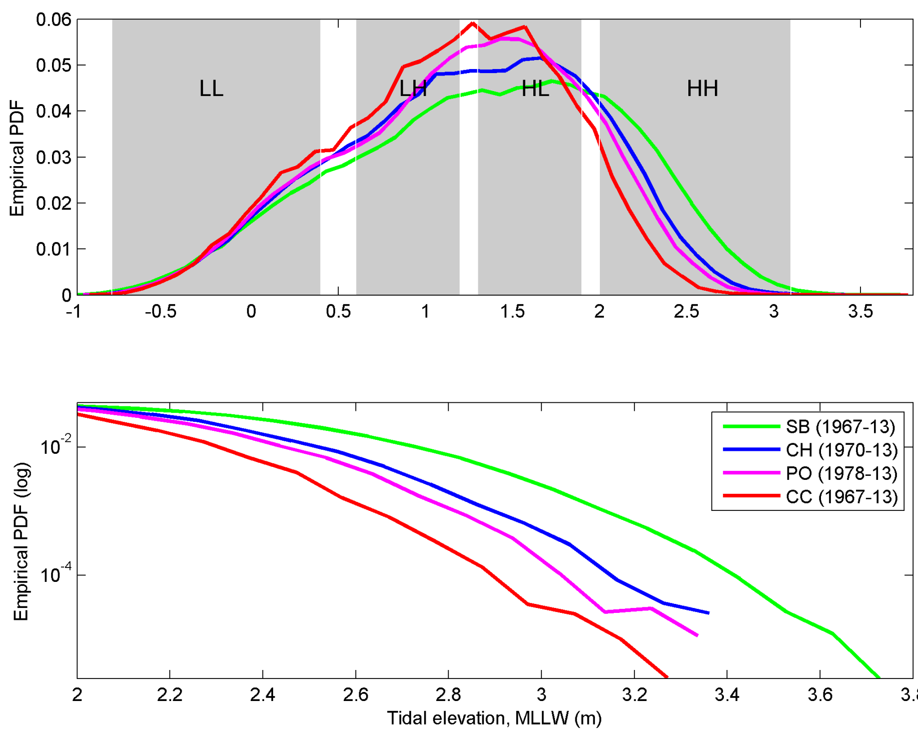

Figure 4-3. Empirical PDFs for SB, CH, PO and CC gauges based on all available data. Top) PDF plot showing the complete range of tidal elevations. LL, LH, HL, and HH denote the Lower Lows, Lower Highs, Higher Lows, and Higher Highs in the tide data. Bottom) PDF truncated to higher water levels.

4.2 Seasonal Changes

Figure 4-4 presents a plot of the characteristic seasonal cycles determined for the four gauges, enabling further examination of their characteristics. All four gauges depict the typical seasonal cycle that reflects the combination of ocean upwelling effects along the coast, and seasonal reversals in the California current system. In general, water levels tend to be highest during the months of December, through March, decreasing to their minimum in the period between May and July. **Figure 4-4** also depicts a pattern whereby the winter peaks progressively increase toward the north, from CC to SB. In contrast, **Figure 4-4** indicates that a southward increase in the water levels during late summer/ early fall period, reaching its peak down in CC; in fact the latter pattern continues south along the U.S. West Coast such that as far south as Los Angelas, the peak in the seasonal cycle has been shifted from its winter peak on the PNW coast to a late summer (September) peak on the southern California coast.

Finally, although not shown in **Figure 4-4**, all the tide gauges are strongly influenced by the El Niño Southern Oscillation phenomena, which periodically causes mean sea levels along the U.S. West Coast to increase (Komar and others, 2011). This response is due to an intensification of the processes, especially enhanced ocean sea surface temperatures offshore from the Oregon coast. This occurred particularly during the unusually strong 1982-83 and 1997-98 El Niños, whereby mean sea levels increased by approximately 20-25 cm (~0.8 ft) above the normal seasonal cycle in mean sea level depicted in **Figure 4-4** (i.e., for a total mean sea level rise of up to 50 cm (1.6 ft) relative to the preceding summer). As a result, under these latter conditions wave swash processes are able to reach to much higher elevations on the beach, potentially eroding dunes and bluffs.

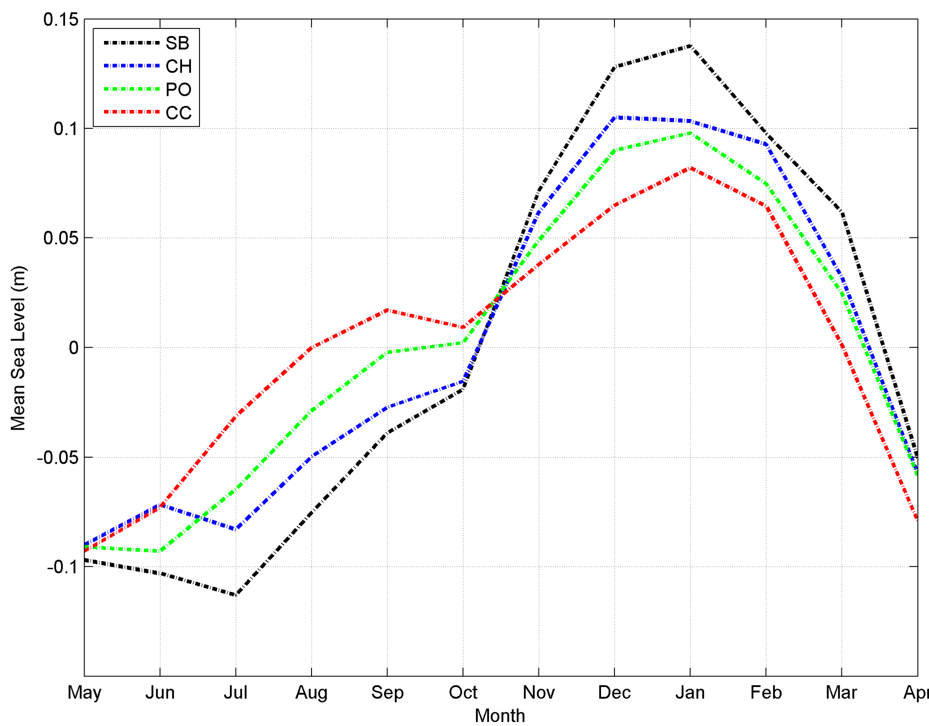

Figure 4-4. Seasonal plot of tides along the central to northern Oregon coast.

4.3 Oregon Storm Surges

The actual level of the measured tide can be considerably higher than the predicted tides provided in standard Tide Tables, and is a function of a variety of atmospheric and oceanographic forces, which ultimately combine to raise the mean elevation of the sea. These latter processes also vary over a wide range of timescales, and may have quite different effects on the coastal environment. For example, strong onshore winds coupled with the extreme low atmospheric pressures associated with a major storm can cause the water surface to be locally raised along the shore as a storm surge, and have been found in tide-gauge measurements to be as much as 1.5 m (4.9 ft) along the Pacific Northwest coast (Allan and Komar, 2002). However, during the summer months these processes can be essentially ignored due to the absence of major storms systems.

Analyses have been undertaken to examine the non-tidal residuals and ultimately the storm surges identified at the various tide gauges on the south central Oregon coast and in Northern California. The objective of this analysis is to provide a better understanding of the spatial and temporal variability of storms as they track across the North Pacific, the magnitudes (and frequency) of the surges, and the potential differences in the non-tidal residuals between the gauges due to variations in the storms tracks, barometric pressures and winds. This last point is particularly important in terms of finalizing the tide gauge time series to be used in the Curry County total water level analyses.

For the PNW, the measured water level (h_t) at a particular tide gauge is given by the following relationship:

$$h_t(t) = z_o + X_{at}(t) + X_{oc}(t) + S(t) \qquad \text{(Eq. 4-1)}$$

where z_o is the mean water level, X_{at} is the predicted astronomical tide, X_{oc} is the altered mean water level due to ocean processes (water temperatures, currents and El Niño “sea-level” waves), and with S being the contribution by the storm surge at time *t*. The predicted astronomical tide for the specific tide gauge is calculated using its harmonic constituents:

$$x_t = \sum_{i=1}^{M} H_i \cos(\sigma_i t + \varphi_i) \qquad \text{(Eq. 4-2)}$$

where H_i is the amplitude of the constituent i, σ_i is its frequency, and φ_i the phase of the constituent, M being the number of tidal constituents included in the analysis.

4.4 Non-Tidal Residual Analyses

The procedures used to analyze the non-tidal residuals and storm surge incidence follow those developed by Allan and others (2011), which used a harmonic analysis method of least squares (HAMELS) approach developed in MATLAB to estimate the amplitude and phase for any set of tidal constituents at each of the tide gauge sites (Boon, 2004). The purpose here is to develop a predicted time series of the water levels produced entirely by astronomic forces that excludes the seasonal component produced by oceanographic processes on the West Coast; the seasonal component can be integrated into tide predictions through the solar annual (Sa) and solar semiannual (Ssa) tide and is integrated as an *average term* in the predicted tides provide by the NOS.

HAMELS analyses of tide gauge data have previously been completed for the SB and TP tide gauges [Allan and others, 2011]. Thus, similar analyses were undertaken using the CH, PO, and CC tide gauges. The specific steps included the following:

- HAMELS was used to derive an estimate of the amplitude and phase for the tidal constituents. This was initially done using just a spring/summer data set for testing purposes and then expanded to the full year of data;
- Having determined the tidal constituents, HAMELS was used to derive the astronomic tide predictions for the entire record on a year-by-year basis (eliminates any long-term

trend). The non-tidal residuals (NTRs) were calculated by subtracting the astronomic tide from the measured tides;

- The NTR time series were then filtered using a moving average filter (averaged over ±30 days) with zero phase shift, and the seasonal cycle was removed from the NTRs;
- The winter standard deviation was calculated and those events exceeding 2*σ were used to define individual surge events (Zhang and others, 2001).

Figure 4-5 presents a series of regression plots of the derived NTRs for the various tide gauges. These data reflect the corresponding NTRs associated with the Higher Highs and Higher Lows of the diurnal tidal cycle, which were determined using a peak detection algorithm in MATLAB. Analyses here span the period of record for the respective tide gauges. Correlation (R^2) values calculated for the three plots are 0.81, 0.88, and 0.77 respectively. Due to their close proximity to one another, the strongest correlations are found between the SB/CH gauges (R^2 = 0.91, not shown in **Figure 4-5**) and the CH/PO tide gauges (R^2 = 0.88) on the open coast, while the weakest correlation shown here is between the PO and the CC tide gauges; although not included a similar comparison was performed between the SB and CC gauges, which resulted in the weakest correlation (R^2 = 0.58).

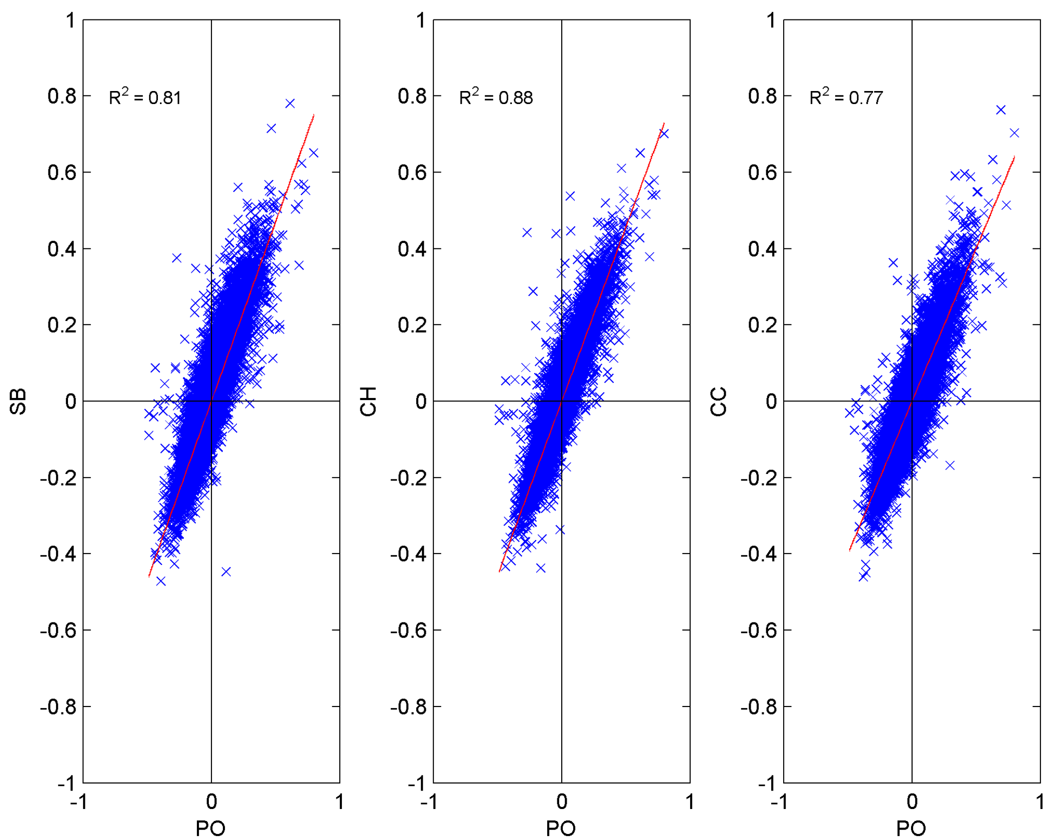

Figure 4-5. Comparison of non-tidal residuals determined for SB versus PO, CH versus PO, and CC versus PO tide gauges. Values plotted here reflect the daily peak values.

Figure 4-6 presents the actual time series of de-seasoned NTRs derived for the SB, CH, PO, and CC tide gauges for the 2007-08 winter. In this example, the NTRs have been time adjusted to a single station. As can be seen in this example, the three Oregon tide gauges tends to track very closely to each other, consistently capturing the same peaks and troughs. In contrast, the CC gauge shows both greater variability as well as phase differences, when compared to the Oregon tide gauges. These differences are further highlighted in the anomaly plot (**Figure 4-6** bottom), which indicates more subtle differences between the three Oregon tide gauges; this latter plot has been smoothed using a LOESS filter. As can be seen from **Figure 4-6** (bottom), the CH and PO gauges is characterized by generally lower anomalies (±0.1 m [0.33 ft]). In contrast, anomalies between the PO and CC tide gauges reveal much larger differences. Such variability is largely a function of differences in the position of the storms relative to the tide-gauges, the storm's barometric pressures, winds, and the associated wave forcing along the coast. Overall, differences between the Oregon tide gauges probably reflect mostly subtle shifts in the timing of the events as they impact the coast, reinforcing our confidence that the effects of North Pacific extratropical storms are indeed widespread, affecting large tracts of the coast at similar times.

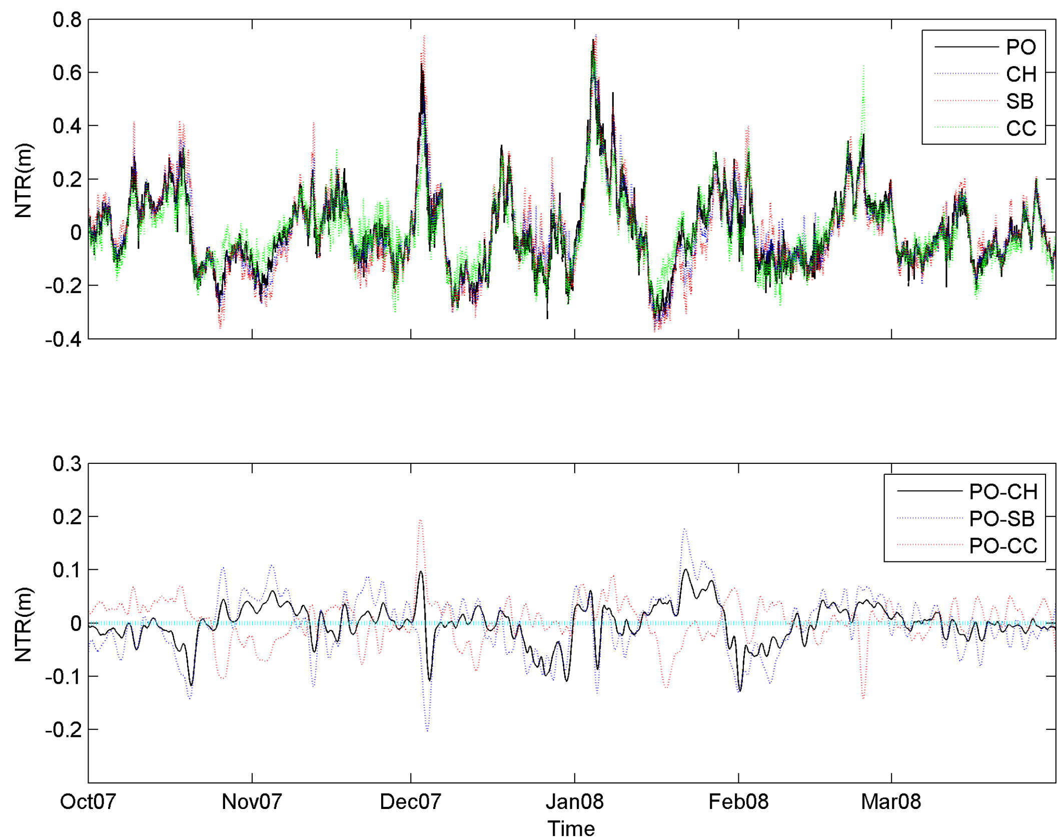

Figure 4-6. Comparison of Top) non-tidal residuals (NTRs), and Bottom) their differences between the SB, CH, PO, and CC tide gauges for the 2007-08 winter.

Having identified the NTRs for each of the tide gauges, individual storm surge events have been identified following the procedures of Zhang and others [2001] and Allan and others [2011]. **Figure 4-7** (left) presents a log number plot of all surge events for SB, CH, PO, and CC gauges. The plot indicates that for the most part the four gauges are showing relatively similar patterns in terms of the storm surge magnitudes. In general, the mean storm surges increase northward (0.42 m [1.4 ft] at CC to 0.5 m [1.6 ft] at SB), while the highest surges have occurred at SB (1.42 m [4.7 ft]); the highest surge observed at CC reached 0.91 m (3.0 ft). **Figure 4-7** (right) presents the empirical CDF calculated for the four gauges, further highlighting the progressive shift in the surge magnitudes to the north. Again, the SB gauge stands out, characterized by higher surges. Of interest, the CDF plot for PO (**Figure 4-7**, right) is generally higher when compared to the CH gauge. This difference probably reflects the fact that the PO gauge is truly an open coast site, whereas the CH (and the other gauges) are located within the estuaries such that their measurements may be somewhat muted when compared to the open coast.

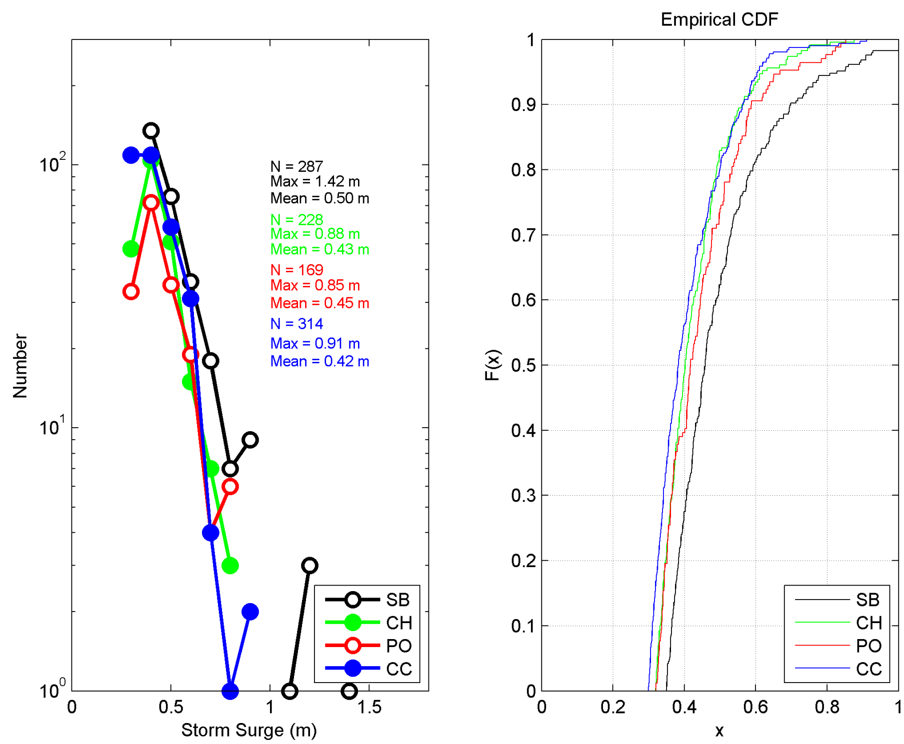

Figure 4-7. Frequency distribution plot showing the incidence and magnitude of storm surges on the Oregon and northern California coast.

Taken together, these analyses confirm that the tide gauges located in Port Orford and at Charleston in Coos Bay, overall provide the best measure of the open-coast still water levels, important in FEMA total water level and overtopping analyses. The main distinction between these two stations is the length of available measurements, with the PO site having the shortest record (~35 years), followed by the Charleston gauge. Furthermore, based on our analyses, we believe that the measured tides at Crescent City is significantly different from the Port Orford gauge such that it should not be used in FEMA flood analyses for the Curry County open coast.

4.5 Curry County Tides

For the purposes of this study, we have based our still water level (SWL) and wave runup calculations on a combined time series that encompasses tides measured primarily at the Port Orford gauge (#9431647, 1978-present), and from the Charleston tide gauge (#9432780) in Coos Bay (1970–present). Additional gaps (primarily from the early to mid-1970s) have been filled using data from the South Beach (#9435380) tide gauge, located at Newport, Oregon, for a combined time series of 1970–2013. **Figure 4-8** shows the tidal elevation statistics derived from the Port Orford tide gauge, with a mean range of 1.59 m (5.2 ft) and a diurnal range of 2.22 m (7.28 ft). The highest tide measured from this record reached 3.5 m (11.5 ft) MLLW, recorded in February 1978 during a major storm. These values are comparable to those measured at the Charleston site (mean = 1.73 m [5.69 ft], diurnal = 2.32 m [7.62 ft]), with the only real difference being the fact that this latter gauge recorded a peak water level of 3.41 m (11.2 ft) in January 1983. **Figure 4-9** presents a summary empirical Probability density function (PDF) plot of the measured tidal elevations from the four tide gauges and the synthesized tide data (solid black line) centered on the Port Orford gauge. As can be seen in the figure, the synthesized PDF is essentially emulating the Port Orford PDF at all tide stages.

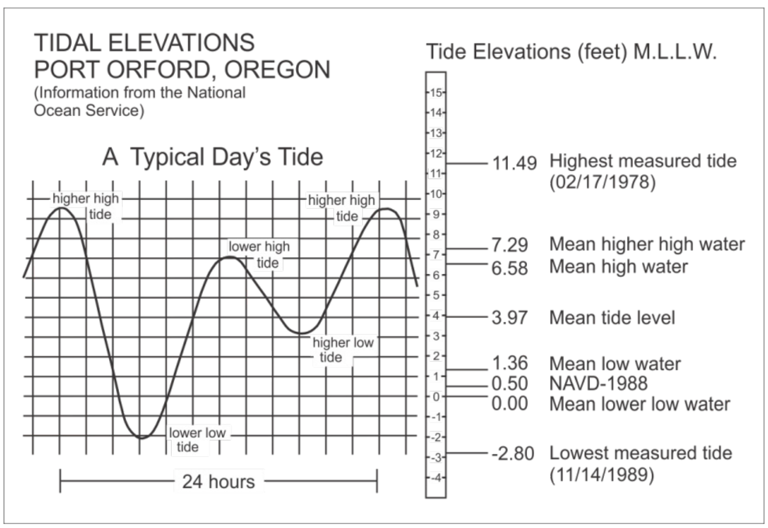

Figure 4-8. Daily tidal elevations measured at Port Orford, on the southern Oregon coast. Data from the National Ocean Service (http://www.co-ops.nos.noaa.gov/data_menu.shtml?stn=9432780%20Charleston,%20OR&type=Bench%20Mark%20Sheets).

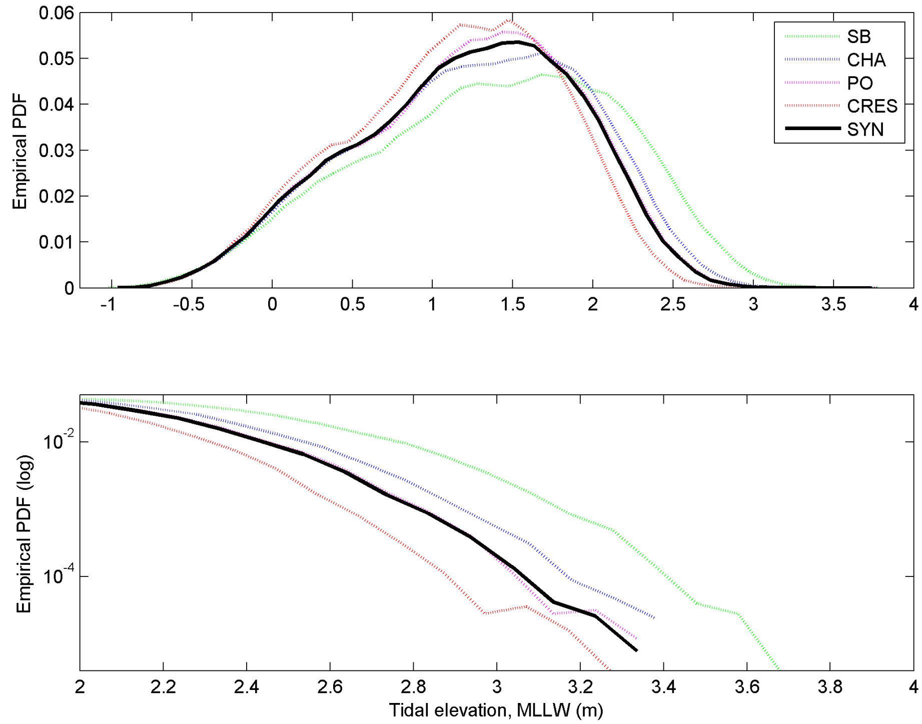

Figure 4-9. Empirical PDF plots for various tide gauges for overlapping years of data (1978–2013), and the synthesized time series centered on the Port Orford tide gauge. Top) PDF plots showing the full range of tidal elevations, Bottom) truncated to higher water levels.

As noted previously, tides on the Oregon coast tend to be enhanced during the winter months due to warmer water temperatures and the presence of northward flowing ocean currents that raise water levels along the shore, persisting throughout the winter rather than lasting for only a couple of days as is the case for a storm surge (Komar, 1997). This effect can be seen in the monthly averaged water levels derived from the combined time series (**Figure 4-10**), but where the averaging process has removed the water-level variations of the tides, yielding a mean water level for the entire month. Based on 43 years of data, the results in **Figure 4-10** show that on average monthly-mean water levels during the winter are 19 cm (0.6 ft) higher than in the summer. Water levels are most extreme during El Niño events, due to an intensification of the processes, largely enhanced ocean sea surface temperatures offshore from the Oregon coast (Komar 1997, Allan and Komar, 2002; Komar and others, 2011). This occurred particularly during the unusually strong 1982-83 and 1997-98 El Niños. As seen in **Figure 4-10**, water levels during those climate events were approximately 25–30 cm (0.8–1 ft) higher than the seasonal peak, and as much as 52 cm (1.7 ft) higher than during the preceding summer, enabling wave swash processes to reach much higher elevations on the beach during the winter months, with storm surges potentially raising the water levels still further.

Aside from seasonal to interannual effects of climate events on ocean water levels, also of interest are the long-term trends associated with relative sea level changes due to climate change along the Curry County coastline. **Figure 4-11** presents results from an analysis of the synthesized time series based on a separate analysis of the summer and winter tide levels. For our purposes "winter" is defined as the combined average tide level measured over a 3-month period around the peak of the seasonal maximum in winter water levels, typically the months of December through February. Similarly, "summer" water levels reflect the combined average tide level measured over a 3-month period around the seasonal minimum, typically the months between May through July when water levels also tend to be less variable (Komar and others, 2011). As observed previously in **Figure 4-10**, the winter tidal elevations are systematically displaced upward by about 19 cm (0.6 ft) above the summer, with the difference between the regression lines reflecting the seasonal change in ocean water levels from summer to winter. **Figure 4-11** also emphasizes the extremes associated with major El Niños, with the peaks between the 1983 and 1997 major events having been systematically shifted upward over the years due to relative sea level changes along this particular section of the coast. In contrast, the summer regression line is characterized by significantly less scatter in the residuals because it effectively excludes the influence of storms and El Niños that are dominant during the winter. With this approach, the resultant trend suggests that the south central Oregon coast is an emergent coast, such that sea level is falling at a rate of ~-0.15 ± 0.87 $mm.yr^{-1}$. However, the identified trend is not significant at the 95% confidence interval; NOTE, the NOS reports a positive trend of ~+0.18 ± 2.18 $mm.yr^{-1}$, which is also not significant at the 95% level. This difference in the sign is due entirely to the fact that the NOS includes all monthly values in their analyses, whereas we have confined our assessment to the summer/winter conditions within each year.

Finally, it is important to appreciate that the trends shown in **Figure 4-11** reflect relative sea level changes due to the fact that the PNW coast of Oregon and Washington is locally influenced by changes in the elevation of the land due to regional tectonics as well as by the global rise in sea level, with the net change being important to both coastal erosion and flood hazards. **Figure 4-12** presents a synthesis of both tectonic land elevation changes and sea level trends derived for multiple stations along the PNW coast (Komar and others, 2011), correlated against differential surveys of first-order NGS benchmarks [e.g., Burgette and others, 2009], and GPS CORS stations. Results here indicate that in general the southern Oregon coast is an emergent coast with tectonic uplift of the land outpacing sea level rise, consistent with the results depicted in **Figure 4-11**. In contrast the central to northern Oregon coast is slowly being transgressed by sea level, even though it is tectonically rising, though at a slower rate than along the south coast. In the far north in Clatsop County, the overall pattern suggests that this portion of the coast varies from slight submergence in the southern County to emergent in the north along the Clatsop Plains.

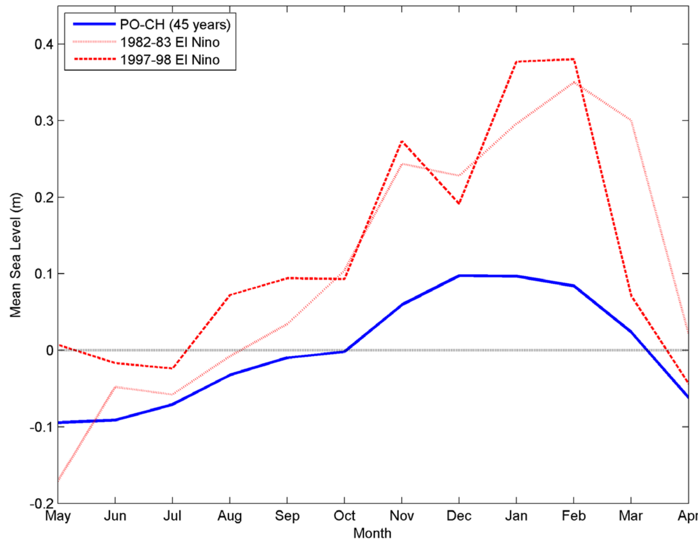

Figure 4-10. Seasonal cycles in monthly-mean water levels based on data from the combined Port Orford/Charleston measured tides.

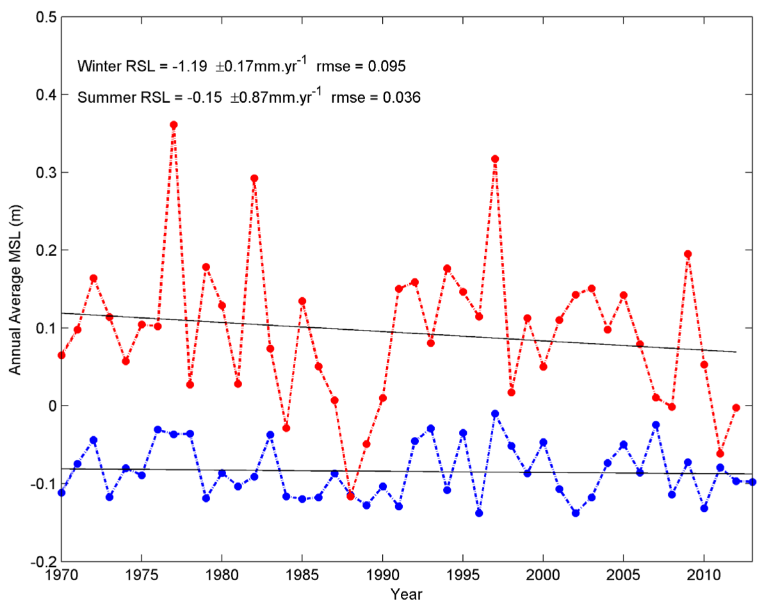

Figure 4-11. The trends of "winter" (red) and "summer" (blue) mean sea levels measured by the PO/CH tide gauges. Results for the regressions are not statistically significant, indicating not valid trend.

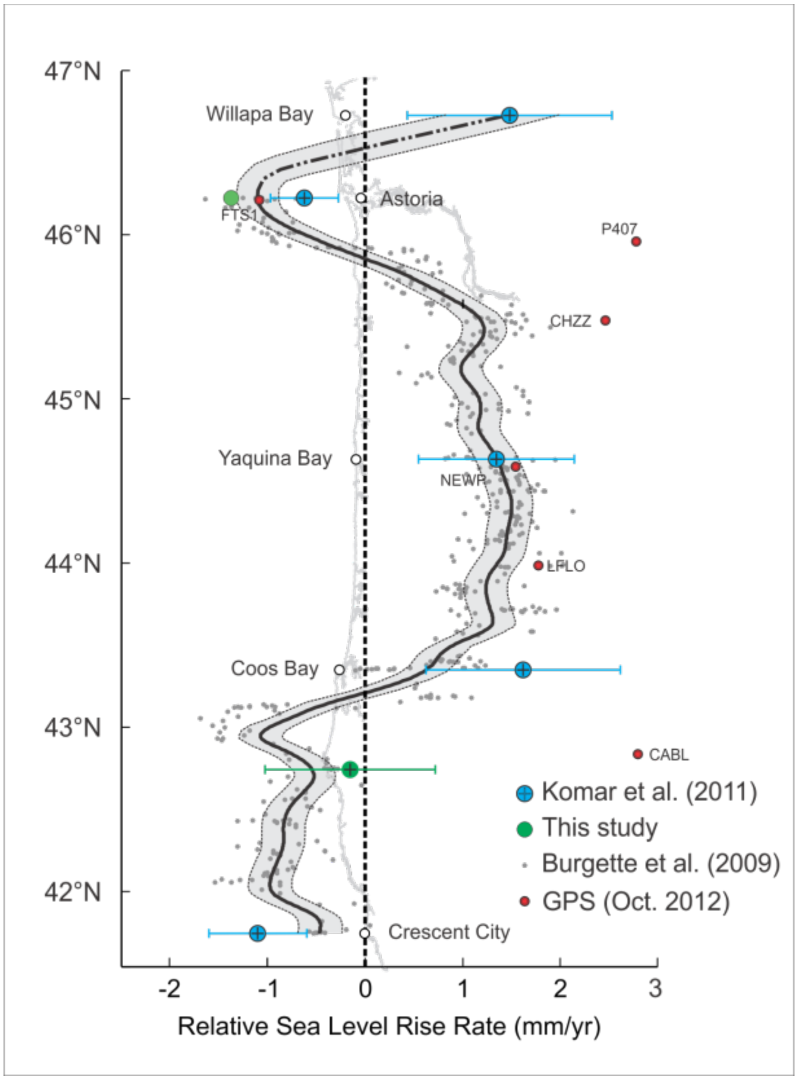

Figure 4-12. Assessments of changes in RSLs based on tide-gauge records compared with benchmark and GPS measurements of land-elevation changes, with their corresponding RSL rates obtained by adding the 2.28 mm/yr PNW eustatic rise in sea level (Komar and others, 2011).

4.6 Still Water Level (SWL)

The Still Water Level (SWL) is the sum of the predicted astronomical tide listed in Tide Tables, plus the effects of processes such as an El Niño or storm surge that can elevate the measured tide above the predicted tide (Northwest Hydraulic Consultants, 2005). Of importance to erosion and flooding hazards are the extremes of the measured tides. In conventional analyses of extreme values, the general assumption is that the data being analyzed (e.g., the annual maxima) represent independent and identically distributed (stationary) sequences of random variables. The generalized extreme value (GEV) family of distributions is the cornerstone of extreme value theory, in which the cumulative distribution function is given as:

$$G(z, \mu, \sigma, \xi) = \exp\left\{-\left[1+\xi\left(\frac{z-\mu}{\sigma}\right)\right]^{-1/\xi}\right\} \qquad (4.3)$$

defined on

$$\left\{z: 1+\frac{\xi(z-\mu)}{\sigma} > 0\right\},$$

where the parameters satisfy $-\infty < \mu < \infty$, $\sigma > 0$, $-\infty < \xi < \infty$, (Coles, 2001). The model has three parameters; μ is a location parameter, σ is a scale parameter, and ξ is a shape parameter. The EV-II (Frechet) and EV-III (Weibull) classes of extreme value distributions correspond respectively to the cases of $\xi > 0$ and $\xi < 0$. When $\xi = 0$, equation 4.3 collapses to the Gumbel or EV-I type extreme value distribution. By inferring the shape parameter ξ (estimated here, along with the other parameters, by maximizing the log-likelihood function), the data themselves determine the most appropriate type of tail behavior and it is not necessary to make an a priori assumption about which individual extreme family to adopt as in a classical Weibull-type extreme wave height analysis (Coles, 2001).

The GEV is often applied to annual maxima data in an approach referred to as the annual maximum method (AMM). However, one of the primary shortcomings of fitting an extreme-value distribution with annual maximum data is that useful information about the extremes is inherently discarded, particularly when data are sampled on either a daily or hourly basis (as in the case of the measured tides and deep-water significant wave heights measured by Charleston tide gauge and NDBC wave buoys). Two well-known approaches exist for characterizing extremes by utilizing data other than simply annual (block) maxima. The first is based on the behavior of the r-largest-order statistics within a block, for low r, and the second is based on exceedances above a high threshold value. For the purposes of this study, we use the peak-over-threshold (POT) approach for determining the extreme SWL and wave heights.

In the peak-over-threshold (POT) method, a high threshold, u, is chosen in which the statistical properties of all exceedances over u and the amounts by which the threshold is exceeded are analyzed. It is assumed that the number of exceedances in a given year follows a Poisson distribution with annual mean vT, where v is the event rate and T = 1 year, and that the threshold excesses $y > 0$ are modeled using the Generalized Pareto Distribution (GPD) given by:

$$H(y, \sigma, \xi) = 1\text{-}\left(1+\frac{\xi y}{\sigma}\right)^{-1/\xi} \qquad \text{(Eq. 4-4)}$$

where ξ is the shape parameter of the GEV distribution and σ is a scale parameter related to GEV parameters by $\sigma = \sigma + \xi(u-\mu)$. The event rate can also be expressed in a form compatible with the GEV distribution provided that

$$v = \left(1+\frac{\xi(u-\mu)}{\sigma}\right)^{-1/\xi}.$$

Estimates of extreme quantiles of the distributions are obtained by inverting the distributions in equation 4.4. For GPD-Poisson analyses the N-year return level, y_N, is given as:

$$y_N = \mu + \frac{\sigma}{\xi}\left[(N n_y \zeta_u)^{\xi} - 1\right] \qquad \text{(Eq. 4-5)}$$

where n_y is the number of observations per year and ζ_u is the probability of an individual observation exceeding the threshold u.

Figure 4-13 presents results of the GEV analyses for the combined PO/CH measured tides. In constructing this plot, we used a threshold of 2.62 m (8.6 ft). Included in the figure are the calculated 1- through 500-year SWLs. As can be seen in **Figure 4-13** (top), the 1% SWL calculated for the combined time series is 3.39 m (11.1 ft, relative to NAVD88; the adjustment from NAVD88 to MLLW is 0.151 m [0.5 ft] at the PO gauge). The 500-year SWL is estimated to be 3.56 m (11.7 ft) relative to the NAVD88 vertical datum. The highest tide measured in the combined time series reached 3.35 m (11.0 ft, relative to NAVD88).

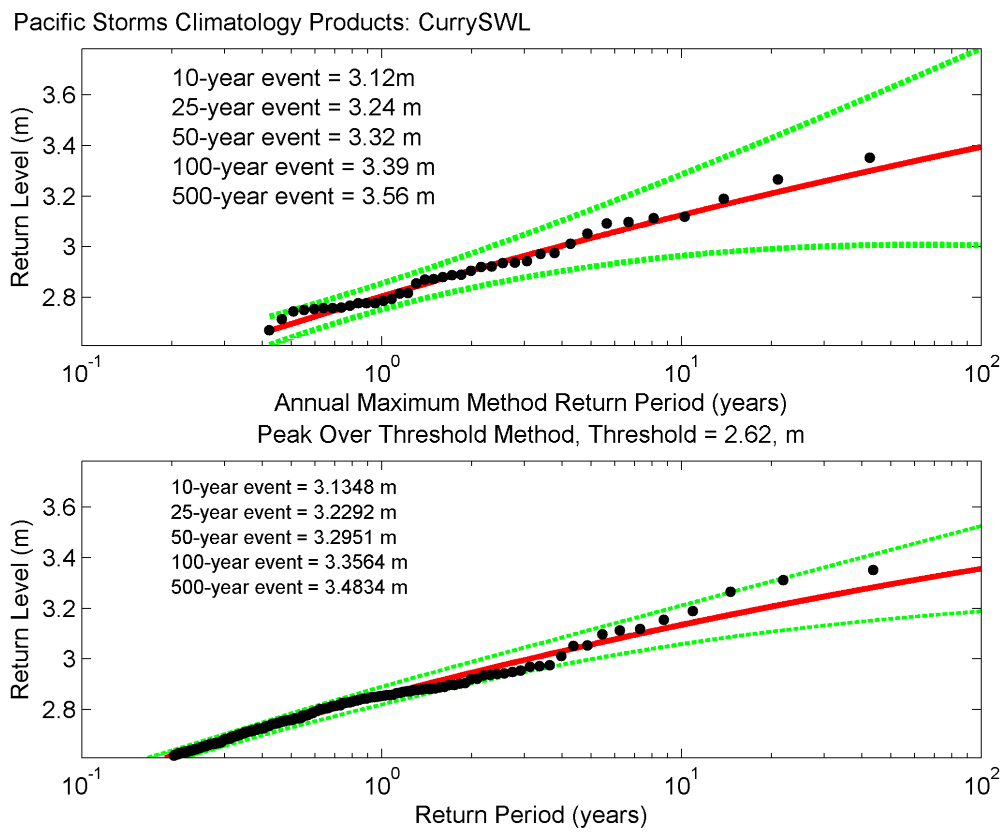

Figure 4-13. Extreme-value analyses of the Still Water Level (SWL) determined for the combined PO/CH tide gauge time series. Data are relative to the NAVD88 vertical datum.

5.0 PACIFIC NORTHWEST WAVE CLIMATE

The wave climate offshore from the Oregon coast is one of the most extreme in the world, with winter storm waves regularly reaching heights in excess of several meters. This is because the storm systems emanating from the North Pacific travel over fetches that are typically a few thousand miles in length and are characterized by strong winds; the two main factors that account for the development of large wave heights and long wave periods (Tillotson and Komar, 1997). These storm systems originate near Japan or off the Kamchatka Peninsula in Russia, and typically travel in a southeasterly direction across the North Pacific toward the Gulf of Alaska, eventually crossing the coasts of Oregon and Washington or along the shores of British Columbia in Canada (Allan and Komar, 2002).

Wave statistics (heights, periods and, more recently, wave direction) have been measured in the Eastern North Pacific using wave buoys and sensor arrays since the mid 1970s. These data have been collected by the National Data Buoy Center (NDBC) of NOAA, and by the Coastal Data Information Program (CDIP) of Scripps Institution of Oceanography. The buoys cover the region between the Gulf of Alaska and Southern California, and are located in both deep and in intermediate to shallow water over the continental shelf. The NDBC operates some 30 stations along the West Coast of North America, while CDIP has at various times carried out wave measurements at 80 stations. Presently there is one CDIP buoy, operating offshore from the mouth of the Umpqua River (#46229), and five NDBC buoys (Port Orford [#46015], Oregon [#46002], SE Papa [#46006], St. Georges [#46027], and Eel River [#46022]) off of southern Oregon (**Figure 5-1**). Wave measurements by NDBC are obtained hourly (CDIP provides measurements every 30 minutes), and are transmitted via satellite to the laboratory for analysis of the wave energy spectra, significant wave heights and peak spectral wave periods. These data can be obtained directly from the NDBC through their website (http://www.ndbc.noaa.gov/maps/Northwest.shtml).

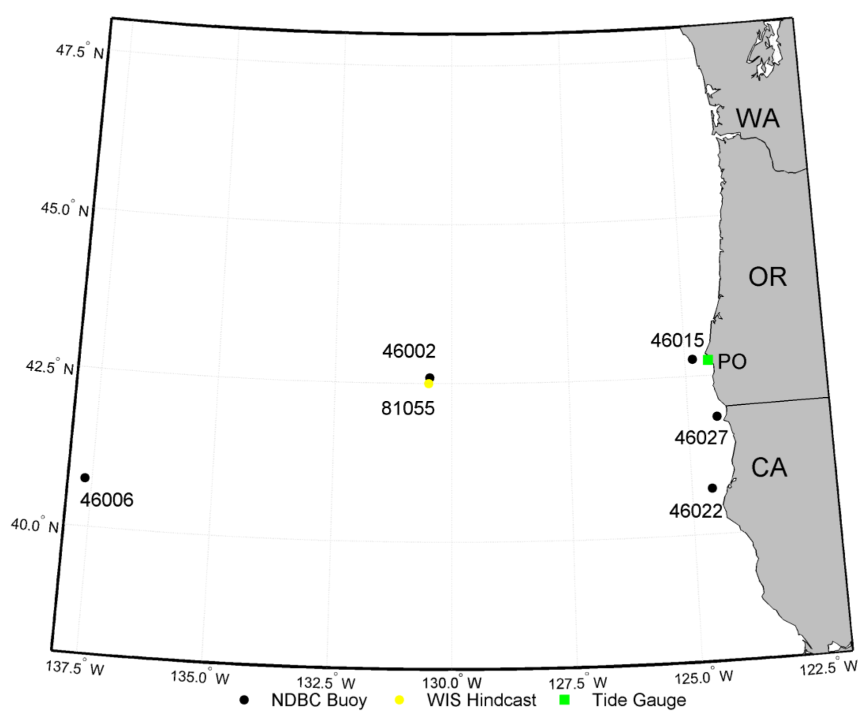

Figure 5-1. Map showing the regional divisions from which synthesized wave climates have been developed.

An alternate source of wave data appropriate for FEMA flood modeling is hindcast wave data such as the Global Reanalysis of Ocean Waves Fine Northeast Pacific Hindcast (GROW-FINE NEPAC), available through Oceanweather Inc., and Wave Information Studies (WIS; http://wis.usace.army.mil/) hindcasts developed by the USACE (Baird, 2005). GROW is a global wave model, while GROW–FINE NEPAC extends the global model by incorporating a higher resolution model analysis (4 times as many data nodes), basin-specific wind adjustments based on QUIKSCAT scatterometry, enhancements in incorporating Southern Ocean swells, and the inclusion of shallow water physics (Oceanweather Inc., 2010). These data can ultimately be applied to offshore structure design, tow-analysis, operability, and other applications where wind and wave data are required. Standard products from GROW include time series of wind and wave parameters (including sea/swell partitions), extremes operability statistics, and wave spectra (Oceanweather Inc., 2010). The advantage of GROW as opposed to measured data is that it provides a continuous time series of wave and wind data suitable for FEMA flood modeling. In contrast, measured data obtained from wave buoys may be characterized by significant data gaps due to the instruments having come off their mooring or from instrument failure. The main disadvantage of GROW-FINE NEPAC data is that it is modeled based on basin-scale wind models and data, and the data time series is 3 hourly as opposed to hourly as provided by the buoys. For the purposes of this study, we have explored both data sets in order to define the most appropriate time series of wave data. To that end, GROW-FINE NEPAC data were purchased for three nodes offshore the Oregon coast. Besides the hourly measured wave buoy data, we also obtained hourly wave hindcast information on the deep-water wave climate through the WIS station located adjacent to NDBC buoy 46002.

Analyses of the wave climate offshore from Curry County were undertaken by DOGAMI staff and, as a subcontract, to Dr. Peter Ruggiero's team at the College of Earth, Ocean, and Atmospheric Sciences (CEOAS) at Oregon State University (OSU). This work included numerical analyses of the 1% or 100-year extreme total water levels (TWLs), which reflect the calculated wave runup superimposed on the tidal level (i.e., the Still Water Level [SWL]) to help determine the degree of coastal flood risk along the coast of Curry County.

OSU performed a series of tests and analyses including wave transformations, empirical wave runup modeling, and TWL modeling. For the purposes of this study, OSU used the SWAN (Simulating Waves Nearshore) wave model to transform deep-water waves to the nearshore (typically the 20 m (65.6 ft) contour). The transformed waves were then linearly shoaled back into deep-water to derive a refracted deep-water equivalent wave parameterization (wave height, peak period, and dominant direction) that can be used to calculate runup levels, which combined with tides, are used to estimate the flood risk along the county's shoreline.

In our Coos County FEMA study (Allan and others, 2012b), we developed an approach that involved several stages:

1. A time series of deep-water wave heights, periods, and directions was first defined for a particular location offshore of the shelf break, which we used to calculate an initial wave runup and TWL time series based on two representative beach slopes characteristic of beaches in the Coos County detailed study areas.
2. Using the above approach, we defined ~135 discrete storm events for the two different slope types. From on these events, we transformed the deepwater wave statistics associated with these events into the nearshore (20 m water depth) to account for wave refraction and shoaling effects. Depth limited breaking, wind growth, quadruplets, and triad interactions were all turned off in the SWAN runs. The derived nearshore wave statistics were then converted back to their adjusted deep-water equivalent wave height in order to perform the wave runup analyses and ultimately compute the 1% TWLs.

The main limitations associated with this approach were:

1. Only a limited number of model runs were performed, ~135 per representative beach slope.
2. Because we used only two representative beach slopes, we may have missed a particular wave condition (wave height [H_s], period [T_P], direction [D_d]) and beach slope (tan β) combination that resulted in a higher TWLs at the shoreline.
3. The structural function approach used to generate the initial extreme TWLs and therefore to pick the offshore wave conditions input in SWAN is fundamentally limited. Nature gave us only 1 combination of waves and water levels during the 30 years we used to generate input conditions, which is not necessarily a statistically robust sample.

For the purposes of the Curry County study, including other detailed FEMA coastal studies already completed for Oregon, we have developed a more refined approach that reflects the following enhancements.

1. Rather than steps 1 and 2 as described for our Coos County study, modeling was carried out based on analyses of the full range of wave and tide combinations observed over the historical period. This approach ultimately provides a more robust measure of the 1% (and other desired return periods) TWLs.
2. We have developed a lookup table approach for analyzing thousands of possible storm combinations rather than only a few hundred as performed in Coos County. The general idea is that a "lookup table" can be developed by transforming all combinations of wave quadruplets (H_S, T_P, D_d, and water levels). We used SWAN to compute the transformed wave characteristics of these waves up to approximately the 20 m contour.
3. Our approach still suffers from the 3rd limitation listed above for the Coos County study.

The area over which the SWAN grid was set up is shown in **Figure 5-2**. In general, our analyses proceeded in the following order:

1. Develop a long time series of both measured (NDBC) and modeled (WIS) wave conditions (~30 years long) at approximately the shelf edge offshore of the study area.
2. Run the SWAN model with a full range of input conditions, using constant offshore boundary conditions, to compute bathymetric induced wave transformations up to wave breaking.
3. Develop "lookup tables" from the suite of SWAN simulations.
4. Transform the long time series through the "lookup tables" such that we generate alongshore varying time series at approximately the 20-m depth contour throughout the study area.
5. Use the deepwater equivalent alongshore varying wave conditions and the appropriate measured tides from the combined Port Orford/Charleston/Yaquina Bay time series to compute time series of TWLs for 109 primary beach profile sites along the Curry County coast. These include transects established in the Brookings area (47 sites), Gold Beach (14 sites), Rogue Shore (13 sites), Nesika Beach (19 sites), and Port Orford (16 sites).
6. Using a Poisson-generalized Pareto distribution, compute the 1-, 10-, 25-, 50-, 100-, and 500-year TWL elevations using a peak-over-threshold (POT) approach.
7. Compare extreme TWLs with topographic elevations of various beach-backing features to determine the potential extent of coastal flooding during extreme events.

The following sections describe in more detail the various procedures used in each of the aforementioned steps in this analysis.

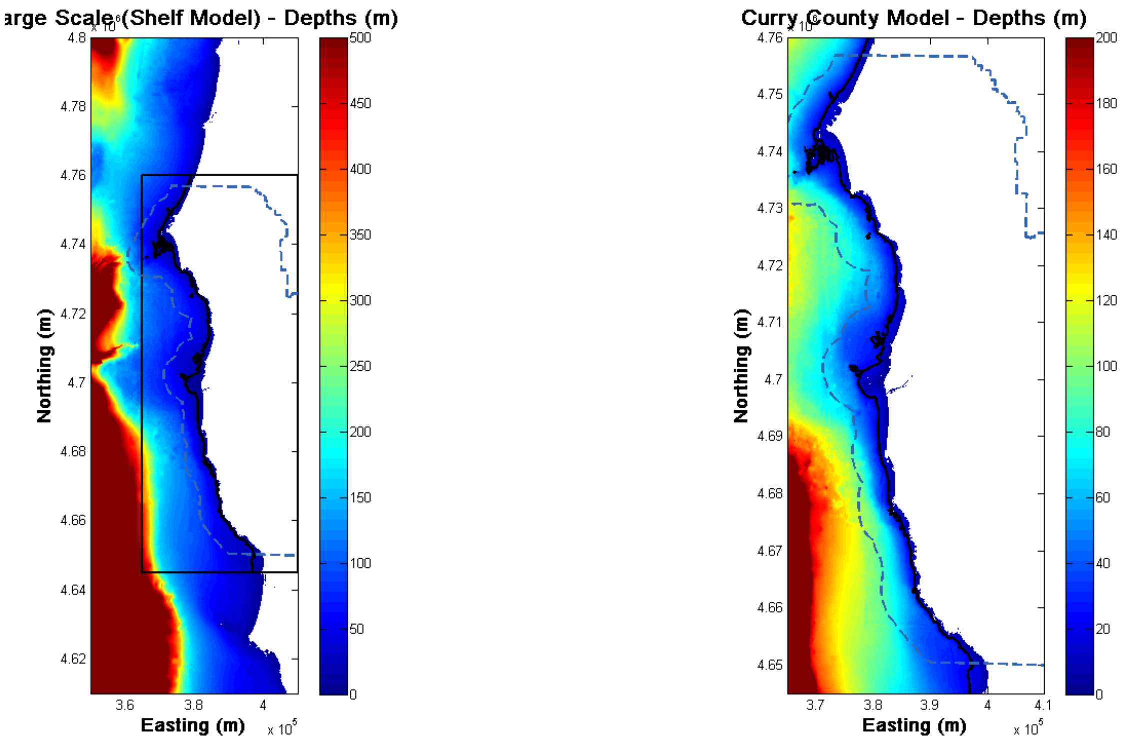

Figure 5-2. The SWAN model domain developed for the Curry County coast. The model bathymetry was developed using 1/3 arc-second (~10 m) DEMs downloaded from the NOAA's NGDC. Color scale reflects depth in meters.

5.1 Development of a Synthesized Wave Climate for Input into SWAN

Our primary goal was to use existing measured and hindcast wave time series to generate as long a record of the deep-water wave climate as possible for the offshore boundary of the SWAN model, approximately the edge of the continental shelf break. To this end, we downloaded all available National Data Buoy Center (NDBC; http://www.ndbc.noaa.gov/) and Coastal Data Information Program (CDIP; http://cdip.ucsd.edu/) hourly wave buoy data in the region for several wave buoys. **Figure 5-1** shows the various buoys used to derived a synthesized southern Oregon coast wave data set (data availability shown in **Figure 5-3**). Besides the hourly measured wave buoy data, we also obtained wave hindcast information on the deep-water wave climate determined through the Wave Information Studies (WIS; http://wis.usace.army.mil/) (Baird & Associates, 2005). For the purposes of this study, we used wave hindcast data determined for station 81055 (**Figure 5-1**), which is located adjacent to NDBC buoy #46002. While both NDBC #46002 and #46006 have high-quality, long records of data (~1979–2013), they are located in 3,444 m (11,300 ft) and 4,151 m (13,615 ft) of water, respectively, and over 400–500 km (250–310 mi) and 1,000 km (620 mi), from the shelf edge. Therefore, NDBC #46015, an intermediate water depth buoy, was selected as the priority buoy to be used in the SWAN analyses, and linearly reverse shoaled to deep water to account for wave height changes in intermediate depths. The on-shelf buoys (Eel River, #46022, St. Georges #46027) were also included in this analysis, and reverse shoaled to deep water.

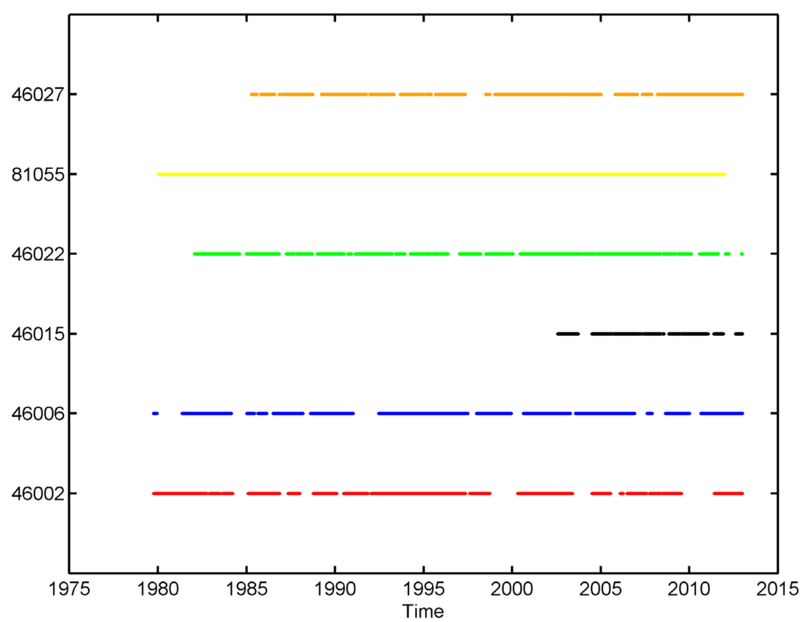

Figure 5-3. Available wave data sets timeline (after Harris, 2011).

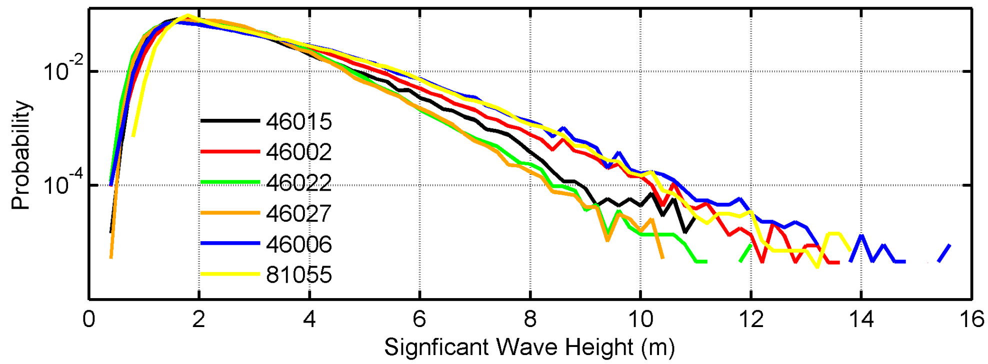

Figure 5-4. Differences in the empirical probability density functions of the onshore and offshore buoys.

Because of the variation in locations and water depths of the buoys, we needed to develop a methodology to transform these "off-shelf" and "on-shelf" waves to the "shelf-edge" offshore boundary condition of the SWAN model. This was necessary as the wave climates observed at 46006, 46002, 46027, and 46022 are different from the climate observed at the Port Orford offshore buoy (**Figure 5-4**).

To transform the 46002, 46006, 46027, and 46022 waves to the shelf edge, we created wave period bins (0–6, 6–8, 8–10, 10–12, 12–14, 14–16, 16–21, and 21–30 s[1]) to evaluate if there has been a wave period dependent difference in wave heights observed at Oregon 46002, SE Papa 46006, St. Georges 46027, and Eel River 46022 compared with the Port Orford buoy. For our comparisons, the time stamps associated with waves measured at offshore and onshore buoys were adjusted based upon the group celerity (for the appropriate wave period bin) and travel time it takes the wave energy to propagate to the wave gauge locations. For example, for waves in the period range 10 to 12 s the group celerity is about 8.3 m/s and therefore it takes 15 hours for the energy to propagate from 46002 to the Port Orford buoy (**Figure 5-5**).

After correcting for the time of wave energy propagation, the differences in wave heights between the two buoys, for each wave period bin, were examined in two ways as illustrated in **Figure 5-5**:

1. A best fit linear regression through the wave height differences was computed for each wave period bin; and
2. A constant offset was computed for the wave height differences for each period bin.

[1] The NDBC wave buoys only relatively coarsely resolve long period waves. Between 21 and 30 s, only a wave period of 25 s is populated in the data set. There are no 30-s waves in the time series. Of the waves with periods between 16 s and 20 s over 80 percent of them are at approximately 16 s. Only a few waves in the record have recorded periods of 17, 18, and 19 s, respectively. This coarse resolution in the raw data determined our choice of period bin widths.

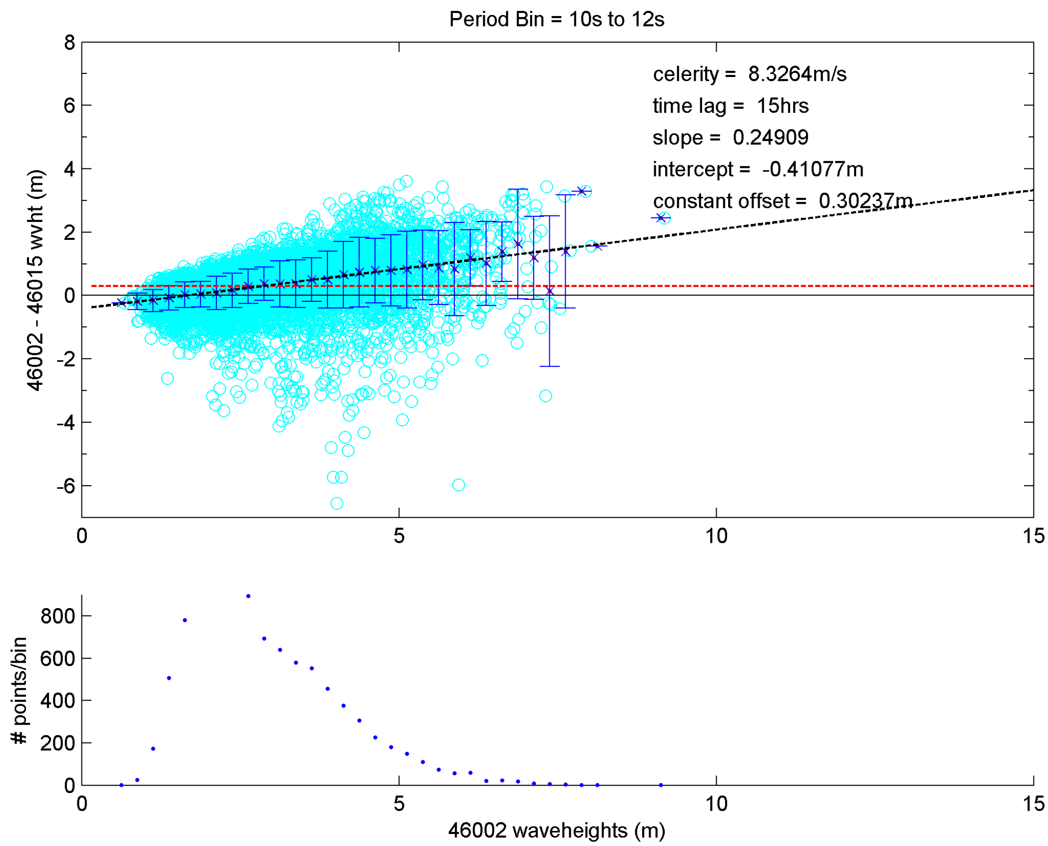

Figure 5-5. Example development of transformation parameters between the Oregon buoy (#46002) and the Port Orford (#46015) buoy for period range 10 s to 12 s. In the top panel the dashed black line is the linear regression and the dashed red line is the constant offset. Blue error bars represent the standard deviation of the wave height differences in each period bin (Harris, 2011).

Upon examination of the empirical probability density functions (PDF) of the buoys' raw time series (using only the years where overlap between the buoys being compared occurred) and after applying both transformation methods (**Figure 5-6**), it was determined that the constant offset method did a superior job of matching the PDFs, particularly for the high wave heights. Therefore, a constant offset adjustment dependent on the wave period was applied to the wave heights of buoys offshore and onshore of the Port Orford buoy. Because the WIS hindcast data used in this study was also located well beyond the boundary of the SWAN model (basically at the location of 46002), the same series of steps comparing WIS wave heights to the Port Orford buoy was carried out, with a new set of constant offsets having been calculated and applied. After applying the wave height offsets to the necessary buoys, gaps in the time series of Port Orford 46015 were filled in respectively with the Oregon, Eel River, St. Georges, and SE Papa buoys. Where there were still gaps following this procedure we then filled in the time series with the corrected WIS data. Because wave transformations (particularly refraction) computed by SWAN are significantly dependent on wave direction, when this information was missing in the buoy records it was replaced with WIS data for the same date in the time series (but the wave height and period remained buoy observations where applicable).

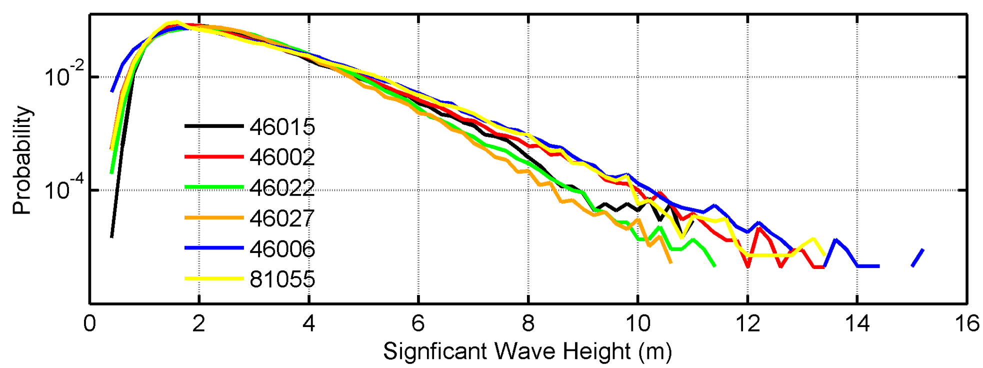

Figure 5-6. Adjusted probability density functions (corrected using the constant offset approach) for buoy 46002 (red line), buoy 46022 (green line), 46027 (orange line), 46006 (blue line), and WIS station 81055 (yellow line) as compared to the raw probability density functions for buoy 46015 (black line).

The final synthesized wave time series developed for Curry County extends from October 1979 through to December 31, 2012, and consists of approximately 32 years of data (measurements including at least wave height and periods) (**Figure 5-7**). Fifty-eight percent of the synthesized wave climate is from NDBC 46002, 23% from NDBC 46015, 14% from NDBC 46022, 3% from NDBC 46027, and ~1% from 46006and WIS station 81055. As can be seen from **Figure 5-7A**, the wave climate offshore from the southern Oregon coast is characterized by episodic, large wave events (> 8 m [26 ft]), with some storms having generated deep-water extreme waves on the order of 14.5 m (48 ft). The average wave height offshore from Curry County is 2.5 m (8.2 ft), while the average peak spectral wave period is 11.0 s, although periods of 20–25 s are not uncommon (**Figure 5-7B**).

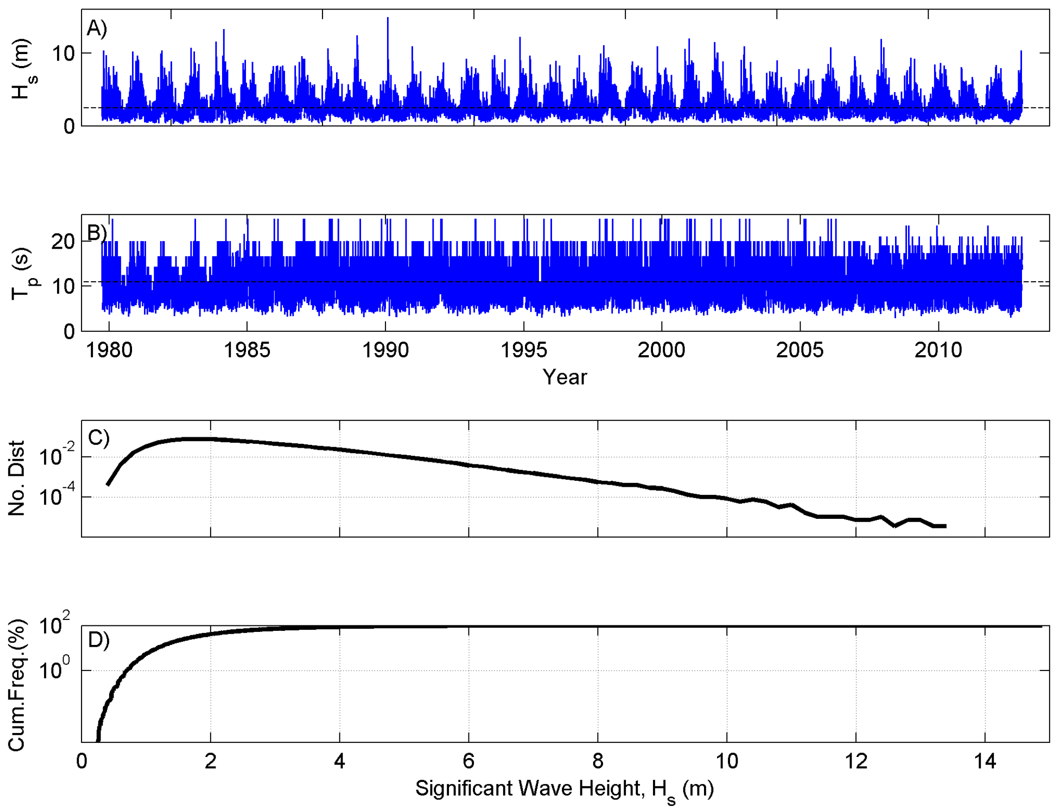

Figure 5-7. Synthesized wave climate developed for Curry County. A) Significant wave height with mean wave height denoted (dashed line), B) Peak spectral wave period with mean period denoted (dashed line), C) Probability distribution of wave heights plotted on a semi-log scale, and D) Significant wave height cumulative frequency curve plotted on a semi-log scale. The groupings evident in the peak periods (Figure 5-7B) are directly from the data and are a product of the data processing methods used by the NDBC to establish the wave frequencies and hence periods. It is for this reason that we chose coarse wave period bins for long period waves (i.e., > 16 s).

The PNW wave climate is characterized by a distinct seasonal cycle that can be seen in **Figure 5-8** by the variability in the wave heights and peak periods between summer and winter. Monthly mean significant wave heights are typically highest in December and January (**Figure 5-8**), although large wave events (>12 m [39.4 ft]) have occurred in all of the winter months except October and March. The highest significant wave height observed in the wave climate record is 14.9 m (49 ft). In general, the smallest waves occur during late spring and in the summer, with wave heights typically averaging ~1.6 m during the peak of the summer (July/August). These findings are consistent with other studies that have examined the PNW wave climate (Tillotson and Komar, 1997; Allan and Komar, 2006; Ruggiero and others, 2010b). **Figure 5-7C** shows a probability density function determined for the complete time series, while **Figure 5-7D** is a cumulative frequency curve. The latter indicates that for 50% of the time waves are typically less than 2.2 m (7.2 ft), and less than 4.2 m (13.8 ft) for 90% of the time. Wave heights exceed 6.7 m (22.0 ft) for 1% of the time. However, although rare in occurrence, these large wave events typically produce the most significant erosion and flooding along the Oregon coast.

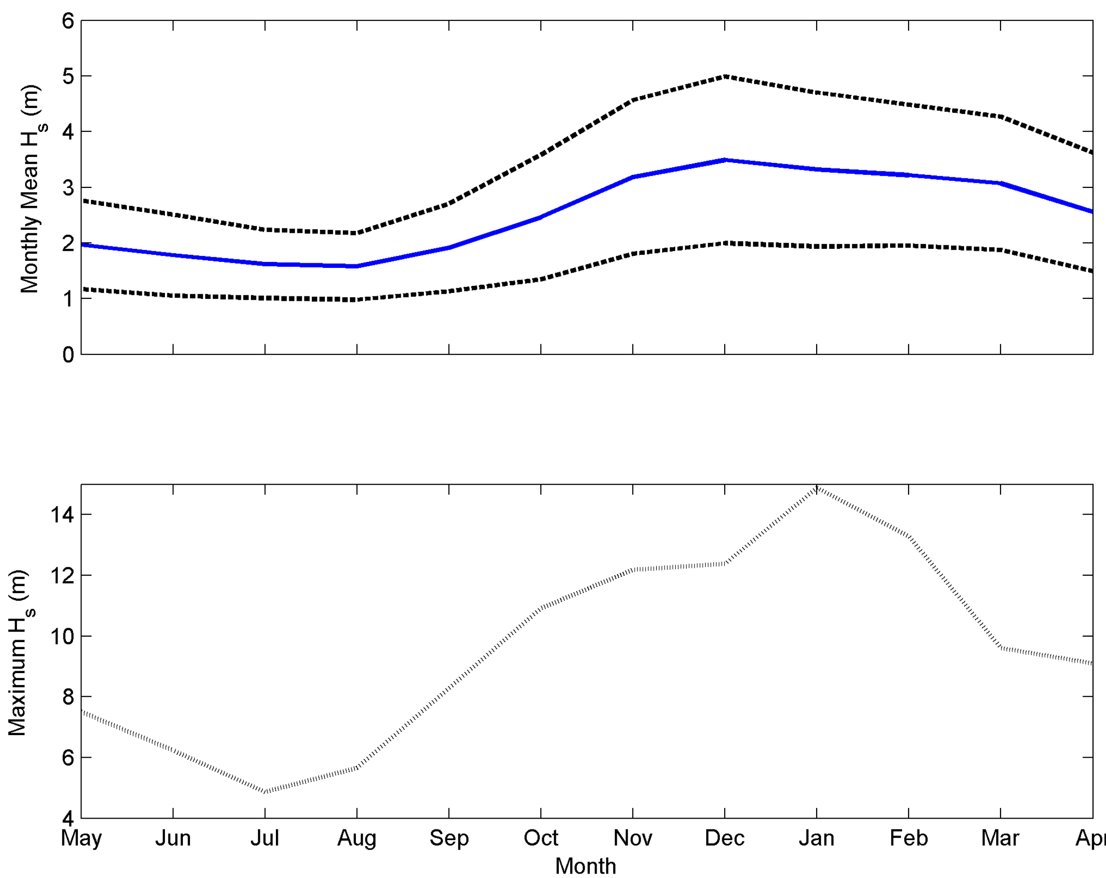

Figure 5-8. Seasonal variability in the deep-water wave climate offshore from the southern Oregon coast. Top) The monthly average wave height (blue line) and standard deviation (dashed line); Bottom) The maximum monthly significant wave height.

Finally, **Figure 5-9** provides a wave rose of the significant wave height versus direction developed for the southern Oregon coast. In general, the summer is characterized by waves arriving from the northwest, while winter waves typically arrive from the west or southwest (Komar, 1997). This pattern is shown in **Figure 5-9**, which is based on separate analyses of the summer and winter directional data developed from the synthesized time series. As can be seen in **Figure 5-9**, summer months are characterized by waves arriving from mainly the west-northwest (~31%) to northwesterly quadrant (~39%), with few waves from the north (10%) and out of the southwest. The bulk of these reflect waves with amplitudes that are predominantly less than 3 m (9.8 ft). In contrast, the winter months are dominated by much larger wave heights out of the west (~21%), and the northwest (~34%), while waves from the southwest account for ~25% of the waves.

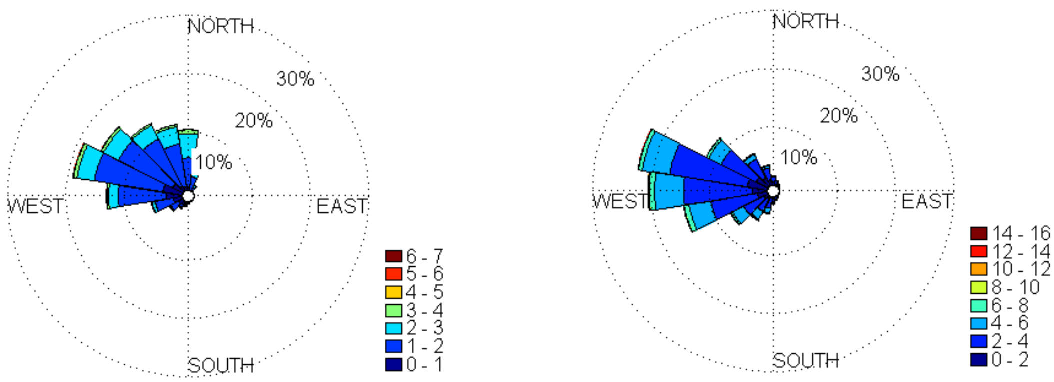

Figure 5-9. Left) Predominant wave directions for the summer months (Jun-Aug), and Right) winter (Dec-Feb). Colored scale indicates the significant wave height in meters.

5.2 Comparison of GROW vs Measured Waves

This section presents a more detailed analysis of GROW Fine Northeast Pacific wave hindcast data and compared with measured waves obtained from selected wave buoys offshore from the Oregon coast. The objective here is to better define the degree of congruence between these two contrasting data sets in order to assess their relative strengths and weaknesses. The approach used here is similar to the tide analyses presented in Section 4, using empirical probability density functions (PDF) to assess the shapes of the distributions. For the purposes of this analysis, PDF plots were derived for GROW station (#18023), and NDBC wave buoy 46089 (located 66 km northwest of 18023) and 46005 located 500 km west of 46029 (**Figure 5-1**).

The first plot (**Figure 5-10**) presents a series of significant wave height empirical PDFs for all measured data from NDBC buoys 46005 and 46089 as well as the GROW hindcast data from site 18023. Data from the stations span the following time frames: NDBC 46005 from 1976 through 2010; NDBC 46089 from 2004 through 2010; GROW 18023 from 1980 through 2009. Based on these PDFs, it is immediately apparent that the GROW data contains a larger number of smaller wave heights (in the 2- to 3-m range) than those measured by the buoys. Additionally, examination of the log-scale plot (bottom of **Figure 5-10**) indicates that the GROW hindcast at 18023 tends to underestimate the more extreme wave heights (waves > 7 m), which are the most important for inundation and erosion vulnerability studies.

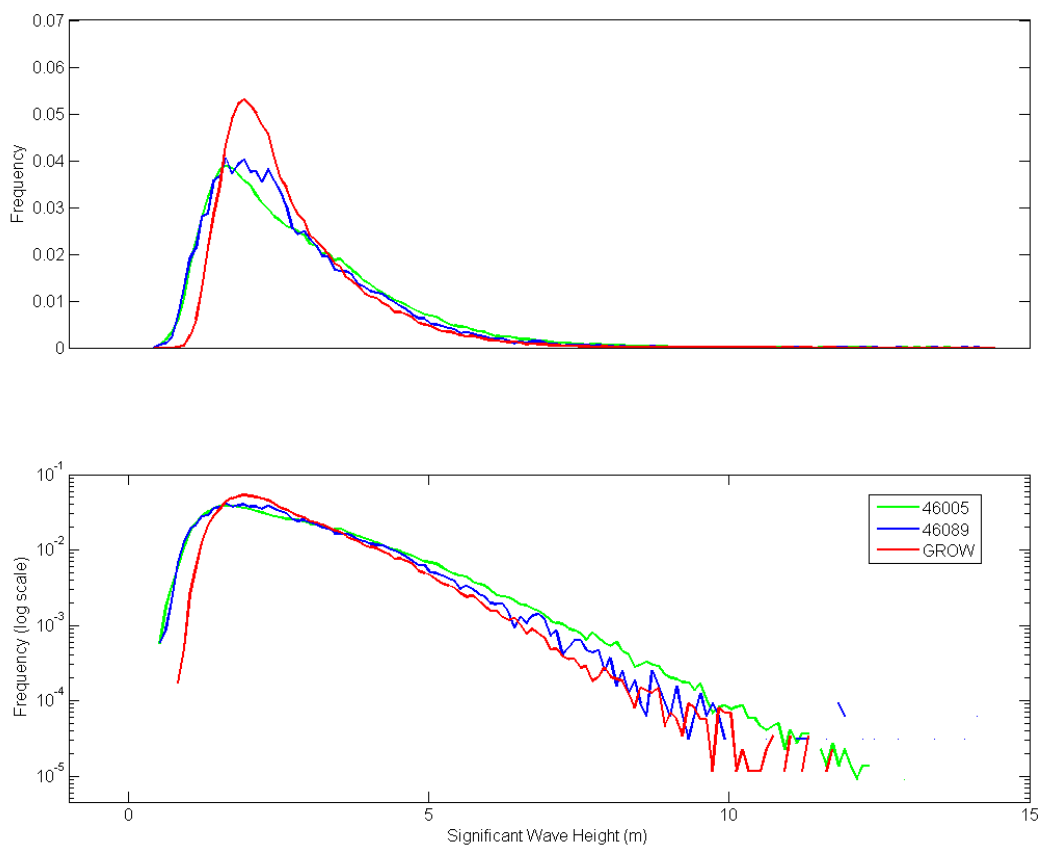

Figure 5-10. PDFs of significant wave heights plotted on a Top) normal and Bottom) log scale. Plots include all existing data from these stations.

Table 5-1 lists general statistics of the various data sets where the maximum wave height modeled by GROW is shown to be nearly 3 m lower than that measured by the 46089 buoy. In contrast, GROW indicates on average slightly higher peak periods when compared with the NDBC stations. While differences between NDBC 46005 and NDBC 46089 may simply reflect buoy locations relative to the tracks of the storms, differences between 46089 and GROW 18023 are almost certainly entirely due to the ability of the numerical model to hindcast the waves. Because NDBC station 46089 spans a much shorter measurement period compared with 46005 and the GROW site, the results from the full PDFs may be construed to be misleading. To better assess this potential bias, we again performed analyses of the truncated time series, which revealed near identical results to those presented in **Figure 5-10**. Summary statistics for the truncated time series are included in **Table 5-1**.

Table 5-1. General statistics of the NDBC buoy and GROW data sets based on the complete time series of data, and truncated time series. Note: *H* denotes the significant wave height and *T* is the wave period.

	46005	46089	GROW
Data Availability	1976–present	2004–present	1980–2009
Mean *H*	2.8 m	2.7 m	2.6 m
Max *H*	13.6 m	14.5 m	11.7 m
Min *H*	0.2 m	0.4 m	0.72 m
H Standard Dev.	1.4 m	1.3 m	1.1 m
Mean *T*	10.8 s	11.1 s	12.6 s
Data Availability	2004–2009	2004–2009	2004–2009
Mean *H*	2.8 m	2.6 m	2.6 m
Max *H*	12.7 m	14.5 m	11.7 m
Min *H*	0.5 m	0.4 m	0.9 m
H Standard Dev.	1.4 m	1.3 m	1.1 m
Mean *T*	10.6 s	11.1 s	12.7 s

Figure 5-11 shows a PDF of the peak periods for 46005, 46089 and GROW for the time period 2004–2009. This last plot clearly indicates that GROW is tending to overestimate the higher peak periods when compared with the measured data

Having examined PDFs of the various data sets, additional analyses were carried out for selected individual storms in order to better assess how well GROW is performing. The approach adopted was to select the five largest storms measured by the NDBC 46089. The storm events were selected by using a 3-day filter to ensure the selection of independent storm events. Once the peak of the storm was identified, the data (±2 days) were plotted with the GROW data. **Figure 5-12** presents results from two of the five selected storms. In general, our results indicate that while the timing of the events seems to be accurately determined by the GROW model, the magnitude is often lower than that measured by the wave gauges. This result may be due to the GROW approach of only estimating model results every 3 hours as opposed to NDBC's hourly buoy measurements. As a result, sampling at 3 hourly intervals has the potential to miss the peak of the storms. In fairness to GROW, the 3 hourly sampling probably reflects the fact that modeling waves on an hourly basis is dependent on having temporally and spatially suitable meteorological information, which remains a challenge for large-scale regional models.

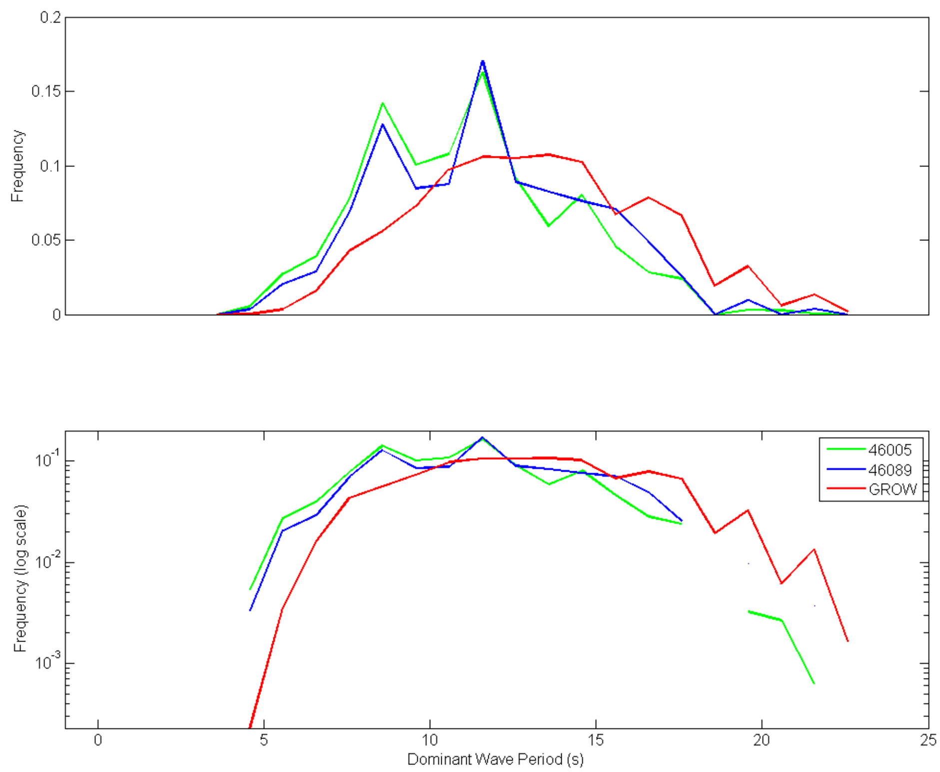

Figure 5-11. PDFs of peak wave periods from 2004 through 2009 on a Top) normal and Bottom) log plot.

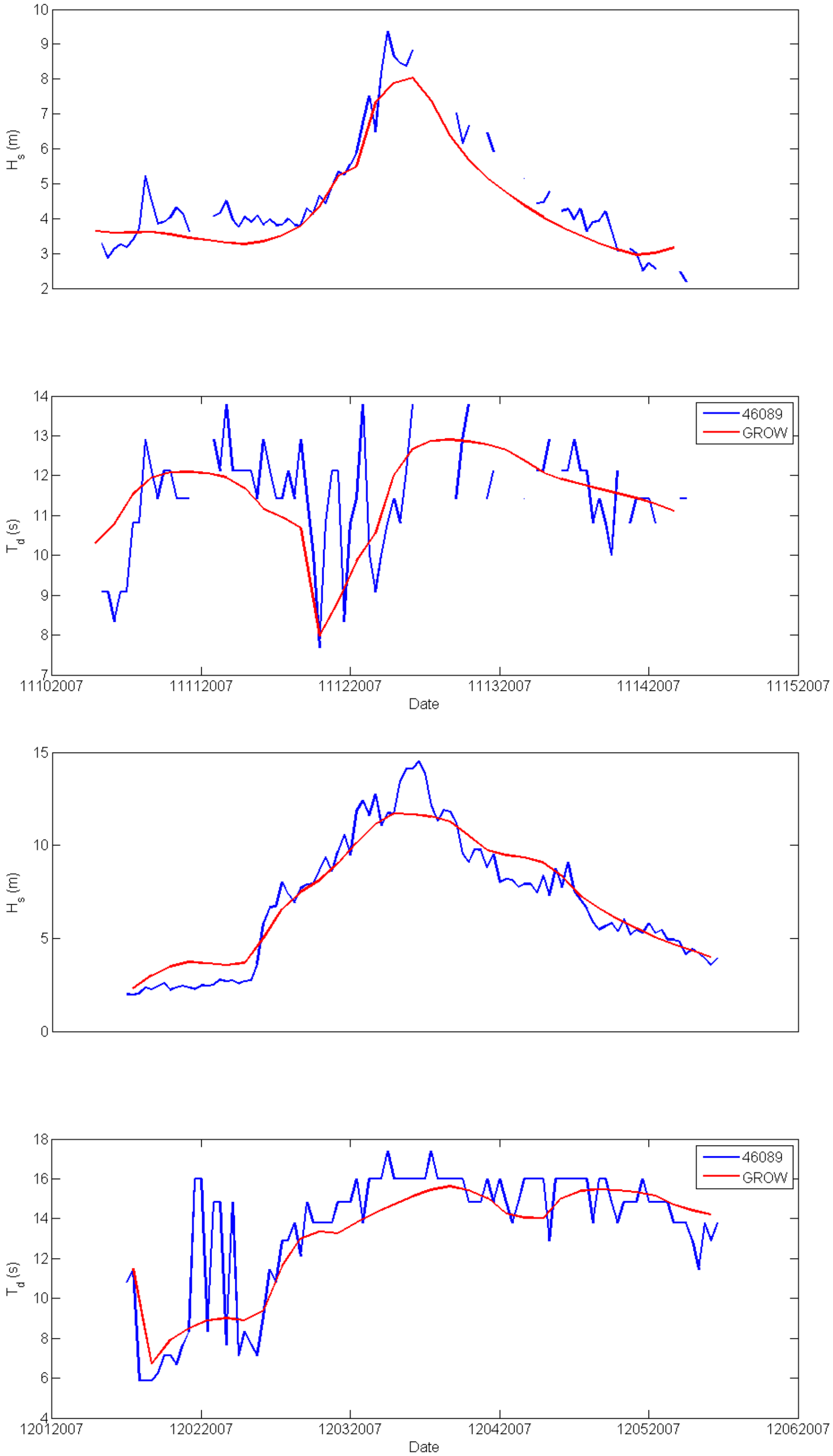

Figure 5-12. Two examples of storms where measured and modeled waves are compared. Top) Storm on November 12, 2007, and Bottom) Major storm event on December 3, 2007.

Finally, we also compared 2% exceedance extreme runup values estimated using the Stockdon and others, (2006) approach and waves from the buoys and the GROW station. These results are presented in **Figure 5-13** and were calculated using a representative beach slope (tan β) of 0.04, which is typical for Oregon beaches. Only data from 2004 through 2009 were included in these calculations to provide a standard time frame for the comparison. Results indicate that, just as with the significant wave height PDFs, the extreme runup levels (> 2.5 m) are underestimated by the GROW model, while the highest calculated runup differs by about 0.4 m (1.3 ft). Although the difference in the calculated runup between GROW and our measured time series is not as large as expected, the shape of the PDF plot would potentially reduce the number of storms available for defining the 100-year wave runup and TWL, as well as in overtopping, inundation and erosion analyses as required for FEMA detailed coastal studies. Based on these findings, we have concluded that all subsequent modeling of waves for Curry County should be based as much as possible on the measured wave time series, as opposed to using GROW hindcast data. Because it is hourly, we use hindcast information from WIS to fill gaps in our combined wave time series developed from buoys.

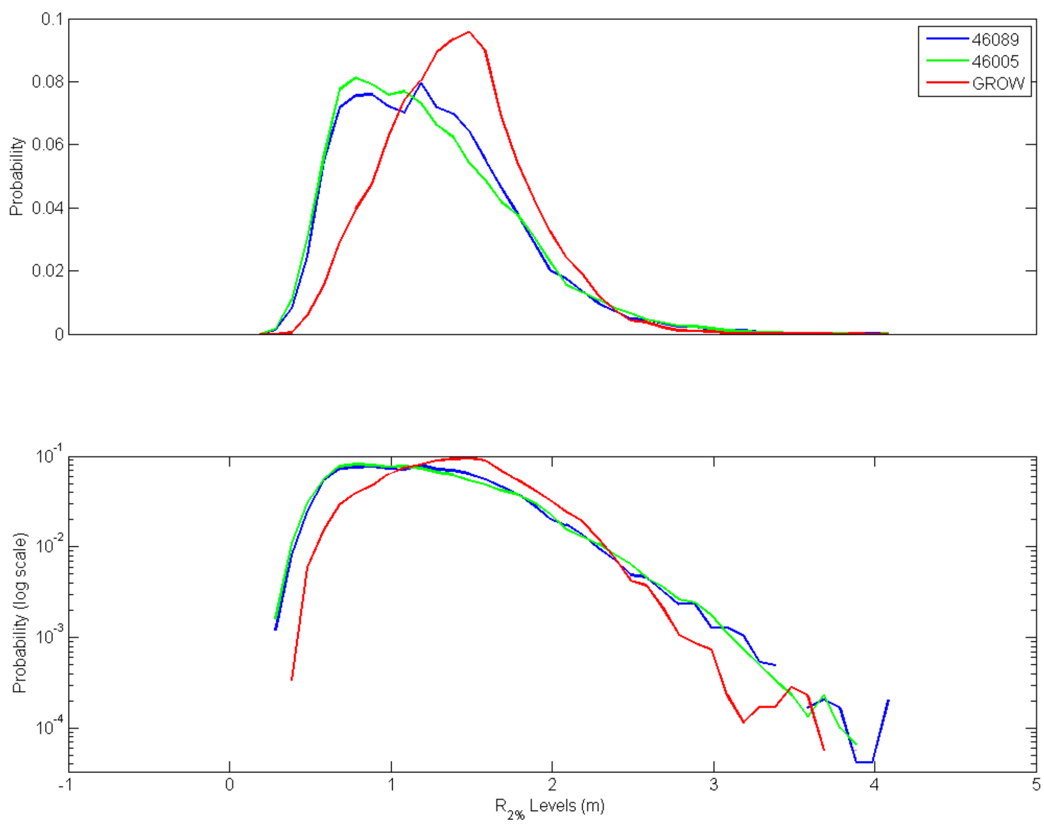

Figure 5-13. PDFs of calculated 2% extreme runup elevations for NDBC 46005, 46089, and GROW hindcast results. An average beach slope of 0.04 was used for runup calculations.

5.3 SWAN Model Development and Parameter Settings

We used the historical bathymetry assembled by the National Geological Data Center (NGDC) (described in Section 3.4) and created a model grid that covers a large portion of the southern Oregon coast (**Figure 5-2**).

SWAN (Simulating WAves Nearshore) version number 40.81, a third generation wave model developed at the Technical University of Delft in the Netherlands (Booij and others, 1999; Ris and others, 1999), was used in this study. The model solves the spectral action balance equation using finite differences for a spectral or parametric input (as in our case) specified along the boundaries. For computational reasons, we perform four different model runs for the Curry County study. A shelf scale model with a horizontal resolution of 100 m, extending south of Crescent City, California, north to Coos Bay, Oregon, and west to 124.8° W. One dimensional SWAN simulations are also completed along the northern and southern extent of the shelf scale grid. A finer resolution (50 m) model applied to the coastal zone is nested to the shelf scale model. This coastal grid covers 45 km × 115 km in length, which yields 903 × 2,301 computational nodes. Bathymetry used for the SWAN model implementation (Booij and others, 1999) was put together by combining ETOPO1 (Amante and Eakins, 2009) and NOAA Tsunami Bathymetry (Carignan and others, 2009) data sets, while were interpolated onto the 50-m spatial grid. The SWAN runs were executed in stationary mode and included physics that account for shoaling, refraction, and breaking, while model settings varying from the default values are discussed in more detail below.

The north, south, and west boundaries of the model were forced using a parameterized JONSWAP spectrum. The functions for spectral peakedness parameters γ and nn in the JONSWAP directional spectra are given as:

$$\gamma = \begin{cases} 3.3 & if\ Tp < 11s \\ 0.5Tp - 1.5 & if\ Tp \geq 11s \end{cases}$$

$$nn = \begin{cases} 4 & if\ Tp < 11s \\ 2.5Tp - 20 & if\ Tp \geq 11s \end{cases} \tag{5.3}$$

Thus, the directional distribution is generated by multiplying the standard JONSWAP frequency spectrum by $cos^{nn}(\theta - \theta_{peak})$ (Smith and others, 2001). Wind wave spectra are broad (low γ and nn values) while swell typically have narrow distributions (high γ and nn values). The values used in the SWAN wave modeling were based on the input peak periods which ranged $4.055 \leq \gamma \leq 11.03$ and $7.775 \leq nn \leq 42.65$. To ensure that the wave directional spread is sufficiently resolved by the model, we specified directional bins giving a 4 degree directional resolution. The spectrum was discretized in frequency space with 29 bins from 0.032 to 1 Hz. Wind was not included in the SWAN simulations and therefore no energy growth due to wind, or quadruplet wave-wave interactions occur in the simulations. Triad interactions, diffraction, and wave setup also were not activated in the model. We used the Janssen frictional dissipation option, which has a default friction coefficient of 0.067 m^2/s^3. No model calibration was performed in this study, although several numerical experiments were implemented to test various assumptions in the wave modeling (e.g., not to use winds).

5.3.1 Wind effects

The decision not to model the effect of winds on wave growth over the continental shelf in our Coos County study was based on two observations:

1. To develop our combined wave time series described previously, we performed a "statistical" wave transformation between buoy 46002 and the buoys at the edge of the continental shelf and found that in general the wave heights during storm events decreased even with hundreds of kilometers of additional fetch. Without understanding the details of this phenomenon (e.g., white capping versus wind wave growth) and with no data for calibration we felt that attempting to model wind growth would add to the uncertainty of our input wave conditions.
2. We also have previous experience with SWAN wave modeling in the region (U.S. Pacific Northwest) in which sensitivity runs including wind were performed with only minor impact on results (Ruggiero and others, 2010a).

To test the validity of the assumptions made in our Coos County study, several wave modeling experiments were performed in order to specifically examine the role of additional wind wave development over the shelf. The basic question that was addressed is: How much do wind fields result in wave growth between locations seaward of the shelf break, roughly equivalent to the offshore extent of the Tillamook (46089) buoy shown in **Figure 5-1** and the inner shelf. The latter was defined as the 100 m (300 ft) isobath. To address this question, hindcast waves were modeled for the months of January and February (i.e., peak of the winter season) and for two representative years (2006 and 2010). The wave modeling was accomplished by running a regional Eastern North Pacific (ENP) model and a 3 arc-min grid for the Oregon coast, with the outer boundary coinciding with the Tillamook buoy station (**Figure 5-14**). The model runs were forced by analyzed Global Forecast System winds with a temporal resolution of 6 hours and a spatial resolution of 1 arc-degree. A similar run was undertaken without winds over the same 3 arc-min grid, just propagating the boundary conditions. Hindcast wave data were obtained from selected points across the shelf at contour depths of 500, 400, 300, 200, and 100 m along a cross-shore transect (A and B in **Figure 5-14**).

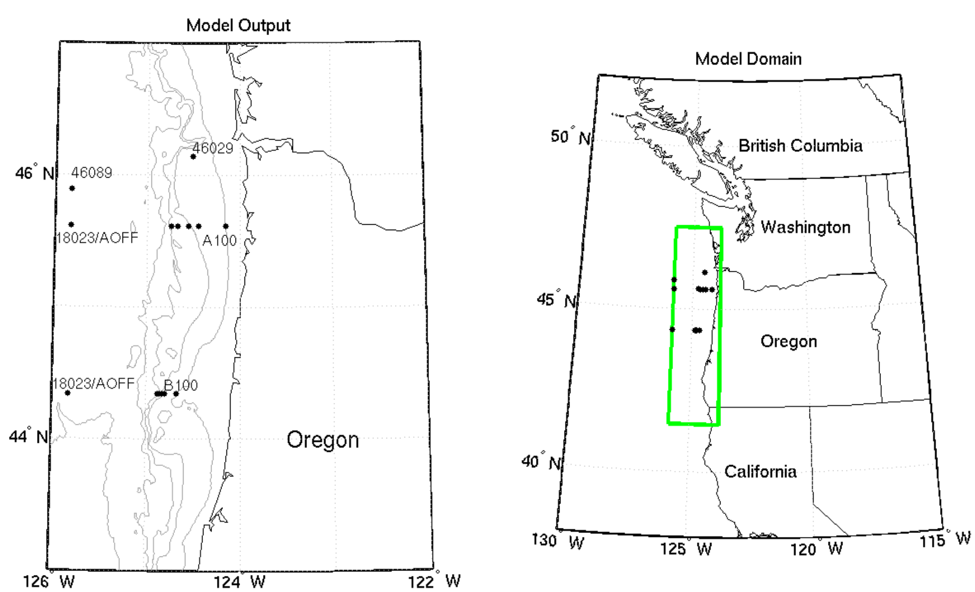

Figure 5-14. Left) Map showing the locations of the northern Oregon coast buoys and transect lines (A and B), and Right) model domain.

Results from the model runs (with and without winds) are presented in **Figure 5-15** and **Figure 5-16**. Modeled and measured waves for two NDBC buoys (46089 and 46029) are included for comparative purposes (**Figure 5-17** and **Figure 5-18**). In general, our experiments indicated that although the addition of wind sometimes changed the timing of the large wave events, producing at times a relatively large % error for part of the "wave hydrograph," the peaks of the wave events showed very little difference between cases where wind was included or excluded (**Figure 5-15** and **Figure 5-16**). Furthermore, in the majority of cases, the differences in the derived wave heights between model runs including (excluding) wind (no wind) were, on the whole, minor. This finding was also observed in the derived peak wave periods, which appear to be virtually identical in all the plots. Of greater concern in these model tests, are the occasional large differences between the modeled runs (irrespective of whether wind/no wind is applied) and the actual measurements derived from NDBC wave buoys (**Figure 5-17** and **Figure 5-18**), as well as the GROW data derived for station 18023. These latter findings will be explored in more detail later in this section.

These experiments support our decision to not include wind growth in our model runs and therefore quadruplet wave-wave interactions were also not incorporated in the simulations. Further, wave setup is not included in the simulations because we extract the transformed wave parameters at the 20-m depth contour and use the Stockdon and others (2006) empirical model to compute wave runup (which incorporates setup) along the coast.

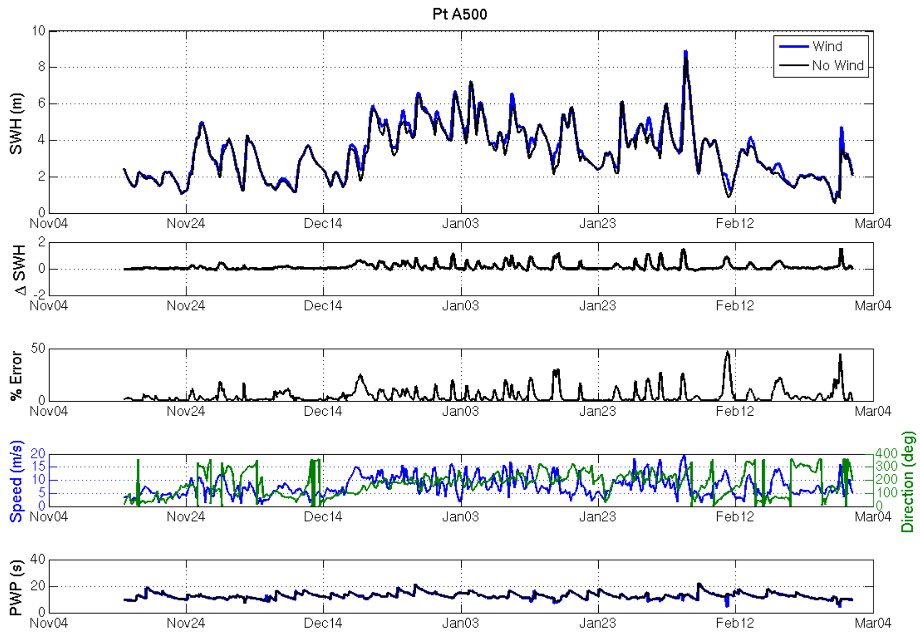

Figure 5-15. Model-model comparison at 500-m depth on transect A for the 2006 simulation.

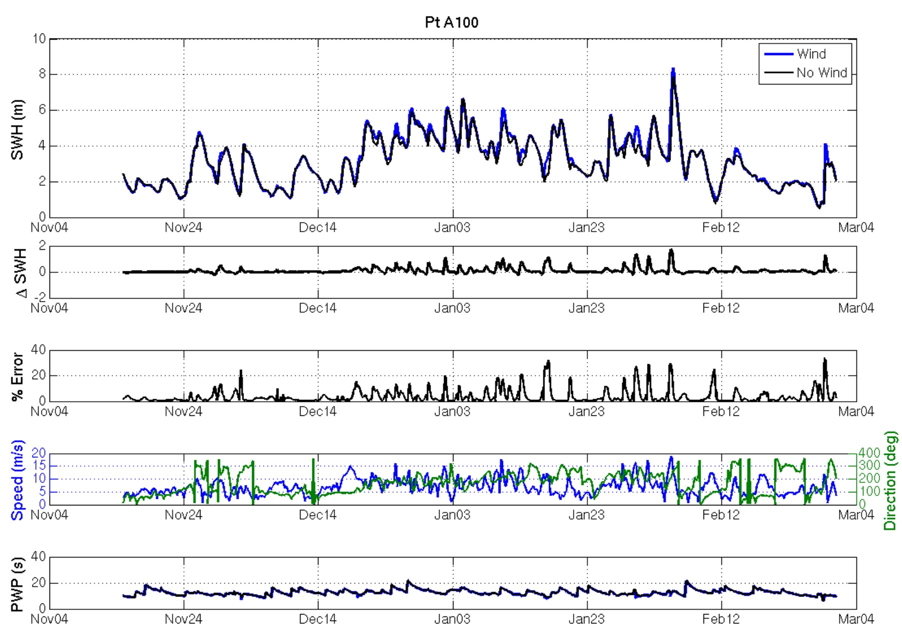

Figure 5-16. Model-model comparison at 100-m depth on transect A for the 2006 simulation.

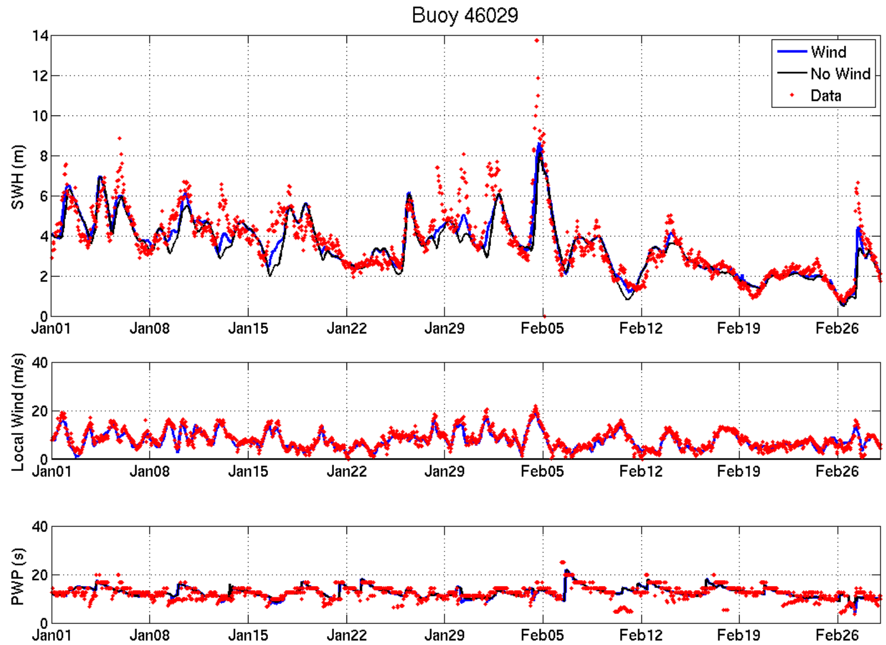

Figure 5-17. Model data comparison at NDBC buoy #46029 for the 2006 simulations.

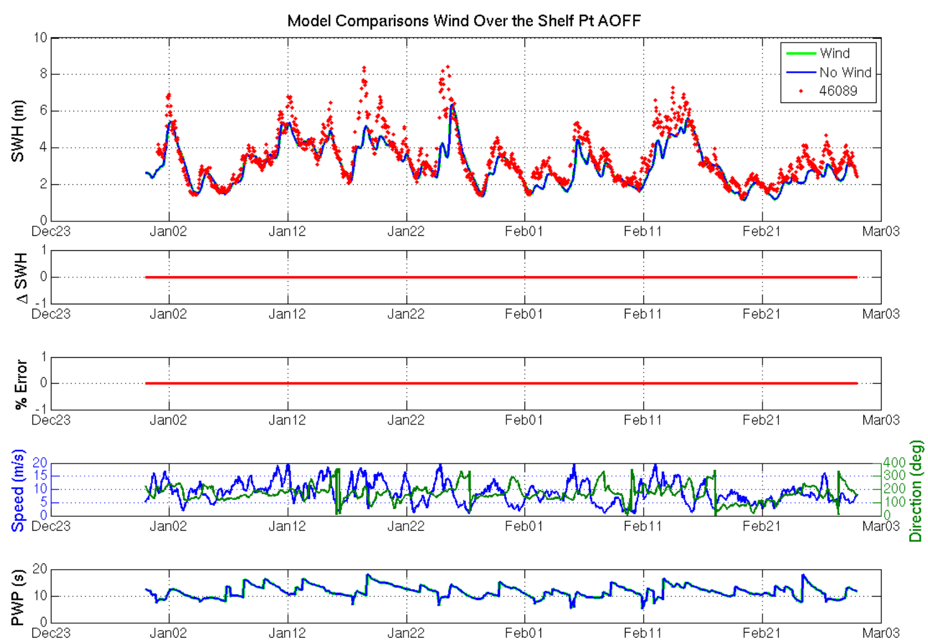

Figure 5-18. Model data comparison at Station Aoff (GROW station location) versus 46089 for the 2010 simulations.

5.3.2 Frictional and whitecapping dissipation of the wave energies

Additional testing was undertaken to explore the effect of not including friction and whitecapping. **Figure 5-19** and **Figure 5-20** provide two test-case conditions; the first is associated with a significant wave height of 10 m and peak period of 20 s, with the waves approaching from a direction of 285 degrees (NW), while the second case is for a significant wave height of 14 m, peak period of 14 s, with the waves approaching from a direction of 270 degrees (W). **Figure 5-19** indicates that for this particular condition, the modeled results are relatively similar until immediately prior to wave breaking, where significant differences arise. However, as the significant wave height increases (**Figure 5-20**) the effect of excluding bottom friction and whitecapping becomes considerably larger. The exclusion of these processes results in an overestimation of wave heights prior to breaking. Therefore, we have chosen to include frictional dissipation and dissipation due to whitecapping in our modeling.

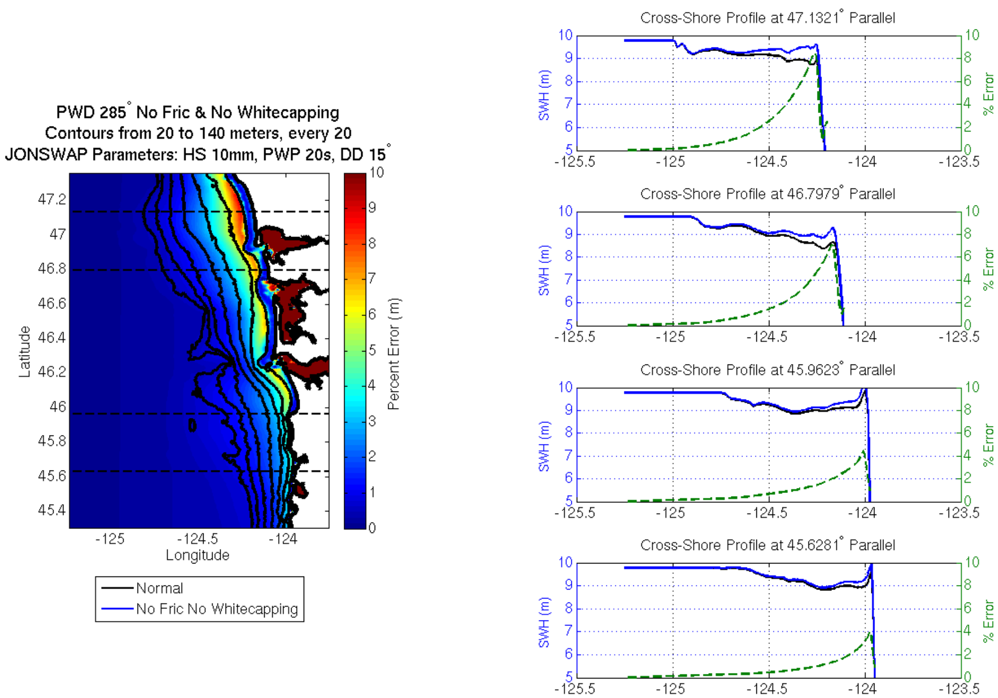

Figure 5-19. The impact of ignoring bottom frictional dissipation and dissipation due to whitecapping for a 10-m significant wave height with a peak period of 20 s approaching from a direction of 285 degrees.

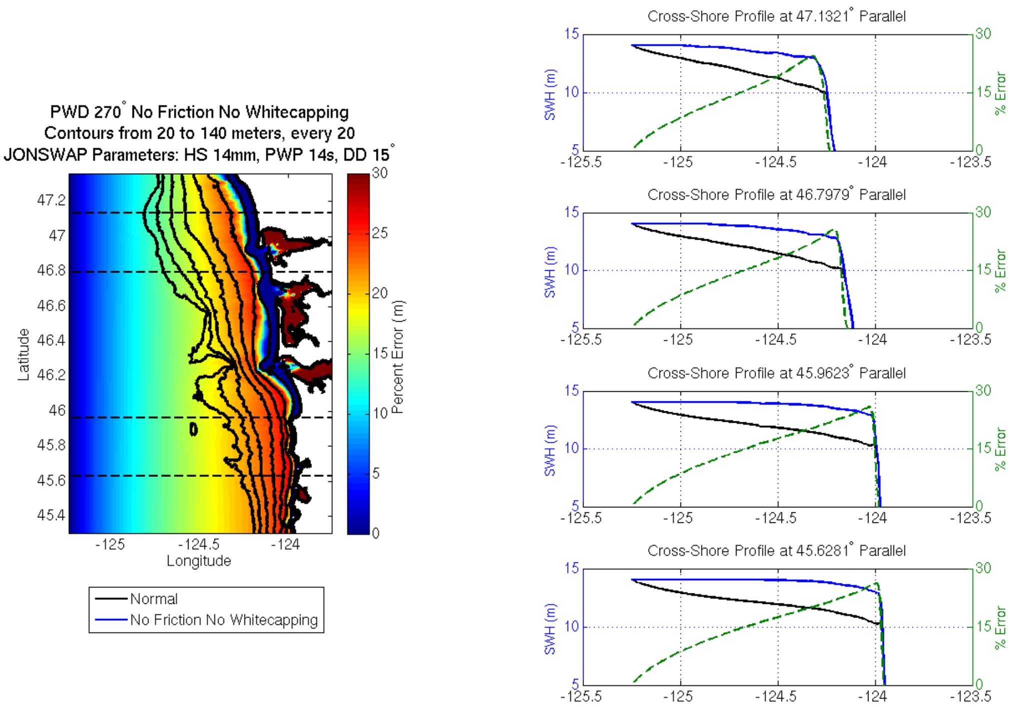

Figure 5-20. The impact of ignoring bottom frictional dissipation and dissipation due to whitecapping for a 14-m significant wave height with a peak period of 14 s approaching from a direction of 270 degrees.

5.3.3 Lookup table development

Having demonstrated that winds have little impact in terms of additional wave development across the continental shelf of Oregon, our next goal was to develop an efficient methodology that could be used to minimize the total number of SWAN runs needed to perform the actual wave modeling and transformations, while ensuring that we resolved the influence of varying parameters on the wave transformations. To do this, we discretized the significant wave height (H_s), peak period (T_p), wave direction (D_p), and water level (WL) time series.

For the direction bins (D_p), the bin widths were made approximately proportional to the probability distribution function of the synthesized wave climate time series. By using this approach in our Clatsop County study, 11 directional bins were created that have approximately an equal probability of occurrence (**Figure 5-21**). For the purposes of the Curry County work, we further refined our original approach to include an additional two directional bins. This was accomplished by refining the spread of the bins to better reflect the observed conditions offshore Tillamook and Lincoln counties. The final bin edges are defined as D_p = [175, 205, 225, 240, 250, 260, 270, 280, 290, 300, 315, 335, 365]. At the bin edges, linear interpolation is used to derive the wave parameters. Based on initial sensitivity runs undertaken as part of our Clatsop County study, we have determined that these bin widths are more than adequate. **Figure 5-22** shows the result of interpolating over a 20-degree bin spacing.

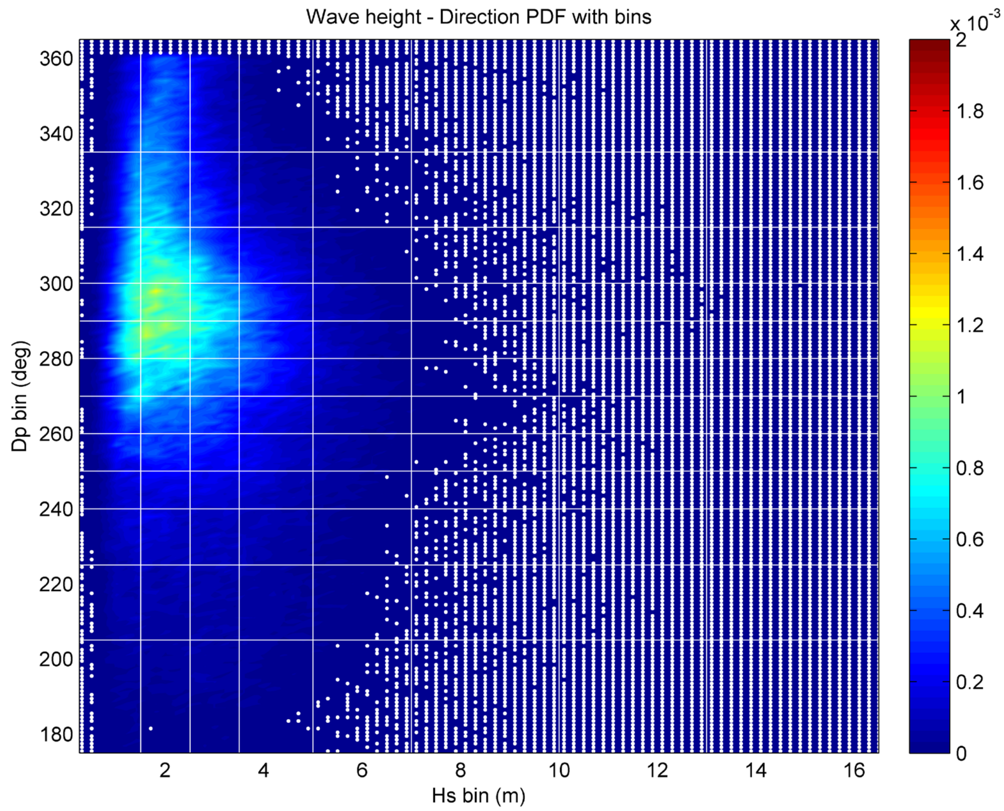

Figure 5-21. Joint probability of wave height and peak period from the combined time series. The white dots represent bin centers, from a much smaller mesh, in which this combination of H_s and T_p does not exist in the combined time series. The red line represents the theoretical wave steepness limit below which waves are non-physical.

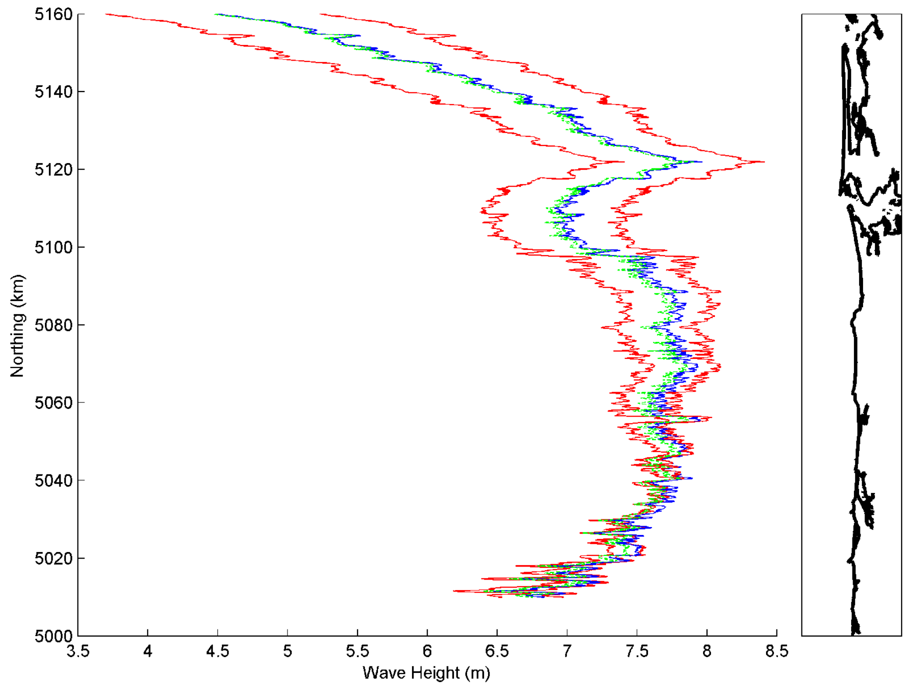

Figure 5-22. SWAN wave modeling and calculated alongshore wave variability using the look-up table approach. The left red line represents the alongshore variable wave height at the 20-m depth contour for an incident angle of 240 degrees (H_s = 10, T_p = 15 s) and the right red line is for an angle of 260 degrees. The blue line is the wave height for an angle of 250 degrees as modeled in SWAN while the green line is the linearly interpolated wave heights using the look-up table. Note that this is a preliminary SWAN model run, meant for testing the interpolation scheme, and the lateral boundary conditions are not dealt with in the same manner as in our production SWAN runs.

For the significant wave heights bins, we identified the following deep-water significant wave heights for inclusion in SWAN: H_s = [0.25, 1.5, 2.5, 3.5, 5, 7, 10, 13, 16.5], which gives us nine cases. From our sensitivity tests, we found that a bin width of 3 m for large waves is sufficient for resolving the linearly interpolated wave conditions (**Figure 5-23**). In the case of the deep-water peak periods, our analyses identified the following period bins for inclusion in SWAN: T_p = [2, 4, 6, 9, 11, 13, 15, 17, 20, 23, 26], which provides a total of 11 additional cases. From our sensitivity tests, we found that the linear interpolation approach for wave period is not quite as good as for direction and wave height. Because wave period affects breaking, shoaling, and whitecapping, there is significant variability in the wave transformations as a function of wave period. For our sensitivity run of H_s = 10 m, and D_p = 260 degrees, **Figure 5-24** illustrates the impact of linear interpolation. However, for the most part in our parameter space we will have interpolation errors only around 10%. In this particular example the maximum error is only approximately 4 %.

Figure 5-25 presents the joint probability of wave height and peak period from the combined time series. The white dots represent bin centers, from a much smaller mesh, in which this combination of H_s and T_p does not exist in the time series. The red line represents the theoretical wave steepness limit below which waves are non-physical. We can use this information to reduce the overall matrix of model runs.

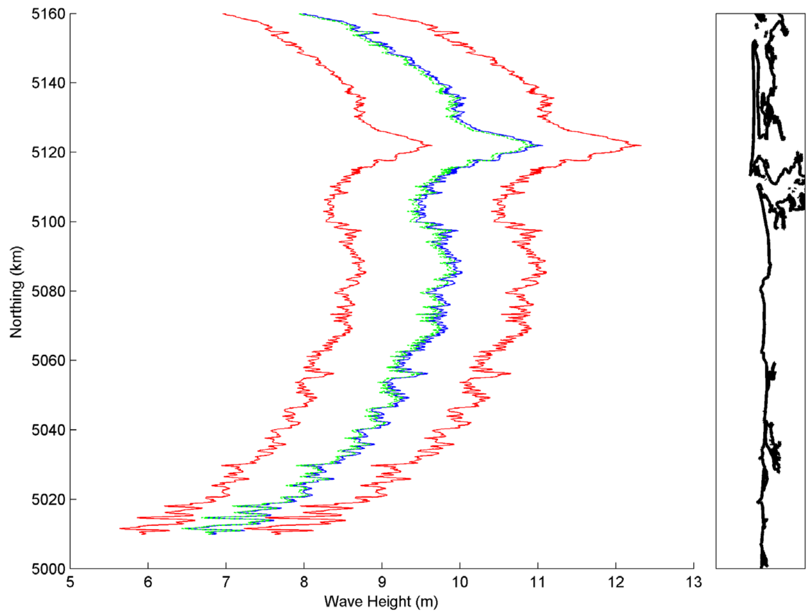

Figure 5-23. SWAN wave modeling and calculated alongshore wave variability using the look-up table approach for an 11-m and 15-m wave. In this example the red lines are the alongshore varying wave height for an 11-m and 15-m incident wave height in 20 m. The blue line is the modeled transformed 13 m wave height, while the green represents a linear interpolation between the 11- and 15-m results.

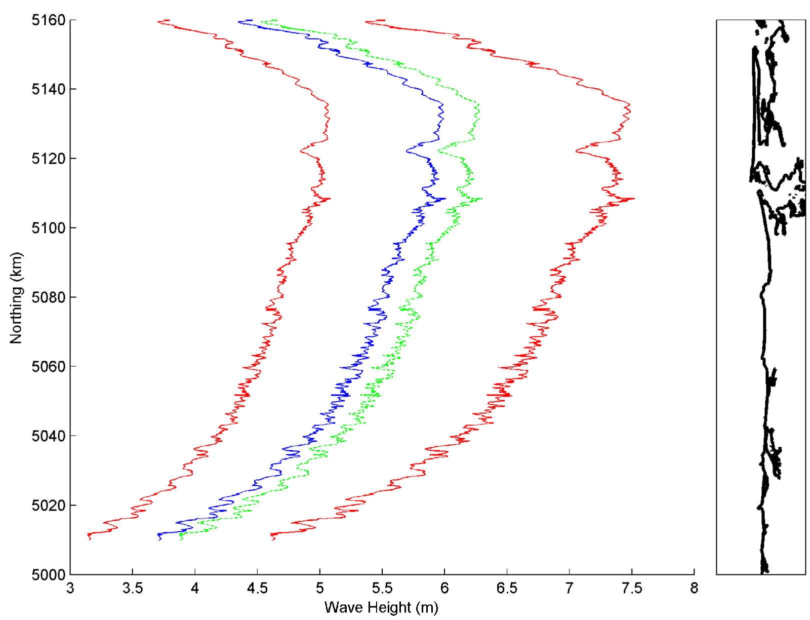

Figure 5-24. SWAN wave modeling and calculated alongshore wave variability using the look-up table approach for a 10-m wave. In this example the red lines are the alongshore varying wave height for a 10-m wave arriving from 260 degrees for 20 s and 24 s. The blue line is the modeled wave height for 22 s, and the green line represents a linear interpolation.

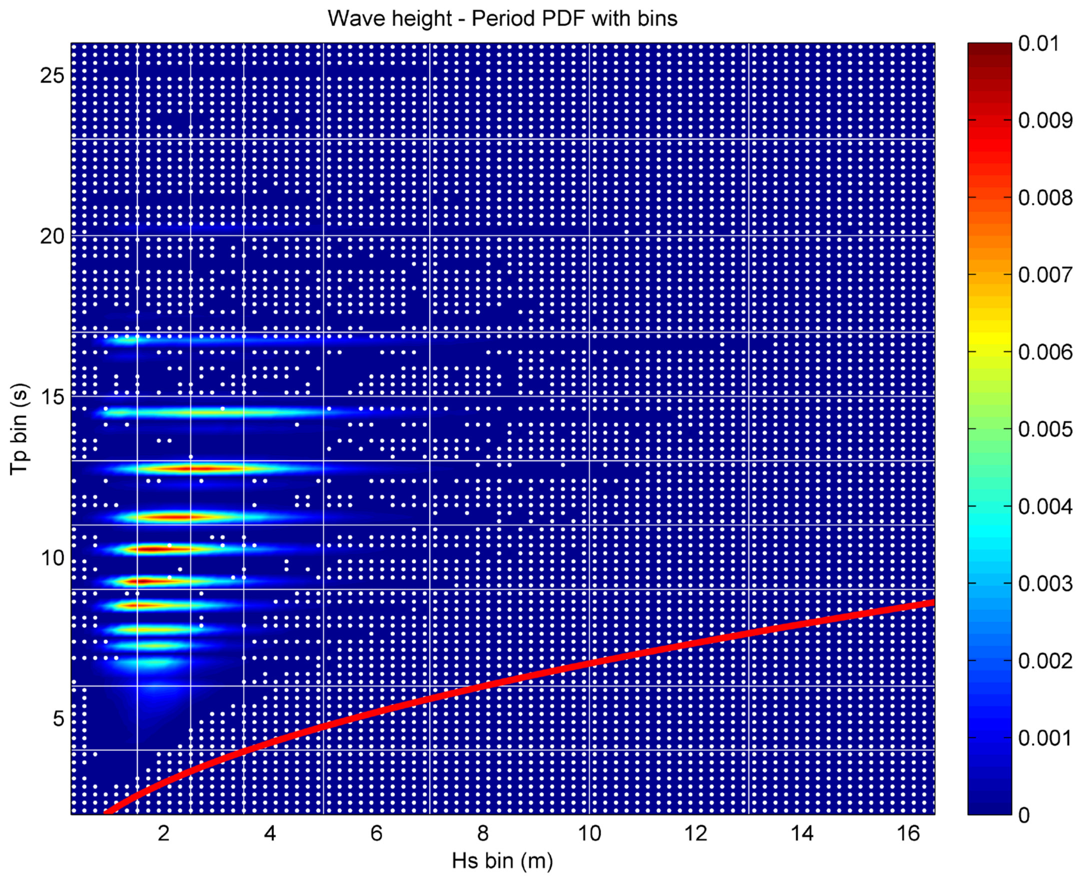

Figure 5-25. Joint probability of wave height and peak period from the combined time series. The white dots represent bin centers, from a much smaller mesh, in which this combination of H_s and T_p does not exist in the combined time series. The red line represents the theoretical wave steepness limit below which waves are non-physical.

Figure 5-26 is the joint probability of peak period and dominant wave height shown here for completeness. Finally, we illustrate our bin choice on the individual parameter PDFs in **Figure 5-27** (buoy data).

In summary, the lookup tables were generated using all wave parameter cases and two contrasting water levels. Our sensitivity tests indicated that varying water levels have a negligible impact on the model and linearly transformed waves. The following matrix of SWAN runs is considered for lookup table development for transforming waves offshore from Curry County:

D_p = [175, 205, 225, 240, 250, 260, 270, 280, 290, 300, 315, 335, 365] — 13 cases
H_s = [0.25, 1.5, 2.5, 3.5, 5, 7, 10, 13, 16.5] — 9 cases
T_p = [2, 4, 6, 9, 11, 13, 15, 17, 20, 23, 26] — 11 cases
WL = [-1.5, 4.5] — 2 cases

In total, this equates to 2,574 model cases that can be used for linearly interpolating the waves from a time series of data. However, **Figure 5-25** indicates that several H_s–T_p combinations are physically not realistic. Multiplying these bins by the D_p and WL bins means that we can eliminate 390 bins for a new total of only 2,184 model runs.

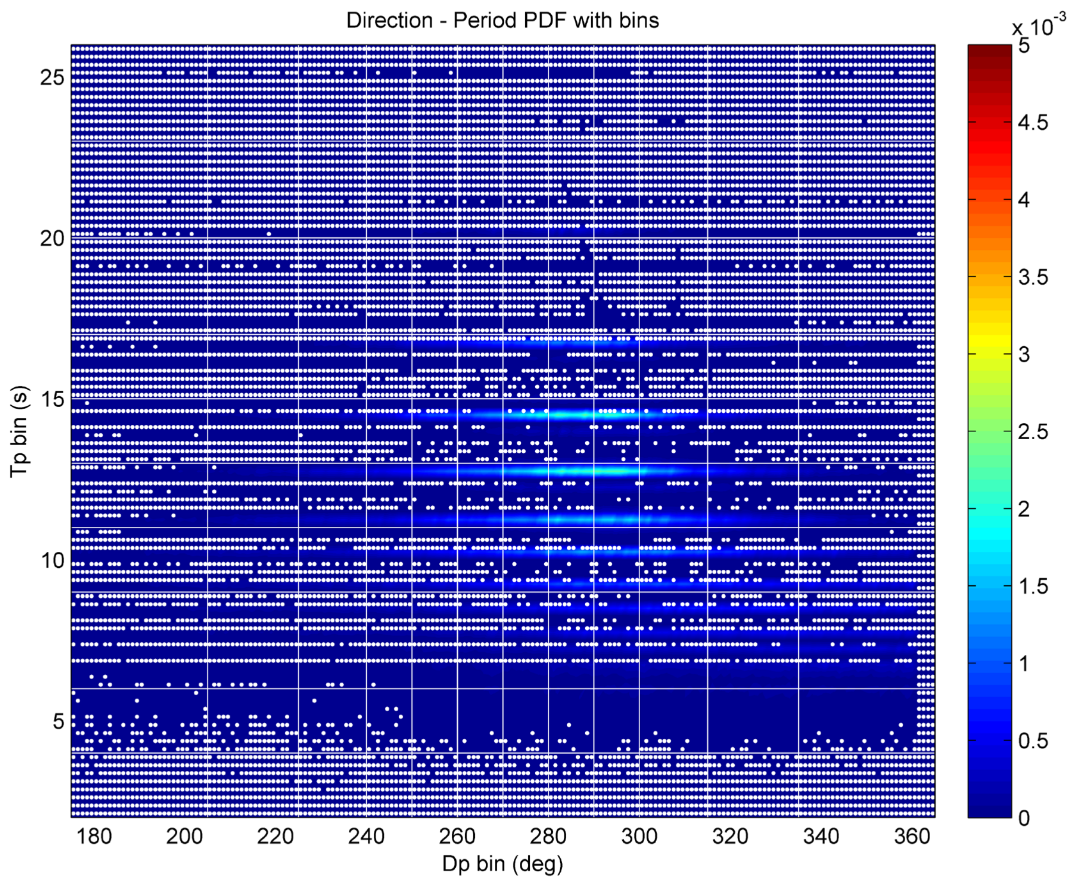

Figure 5-26. Joint probability of dominant direction and peak period from the combined time series. The white dots represent bin centers, from a much smaller mesh, in which this combination of D_p and T_p does not exist in the combined time series. The white lines depict the boundaries of the bin edges.

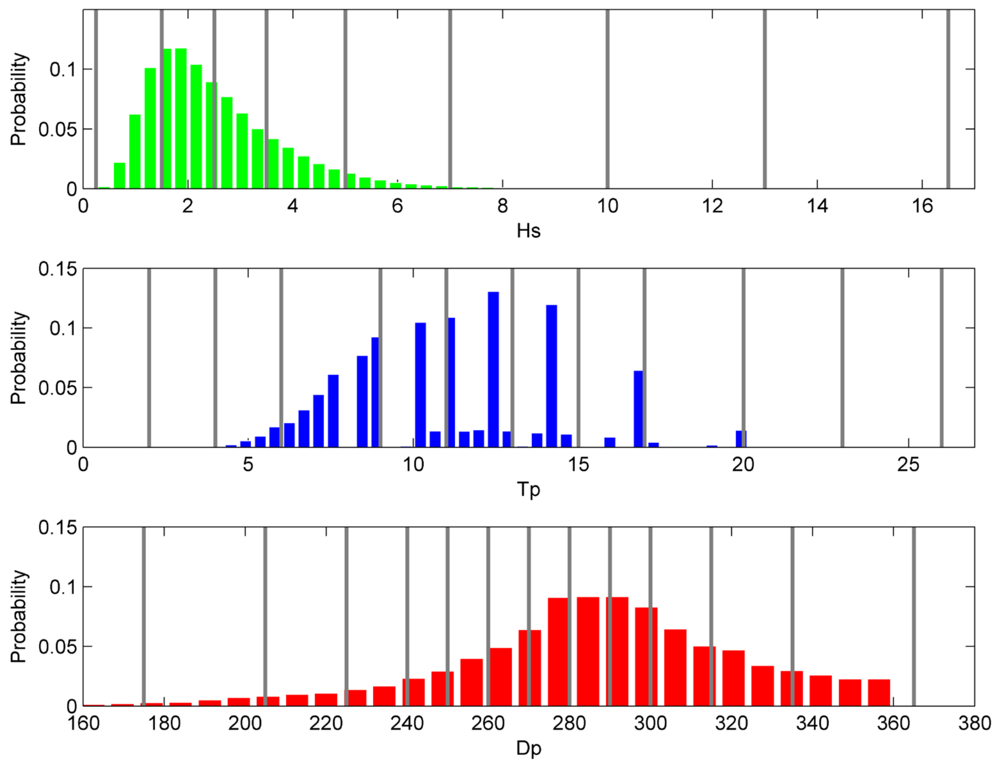

Figure 5-27. Individual parameter PDFs and bin edges using the combined buoy wave time series.

5.4 Summary of SWAN Results

Significant alongshore variability is apparent in many of the conditions examined with SWAN (**Figure 5-28**). Differences on the order of 3 m in significant wave height along the 20m isobaths are not uncommon in Curry County. To calculate the wave runup along the county's shoreline we subsequently extracted the wave characteristics along the 20-m contour, or the seaward most location where the wave breaking parameter equaled 0.4, throughout the model domain (right panel **Figure 5-28**). For one particular transect, transect 73, we extracted wave characteristics at the 30-m contour because of complicated nearshore bathymetry. Because all of the parametric runup models used in this study rely on information on the deep-water equivalent wave height and peak periods as inputs, we then computed the linear wave theory shoaling coefficient and back shoaled our transformed waves to deep-water. These transformed deep-water equivalent waves were then used to calculate the wave runup and generate the TWL conditions used in the subsequent extreme value analysis.

To confirm that our approach of interpolating wave transformations using lookup tables yields acceptable results, we ran several additional SWAN runs that were not part of our original matrix. These additional runs extended across a range of conditions, including extreme events capable of forcing high water levels at the coast. We then compare the results from using the lookup tables to these additional direct SWAN computations at the 20-m contour location. **Figure 5-29** to **Figure 5-31** show a sample of these results for wave heights, peak periods, and directions respectively, for a SWAN run driven with an offshore boundary condition of H_s = 5 m, T_p = 10 s, D_p = 202, and a water level of -1.5 m NAVD88. In all cases, the percentage error between the lookup table and direct computation is low, typically averaging less than 5%. In only a few locations, near model boundaries, complex offshore reefs, or inlets, are the errors significant. None of the transects analyzed in detail for extreme flooding later in this report have unreasonable errors.

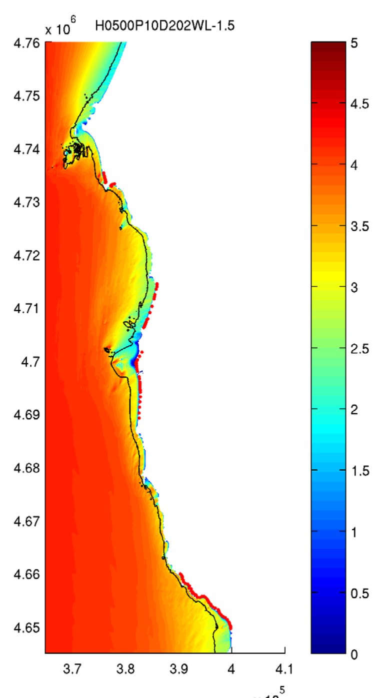

Figure 5-28. Example SWAN simulation offshore from Curry County (offshore significant wave height 5 m, peak wave period 10 s, and peak wave direction of 202 degrees) . Significant wave height in the modeling domain is shown in colors. Dissipation processes result in the reduced inner shelf wave height.

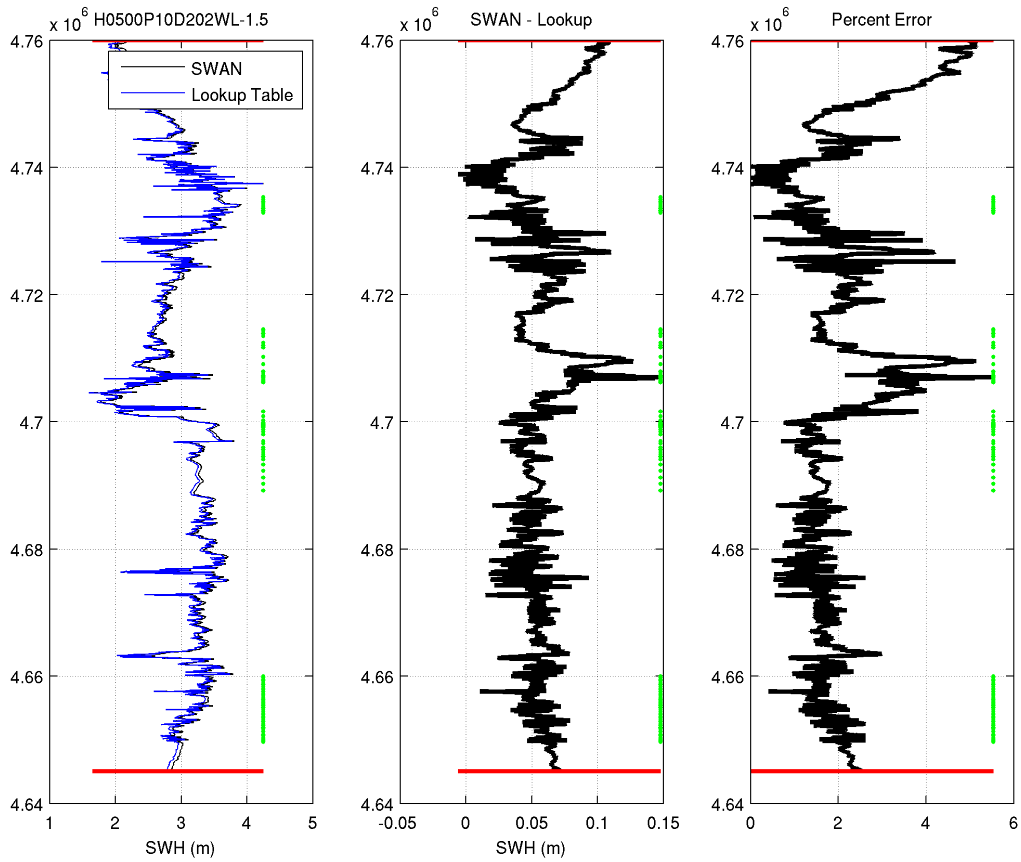

Figure 5-29. Comparison of alongshore varying wave height at the 20-m contour extracted from the lookup tables (blue line) and from a direct SWAN computation (black line) with an offshore boundary condition characterized as H_s = 5 m, T_p = 10, D_p = 202, and a water level of -1.5-m NAVD88. Solid red line denotes Curry County boundary.

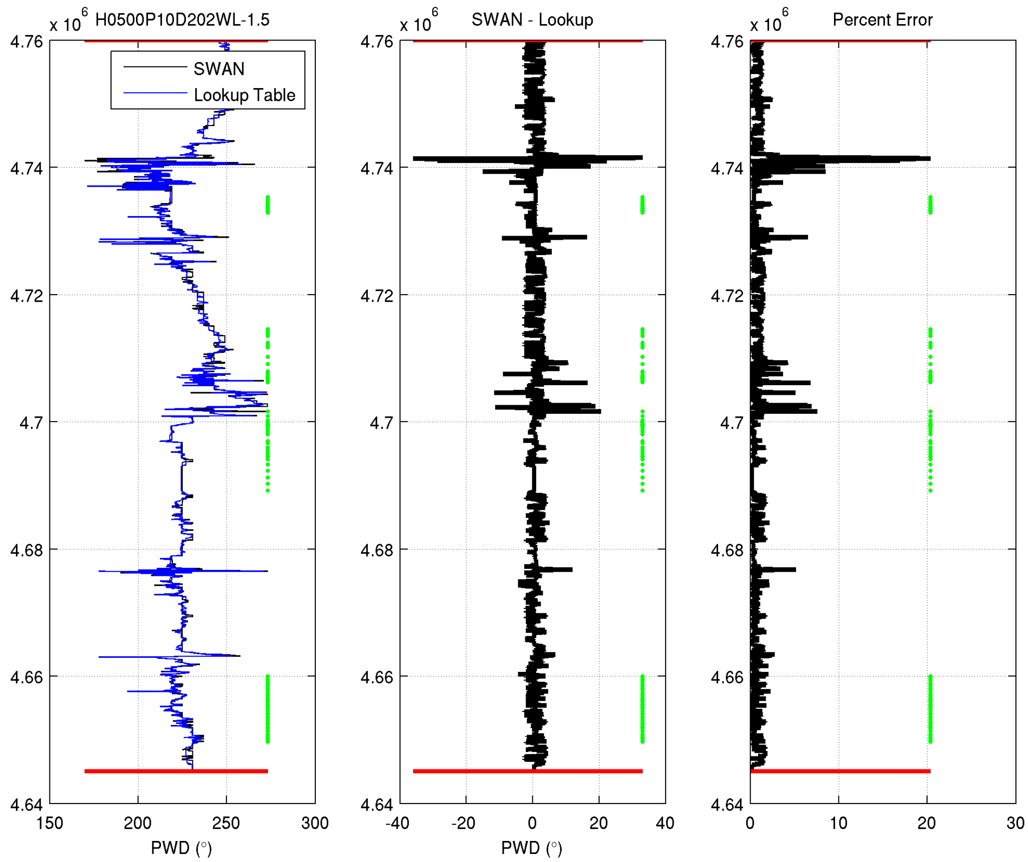

Figure 5-30. Comparison of alongshore varying wave period at the 20-m contour extracted from the lookup tables (blue line) and from a direct SWAN computation (black line) with an offshore boundary condition characterized as H_s = 5 m, T_p = 10, D_p = 202, and a water level of -1.5-m NAVD88. Solid red line denotes Curry County boundary.

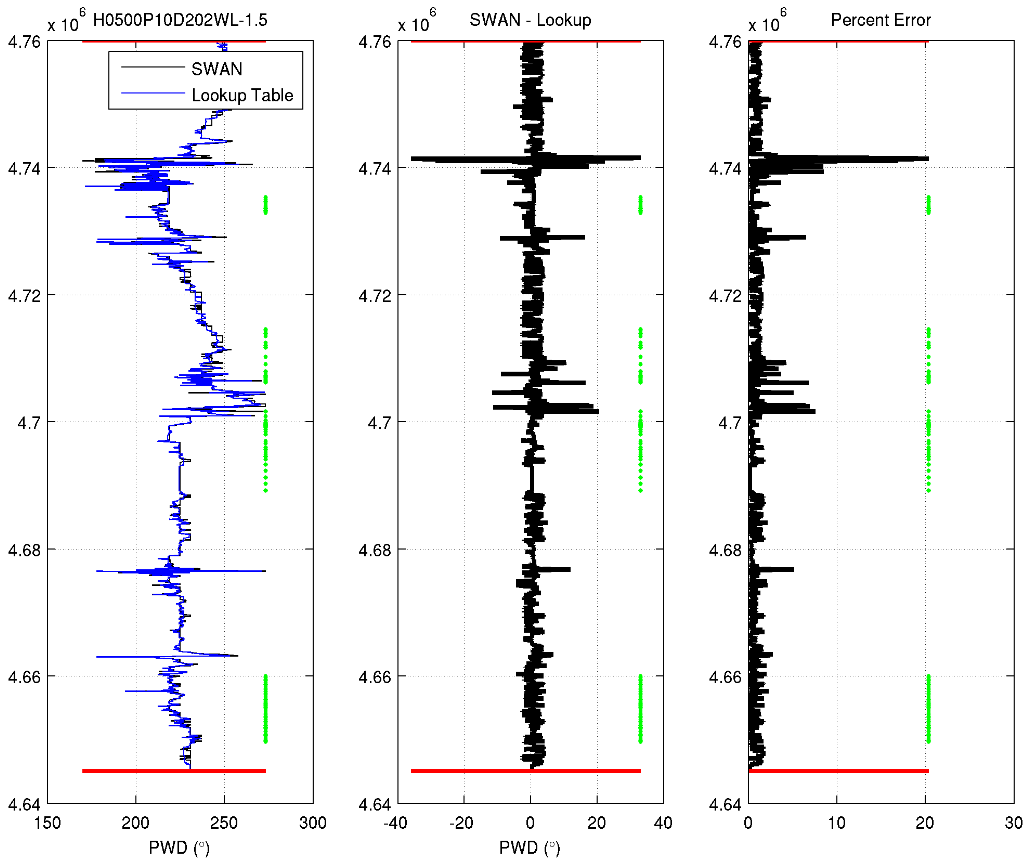

Figure 5-31. Comparison of alongshore varying wave direction at the 20-m contour extracted from the lookup tables (blue line) and from a direct SWAN computation (black line) with an offshore boundary condition characterized as H_s = 5m, T_p = 10, D_p = 202, and a water level of -1.5-m NAVD88. Solid red line denotes Curry County boundary.

6.0 WAVE RUNUP AND OVERTOPPING

Wave runup is the culmination of the wave breaking process whereby the swash of the wave above the still water level is able to run up the beach face, where it may encounter a dune, structure, or bluff, potentially resulting in the erosion, or overtopping and flooding of adjacent land (**Figure 6-1**). Runup, *R*, or wave setup plus swash, is generally defined as the time-varying location of the intersection between the ocean and the beach, and as summarized is a function of several key parameters.

These include the deepwater wave height (H_o or H_s), peak spectral wave period (T_p) and the wave length (L_o) (specifically the wave steepness, H_o/L_o), and through a surf similarity parameter called the Iribarren number,

$$\xi_o = \frac{\beta}{\sqrt{H_o/L_o}},$$

which accounts for the slope (β) of a beach or an engineering structure, as well as the steepness of the wave.

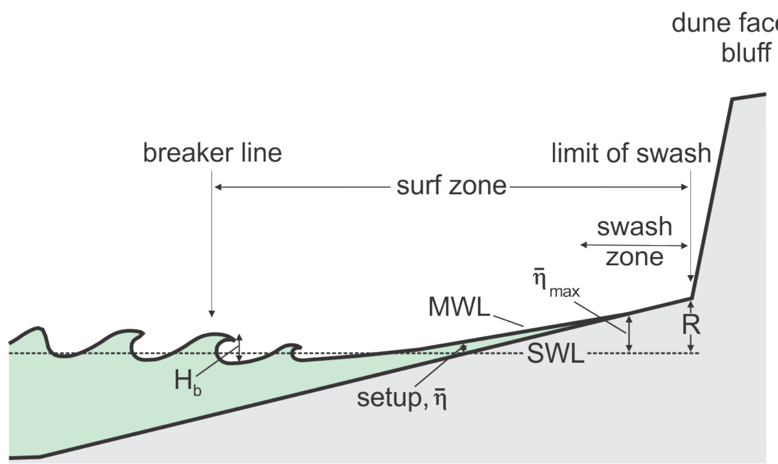

Figure 6-1. Conceptual model showing the components of wave runup associated with incident waves (modified from Hedges and Mase, 2004).

The total runup, *R*, produced by waves includes three main components:

- wave setup, $\overline{\eta}$;
- a dynamic component to the still water level, $\widehat{\eta}$; and
- incident wave swash, S_{inc}

$$R = \overline{\eta} + \widehat{\eta} + S_{inc} \tag{6.1}$$

Along the Pacific Northwest Coast of Oregon and Washington, the dynamic component of still water level, $\widehat{\eta}$, has been demonstrated to be a major component of the total wave runup due to relatively high contributions from infragravity energy (Ruggiero and others, 2004). This process occurs due to a transfer of energy from the incident wind-generated waves to the longer-period infragravity wave energy, the division being placed at ~20-s periods. On the dissipative beaches of the Oregon coast, it is the infragravity energy that increases swash runup levels during major storms that is ultimately responsible for erosion and overwash events. The combination of these processes produces "sneaker waves," yielding the most extreme swash runup levels.

A variety of models have been proposed for calculating wave runup on beaches (Ruggiero and others, 2001; Hedges and Mase, 2004; Northwest Hydraulic Consultants, 2005; Stockdon and others, 2006). Here we explore two approaches available for runup calculations along Curry County, Oregon. These included the runup model developed by Stockdon and others (2006) and the direct integration method (DIM) described in NHC (2005).

6.1 Runup Models for Beaches

6.1.1 Stockdon runup model

For sandy beaches, Stockdon and others (2006) developed an empirical model based on analyses of 10 experimental runup data sets obtained from a wide variety of beach and wave conditions, including data from Oregon [Ruggiero and others, 2004], and by separately parameterizing the individual runup processes: setup and swash. Stockdon and others (2006) proposed the following general relationship for the elevation of the 2% exceedance elevation of swash maxima, R_2, for any data run:

$$R_2 = 1.1[\,\overline{\eta} + \frac{S}{2}] \tag{6.2}$$

where:

$$S = \sqrt{(S_{inc})^2 + (\widehat{\eta})^2} \tag{6.3}$$

and:

$$\overline{\eta}, S_{inc}, \widehat{\eta} = f(H_o, T_o, \beta_f)$$

where β_f is the slope of the beach face, and S reflects both the dynamic, $\widehat{\eta}$, and incident swash, S_{inc}, components. The 1.1 coefficient value was determined because the swash level assumes a slightly non-Gaussian distribution. The final parameterized runup equation is:

$$R_{2\%} = 1.1\left(0.35\tan\beta\,(H_oL_o)^{\frac{1}{2}} + \frac{[H_oL_o(0.563\tan\beta^2 + 0.004)]^{\frac{1}{2}}}{2}\right) \tag{6.4}$$

which may be applied to natural sandy beaches over a wide range of morphodynamic conditions. In developing equation 6.4, Stockdon and others (2006) defined the slope of the beach as the average slope over a region ±2σ around the wave setup, $\overline{\eta}$, where σ is the standard deviation of the continuous water level record, η(t). Simply put, the setup reflects the height of the mean-water level (MWL) excursion above the SWL, such that the slope is determined to span the region around this MWL. For Curry County, the slope of the beach was determined by fitting a linear regression through those data points spanning the region located between 2 to 4 m.

Combining equation 6.4 with the measured water level at tide gauges produces the total water level (TWL) at the shore, important for determining the erosion or flood risk potential. Given that equation 6.4 has been derived from quantitative runup measurements spanning a range of beach slopes (beach slopes ranged from 0.01 to 0.11 and Iribarren numbers [**ξ**], ranged from 0.1 [fully dissipative conditions] to ~2.2 [reflective conditions]; Table 1 in Stockdon and others [2006]), the model is valid for the range of slopes and conditions observed along the Curry County coastline and elsewhere on the Oregon coast.

6.1.2 Direct integration method—beaches

The FEMA coastal flood mapping guidelines (NHC, 2005) for the U.S West Coast presents an alternative method for calculating runup. According to NHC (2005), the direct integration method (DIM) approach allows for the wave and bathymetric characteristics to be taken into consideration, specifically the spectral shape of the waves and the actual bathymetry can be represented. Here we review the parameterized set of runup equations that may be used to calculate runup on beaches. The equations are based on a parameterized JONSWAP spectra and uniform beach slopes.

Similar to equation 6.1, the runup of waves using DIM can be defined according to its three components that include the wave setup, $\overline{\eta}$, a dynamic nent, $\widehat{\eta}$, and the incident band swash, S_{inc}. Wave setup can be calculated using:

$$\overline{\eta} = 4.0\,F_H F_T F_{Gamma} F_{slope} \tag{6.5}$$

while the root mean square (rms) of the dynamic component, $\widehat{\eta}_{rms}$, may be estimated using:

$$\widehat{\eta}_{rms} = 2.7\ G_H G_T G_{Gamma} G_{slope} \quad (6.6)$$

where the units of $\overline{\eta}$ and $\widehat{\eta}_{rms}$ are in *feet* and the factors (F) are for the wave height (F_H and G_H), wave period (F_T and G_T), JONSWAP spectrum narrowness (F_{Gamma} and G_{Gamma}), and the nearshore slope (F_{slope} and G_{slope}). These factors are summarized as a series of simple equations in Table D.4.5-1 (NHC, 2005). For the purposes of defining an average slope, NHC recommended that the nearshore slope be based on the region between the runup limit and twice the wave breaking depth, h_b, where:

$$h_b = H_b/k \quad (6.7)$$

and

$$H_b = 0.39 g^{0.2} \left(T_p H_o^2\right)^{0.4} \quad (6.8)$$

where H_b is the breaker height calculated using equation 6.8 (Komar, 1998a), g is acceleration due to gravity (9.81 m/s), and for the purposes here k (breaker depth index) can be taken to be 0.78. Thus, one important distinction between the DIM and Stockdon methods for calculating runup, is the method used to define the beach slope; the former accounts for a larger portion of the nearshore slope, while the latter is based on the slope calculated around the mid beach-face.

To derive the statistics of the oscillating wave set-up and the incident swash components, the recommended approach is to base the calculations on the standard deviations (σ) of each component. The standard deviation of the incident wave oscillation (σ_2) on natural beaches may be calculated from:

$$\sigma_2 = 0.3 \xi_o H_o \quad (6.9)$$

Because the standard deviation of the wave setup fluctuations (σ_1) is proportional to equation 6.6, the total oscillating component of the dynamic portion of the wave runup can be derived from:

$$\widehat{\eta_T} = 2.0 \sqrt{\sigma_1^2 + \sigma_2^2} \quad (6.10)$$

Combining the results of equations 6.10 and 6.5 yields the 2% wave runup, and when combined with the tidal component results in the TWL.

6.1.3 Comparison between Stockdon and DIM runup calculations

Fundamentally, the wave runup model proposed by Stockdon and others (2006) and the DIM method described in NHC (2005) are similar, because both models account for the three components of runup described in equation 6.1. Here we examine the results derived from both runup models based on a range of conditions characteristic of the Clatsop County shoreline (**Figure 6-2** and **Figure 6-3**). We include results from Clatsop only because this was where we did the bulk of our initial testing of our overall approach for modeling runup and TWLs along the Oregon coast.

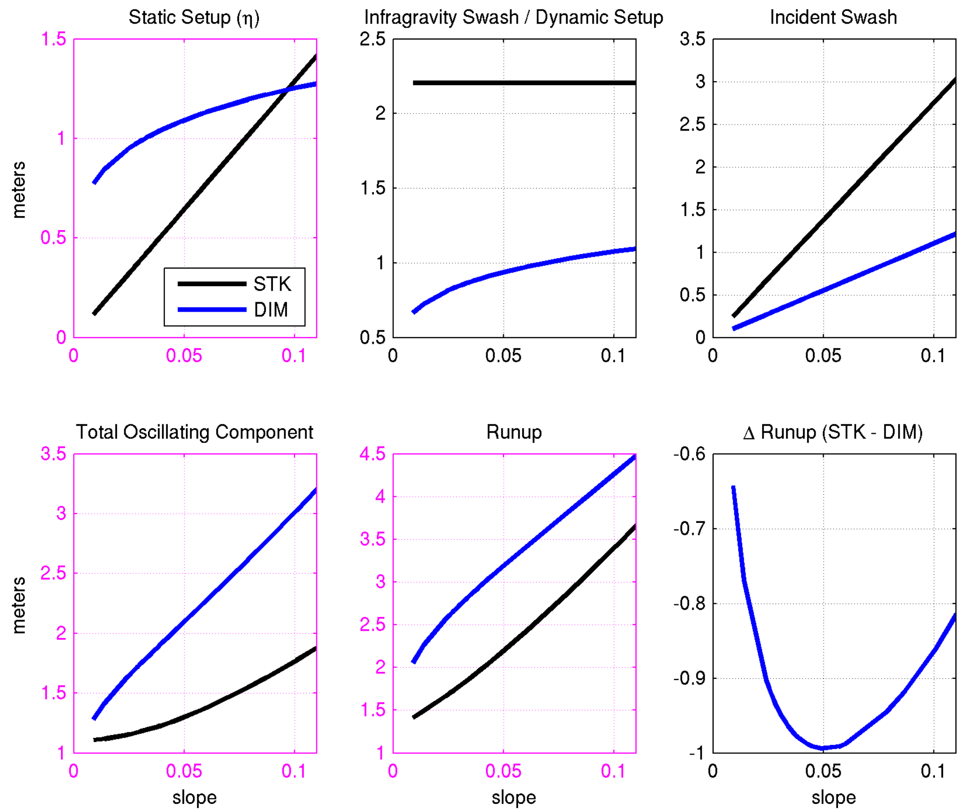

Figure 6-2. Calculated setup, swash and runup using the Stockdon and DIM runup equations. In this example, slope values are defined similarly for both methods, at a mid-beach elevation range of 2-4 m (6.6–13 ft). A 6 m (19.7 ft) significant wave height, 12-s peak wave period, and 270-degree wave direction were used to drive the models. Due to the semi-empirical nature of the equations, only the magnitudes of the subplots outlined in magenta are directly comparable (the two panels showing swash results are not directly comparable). The total oscillating component compares the results from equation 6.3 (S/2) with equation 6.10.

Figure 6-2 provides a comparison of the various calculated parameters (setup, infragravity swash, incident swash, total oscillating component, and runup) determined using the Stockdon and DIM approaches. In this example, we use the same slope defined for the mid-beach region in order to provide a direct comparison between DIM and Stockdon. Upper estimates have been truncated to tan β = 0.11, which reflects the slope limit on which Stockdon has been tested. In contrast, it is unclear the range of slope conditions on which DIM may be applied as there is no quantitative field testing of this particular formulation. As can be seen in **Figure 6-2**, although there are notable differences in the various parameterizations, the derived runup (bottom, middle plot) is similar. Nevertheless, as can be seen from the ΔR plot (bottom right), the DIM approach tends to estimate a slightly higher runup when compared to Stockdon, which in this example reaches a maximum of ~1 m (3.3 ft) for a beach slope of 0.04 to 0.05. Thus, overall, we can conclude that the two approaches are performing in a similar fashion when tested using the same slope.

Figure 6-3 presents a similar suite of comparisons under the same hydrodynamic conditions. Therefore the Stockdon and others (2006) results are identical to **Figure 6-2** in all panels. However, in this example we now account for the appropriate nearshore slope in the DIM runup calculations as defined above in Section 6.1.2. This was originally done by computing the DIM runup components for this hydrodynamic condition using the full nearshore slope at 85 transects spread along the Clatsop County coastline [Allan and others, 2014]. The DIM values are, however, plotted against the foreshore beach slopes defined for all 85 transects in order to make the comparisons with Stockdon meaningful. As can be seen in **Figure 6-3**, application of the nearshore slope significantly changes the magnitudes of all the runup components, and in particular reduces the calculated runup when compared to Stockdon for most foreshore slopes. In general, at lower slopes (tan $\beta < 0.05$) runup calculated by DIM is slightly higher than Stockdon, which reverses at steeper slopes (tan $\beta > 0.05$). This pattern is consistent with analyses performed by Allan and others (2012) in Coos County.

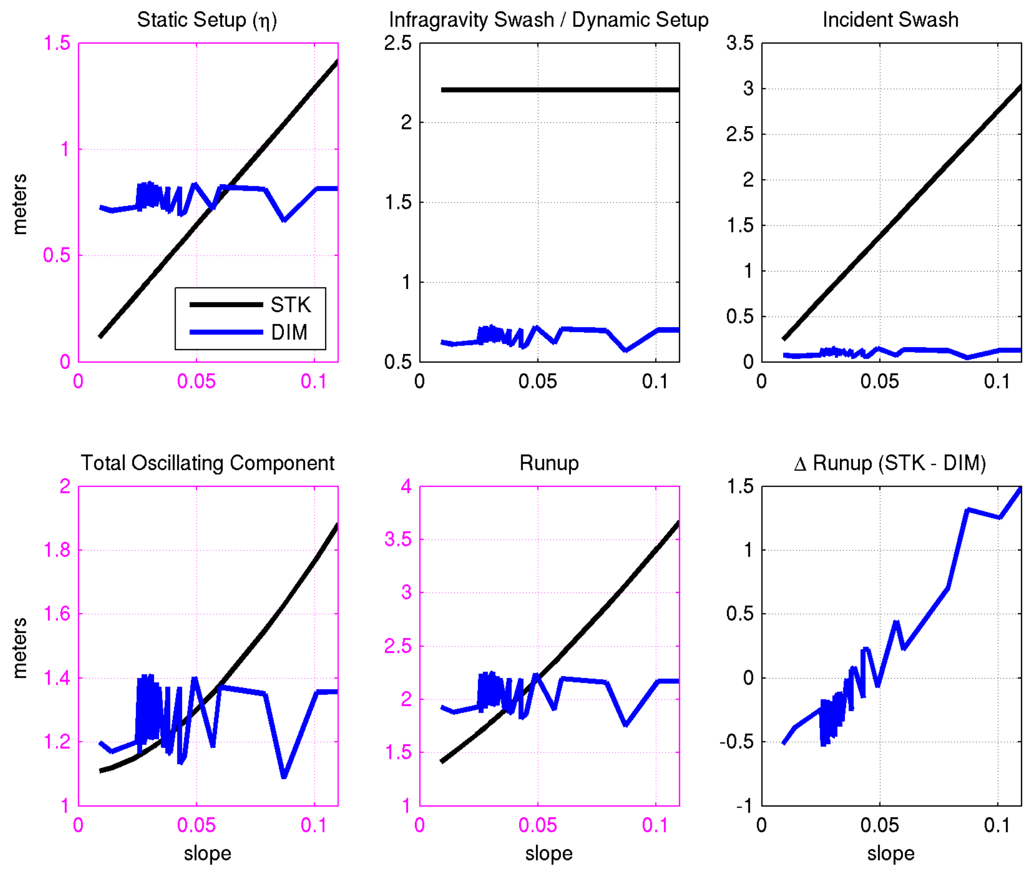

Figure 6-3. Total water level calculations using the Stockdon (foreshore slope) and DIM runup equations (nearshore slope). A 6 m (19.7 ft) significant wave height, 12-s peak wave period, and 270 degree wave direction was used to drive the models. Due to the semi-empirical nature of these equations only the magnitudes of the subplots outlined in magenta are directly comparable. The results for DIM are sorted in ascending order as a function of foreshore beach slope.

Most interesting in the comparisons shown in **Figure 6-3** is that the DIM runup components actually do not vary as a function of the foreshore slope. The total runup (**Figure 6-3** bottom-center) produced by DIM is relatively constant, oscillating between 1.7 and 2.3 m (5.6 and 7.5 ft). The oscillations are due primarily to the variability in the nearshore slopes, which are a function of wave height (equations 6.7-6.8). Because waves in the PNW are relatively large and upper shoreface slopes relatively shallow, the DIM runup values are controlled by the nearshore slope with little influence from the upper beach. This lack of dependence on the foreshore is in contrast to field measurements made in Oregon (Ruggiero and others, 2004) in which runup is clearly a function of the foreshore slope. Because the Stockdon model has been extensively validated against measured runup data, including measurements on the Oregon coast (e.g., Ruggiero and others, 2001; Ruggiero and others, 2004), together with qualitative observations of runup during storms by DOGAMI staff at multiple sites along the coast, 1% extreme values of TWLs calculated for sandy beaches along the Curry County coast will be based primarily on the Stockdon and others (2006) model.

6.2 "Barrier" Runup Calculations

6.2.1 Introduction

According to NHC (2005), an alternate approach is recommended for use in calculating runup on steep barriers. By definition, *barriers include "steep dune features and coastal armoring structures such as revetments"* (NHC, 2005, p. D.45-10), although little guidance is offered in terms of the range of slopes to which this alternate approach would apply. Throughout this document we use the generic term *barrier* to define the range of morphological and engineering conditions where barrier runup calculations may apply. In general, runup on barriers depends not only on the height and steepness of the incident waves defined through the Iribarren number or breaker parameter ($\xi_{m-1,0}$), but also on the geometry (e.g., the slope of the barrier and/or if a berm is present), design characteristics of the structure and its permeability.

The recommended approach for calculating runup on barriers is to use the TAW (Technical Advisory Committee for Water Retaining Structures) method, which provides a mechanism for calculating the runup, adjusted for various reduction factors that include the surface roughness, the influence of a berm (if present), and effects associated with the angle of wave approach (van der Meer, 2002; Northwest Hydraulic Consultants, 2005; Pullen and others, 2007). According to NHC (2005) the TAW method is useful as it includes a wide range of conditions for calculating the wave runup (e.g., both smooth and rough slopes), and because it agrees well with both small- and large-scale experiments.

Figure 6-4 is a conceptual model of the various components required to determine the extent of runup on barriers. Of importance is first determining the 2% dynamic water level ($DWL_{2\%}$) at the barrier, which includes the combined effects of the measured still water level (SWL), the wave setup ($\overline{\eta}$) and the dynamic portion ($\widehat{\eta}$) of the runup (**Figure 6-4**), which is then used to establish the spectral significant wave height (H_{mo}) at the toe of the "barrier" (NHC, 2005).

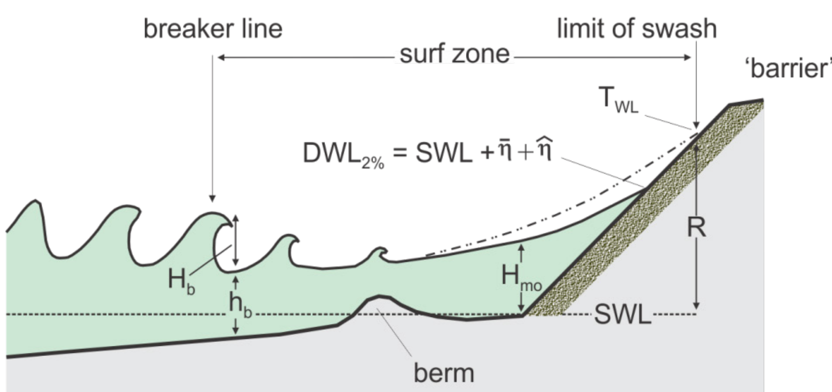

Figure 6-4. Wave runup on a beach backed by a structure or bluff (modified from NHC, 2005).

The general formula for calculating the 2% wave runup height on barriers is given in a non-dimensional form by equation 6.11:

$$\frac{R_{2\%}}{H_{mo}} = c_1 . \gamma_b . \gamma_f . \gamma_\beta . \xi_{m-1,0} \tag{6.11}$$

with a maximum of:

$$\frac{R_{2\%}}{H_{mo}} = \gamma_f . \gamma_\beta \left(c_2 - \frac{c_3}{\sqrt{\xi_{m-1,0}}} \right)$$

where:

$R_{2\%}$ = wave runup height exceeded by 2% of the incoming waves

H_{mo} = spectral significant wave height at the structure toe

c_1, c_2, and c_3 = empirical coefficients with:

γ_b = influence factor for a berm (if present)

γ_f = influence factor for roughness element of slope

γ_β = influence factor for oblique wave attack

$\xi_{m-1,0}$ = breaker parameter

$$\left(\tan\beta / \left(H_{mo}/L_{m-1,0}\right)^{0.5}\right),$$

$\tan\beta$ = slope of the “barrier,”

$L_{m-1,0}$ = the deepwater wave length $\left(gT_{m-1,0}^2/2\pi\right)$,

$T_{m-1,0}$ can be calculated from $T_p/1.1$, where T_p is the peak spectral wave period.

Substituting the empirical coefficients derived from wave tank experiments and incorporating a 5% upper exceedance limit into the general equations of 6.11 (van der Meer, 2002; Pullen and others, 2007), runup on barriers may be calculating using:

$$R_{2\%} = H_{mo}\left(1.75 . \gamma_b . \gamma_f . \gamma_\beta . \xi_{m-1,0}\right), where\ 0 < \gamma_b . \xi_{m-1,0} < 1.8 \tag{6.12}$$

with a maximum of:

$$R_{2\%} = H_{mo}\left(1.0 . \gamma_f . \gamma_\beta \left(4.3 - \frac{1.6}{\sqrt{\xi_{m-1,0}}}\right)\right), where\ \gamma_b . \xi_{m-1,0} \geq 1.8$$

There are, however, notable differences between equation 6.12 originally described in van der Meer (2002) and Pullen and others (2007) from that presented in equation D.4.5-19 in the FEMA West Coast methodology [NHC, 2005]. For example, equation D.4.5-19 in the NHC report contains a higher coefficient value (1.77), along with one additional reduction factor (porosity) for calculating runup when the breaker parameter is less than 1.8. Similarly, for conditions where the breaker parameter exceeds 1.8 and the maximum runup equation is used, equation D.4.5-19 in the NHC report contains two extra reduction factors (berm and porosity reduction factors) that are not included in the original solution, which potentially could have a very significant effect on the calculated runup. Based on these differences, we have used the original solution presented as equation 6.12 of van der Meer (2002) and Pullen and others (2007).

6.2.2 Specific procedure for calculation “barrier” runup

For those cases where the TAW method is used for determining runup on barriers (i.e., beaches backed by structures, cobble berms, and/or bluffs), we have followed the general approach laid out in section D.4.5.1.5.2 in NHC (2005), with the exception that we use Stockdon to define the $DWL_{2\%}$ (instead of DIM) at the structure toe, and TAW to calculate the incident swash on the barrier (i.e., equation 6-12). Because waves are depth limited at the barrier toe, H_{mo} may be estimated from $DWL_{2\%}$ using a breaker index of 0.78 (i.e., $H_{mo} = DWL_{2\%} \times 0.78$). In performing these various derivations, $DWL_{2\%}$ was first determined using equation 6.13:

$$DWL_{2\%} = SWL + 1.1 * \left(\overline{\eta} + \frac{\widehat{\eta}}{2}\right) - D_{low} \qquad (6.13)$$

where:

SWL = measured tide

$$\overline{\eta} = 0.35 * \tan\beta\sqrt{H_s * L}$$ *Eqn. 10 in Stockdon and others (2006)*

$$\widehat{\eta} = 0.06 * \sqrt{H_s * L}$$ *Eqn. 12 in Stockdon and others (2006)*

D_{low} = the toe of the structure or bluff

$\tan\beta$ = the beach slope defined for the region between 2 and 4 m.

Having calculated $DWL_{2\%}$ and H_{mo}, the TAW runup calculation can be implemented. equation 6.12 requires information on the slope of the barrier, used in the breaker parameter ($\xi_{m-1,0}$) calculation, which can be somewhat challenging to define. This is especially the case if the morphology of the barrier exhibits a composite morphology characterized by different slopes, such that errors in estimating the slope will translate to either significant underestimation or overestimation of the runup. According to van der Meer (2002) and Pullen and others (2007), because the runup process is influenced by the change in slope from the breaking point to the maximum wave runup, the characteristic slope should be specified for this same region. On the Oregon coast, the most common composite slope example is the case where a broad, dissipative sand beach fronts a structure or bluff that is perched relatively high on the back of the beach (structure toe > ~4-5 m). In this example, the wave runup is first influenced by the sandy beach slope and finally by the slope of the structure itself. To address this type of situation, we define a "local barrier slope," as the portion of the barrier that ranges from the calculated storm TWL (calculated initially using equation 6.4) down to a lower limit defined by the wave setup plus the SWL (i.e., $(1.1 * \overline{\eta}) + SWL$). In a few cases, the TWL was found to exceed the barrier crest in which case we used the structure crest as the upper limit for defining the local slope. This process is repeated for every storm condition. Having determined the barrier slope, the TAW runup is calculated using equation 6.12 and reduced based on the appropriate site specific reduction factors.

Under certain conditions, we identified events that generated extreme runup that made little physical sense. For these (rare) cases, we calculated the TAW runup using an iterative approach based on procedures outlined in the Eurotop (2007) manual. Because the maximum wave runup is the desired outcome and is unknown when initially defining the slope, the process is iterative requiring two steps. First, the breaking limit is defined as $1.5H_{mo}$ *below* the SWL, while $1.5H_{mo}$ *above* the SWL defines the upper limit of the first slope estimate (**Figure 6-5**). Having determined the first slope estimate, the TAW runup is calculated using equation 6.12 and reduced based on the appropriate reduction factors. A second slope estimate is then performed based on the initial runup calculation, while a third iteration is not necessary based on our tests because this method converges quickly. The breaking limit is again defined as $1.5H_{mo}$ *below* the SWL, while $R_{2\%}$ *above* the SWL defines the upper limit, and the final barrier runup estimate is again calculated using equation 6.12 and reduced based on the appropriate reduction factors.

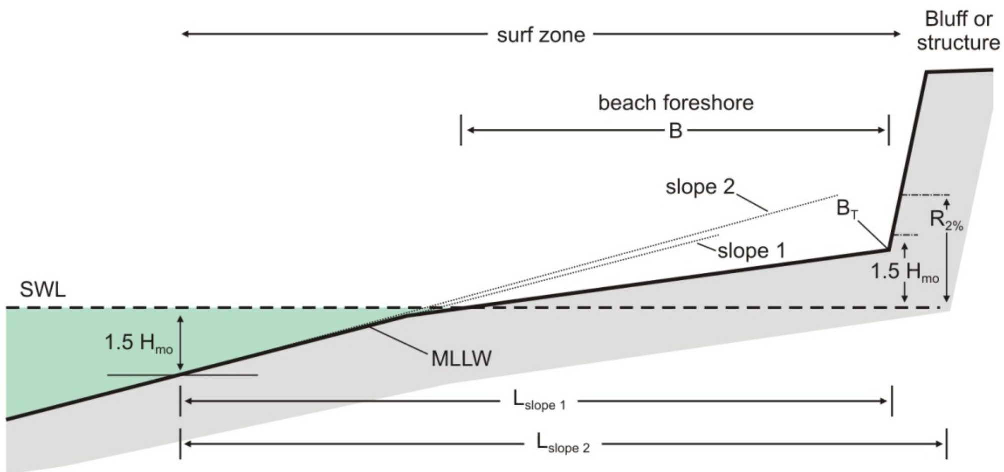

Figure 6-5. Determination of an average slope based on an iterative approach. The first estimate is initially based on 1.5H_{mo} ± SWL, while the second estimate is based on 1.5H_{mo} below the SWL and the calculated $R_{2\%}$ above the SWL that is based on the first slope estimate.

Finally, it is important to note that the runup estimates based on the "barrier" runup calculations is sensitive to the slope. Similar to our study in Coos, Clatsop, Tillamook, and Lincoln counties, for those sites where the calculated TWLs unreasonably low (relative to the morphology of the beach and observations of storm wave runup along this shore and elsewhere), we have defaulted to the TWLs calculated using the Stockdon and others model. These few cases are entirely due to there being a very wide dissipative surf zone at these transect locations that results in very low slopes being defined.

6.2.3 "Barrier" runup reduction factors

Table 6-1 below presents information pertaining to the suite of parameters used to define wave runup (R) and ultimately the 1% TWLs along the Curry County coast. In the case of bluff roughness along the Curry shore, we used a value of 0.6 for those situations where a bluff face was highly vegetated. These bluffs are typically located at or near their stable angle of repose and are covered with Salal plants (*Gaultheria shallon*), forming a deep, nearly impenetrable thicket. The decision to use 0.6 was based on discussions with Dr. W.G. McDougal (Coastal Engineer, OSU and Technical Coordinator of the North Pacific FEMA West Coast Guidelines, pers. comm., April 2010). Where beaches were identified as being backed by a significant riprap structure, we used a reduction factor of 0.55. In other cases, this was increased to 0.6 to 0.8, depending on whether the beach was backed by gravels/cobbles, a vegetated bluff face, or poor quality riprap . Wave direction (γ_β) reduction factors were determined based on the shoreline orientation at every transect site and the actual wave directions measured during each storm condition. The reduction factor was calculated using equation D.4.5-22 (NHC, 2005, p. D.4.5-13). Finally, of the 109 primary transects established along the Curry County coast, two of these are characterized with having a broad rock (basalt) platform within the intertidal zone that is akin to a protective berm. For these sites, we calculated a berm reduction factor using equation D.4.5-21 (NHC, 2005, p. D.4.5-13).

Table 6-1. Various parameters used to define runup (R) and total water levels (TWLs) on beaches backed by dunes, structures, and bluffs.

Reach	Transect (CURRY)	D_{HIGH} (m)	D_{LOW} (m)	Beach Slope (tan θ)	Wave Dir. ($\Upsilon\theta$)	Rough-ness (Υr)	Approach	Description
Brookings	1	12.787	4.603	0.063	262.7	1	3	coarse sand beach backed by moderately high cliffs
	2	12.35	4.579	0.093	262.2	1	3	coarse sand beach backed by moderately high cliffs
	3	7.068	5.458	0.076	254.6	1	3	coarse sand beach backed by low cliffs
	4	7.056	6.786	0.1	253.8	1	3	coarse sand beach backed by dune
	5	7.763	5.775	0.073	253.3	1	3	coarse sand beach backed by dune
	6	6.524	6.216	0.079	240	1	3	coarse sand beach backed by dune
	7	5.539	5.388	0.075	251.6	1	3	coarse sand beach backed by dune
	8	5.833	4.414	0.075	234.6	0.6	3	coarse sand beach backed by moderately high cliffs
	9	5.604	5.788	0.111	219.6	0.6	3	coarse sand beach backed by moderately high cliffs
	10	18.288	5.189	0.116	219.3	0.6	3	coarse sand beach backed by moderately high cliffs
	11	15.733	4.273	0.104	230.9	0.6	1	coarse sand beach backed by moderately high cliffs
	12	16.687	8.049	0.109	236.7	0.6	3	coarse sand beach backed by moderately high cliffs
	13	10.896	5.298	0.112	237.8	0.6	1	coarse sand beach backed by low cliffs
	14	**13.796**	**4.115**	**0.066**	**242.4**	**0.95**	**1**	**coarse sand beach backed by moderately high cliffs**
	15	15.389	3.664	0.07	247.6	0.6	1	coarse sand beach backed by moderately high cliffs
	16	18.755	5.202	0.118	226.2	0.6	1	coarse sand beach backed by moderately high cliffs
	17	8.195	4.465	0.095	214.2	0.6	3	coarse sand beach backed by moderately high cliffs
	18	16.013	5.443	0.104	218.4	0.6	3	coarse sand beach backed by moderately high cliffs
	19	19.918	7.33	0.111	229.2	0.6	3	coarse sand beach backed by moderately high cliffs
	20	18.321	5.206	0.111	235.1	0.6	1	coarse sand beach backed by moderately high cliffs
	21	**20.634**	**5.332**	**0.087**	**235.8**	**0.95**	**1**	**coarse sand beach backed by moderately high cliffs**
	22	**24.004**	**4.821**	**0.086**	**237**	**0.6**	**1**	**coarse sand beach backed by moderately high cliffs**
	23	5.895	5.895	0.071	242.7	1	3	coarse sand beach backed by moderately high cliffs
	24	7.734	5.823	0.089	229.5	0.75	1	coarse sand beach backed by riprap
	25	6.674	5.007	0.087	216.7	0.55	1	coarse sand beach backed by riprap
	26	9.569	5.198	0.095	203.4	0.55	1	coarse sand beach backed by moderately high cliffs
	27	19.643	3.735	0.096	180.6	0.6	1	coarse sand beach backed by moderately high cliffs
	28	**23.601**	**4.009**	**0.065**	**192.7**	**0.95**	**1**	**rocky beach backed by high cliffs**
	29	21.048	4.181	0.073	182.5	0.75	1	rocky beach backed by high cliffs
	30	16.663	5.023	0.051	224.9	0.95	1	sand beach backed by moderately high cliffs
	31	15.179	4.519	0.05	175.6	0.95	1	sand beach backed by low bluff

Reach	Transect (CURRY)	D_{HIGH} (m)	D_{LOW} (m)	Beach Slope (tan θ)	Wave Dir. ($\Upsilon\theta$)	Rough-ness (Υr)	Approach	Description
	32	31.548	3.839	0.08	233.2	0.6	1	rocky beach backed by moderately high cliffs
	33	31.948	4.329	0.059	237.7	0.95	1	rocky beach backed by moderately high cliffs
	34	**34.153**	**1.853**	**0.046**	**246.9**	**0.9**	**1**	**rocky beach backed by moderately high cliffs**
	35	33.985	0.432	0.13	252.4	0.95	1	rocky beach backed by high cliffs
	36	36.718	3.684	0.072	248.5	0.6	1	rocky beach backed by high cliffs
	37	19.206	3.567	0.072	240.2	0.95	1	coarse sand beach backed by high cliffs
	38	24.669	3.749	0.054	237.7	0.6	1	coarse sand beach backed by high cliffs
	39	9.885	3.6	0.084	221.2	0.6	1	coarse sand beach backed by moderately high cliffs
	40	10.97	3.394	0.036	204.8	0.8	1	coarse sand beach backed by sloping wall
	41	12.655	3.219	0.038	239.8	0.6	1	coarse sand beach backed by moderately high cliffs
	42	25.783	3.511	0.086	244.5	0.6	1	coarse sand beach backed by high cliffs
	43	15.497	3.011	0.066	249.6	0.6	1	coarse sand beach backed by moderately high cliffs
	44	23.73	4.008	0.066	242.1	0.6	1	coarse sand beach backed by high cliffs
	45	26.866	4.783	0.063	243.5	0.6	1	coarse sand beach backed by high cliffs
	46	21.069	3.61	0.037	229.7	0.6	1	coarse sand beach backed by high cliffs
	47	37.239	1.995	0.041	230.7	0.55	1	rocky beach backed by high cliffs
Gold Beach	48	10.938	6.384	0.092	277.6	1	3	coarse sand beach backed by dune and high bluffs
	49	8.217	5.304	0.11	271.4	1	3	coarse sand beach backed by dune and high bluffs
	50	9.597	5.215	0.102	273.9	1	3	coarse sand beach backed by dune and high bluffs
	51	9.759	5.063	0.072	278.1	1	3	coarse sand beach backed by dune
	52	8.451	5.822	0.073	271.6	1	3	coarse sand beach backed by dune
	53	4.987	4.141	0.073	270.2	1	3	coarse sand beach backed by dune
	54	7.73	5.037	0.079	263	1	3	coarse sand beach backed by dune
	55	7.488	5.802	0.077	264	1	3	coarse sand beach backed by dune
	56	6.727	5.16	0.077	273.2	1	3	coarse sand beach backed by dune
	57	8.342	5.873	0.08	269	1	3	coarse sand beach backed by dune
	58	8.191	5.251	0.072	268.7	1	3	coarse sand beach backed by dune
	59	6.405	5.278	0.089	268.9	1	3	coarse sand beach backed by dune
	60	6.414	5.27	0.082	265.8	1	3	coarse sand beach backed by dune
	61	6.817	5.929	0.107	255.7	1	3	coarse sand beach backed by dune

Reach	Transect (CURRY)	D_{HIGH} (m)	D_{LOW} (m)	Beach Slope (tan β)	Wave Dir. ($\Upsilon\beta$)	Rough-ness (Υr)	Approach	Description
Rogue Shores	62	5.3	5.3	0.062	262	1	3	coarse sand beach backed by dune
	63	4.894	4.8	0.053	258.4	1	3	coarse sand beach backed by dune
	64	5.584	5.308	0.08	262	1	3	coarse sand beach backed by dune
	65	5.211	5.143	0.064	256.3	1	3	coarse sand beach backed by dune
	66	5.277	4.299	0.051	263.4	1	3	coarse sand beach backed by dune
	67	5.333	4.621	0.047	274.1	1	3	coarse sand beach backed by dune
	68	6.106	4.792	0.045	279	1	3	coarse sand beach backed by dune
	69	6.871	3.818	0.04	286.1	0.9	3	sand beach backed by poor riprap
	70	7.797	4.996	0.047	288.8	1	3	coarse sand beach backed by dune
	71	8.944	4.8	0.047	290.3	1	3	coarse sand beach backed by dune
	72	6.214	5.215	0.048	301.7	1	3	coarse sand beach backed by dune
	73	6.355	4.438	0.034	301.5	1	3	coarse sand beach backed by dune
	74	5.547	4.453	0.038	288.2	1	3	coarse sand beach backed by dune & high cliff
Nesika Beach	75	24.855	4.094	0.074	308.1	0.95	1	coarse sand beach backed by moderately high bluff
	76	25.739	4.403	0.054	299.2	0.95	1	coarse sand beach backed by moderately high bluff
	77	26.867	4.305	0.063	294	0.95	1	coarse sand beach backed by moderately high bluff
	78	22.964	4.334	0.056	292.6	0.95	1	coarse sand beach backed by moderately high bluff
	79	21.675	4.105	0.076	292.6	0.95	1	coarse sand beach backed by moderately high bluff
	80	20.923	4.502	0.093	291.7	0.95	1	coarse sand beach backed by moderately high bluff
	81	15.649	5.22	0.105	296.3	0.95	1	coarse sand beach backed by moderately high bluff
	82	10.082	4.264	0.083	295.9	0.95	1	coarse sand beach backed by moderately high bluff
	83	24.455	5.373	0.085	296.8	0.95	1	coarse sand beach backed by moderately high bluff
	84	21.697	5.025	0.086	293	0.95	1	coarse sand beach backed by moderately high bluff
	85	30.639	2.831	0.095	286	0.55	1	coarse sand beach backed by riprap wall
	86	9.227	5.834	0.092	289.6	1	3	coarse sand beach backed by dune & bluff
	87	12.406	4.299	0.077	279.8	1	3	coarse sand beach backed by low bluff
	88	8.737	6.446	0.1	287.1	1	3	coarse sand beach backed by dune
	89	8.661	5.377	0.08	287.1	1	3	coarse sand beach backed by dune
	90	7.983	5.293	0.086	273.4	1	3	coarse sand beach backed by dune & bluff
	91	7.071	6.915	0.086	278.7	1	3	coarse sand beach backed by dune & bluff
	92	6.749	6.387	0.098	275.2	1	3	coarse sand beach backed by dune & bluff
	93	6.683	5.238	0.097	251	1	3	coarse sand beach backed by dune & bluff

Reach	Transect (CURRY)	D_{HIGH} (m)	D_{LOW} (m)	Beach Slope (tan β)	Wave Dir. ($\Upsilon\beta$)	Rough-ness (Υr)	Approach	Description
Port Orford	94	17.803	3.81	0.055	198.9	0.95	1	coarse sand beach backed by moderately high cliffs
	95	6.416	5.127	0.069	161.5	1	3	coarse sand beach backed by dune & moderately high cliffs
	96	8.189	5.257	0.076	161	1	3	coarse sand beach backed by dune & moderately high cliffs
	97	7.718	5.418	0.074	150.5	1	3	coarse sand beach backed by dune & low cliffs
	98	7.913	0.388	0.106	230.3	0.9	1	Steep rock platform & seawall at port
	99	8.083	0.533	0.078	238.3	0.95	1	Steep rock platform & seawall at port
	100	16.495	6.888	0.117	310.7	1	3	coarse sand beach backed by dune
	101	6.854	5.389	0.081	281.9	1	3	coarse sand beach backed by low bluff
	102	12.147	5.327	0.074	278	1	3	coarse sand beach backed by moderately high bluff
	103	7.589	6.272	0.107	277.2	1	3	coarse sand beach backed by moderately high bluff
	104	8.235	7.427	0.107	265.9	1	3	barrier beach
	105	8.903	6.375	0.109	263.2	1	3	barrier beach
	106	6.466	4.916	0.093	259.7	1	3	barrier beach
	107	7.179	5.555	0.109	263.7	1	3	barrier beach
	108	7.957	7.141	0.11	261.6	1	3	barrier beach
	109	20.22	5.971	0.111	259.6	0.95	3	coarse sand beach backed by moderately high bluff
Brookings Supple-mental	7_1340	4.582	4.23	0.056	251.6	1	3	coarse sand beach backed by dune

Notes:

D_{HIGH} denotes the crest of the dune, bluff, or structure;

D_{LOW} denotes the toe of the dune (i.e., E_j), bluff, or structure;

Beach slope reflects the calculated slope spanning the region between 2 and 4-m elevation;

Wave direction denotes the shoreline orientation used to calculate the wave reduction (Υ_β) factor used in TAW runup calculations;

Roughness (Υ_r) defines the backshore roughness used in TAW runup calculations. Bold values indicate sites where the local slope goes to 1 due to the presence of a vertical bluff; and

Approach defines the final runup approach used to calculate the wave runup, where STK (3) = Stockdon, Snsh/TAW (2) = nearshore slope and TAW, and LocSlp/TAW (1) = the local barrier slope and TAW.

6.3 Curry County Wave Runup and Total Water Level Calculations

The complete hourly combined time series is run through the lookup tables to derive alongshore varying transformed wave time series. Using the transformed wave conditions, and the measured alongshore varying beach and barrier slopes, initial TWL time series based on the Stockdon approach are developed at all transect locations. From these time series we identify the ~150 highest independent TWLs at each transect over the length of the record. Wave runup is then computed for each of these storm input conditions (about five events per year) at every profile site shown in **Figure 3-1** to **Figure 3-5** using a combination of the Stockdon and others (2006) runup equation for dune-backed beaches (equation 6.4) and TAW (equation 6-12) for wave runup on a barrier. The specific approaches used in our calculations are defined above in **Table 6-1**. For both models, the calculated runup is combined with the SWL (measured tides) to develop the TWL conditions used to generate the 10-, 50-, and 100-year return level event as well as the 500-year return event. The input wave conditions from the SWAN modeling used in the various calculations were determined for each transect location by extending the shore-perpendicular transects from the backshore to where they intersected the 20-m contour, or the seaward most location of H_{mo}/depth = 0.4, whichever was farther offshore (but almost always shallower than 30 m). This ensured that only minor dissipation due to wave breaking influenced the model results. These intersections are where wave statistics from the SWAN output were extracted.

Having calculated the storm-induced TWLs, we used the generalized extreme value (GEV) family of distributions (specifically the peak over threshold (POT) approach) to estimate the 100-year and 500-year total water levels for each of the beach profile sites. Specific information about the extreme value techniques used to estimate these TWLs is described in Section 4.6. **Figure 6-6** gives an example of the extreme value (GPD-Poisson) model for the CURRY58 profile site in which the 100-year event is calculated to be 7.82 m (25.6 ft) and the 500-year event is estimated to be 7.92 m (26 ft). The results for all of the profiles can be found in **Table 6-2**.

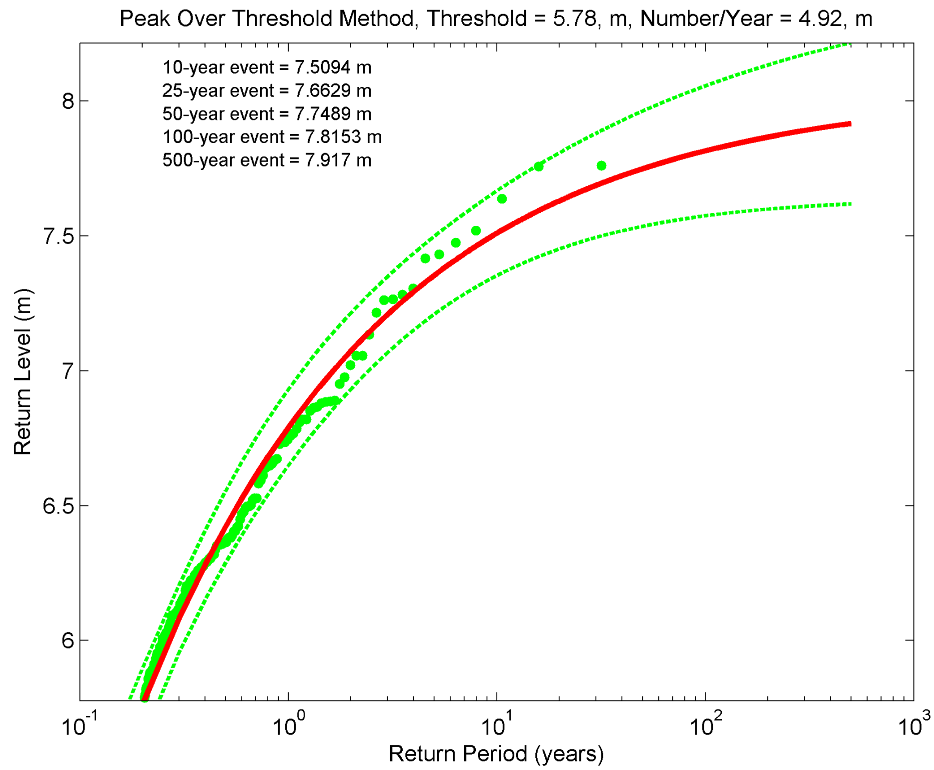

Figure 6-6. Example peak over threshold (POT) extreme value theory results for the CURRY58 transect site (with 95% confidence levels) located in the Gold Beach littoral cell. Note that the y-axis vertical datum is relative to the NAVD88 vertical datum.

Table 6-2. 100-year (1%) and 500-year (0.2%) total water levels calculated for the Curry County transect sites.

Reach	Transect (CURRY)	D_{HIGH} (m)	D_{LOW} (m)	100-Year (m)	500-Year (m)	Description
Brookings	1	12.787	4.603	7.64	7.99	coarse sand beach backed by moderately high cliffs
	2	12.35	4.579	9.55	10.37	coarse sand beach backed by moderately high cliffs
	3	7.068	5.458	8.32	8.65	coarse sand beach backed by low cliffs
	4	7.056	6.786	9.44	9.7	coarse sand beach backed by dune
	5	7.763	5.775	8.28	8.77	coarse sand beach backed by dune
	6	6.524	6.216	8.32	8.42	coarse sand beach backed by dune
	7	5.539	5.388	8.26	8.72	coarse sand beach backed by dune
	8	5.833	4.414	8.14	8.38	coarse sand beach backed by moderately high cliffs
	9	5.604	5.788	10.09	10.44	coarse sand beach backed by moderately high cliffs
	10	18.288	5.189	10.46	10.77	coarse sand beach backed by moderately high cliffs
	11	15.733	4.273	11.12	11.61	coarse sand beach backed by moderately high cliffs
	12	16.687	8.049	10.57	11.44	coarse sand beach backed by moderately high cliffs
	13	10.896	5.298	10.1	11.55	coarse sand beach backed by low cliffs
	14	13.796	4.115	10.52	10.62	coarse sand beach backed by moderately high cliffs
	15	15.389	3.664	10.05	10.12	coarse sand beach backed by moderately high cliffs
	16	18.755	5.202	12.23	14.2	coarse sand beach backed by moderately high cliffs
	17	8.195	4.465	10.17	11.06	coarse sand beach backed by moderately high cliffs
	18	16.013	5.443	10.01	10.52	coarse sand beach backed by moderately high cliffs
	19	19.918	7.33	10.62	11.43	coarse sand beach backed by moderately high cliffs
	20	18.321	5.206	10.02	10.24	coarse sand beach backed by moderately high cliffs
	21	20.634	5.332	10.43	11.51	coarse sand beach backed by moderately high cliffs
	22	24.004	4.821	9.55	10.01	coarse sand beach backed by moderately high cliffs
	23	5.895	5.895	9.27	10.36	coarse sand beach backed by moderately high cliffs
	24	7.734	5.823	9.56	10.28	coarse sand beach backed by riprap
	25	6.674	5.007	9.1	9.69	coarse sand beach backed by riprap
	26	9.569	5.198	9.18	9.48	coarse sand beach backed by moderately high cliffs
	27	19.643	3.735	11.39	11.59	coarse sand beach backed by moderately high cliffs
	28	23.601	4.009	11.71	12.04	rocky beach backed by high cliffs
	29	21.048	4.181	10.26	10.77	rocky beach backed by high cliffs
	30	16.663	5.023	7.33	7.64	sand beach backed by moderately high cliffs
	31	15.179	4.519	8.01	8.58	sand beach backed by low bluff
	32	31.548	3.839	10.17	10.27	rocky beach backed by moderately high cliffs
	33	31.948	4.329	10.44	11.38	rocky beach backed by moderately high cliffs
	34	34.153	1.853	15.02	15.28	rocky beach backed by moderately high cliffs
	35	33.985	0.432	12.89	12.95	rocky beach backed by high cliffs
	36	36.718	3.684	9.9	10.07	rocky beach backed by high cliffs
	37	19.206	3.567	7.98	8.54	coarse sand beach backed by high cliffs
	38	24.669	3.749	7.96	8.29	coarse sand beach backed by high cliffs
	39	9.885	3.6	9.88	10.06	coarse sand beach backed by moderately high cliffs
	40	10.97	3.394	8.17	8.41	coarse sand beach backed by sloping wall
	41	12.655	3.219	8.25	8.5	coarse sand beach backed by moderately high cliffs
	42	25.783	3.511	11.28	11.37	coarse sand beach backed by high cliffs
	43	15.497	3.011	10.11	10.24	coarse sand beach backed by moderately high cliffs
	44	23.73	4.008	8.91	9.12	coarse sand beach backed by high cliffs
	45	26.866	4.783	7.4	7.56	coarse sand beach backed by high cliffs
	46	21.069	3.61	7.55	7.95	coarse sand beach backed by high cliffs
	47	37.239	1.995	9.45	9.58	rocky beach backed by high cliffs

Reach	Transect (CURRY)	D_{HIGH} (m)	D_{LOW} (m)	100-Year (m)	500-Year (m)	Description
Gold Beach	48	10.938	6.384	8.93	9.25	coarse sand beach backed by dune and high bluffs
	49	8.217	5.304	9.72	9.92	coarse sand beach backed by dune and high bluffs
	50	9.597	5.215	9.01	9.14	coarse sand beach backed by dune and high bluffs
	51	9.759	5.063	7.55	7.64	coarse sand beach backed by dune
	52	8.451	5.822	7.43	7.51	coarse sand beach backed by dune
	53	4.987	4.141	7.75	7.86	coarse sand beach backed by dune
	54	7.73	5.037	7.99	8.13	coarse sand beach backed by dune
	55	7.488	5.802	7.93	8.09	coarse sand beach backed by dune
	56	6.727	5.16	8.01	8.25	coarse sand beach backed by dune
	57	8.342	5.873	8.34	8.62	coarse sand beach backed by dune
	58	8.191	5.251	7.9	8.06	coarse sand beach backed by dune
	59	6.405	5.278	8.71	8.91	coarse sand beach backed by dune
	60	6.414	5.27	8.58	8.85	coarse sand beach backed by dune
	61	6.817	5.929	10.13	10.53	coarse sand beach backed by dune
Rogue Shore	62	5.3	5.3	8.22	8.81	coarse sand beach backed by dune
	63	4.894	4.8	7.33	7.52	coarse sand beach backed by dune
	64	5.584	5.308	8.99	9.47	coarse sand beach backed by dune
	65	5.211	5.143	8.05	8.48	coarse sand beach backed by dune
	66	5.277	4.299	7.48	7.71	coarse sand beach backed by dune
	67	5.333	4.621	7.02	7.26	coarse sand beach backed by dune
	68	6.106	4.792	7.27	7.56	coarse sand beach backed by dune
	69	6.871	3.818	7.24	7.68	sand beach backed by poor riprap
	70	7.797	4.996	7.68	8.38	coarse sand beach backed by dune
	71	8.944	4.8	7.52	8.06	coarse sand beach backed by dune
	72	6.214	5.215	7.46	7.83	coarse sand beach backed by dune
	73	6.355	4.438	6.53	6.65	coarse sand beach backed by dune
	74	5.547	4.453	6.49	6.7	coarse sand beach backed by dune & high cliff
Nesika Beach	75	24.855	4.094	12.48	12.72	coarse sand beach backed by moderately high bluff
	76	25.739	4.403	10.01	10.31	coarse sand beach backed by moderately high bluff
	77	26.867	4.305	11.33	11.64	coarse sand beach backed by moderately high bluff
	78	22.964	4.334	10.03	10.17	coarse sand beach backed by moderately high bluff
	79	21.675	4.105	12.18	12.26	coarse sand beach backed by moderately high bluff
	80	20.923	4.502	12.57	12.83	coarse sand beach backed by moderately high bluff
	81	15.649	5.22	12.25	12.76	coarse sand beach backed by moderately high bluff
	82	10.082	4.264	12.29	12.58	coarse sand beach backed by moderately high bluff
	83	24.455	5.373	10.28	11.48	coarse sand beach backed by moderately high bluff
	84	21.697	5.025	11.48	12.1	coarse sand beach backed by moderately high bluff
	85	30.639	2.831	11.94	12.09	coarse sand beach backed by riprap wall
	86	9.227	5.834	8.39	8.47	coarse sand beach backed by dune & bluff
	87	12.406	4.299	7.85	8	coarse sand beach backed by low bluff
	88	8.737	6.446	9.22	9.59	coarse sand beach backed by dune
	89	8.661	5.377	7.52	7.65	coarse sand beach backed by dune
	90	7.983	5.293	8.5	8.92	coarse sand beach backed by dune & bluff
	91	7.071	6.915	8.9	9.51	coarse sand beach backed by dune & bluff
	92	6.749	6.387	9.16	9.52	coarse sand beach backed by dune & bluff
	93	6.683	5.238	9.16	9.63	coarse sand beach backed by dune & bluff

Reach	Transect (CURRY)	D_{HIGH} (m)	D_{LOW} (m)	100-Year (m)	500-Year (m)	Description
Port Orford	94	17.803	3.81	9.17	9.41	coarse sand beach backed by moderately high cliffs
	95	6.416	5.127	7.74	7.89	coarse sand beach backed by dune & moderately high cliffs
	96	8.189	5.257	8.04	8.19	coarse sand beach backed by dune & moderately high cliffs
	97	7.718	5.418	8.66	8.93	coarse sand beach backed by dune & low cliffs
	98	7.913	0.958	12.79	12.85	Steep rock platform & seawall at port
	99	8.083	0.533	13.01	13.42	Steep rock platform & seawall at port
	100	16.495	6.888	10.75	11.35	coarse sand beach backed by dune
	101	6.854	5.389	8.36	8.65	coarse sand beach backed by low bluff
	102	12.147	5.327	7.99	8.26	coarse sand beach backed by moderately high bluff
	103	7.589	6.272	9.84	10.39	coarse sand beach backed by moderately high bluff
	104	8.235	7.427	10.01	10.6	barrier beach
	105	8.903	6.375	9.95	10.5	barrier beach
	106	6.466	4.916	8.83	9.17	barrier beach
	107	7.179	5.555	10.49	11.32	barrier beach
	108	7.957	7.141	10.66	11.54	barrier beach
	109	20.22	5.971	10.21	10.62	coarse sand beach backed by moderately high bluff
Brookings Supple-mental	7_13401	4.582	4.23	7.08	7.29	coarse sand beach backed by dune

Notes:

100-year and 500-year total water level (TWL) values relative to NAVD88 vertical datum.

D_{HIGH} is the crest of the dune, bluff, or barrier determined for the eroded profile. *Red text denotes that the crest is overtopped*.

6.4 Overtopping Calculations

Overtopping of natural features such as foredunes, spits and coastal engineering structures and barriers occurs when the wave runup superimposed on the tide exceeds the crest of the foredune or structure (**Figure 6-7**). Hazards associated with wave overtopping can be linked to a number of simple direct flow parameters including (Pullen and others, 2007):

- mean overtopping discharge, q;
- overtopping velocities over the crest and farther landward, V;
- landward extent of green water and splash overtopping $y_{G,\,outer}$; and
- overtopping flow depth, h at a distance y landward of the foredune crest or "barrier."

NHC (2005) notes that there are three physical types of wave overtopping:

1. *Green water or bore overtopping* occurs when waves break onto or over the foredune or barrier and the overtopping volume is relatively continuous;
2. *Splash overtopping* occurs when the waves break seaward of the foredune or barrier, or where the foredune or barrier is high relative to the wave height and overtopping consists of a stream of droplets. Splash overtopping can be a function of its momentum due to the runup swashing up the barrier and/or may be enhanced due to onshore direct winds; and
3. *Spray overtopping* is generated by the effects of wind blowing droplets and spray that are derived from the wave crests.

Mapping these respective flood inundation zones requires an estimate of the velocity, V, the overtopping discharge, q, of the water that is carried over the crest, the inland extent of green water and splash overtopping, and the envelope of the water surface that is defined by the water depth, h, landward of the barrier crest. According to NHC (2005) these hazard zones are ultimately defined based on the following two derivations:

- Base Flood Elevations (BFEs) are determined based on the water surface envelope landward of the barrier crest; and
- Hazard zones are determined based on the landward extent of green water and splash overtopping, and on the depth and flow velocity in any sheet flow areas beyond that, defined as $hV^2 = 5.7\ m^3/s^2$ *or* $200\ ft^3/s^2$.

A distinction can be made between whether green water (or bore) or splash overtopping predominates at a particular location that is dependent on the ratio of the calculated wave runup height relative to the barrier crest elevation, R/Z_C. When $1 < R/Z_C < 2$, splash overtopping dominates and for $R/Z_C > 2$, bore propagation occurs. In both cases, R and Z_C are relative to the 2% dynamic water level ($DWL_{2\%}$) at the barrier (Figure D.4.5-12 in NHC [2005, p. D.4.5-22]).

6.4.1 Mean overtopping rate at the "barrier" crest

Wave overtopping of dunes and barrier is a function of both hydraulic and barrier structure parameters whereby:

$$q = f(H_{mo}, T_p, \beta, F_c, DWL_{2\%}, geometry) \qquad (6.14)$$

where q is the overtopping discharge (expressed as cubic meters per second per meter, $m^3/s/m$ [$ft^3/s/ft$]), H_{mo} is the significant wave height at the toe of the structure, T_p is the peak period, β is the angle of wave attack, F_c is the freeboard, and $DWL_{2\%}$ is 2% dynamic water level at the toe of the structure (**Figure 6-7**).

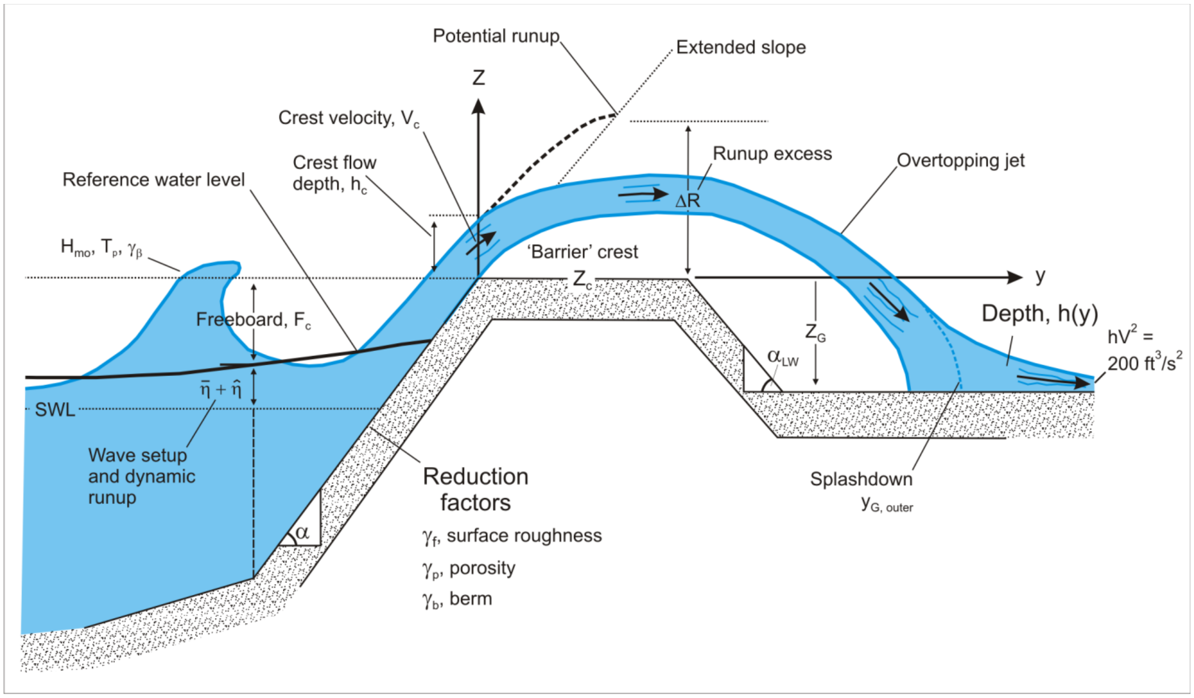

Figure 6-7. Nomenclature of overtopping parameters available for mapping base flood elevations (BFEs) and flood hazard zones (after NHC, 2005).

Prior to calculating the mean overtopping rate at the barrier crest it is necessary to first distinguish between four contrasting types of wave breaking situations that may impact a particular barrier or dune overtopping situation. There four conditions include *non-breaking* or *breaking* on a normally sloped barrier (where $0.067 < \tan\alpha < 0.67$), and *reflecting* or *impacting* on steeply sloping or vertical barriers (where $\tan\alpha \geq 0.67$). Of these, the breaking wave situation is the dominant condition in Curry County, where the waves have already broken across the surf zone and are reforming as bores prior to swashing up the beach face or barrier.

For beaches and normally sloping barriers (where $0.067 < \tan\alpha < 0.67$), a distinction can be made between situations where waves break directly on the barrier versus those conditions where the waves have not yet broken. These conditions can be determined using the surf similarity parameter (Iribarren number) defined here in terms of the beach or structure slope ($\tan\alpha$), and the wave steepness ($S_{op} = H_{mo}/L_o$):

$$\xi_{op} = \frac{tan\alpha}{\sqrt{\frac{H_{mo}}{L_o}}} = \frac{tan\alpha}{\sqrt{S_{op}}} \tag{6.15}$$

Breaking on normally sloping surfaces generally occurs where the surf similarity number, $\xi_{op} \leq 1.8$, while non-breaking conditions occur when $\xi_{op} > 1.8$. As noted above, for the Curry County coastline the identified Iribarren numbers almost always fell below the 1.8 criteria, indicating that the incident waves are always broken prior to reaching the beach or the barrier face.

At the beach or barrier crest, the relative freeboard (F_c/H_{mo}), **Figure 6-7**, is a particularly important parameter because changing these two parameters controls the volume of water that flows over the barrier crest. For example, increasing the wave height or period increases the overtopping discharge, as does reducing the beach or barrier crest height or raising the water level.

A variety of prediction methods are available for calculating the overtopping discharge and are almost entirely based on laboratory experiments based on a range of structure slopes (slopes between 1:1 and 1:8, with occasional tests at slopes around 1:15 or lower). Factors that will serve to reduce the potential overtopping discharge include the barrier *surface roughness* (γ_f), the presence of a *berm* (γ_b), *wave approach directions* (γ_β), and the *porosity* of the barrier (γ_p) (**Figure 6-7**). In terms of porosity, increasing this variable effectively reduces the wave runup and overtopping discharge because more of the water is able to be taken up by the voids between the clasts and particles. As noted by NHC (2005), the effect of the *porosity* factor makes it convenient to distinguish between impermeable and permeable structures. Methods for determining the various reduction factors are described in Table D.4.5-3 in NHC (2005, pD.4.5-13), with one difference whereby the approach recommended for determining the wave approach (γ_β) reduction factor for wave overtopping calculations is based on the following equation:

$$\gamma_\beta = \begin{Bmatrix} 1 - 0.0033|\beta|, (0 \leq |\beta| \leq 80°) \\ 1 - 0.0033|80|, (|\beta| \geq 80°) \end{Bmatrix} \tag{6.16}$$

Table D.4.5-3 in NHC (2005, pD.4.5-13) identifies four general categories of overtopping applications: overtopping on a normally sloping barrier (e.g., riprap structure), steep sloping or vertical barrier (e.g., seawall or bluff where some waves broken); steep sloping or vertical barrier (all waves broken), and shallow foreshore slopes subject to large Iribarren numbers.

For a normally sloping barrier, where $0.05 < \tan\alpha < 0.67$ and the Iribarren number (ξ_{op}) ≤ 1.8 (breaking wave condition), the following formulation can be used to determine the mean overtopping discharge (both dimensional (q) and non-dimensional (Q) forms) at the barrier crest:

$$q = Q\sqrt{\frac{gH_{mo}\tan\alpha}{S_{op}}} \tag{6.17}$$

where:

$$Q = 0.06e^{-4.7F'}$$

and

$$F' = \frac{F_c}{H_{mo}} \frac{\sqrt{S_{op}}}{\tan\alpha} \frac{1}{\gamma_f\gamma_b\gamma_\beta\gamma_p}$$

For non-breaking conditions (Iribarren number (ξ_{op}) > 1.8):

$$q = Q\sqrt{gH_{mo}^3} \tag{6.18}$$

where:

$$Q = 0.2e^{-2.3F'}$$

and

$$F' = \frac{F_c}{H_{mo}} \frac{1}{\gamma_f\gamma_\beta}$$

For steep sloping or vertical barrier, where tan α > 0.67 and h_* ≥ 0.3 (reflecting condition, where

$$h_* = \frac{h}{H_{mo}}\left(\frac{2\pi h}{gT_m^2}\right)$$

and h is the water depth at the structure toe), the following formulation can be used:

$$q = Q\sqrt{gH_{mo}^3} \text{ where:} \qquad (6.19)$$

$$Q = 0.05e^{-2.78F_c/H_{mo}}$$

For impacting conditions (h_* < 0.3):

$$q = Q\sqrt{gh^3}\ h_*^2 \text{ where:} \qquad (6.20)$$

$$Q = 1.37 * 10^{-4}(F')^{-3.24} \text{ and,}$$

$$F' = \frac{F_c}{H_{mo}}\ h_*$$

For steep sloping or vertical barrier (all waves are broken) where the structure toe <$DWL_{2\%}$ water level and where $(F_c/H_{mo})*h_*$ ≤0.03:

$$q = Q\sqrt{gh^3}\ h_*^2 \text{ where:} \qquad (6.21)$$

$$Q = 0.27 * 10^{-4}e^{-3.24\,(F_c/H_{mo})h_*}$$

For steep sloping or vertical barrier (all waves are broken) where the structure toe >$DWL_{2\%}$ water level:

$$q = Q\sqrt{gh^3}\ h_*^2 \text{ where:} \qquad (6.22)$$

$$Q = 0.06e^{-4.7\,F_cS_{op}^{-0.17}}$$

We have implemented two additional overtopping calculations following discussions with Dr. W.G. McDougal, which may be applied to beaches subject to gently sloping (tan β < 0.4), dissipative foreshores:

$$q = Q\sqrt{gh^3}h_*^2 \text{ where:} \qquad (6.23)$$

$$Q = 0.21\sqrt{gH_{mo}^3}e^{-F'} \text{ and}$$

$$F' = \frac{F_c}{\gamma_f\gamma_\beta H_{mo}(0.33 + 0.022\xi_{op})}$$

and cases where there is negative freeboard. The latter occurs when the dynamic water level (DWL2%) is higher than the barrier crest, which produces a negative freeboard (i.e., $-F_c$). In this situation we apply the well-known weir type formula to define the volume of water that is overflowing the crest (Eurotop, 2007). The formulation used is:

$$q = Q_s + q_w \text{ where:} \qquad (6.24)$$

$$Q_s = 0.4583(-F_C)\sqrt{-F_Cg} \text{ and}$$

$$Q_w = 0.21\sqrt{gH_{mo}^3} \text{ and}$$

$$q_w = Q_w\sqrt{gh^3}h_*^2$$

6.4.2 Overtopping limits and flood hazard zones landward of the "barrier" crest

Estimates of the landward limit of the splashdown distance associated with wave overtopping and the landward limit of the hazard zone require several calculation steps. These include:

1. The following three initial parameters are first calculated:
    a. excess potential runup: $\Delta R = R - Z_c$;
    b. crest flow rate, $V_c \cos\alpha$ (where $V_c = 1.1\sqrt{g\Delta R}$ for cases where splash overtopping, and $V_c = 1.8\sqrt{g\Delta R}$ for bore overtopping); and
    c. initial flow depth, h_c (where $h_c = 0.38\Delta R$).
2. The associated onshore wind component, *Wy* is determined from available wind data. For the purposes of this study, we used *Wy* = 19.6 m/s (64.3 ft/s), which was determined from an analysis of winds (mean from a select number of storms) measured at the Cape Arago C-MAN station operated by the NDBC. In the absence of wind data, NHC (2005) recommends a wind speed of *13.4 m/s (44 ft/s)*.
3. The enhanced onshore water velocity component $(V_c \cos\alpha)'$ is then calculated using equation 6.25:

    For vertical bluffs and seawalls; (6.25)

    $$(V_c \cos\alpha)' = 0.3 * W_y$$

    All other cases: $(V_c \cos\alpha)' = V_c \cos\alpha + 0.3(W_y - V_c \cos\alpha)$
4. The effective angle, α_{eff}, is calculated from:

    $$\tan\alpha_{eff} = \frac{V_c sin\alpha}{(V_c cos\alpha)'}.$$
5. Having determined the above parameters, the outer limit of the splash region, $y_{G\ outer}$ is calculated using equation 6.26. Here we have used an algorithm developed by Dr. Bill McDougal (Coastal Engineer, OSU and Technical Coordinator of the North Pacific FEMA West Coast Guidelines) of the form:

$$y_{G\ outer} = \frac{(V_c \cos\alpha)'}{g} * (V_c \sin\alpha - mBackshore * (V_c \cos\alpha)') * \left(1 + \sqrt{1 - \frac{2g * bBackshore}{(V_c \sin\alpha - mBackshore * (V_c \cos\alpha)'^2)}}\right) \tag{6.26}$$

and

$$Z_G = bBackshore + (mBackshore * y_{G\ outer}) \tag{6.27}$$

where *bBackshore* is the intercept for the backshore slope adjacent to the barrier crest and *mBackshore* is the slope of the backshore. Equation 6.26 is ultimately based on Figure D.4.5-15 in NHC (2005, p. D.4.5-30).

6. The total energy, E, of the splashdown is calculated from $E = \Delta R\text{-}Z_G$.
7. Finally, the initial splashdown velocity, V_o (where $V_o = 1.1\sqrt{gE}$), and depth, h_o (where h_o = 0.19E) are calculated. In the case of green water or bore overtopping, the flow depth is determined as $h_o = 0.38E$.

Having determined the initial splashdown velocity, V_o, and flow depth, h_o, the landward extent of the overland flow is calculated using an approach modified from that originally proposed by Cox and Machemehl (1986). The version presented in NHC (2005) effectively calculates the flow depth, h, with distance, y, from the barrier crest, such that the flow depth decays asymptotically as y-distance increases away from the barrier crest, eventually approaching zero. The NHC (2005) equation is shown as equation 6.28:

$$h(y) = \left[\sqrt{h_o} - \frac{5(y - y_o)}{A\sqrt{gT^2}}\right]^2 \quad (6.28)$$

where h_o is determined from step 7 above and for an initial approximation the non-dimensional A parameter may be taken as unity. For sloping backshores, the A parameter in equation 6.28 can be modified such that $A_m = A(1 - 2 * \tan\alpha_{LW})$, and the value in parentheses is limited to the range 0.5 to 2. According to NHC (2005) if the maximum distance of splash or bore propagation calculated using equation 6.28 does not appear reasonable or match field observations, the A parameter can be adjusted in order to increase or decrease the landward wave propagation distance. In addition, for green water or bore propagation the A parameter value is taken, initially, to be 1.8.

For the purposes of this study we have adopted a modified version of equation 6.28 developed by Dr. WG McDougal of the form:

$$h(y) = \left[h_o^{1/2} - \frac{y - y_o}{2\alpha(\alpha+1)^{\frac{3}{2}}\,(1 - 2m)\, g^{0.5}T}\right]^2 \quad (6.29)$$

where m is the slope of the backshore and α is a constant that can be varied in order to increase or decrease the landward wave propagation distance.

Finally, the landward limit of the hazard zone defined as $hV^2 = 5.7\ m^3/s^2$ (or $200\ ft^3/s^2$) is determined, whereby h is the water depth given by the modified Cox and Machemehl (1986) method (equation 6.29) and $V = V_o$ calculated from step 7 above.

6.4.3 Initial testing of the landward limit of wave overtopping

Our initial computations of the landward extent of wave overtopping using the steps outlined above yielded narrow hazard zones for our original coastal FIRM study in Coos County. In order to calibrate equation 6.29, we performed wave overtopping calculations and inundation for a site on the northern Oregon coast, where there are field observations of wave overtopping. The site is Cape Lookout State Park located on the northern Oregon coast in Tillamook County (Allan and others, 2006; Allan and Komar, 2002a; Komar and others, 2003). The southern portion of Cape Lookout State Park is characterized by a wide, gently sloping, dissipative sand beach, backed by a moderately steep gravel berm and ultimately by a low foredune that has undergone significant erosion since the early 1980s (Komar and others, 2000).

On March 2-3, 1999, the crest of the cobble berm/dune at Cape Lookout State Park was overtopped during a major storm; the significant wave heights reached 14.1 m (46.3 ft), while the peak periods were 14.3 seconds measured by a deepwater NDBC wave buoy (Allan and Komar, 2002b). Wave overtopping of the dune and flooding extended ~70 m (230 ft) into the park (P. Komar, Emeritus Professor, College of Oceanic and Atmospheric Sciences, pers. comm., 2010), evidence for which included photos and field evidence including pockmarks at the base of the tree trunks located in the park. These pock-marks were caused by cobbles having been carried into the park from the beach by the overtopping waves, where they eventually slammed into the base of the trees as ballistics. Because the average beach slopes at Cape Lookout State Park are analogous to those observed elsewhere along the Curry County coastline and because large wave events associated with extratropical storms affect significant stretches (100s to 1,000 kilometers) of the coast at any single point in time, we believe these data provide a reasonable means in which to investigate a range of alpha (α) values that may be used to determine the landward extent of wave inundation in the park.

Using beach morphology data (slope [tan β] = 0.089, barrier crest = 5.5 m [18 ft]) from Cape Lookout State Park, and deepwater wave statistics from a nearby NDBC wave buoy (#46050), we experimented with a range of α values (**Figure 6-8**) in order to replicate the landward extent of the inundation. As can be seen in **Figure 6-8**, in order to emulate the landward extent of flooding observed at Cape Lookout our analyses yielded an α of 0.58. Using α = 0.58, we in turn calculated the extent of the hazard zone where $h(y)$ = 200 ft^3/s^2, which was found to be ~34 m from the crest of the cobble berm/dune, consistent with damage to facilities in the park.

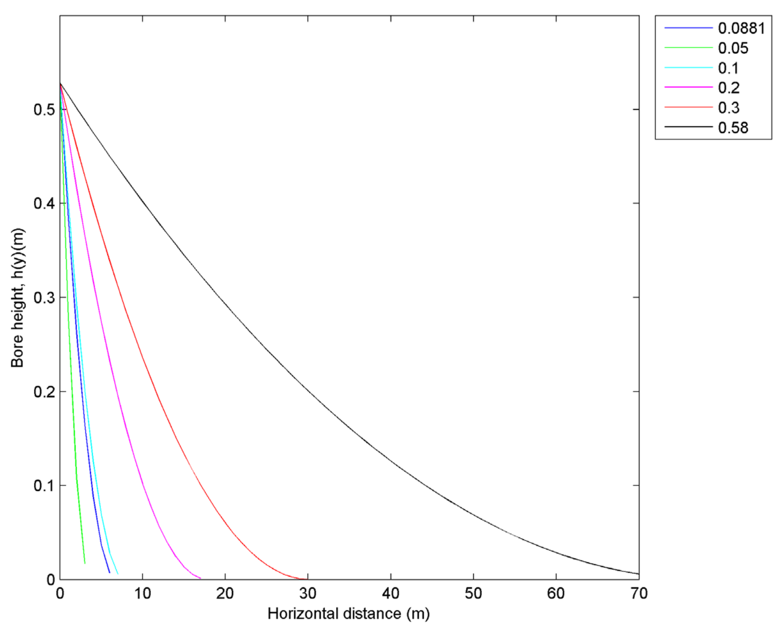

Figure 6-8. Calculations of bore height decay from wave overtopping at Cape Lookout State Park at the peak of the March 2-3, 1999, storm based on a range of alpha (α) values.

Wave overtopping and hazard zone limits calculated for Curry County

Table 6-3 presents the results of the calculated splashdown distances ($y_{G\ outer}$) and the landward extent of the flow (hV^2) where the flows approach 5.7 m^3/s^2 (or 200 ft^3/s^2). **Table 6-3** includes a more conservative splashdown distance, based on an enhanced wind velocity of 19.6 m/s (64.3 ft/s); this contrasts with the default wind speed of 13.4 m/s (44 ft/s) suggested by NHC (2005). This enhanced wind velocity was determined from an analysis of wind speeds measured by the Cape Arago C-MAN station (http://www.ndbc.noaa.gov/station_page.php?station=CARO3) located adjacent to the mouth of Coos Bay (Allan and others, 2012b). Essentially, Allan and others examined the wind speeds identified at Cape Arago for a range of storm events and identified a wide range of values, with a maximum mean wind speed of 19.6 m/s (64.3 ft/s). Because the measured wind speeds reflect a 2-minute average such that higher wind speeds have been measured throughout the entire record (e.g., the maximum 2-minute average wind speed is 29.3 m/s [96 ft/s], while the maximum 5-s wind gust reached 38.1 m/s [125.0 ft/s]), we believe it is justified to use the more conservative enhanced wind velocity of 19.6 m/s (64.3 ft/s). Furthermore, comparisons by Allan and others (2012b) indicated that the relative difference between the value suggested by NHC (2005) and the enhanced wind used here differs by about 30%. As can be seen from the **Table 6-3**, the calculated splashdown distances ($y_{G\ outer}$) indicate splash distances that range from negligible to a maximum of 8.57 m (28 ft); the mean splash distance is 2.0 m (6.7 ft), while the standard deviation is 1.7 m (5.6 ft). Thus, adopting the reduced wind velocity would cause the zones to narrow by ~2.6 m (8 ft) for the highest splash distance. Overall, these differences are negligible given the tremendous uncertainties in calculating splash and overtopping (NHC, 2005).

Hazard zone calculations shown in **Table 6-3** indicate a similarly broad range of values that vary from negligible (i.e., effectively where the 1% TWL intersects with the backshore, plus the width of the splash zone where applicable) to as much as 124 m (406 ft) wide, with the widest zones having occurred where overtopping significantly exceeds the eroded beach crest elevations such as north of Crissey Field and at the port of Port Orford. Qualitative field observations of past storm wave overtopping events at all sites subject to overtopping calculated in this study confirm that this is indeed the case. Hence, field-based observations appear to be consistent with the calibrated results identified in **Table 6-3**. The depth of flooding at each mapped overtopping zone is indicated in **Table 6-4**.

Table 6-3. Splashdown and hazard zone limits calculated for Curry County detailed coastal sites. Values reported in the table reflect the maximum values derived from all the storm runup and overtopping calculations. Note: Dist_3, Dist_2 and Dist_1 reflect the landward extent at which the calculated bore height decreases from 0.9 m (3 ft), to 0.6 m (2 ft) and, finally, to 0.3 m (1 ft). In all cases, the hazard zones are ultimately defined relative to the location of the dune/structure crest.

Profiles	Transect (Curry)	Splashdown $y_{G\ outer}$ (m)	Bore Ht (m)	Dist_3 (≥0.91 m)	Dist_2 (>0.61 <0.91 m)	Dist_1 (≤0.31 m)	hV^2 > $5.7m^3/s^2$ (m)
Brookings	3	2.48	0.3				
	4	0.6	0.48			23.96	44.06
	5	0.25	0.1				
	6	1.57	0.37				18.94
	7	0	0.48			22.98	42.08
	8	0.98	0.44			22.33	42.02
	9	2.76	0.9		33.19	78.31	124.63
	17	5.45	0.64		0.79	8.91	15
	23	1.25	0.64		2.89	38.81	66.33
	24	2.65	0.37			9.34	18.94
	25	4.04	0.49			27.47	50
Gold Beach	49	1.88	0.31			0.89	3.03
	53	1.05	0.51			19.68	35.59
	54	0.88	0.06				
	55	0.28	0.09				
	56	1.46	0.26				
	59	1.03	0.44			20.38	38.42
	60	2.3	0.45			16.24	30.4
	61	2.23	0.64		3.13	43.44	74.28
Rogue Shores	62	1.65	0.56			37.99	66.93
	63	2.41	0.51			30.45	55.06
	64	1.48	0.65		5.08	48.44	82.42
	65	1.4	0.54			32.26	57.3
	66	1.41	0.43			19.92	37.79
	67	1.08	0.33			3.65	8.34
	68	0.83	0.22				
	69	1.55	0.11				
	72	2.07	0.28				
	73	2.05	0.11				
	74	0.03	0.18				
Nesika Beach	82	3.94	0.38			11.03	21.86
	88	1.92	0.14				
	90	0.55	0.1				
	91	0.84	0.34			6.83	14.49
	92	1.64	0.47			23.53	43.51
	93	1.63	0.47			26.46	48.87
Port Orford	95	0.96	0.26				
	97	1.66	0.22				
	98	7.71	1.07	9.86	31.46	59.6	91.79
	99	8.57	1.05	8.55	30.57	59.28	91.68
	101	2.44	0.34			8.05	17.44
	103	0.59	0.42			19.59	37.43
	104	2.61	0.39			13.81	27.2
	105	2.5	0.26				
	106	1.44	0.45			24.03	44.77
	107	2.6	0.63		2.87	47.47	81.31
	108	2.52	0.54			32.72	58.16
Brookings Supplemental	7_13401	1.08	0.48			20.53	37.68

Table 6-4. Depth of flooding at the overtopping zones landward of the structure crest.

Profiles	Transect (Curry)	Dist_3 (≥0.91 m)	Dist_2 (>0.61 <0.91 m)	Dist_1 (≤0.31 m)	$hV^2 > 5.7 m^3/s^2$ (m)	Comments
Brookings	4			0.31	0.31	this transect is not included because it is outside Curry County
	6				0.31	overtopping stops seaward of PFD
	7			0.31	0.31	HV2 mapped landward of PFD
	8			0.31	0.31	narrow D1 added to HV2
	9		0.61	0.31	0.31	D2, D1 and HV2 cut short by topo barrier
	17		0.61	0.31	0.31	narrow D2 added to splashdown; D1 and HV2 cut short by topo barrier
	23		0.61	0.31	0.31	HV2 cut short by topo barrier
	24			0.31	0.31	narrow D1 added to HV2
	25			0.31	0.31	narrow D1 added to HV2
Gold Beach	49			0.31	0.31	overtopping stops seaward of PFD
	53			0.31	0.31	narrow D1 added to HV2
	59			0.31	0.31	
	60			0.31	0.31	narrow HV2 not mapped landward of PFD
	61		0.61	0.31	0.31	PFD cuts through D1 distance
Rogue Shore	62			0.31	0.31	PFD cuts through D1 distance; narrow D1 added to HV2
	63			0.31	0.31	PFD cuts through D1 distance; narrow D1 added to HV2
	64		0.61	0.31	0.31	PFD cuts through D1 distance; narrow D1 added to HV2
	65			0.31	0.31	PFD cuts through D1 distance; narrow D1 added to HV2
	66			0.31	0.31	PFD cuts through D1 distance; narrow D1 added to HV2
	67			0.31	0.31	narrow D1 added to HV2
Nesika Beach	82			0.31	0.31	narrow D1 added to HV2
	91			0.31	0.31	narrow D1 added to HV2
	92			0.31	0.31	HV2 cut short by topo barrier
	93			0.31	0.31	HV2 cut short by topo barrier
Port Orford	98		0.61	0.31	0.31	narrow D3 added to D2; D1 and HV2 cut short by zone break
	99		0.61	0.31	0.31	narrow D3 added to D2; HV2 cut short by zone break
	101			0.31	0.31	narrow D1 added to HV2
	103			0.31	0.31	overtopping stops seaward of PFD
	104			0.31	0.31	overtopping stops seaward of PFD
	106			0.31	0.31	overtopping stops seaward of PFD
	107		0.61	0.31	0.31	HV2 mapped landward of PFD
	108			0.31	0.31	PFD cuts through D1 distance
New Line	7_13401			0.31	0.31	overtopping stops seaward of PFD

Supplemental Transects	7_13427		0.31	0.31	overtopping stops seaward of PFD
	7_13419		0.31	0.31	HV2 mapped landward of PFD
	50_7459	0.61	0.31	0.31	PFD limits overtopping
	50_7429		0.31	0.31	overtopping stops seaward of PFD
	50_7406		0.31	0.31	PFD limits overtopping
	50_7383		0.31	0.31	overtopping stops seaward of PFD
	57_7022		0.31	0.31	overtopping stops seaward of PFD
	58_6970		0.31	0.31	PFD cuts through D1 distance; narrow D1 added to HV2
	58_6965		0.31	0.31	overtopping stops seaward of PFD
	59_6958		0.31	0.31	overtopping stops seaward of PFD
	59_6950		0.31	0.31	overtopping stops seaward of PFD
	59_6934		0.31	0.31	PFD cuts through D1 distance
	59_6927		0.31	0.31	PFD cuts through D1 distance
	71_6560		0.31	0.31	overtopping stops seaward of PFD
	71_6556		0.31	0.31	PFD cuts through D1 distance
	71_6554		0.31	0.31	PFD cuts through D1 distance

7.0 COASTAL EROSION

To estimate beach (or bluff) erosion and the resulting profile changes that occur during a particular storm, it is important to establish first the initial profile conditions that existed prior to that storm. As outlined in Section 3.2, this initial profile morphology is represented by the most likely winter profile (MLWP), which forms the basis for determining profile changes that could eventuate from a particularly severe storm(s). After the MLWP is established for a site, the profile is modified according to the amount of erosion estimated to occur during a specified storm as a result of the increased water levels (tide + surge + ENSO) as well as from wave processes, specifically wave runup. This section explores two approaches described in the revised FEMA guidelines, which may be used to establish the eroded profiles along the Curry County coastline. The second half of the section describes the specific approach adopted for Curry County and the results from our erosion analyses.

7.1 Models of Foredune Erosion

7.1.1 The Komar and others (1999) model

The erosion potential of sandy beaches and foredunes along the Pacific Northwest coast of Oregon and Washington is a function of the total water level produced by the combined effect of the wave runup plus the tidal elevation (E_T), exceeding some critical elevation of the fronting beach, typically the elevation of the beach-dune junction (E_J). This basic concept is depicted conceptually in **Figure 7-1A** based on the model developed by Ruggiero and others (1996), and in the case of the erosion of a foredune backing the beach the application of a geometric model (**Figure 7-1B**) formulated by Komar and others (1999). Clearly, the more extreme the total water level elevation, the greater the resulting erosion that occurs along both dunes and bluffs.

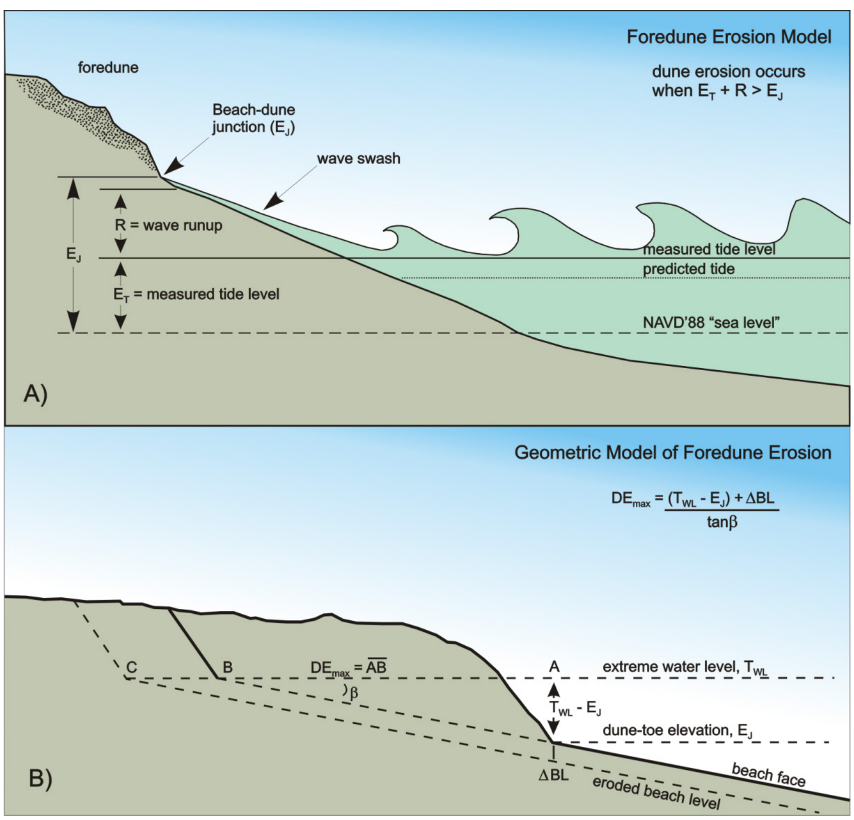

Figure 7-1. A) The foredune erosion model. B) The geometric model used to assess the maximum potential beach erosion in response to an extreme storm (Komar and others, 1999).

As can be seen from **Figure 7-1B**, estimating the maximum potential dune erosion (DE_{MAX}) is dependent on first determining the total water level (TWL) elevation diagrammed in **Figure 7-1A** which includes the combined effects of extreme high tides plus storm surge plus wave runup, relative to the elevation of the beach-dune junction (E_J). Therefore, when the TWL > E_J the foredune retreats landward by some distance, until a new beach-dune junction is established, whose elevation approximately equals the extreme water level. Because beaches along the high-energy Oregon coast are typically wide and have a nearly uniform slope (tan β), the model assumes that this slope is maintained, and the dunes are eroded landward until the dune face reaches point B in **Figure 7-1B**. As a result, the model is geometric in that it assumes an upward and landward shift of a triangle, one side of which corresponds to the elevated water levels, and then the upward and landward translation of that triangle and beach profile to account for the total possible retreat of the dune (Komar and others, 1999). An additional feature of the geometric model is its ability to accommodate further lowering of the beach face due to the presence of a rip current, which has been shown to be important to occurrences on the Oregon coast of localized "hot spot" erosion and property impacts (Komar, 1997). This feature of the model is represented by the beach-level change ΔBL shown in **Figure 7-1B**, which causes the dune to retreat some additional distance landward until it reaches point C. As can be seen from **Figure 7-1B**, the distance from point A to point C depicts the total retreat, DE_{MAX}, expected during a particularly severe storm event (or series of storms) that includes the localized effect enhancement by a rip current. Critical then in applying the model to evaluate the susceptibility of coastal properties to erosion, is an evaluation of the occurrence of extreme tides (E_T), the runup of waves, and the joint probabilities of these processes along the coast (Ruggiero and others, 2001), this having been the focus of Section 6 described previously.

The geometric model gives the maximum potential equilibrium cross-shore change in the shoreline position landward of the MLWP resulting from a storm. However, in reality it is unlikely that this extreme degree of response is ever fully realized, because of the assumptions that had been made in deriving the geometric model with the intent of evaluating the maximum potential dune erosion. As noted by Komar and others (1999), in the first instance the geometric model projects a mean linear beach slope. As a result, if the beach is more concave, it is probable that the amount of erosion would be less, though not by much. Perhaps of greater significance is that the geometric model assumes an instantaneous erosional response, with the dunes retreating landward as a result of direct wave attack. However, the reality of coastal change is that it is far more complex, there in fact being a lag in the erosional response behind the forcing processes. As noted by Komar and others (1999), the extreme high runup elevations typically occur for only a relatively short period of time (e.g., the period of time in which the high wave runup elevations coincide with high tides). Because the elevation of the tide varies with time (e.g., hourly), the amount of erosion can be expected to be much less when the water levels are lower. Thus, it is probable that several storms during a winter may be required to fully realize the degree of erosion estimated by the geometric model; this did, for example, occur during the winter of 1998-99, with the last in the series of five storms having been the most extreme and erosive (Allan and Komar, 2002). In addition, as beaches erode, the sediment is removed offshore (or farther along the shore) into the surf zone where it accumulates in near shore sand bars. This process helps to mitigate the incoming wave energy by causing the waves to break farther offshore, dissipating some of the wave energy, and forming the wide surf zones that are characteristic of the Oregon coast. In turn, this process helps to reduce the rate of beach erosion that occurs. In summary, the actual amount of beach erosion and dune recession is dependent on many factors, the most important of which include the incident wave conditions, the TWL, and the duration of the storm event(s).

7.1.2 The Kriebel and Dean (1993) model

Kriebel and Dean (1993), hereafter known as K&D, developed a dune erosion model that is broadly similar to the Komar and others (1999) geometric model. At its core is the assumption that the beach is in statistical equilibrium with respect to the prevailing wave climate and mean water levels (Bruun, 1962). As water levels increase, the beach profile is shifted upward by an amount equal to the change in water level (S) and landward by an amount R_∞ until the volume of sand eroded from the subaerial beach matches the volume deposited offshore in deeper water (**Figure 7-2**); *note that DE_{MAX} and R_∞ are essentially synonymous with each other*. One important distinguishing feature in the K&D model relative to Bruun (1962) is that it relies on the equilibrium beach profile theory proposed by Dean (1977) to account for the erosion following an increase in the water level. The Dean model is a simplified equilibrium form for open-coast beach profiles expressed as a power-law curve of the form:

$$h = Ax^{2/3} \text{ or equivalently as } x = \left(\frac{h}{A}\right)^{3/2} \tag{7.1}$$

where h is the water depth at a distance x offshore from the still-water level and A is a parameter that governs the overall steepness (and slope) of the profile and is a function of the beach grain size. Thus, incorporating the assumed components of Bruun (1962) and Dean (1977), the maximum erosion potential, R_∞, was determined by K&D to be a function of the increase in mean water level (S) caused by a storm, the breaking wave water depth (h_b), surf zone width (W_b), berm or dune height (B or D), and the slope (β_f) of the upper foreshore beach face. The breaking wave depth (h_b) may be calculated from the wave breaker height (equation 6.8) multiplied by 0.78 (the breaker index).

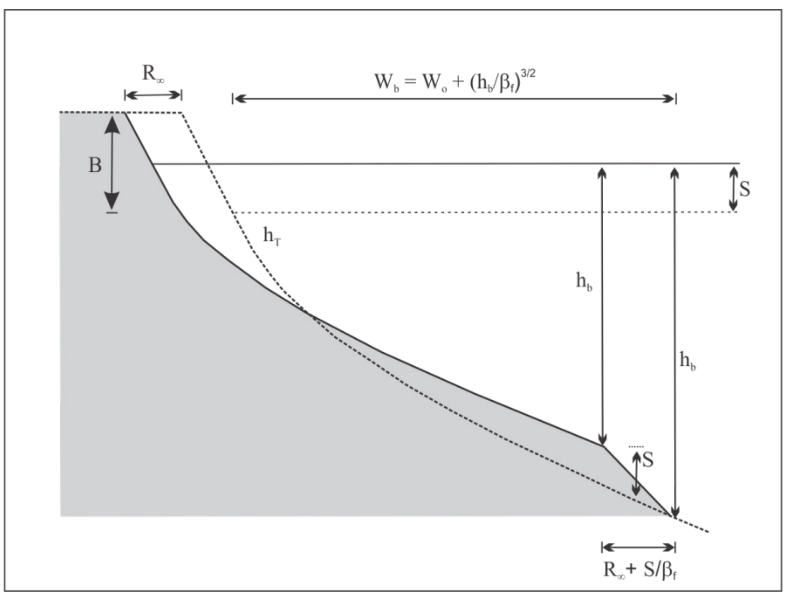

Figure 7-2. Maximum potential erosion (R_∞) due to a change in water levels (after Kriebel and Dean, 1993).

As a result of the above concepts, K&D developed two approaches for determining the maximum erosion potential. These include:

- A beach backed by a low sand berm

$$R_\infty = \frac{S\left(W_b - h_b/\beta_f\right)}{B + h_b - S/2} \qquad (7.2)$$

- A beach backed by high sand dune

$$R_\infty = \frac{S\left(W_b - h_b/\beta_f\right)}{D + h_b - S/2} \qquad (7.3)$$

Like the Komar and others (1999) model, the Kriebel and Dean (1993) dune erosion model estimates the maximum potential erosion (DE_{MAX}) associated with a major storm, and assume that a particular storm will last sufficiently long enough to fully erode the dune. In reality, DE_{MAX} is almost never fully realized because storms rarely last long enough to fully erode the dune to the extent of the model predictions. Because the duration of a storm is a major factor controlling beach and dune erosion, K&D developed an approach to account for the duration effects of storms with respect to the response time scale required to fully erode a beach profile. The time scale for the erosion of a dune to the extent R given by equation (7.2) can be estimated using equation 7.4:

$$T_S = C_1 \frac{H_b^{3/2}}{g^{1/2} A^3} \left(1 + \frac{h_b}{B} + \frac{\beta_f W_b}{h_b}\right)^{-1} \qquad (7.4)$$

where T_S is the time scale of response, C_1 is an empirical constant (320), H_b is the breaker height, h_b is the breaker depth, g is acceleration due to gravity, B is the berm elevation, β_f is the slope of the foreshore, W_b is the surf zone width and A is the beach profile parameter that defines an equilibrium profile. Using equation 7.4 yields typical response times for complete profile erosion that are on the order of 10 to 100 hours [NHC, 2005]. In general, as the surf zone width increases due to larger wave heights, smaller grain sizes or gentler slopes, the response time increases. In addition, the response time will also increase as the height of the berm increases.

The beach profile response is determined by a convolution integral. According to NHC (2005), the time dependency of the storm hydrograph may be approximated by:

$$f(t) = sin^2\left(\pi \frac{t}{T_D}\right) \; for \; 0 < t < T_D \qquad (7.5)$$

where t is time from the start of the storm and T_D is the storm duration. The convolution integral is:

$$DE(t) = \frac{DE_{MAX}}{T_S} \int_0^t f(\tau) e^{-(t-\tau)/T_S} \, d\tau \qquad (7.6)$$

which integrates to:

$$\frac{DE(t)}{DE_{MAX}} = 0.5\left\{1 - \frac{\beta^2}{1+\beta^2}\exp\left(-\frac{t}{T_S}\right) - \frac{1}{1+\beta^2}\left[\cos\left(\frac{2\pi t}{T_D}\right) + \beta\sin\left(\frac{2\pi t}{T_D}\right)\right]\right\} \quad (7.7)$$

where $\beta = 2\pi T_S/T_D$ and DE_{MAX} is the maximum potential recession that would occur if the storm duration was infinite. Thus, if the storm duration, T_D, is long relative to the time scale of profile response, T_S, then a significant portion of the estimated erosion determined by the K&D or geometric model will occur. As the ratio of these two values decreases, the amount of erosion will also decrease. The time required for maximum beach and dune recession is determined by setting the derivative of equation 7.7 to zero and solving for time. This yields:

$$exp\left(-\frac{t_m}{T_D}\right) = cos\left(\frac{2\pi t_m}{T_S}\right) - \frac{T_D}{2\pi T_S}sin\left(\frac{2\pi t_m}{T_S}\right) \quad (7.8)$$

in which t_m is the time that the maximum erosion occurs with respect to the beginning of the storm. Unfortunately, this equation can only be solved by approximation or numerically. Thus the maximum recession associated with a duration limited storm can be calculated by:

$$\alpha = \frac{DE_m}{DE_{MAX}} = 0.5\left[1 - cos\left(2\pi\frac{t_m}{T_D}\right)\right] \quad (7.9)$$

where α is the duration reduction factor and DE_m is the maximum recession that occurs for a given storm duration that occurs at time t_m. As a result, the duration limited recession is:

$$DE_m = \alpha DE_{MAX} \quad (7.10)$$

7.2 Erosion Modeling on Curry County Beaches

In order to determine the duration reduction factor, α, the duration of each storm event has, first, to be identified. The approach used here involved an analysis of the number of hours a specific TWL event was found to exceed a particular beach profile's beach-dune junction elevation, applying the Ruggiero and others (2001) analysis approach. **Figure 7-3** is an example of the approach we used, which is based on a script developed in MATLAB. In essence, the blue line is the TWL time series for a particular profile, ±3 days from the event. The script moves backwards and forwards in time from the identified event until the TWL falls below the critical threshold shown as the black line in **Figure 7-3**, which reflects the beach-dune junction elevation. The duration of the storm was then determined as the period where the TWL exceeds the threshold and includes the shoulders of the event (i.e., when the TWL first falls below the critical threshold). This process was undertaken for every storm and for each of the profile sites. One limitation of this approach that was encountered is that it is possible for the duration to be underestimated if the TWL dips below the threshold for an hour or more and then rises again above the threshold, as seen in the example in **Figure 7-3**.

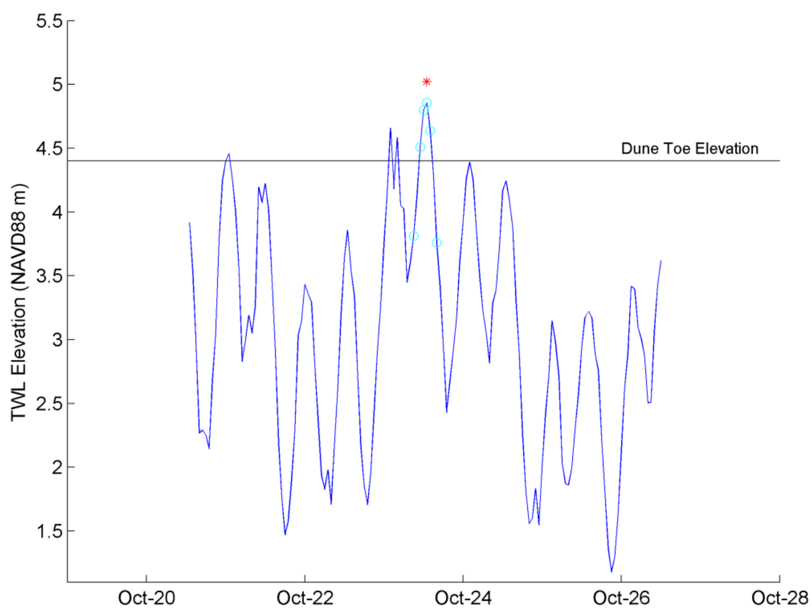

Figure 7-3. Example plot of the approach used to define storm duration along the Coos County shoreline. Note: The red asterisk denotes the location of the storm peak. The blue circles denote the hours when the event exceeded the critical beach-dune junction toe elevation (including the shoulders) that are used to define the "duration" of the event.

As described previously, the breaker height, H_b, was calculated by using equation 6.8 and the breaker depth, h_b, was calculated by using a breaker index of 0.78. The berm elevation was established at 3 m (typical for PNW beaches), while the surf zone width, W_b, was determined for each breaker depth value by interpolating along a profile line of interest (**Figure 7-4**). Although we have grain size information available that could have been used to define the A parameter for Curry County, the approach we took was to iteritively determine an equilibrium A value based on the actual beach profile data. Here we used the profile data seaward to the 8-m (26.3 ft) water depth and a range of A values were fit to the data until a value was found that best matched the profile morphology. This approach was adopted for all the profile sites. **Figure 7-5** presents the alongshore varying dune erosion parameters (beach slope, A, surf zone width, and breaker depth) calculated for each transect site and averaged over every storm. These data are also summarized in **Table 7-1**.

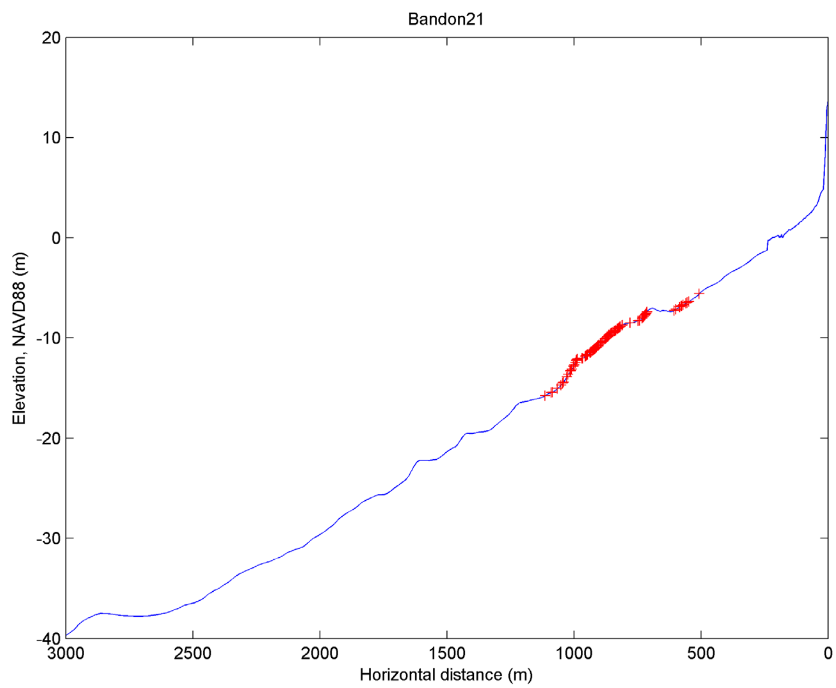

Figure 7-4. Example transect from Coos County showing the locations of h_b, used to define the cross-shore width (W_b) of the surf zone.

Figure 7-6 presents the alongshore varying time scale for the erosion of a dune (T_S), storm duration (T_D), and duration reduction factor (α) values determined for those transect sites characterized as "dune-backed" in Curry County. In all cases, we used the surf zone width, breaking depth, and water levels determined at the respective transect site (along with information pertaining to the site's beach/dune morphology) to calculate T_S and T_D for each storm, while the final parameter, T_m, was solved numerically using equation 7.8 in order to define the duration reduction factor (α). These data have subsequently been averaged for each of the transect locations and are ultimately included in **Table 7-1** and presented in **Figure 7-5** and **Figure 7-6**.

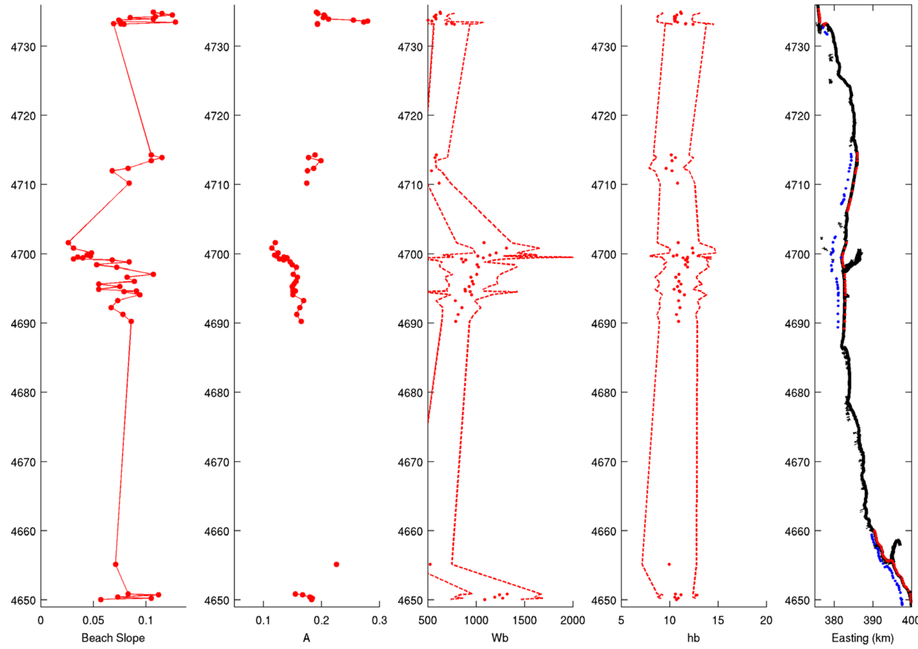

Figure 7-5. Plot showing the dune erosion parameters (tan *β*, *A*, W_b, and h_b) used to calculate the profile responses (T_S), storm durations (T_D), α, and the storm-induced dune erosion. For W_b and h_b we show the mean value and ±1 standard deviation computed using all of the storms.

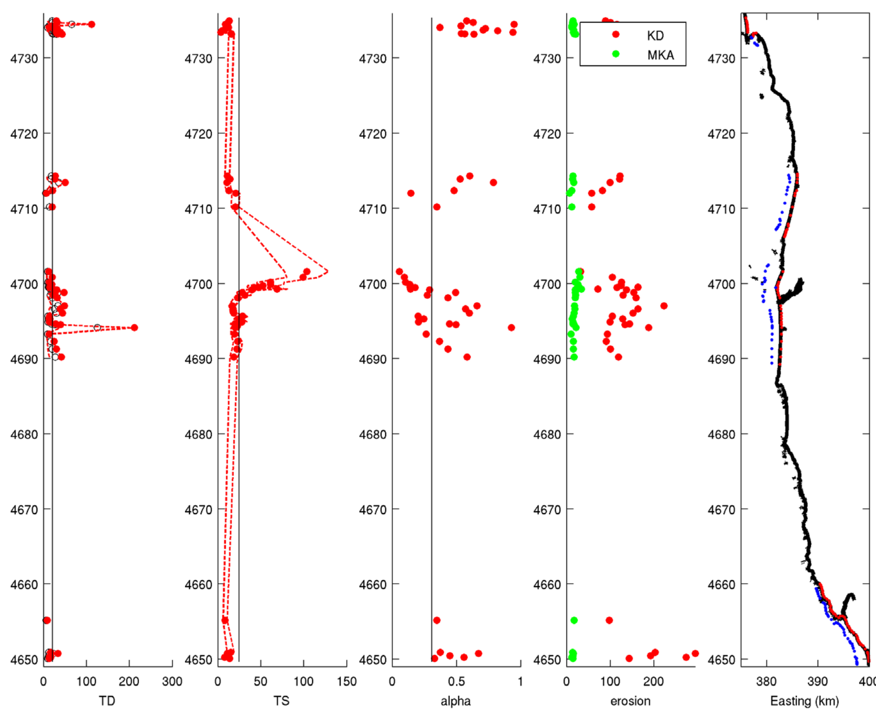

Figure 7-6. Plot showing the storm duration hours (T_D), the calculated time scale of profile response hours (T_S), α, and the storm-induced K&D and geometric model erosion adjusted using equation 7.10 for the dune-backed profiles along the Curry County shore.

Having defined the duration reduction factor (α) for each transect location, the storm-induced erosion was calculated using equation 7.10. As can be seen in **Table 7-1**, calculations of the maximum potential dune erosion (DE_{MAX}) using the Komar and others (1999) geometric model yielded results that are smaller than those derived by the Kriebel and Dean (1993) approach. To reduce the large erosion responses observed at the individual transect sites, we defined an alongshore averaged duration reduction factor (α) of 0.307 (**Table 7-1** and **Table 7-2**), which was used to calculate the final storm-induced erosion (DE_m) at each of the dune-backed transects. This is consistent with the approach adopted elsewhere on Oregon coast.

Using the alongshore averaged duration reduction factor (α), we adjusted the calculated maximum erosion potential, the results of which is presented in the final two columns in **Table 7-1** for both dune-erosion models. As can be seen in the table, the reduced K&D 1% storm erosion ranges from 32.3 to 294.4 m (105.9–966 ft), while the geometric model yields erosion values that range from 6.7 to 33.7 m (22–110.4 ft). A summary of these results is also provided in **Table 7-2**, along with the results from similar calculations determined for Clatsop, Tillamook, and Lincoln counties.

As can be seen in **Table 7-2**, the values for *A*, *TD*, *TS*, and α in Curry County are noticeably different from those values derived from beaches on the central to northern Oregon coast. In particular, the *A* parameter determined for Curry County is ~40–67% larger than the *A* values determined for Clatsop, Tillamook and Lincoln County beaches. This difference is entirely due to the overall steepness (and slope) of the Curry beach profiles (a function of the beach grain size), when compared with beaches on the central to northern Oregon coast. Because *A* is to the third power in the denominator of equation 7.4, used to calculate the time scale (*TS*) for the erosion of a dune, the effect of having a steeper beach produces a lowering of the characteristic response time (T_s) for erosion. This further affects the calculations for *TD* and α and ultimately the calculated reduced storm erosion. (We observed similar issues related to the effect of slope on the calculated *A*, T_D, T_S, and *α* parameters in our original Coos County study.) With these points in mind, it can be seen in **Table 7-2** that the calculated mean K&D reduced erosion is almost an order of magnitude larger than the mean values determined for the central to northern Oregon coast. Furthermore, there is no evidence of erosion of this magnitude having ever occurred from a single storm on the Oregon coast. Instead, measured storm-induced erosion has been found to be about 10-15 m for a single event, derived from actual field observations using both GPS beach surveys and from previous analyses of topographic change data measured using lidar [Allan and Harris, 2012; Allan and Stimely, 2013]. Accordingly, for Curry County we have used the geometric reduced erosion values for adjusting the dune-backed MLWP profile data.

Figure 7-7 and **Figure 7-8** provide two examples where the most eroded winter profile is eroded to reflect the storm-induced erosion values identified in **Table 7-1**. The first example is the CURRY100 profile site where the beach is backed by a prominent foredune. In this example, the calculated duration reduced recession is ~15.1 m (49 ft). The location of the eroded beach-dune junction is depicted in **Figure 7-7** by the magenta circle, while the *eroded winter profile* is shown as the black line. Because the underlying principle of the K&D and geometric models is for the slope to remain constant, the dune is eroded landward by shifting the location of the beach-dune junction landward by 15.1 m (49 ft) and upward to its new location where it forms an erosion scarp (**Figure 7-7**). Because the crest of the foredune (red circle) exceeds the calculated 1% TWL, overtopping does not take place at this particular location. **Figure 7-8** provides an example where dune breaching and overtopping occurs in response to the calculated 1% TWL for the CURRY62 profile site. The calculated dune erosion for CURRY62 is ~19.4 m (64 ft). The location of the eroded beach-dune junction is depicted in **Figure 7-8** by the magenta circle, while the MLWP is shown as the black line. As noted by NHC (2005), when dunes are subject to major overtopping events, breaching of the dune typically results in significant lowering of the dune morphology and the development of an overwash fan on the lee side of the dune. Because the present methodologies are unable to account for such responses, NHC recommends that the dune profile is adjusted by extending the MLWP slope to the backside of the dune. This type of adjustment is demonstrated in **Figure 7-8** where the entire foredune is assumed to be eroded and removed as a result of a major storm.

There are few measured examples of the type of response depicted in **Figure 7-8** on the Oregon coast, with the best having been observed down on the Curry County coast. Monitoring of beaches by DOGAMI on the southern Oregon coast suggest that the approach depicted in **Figure 7-8** is probably reasonable. **Figure 7-9** is an example of beach profile changes measured along the Garrison Lake barrier beach near Port Orford. In this example, the barrier beach, which had a crest elevation of 8-9 m NAVD88 (26–29 ft), is known to have been overtopped during several major storms in February/March 1999 (**Figure 3-19**) (Allan and others, 2003). Analyses of the mean shoreline position at this site indicate that changes in the morphology of the beach is controlled primarily by the occurrence of these major storms as well as by El Niño climate events that result in hotspot erosion. Examination of the beach profile changes along the Garrison Lake shore indicate that during major events characterized by overtopping, the crest of the barrier beach is lowered, with some of the eroded sand having been carried landward where they form washover fans, while the bulk is removed seaward to form sand bars. Ultimately, though, any dune located at the back of the profile is removed entirely, as the barrier rolls landward, consistent with the response depicted in **Figure 7-8**.

Table 7-1. Calculated storm-induced erosion parameters for dune-backed beaches in Curry County. Note: MKA denotes the geometric model and K&D is the Kriebel and Dean model.

Profiles	Transect (CURRY)	A	W_B	T_D	T_S	α	K&D (DE_{MAX})	MKA (DE_{MAX})	K&D (DE_m)	MKA (DE_m)
Brookings	3	0.183	1085.826	12.684	13.798	0.330	466.540	47.818	143.068	14.664
	4	0.184	1274.722	16.621	7.897	0.559	893.830	38.723	274.100	11.875
	5	0.180	1190.224	16.160	11.287	0.447	626.975	46.765	192.267	14.341
	6	0.167	1241.754	33.281	10.781	0.672	960.155	48.831	294.439	14.974
	7	0.155	1318.408	16.365	14.889	0.375	660.679	42.923	202.603	13.163
	23	0.226	523.397	8.312	8.453	0.347	319.026	56.102	97.832	17.204
Gold Beach	49	0.165	788.428	41.713	18.400	0.581	388.250	56.485	119.060	17.322
	50	0.157	813.081	29.973	22.020	0.432	327.836	50.034	100.534	15.343
	51	0.163	850.849	24.652	23.090	0.367	296.503	50.437	90.925	15.467
	52	0.170	782.816	13.079	19.286	0.262	305.465	33.852	93.673	10.381
	53	0.151	950.139	211.396	20.242	0.928	614.060	71.423	188.307	21.903
	54	0.151	938.778	39.748	23.466	0.495	434.519	55.046	133.249	16.880
	55	0.155	887.061	27.951	19.734	0.444	469.697	47.132	144.036	14.454
	56	0.151	883.787	13.784	27.702	0.204	324.886	46.627	99.629	14.298
	57	0.149	925.317	14.993	23.994	0.246	417.417	42.312	128.004	12.975
	58	0.153	970.461	14.158	28.898	0.202	342.432	49.196	105.010	15.086
	59	0.156	958.552	44.368	18.477	0.598	496.322	56.390	152.201	17.292
	60	0.158	945.935	38.386	17.532	0.571	532.131	60.669	163.182	18.605
	61	0.151	1004.068	48.639	16.549	0.658	728.453	58.176	223.386	17.840
Rogue Shores	62	0.157	1024.127	31.339	23.092	0.432	519.445	63.146	159.292	19.364
	63	0.150	1009.816	22.254	31.504	0.271	421.162	67.741	129.153	20.773
	64	0.146	866.020	47.415	28.312	0.492	501.580	65.675	153.814	20.140
	65	0.135	892.552	30.467	39.265	0.291	446.260	63.898	136.849	19.595
	66	0.128	847.740	22.297	68.937	0.141	231.671	109.759	71.044	33.659
	67	0.141	1072.592	17.894	42.683	0.177	374.381	78.517	114.807	24.078
	68	0.135	1454.894	14.777	46.558	0.139	531.764	87.607	163.070	26.865
	70	0.123	1017.038	16.991	52.383	0.142	407.200	88.082	124.871	27.011
	71	0.119	1142.434	18.781	61.023	0.135	406.890	85.667	124.776	26.270
	72	0.125	1205.679	13.867	61.240	0.103	409.747	64.199	125.652	19.687
	73	0.114	1312.487	20.056	98.822	0.093	341.713	98.132	104.789	30.093
	74	0.120	1080.411	12.086	103.276	0.056	105.293	89.109	32.289	27.326
Nesika Beach	86	0.175	614.929	19.633	20.071	0.345	188.173	38.990	57.705	11.957
	88	0.176	536.270	6.818	20.681	0.144	186.991	21.842	57.342	6.698
	89	0.186	498.339	20.618	12.777	0.481	265.829	39.927	81.519	12.244
	90	0.199	477.853	50.213	10.559	0.787	325.584	52.458	99.843	16.087
	91	0.178	574.818	26.392	13.856	0.529	394.766	43.722	121.058	13.408
	92	0.189	587.948	26.873	11.013	0.603	397.780	46.563	121.983	14.279
Port Orford	95	0.193	748.964	30.442	15.574	0.537	297.755	57.318	91.309	17.577
	96	0.193	690.393	33.131	15.555	0.563	278.533	55.335	85.414	16.969
	97	0.193	774.670	43.177	15.866	0.635	364.536	68.559	111.788	21.024
	100	0.273	744.176	39.967	3.491	0.938	340.642	49.132	104.461	15.067
	101	0.279	542.703	26.313	4.833	0.819	246.356	52.891	75.547	16.219
	102	0.255	501.775	26.599	7.647	0.706	153.475	53.703	47.064	16.469
	103	0.212	584.528	31.642	8.459	0.726	349.431	45.772	107.156	14.036
	104	0.203	579.562	13.244	12.216	0.371	225.646	38.010	69.196	11.656
	105	0.206	566.654	18.988	9.789	0.535	265.040	37.178	81.277	11.401
	106	0.204	584.015	111.825	8.885	0.947	374.963	55.089	114.985	16.894
	107	0.194	630.094	31.464	11.841	0.628	326.921	45.104	100.253	13.831
	108	0.192	626.650	29.385	13.081	0.578	289.311	47.520	88.720	14.573
Summary		0.170	825.335	32.972	26.807	0.307	363.879	57.870	111.587	17.746

Note: A is the beach profile parameter that defines an equilibrium profile; W_b is the surf zone width; T_D is the storm duration; T_S is the time scale of response; α is the duration reduction factor.

Table 7-2. Summary storm-induced erosion parameters determined for Oregon coast dune-backed beaches. Note: MKA denotes the geometric model and K&D denotes the Kriebel and Dean model.

County	A	W_b	T_D	T_S	α _100yr	K&D (DE_{MAX})	MKA (DE_{MAX})	K&D (DE_m)	MKA (DE_m)
Clatsop	0.102	1353.892	7.067	102.985	0.033	384.836	49.752	12.777	1.652
Tillamook	0.118	906.214	9.963	75.447	0.047	276.270	58.674	12.912	2.742
Lincoln	0.121	1038.609	11.468	83.462	0.048	339.002	72.610	15.951	3.480
Curry	0.170	825.335	32.972	26.807	0.307	363.879	57.870	111.587	17.746

Note: A is the beach profile parameter that defines an equilibrium profile; W_b is the surf zone width; T_D is the storm duration; T_S is the time scale of response; α is the duration reduction factor.

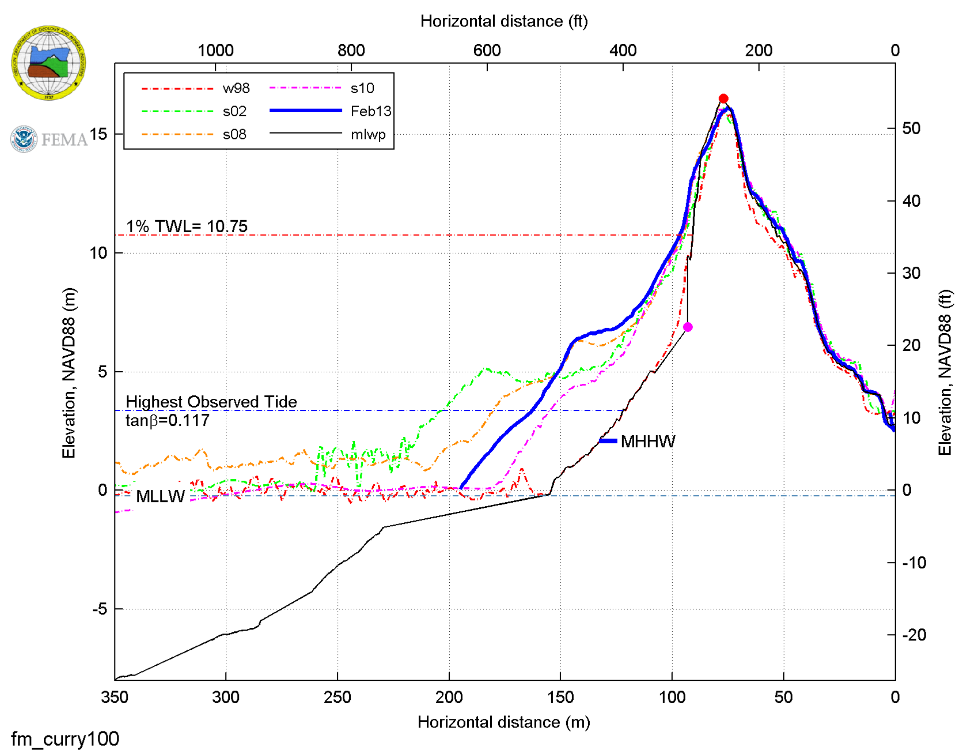

Figure 7-7. Application of the duration reduced erosion estimate to the most likely winter profile (MLWP) at CURRY100.

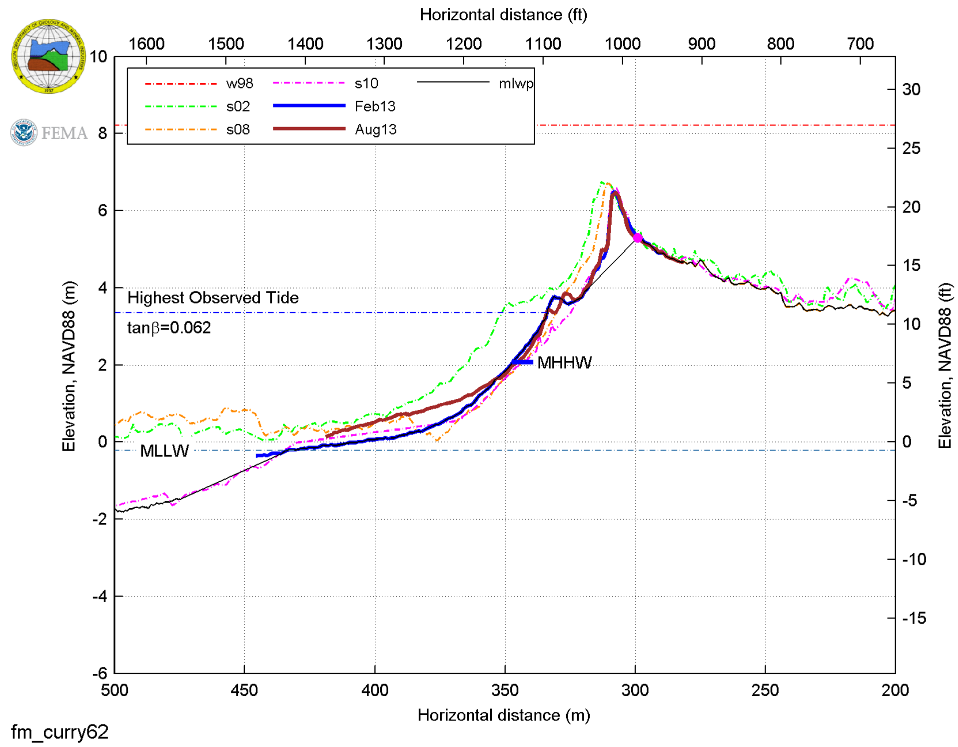

Figure 7-8. Application of the duration reduced erosion estimate to the most likely winter profile *(*MLWP*)* at CURRY62 where overtopping and breaching occurs.

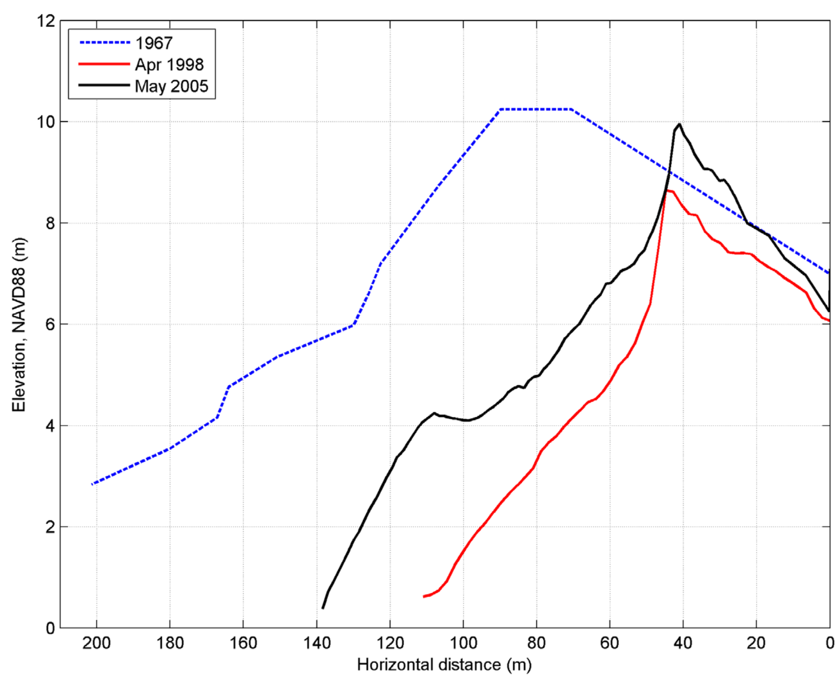

Figure 7-9. Example profile where a barrier beach is overtopped and eroded. This example is based on measured beach profile changes at Garrison Lake, Port Orford, on the southern Oregon coast. The 1967 morphology was derived from Oregon Department of Transportation surveys of the beach on September 25, 1967, used to define the Oregon statutory vegetation line.

8.0 FLOOD MAPPING

8.1 Detailed Coastal Zone VE Flood Zone Mapping

Detailed mapping of the 1% chance flood event within selected areas of Curry County was performed using two contrasting approaches, controlled ultimately by the geomorphology of the beach and backshore. In all cases we followed the methods described in section D.4.9 in the final draft guidelines of the Coastal Flood Hazard Analysis and Mapping for the Pacific Coast of the United States (NHC, 2005). Due to the complexities of each mapping approach for the 1% chance flood event, it was not possible to reasonably map the 0.2% chance event. The reasons for this are described in more detail in the following sections.

8.1.1 Bluff-backed beaches

For bluff-backed beaches the total water level (TWL) values calculated in Section 6.3 were extended into the bluff. The first step involved identifying specific contours of interest, which were extracted from the 1-meter resolution bare earth lidar grid DEM (surveyed in 2008). For the bluff-backed beaches the landward extent of the coastal Zone VE is defined by the contour representing the TWL elevation calculated for each of the represented detailed surveyed transects (e.g., **Figure 8-1** and **Table 6-2**). FEMA Operating Guidance 9-13 (2013) dictates that areas near the landward extent of Zone VE, where the difference between the TWL and ground elevation are less than 3 feet, be designated as Zone AE. However, due to the steepness of the shoreline along bluff-backed beaches such areas are too thin in Curry County to be visible at the prescribed map scale, and therefore Zone AE was not designated in these environments.

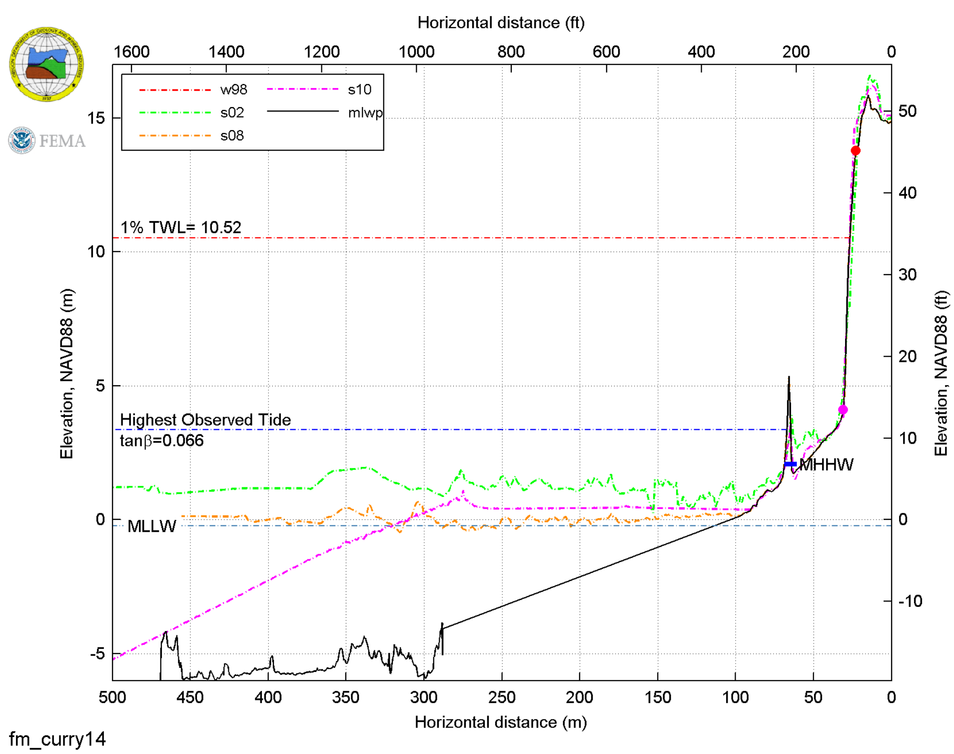

Figure 8-1. Example of a bluff-backed beach (CURRY 14) where the calculated total water level and defined velocity (VE) zone extends into the bluff.

To define the velocity zones between transects, we used professional judgment to establish appropriate zone breaks between the various transects. For example, along-shore geomorphic barriers were identified within which the transect TWL value is valid (**Figure 8-2**). Slope and hillshade derivatives of the lidar DEM, as well as 1-m orthophotos (acquired in 2009), provided the base reference. An effort was made to orient zone breaks perpendicular to the beach at the location of the geomorphic barrier. The seaward extent for the majority of Zone VE was inherited from the preliminary DFIRM (2011). In some cases adopting the effective extent produced inconsistent zone widths (too thin) and the boundaries were subsequently extended seaward.

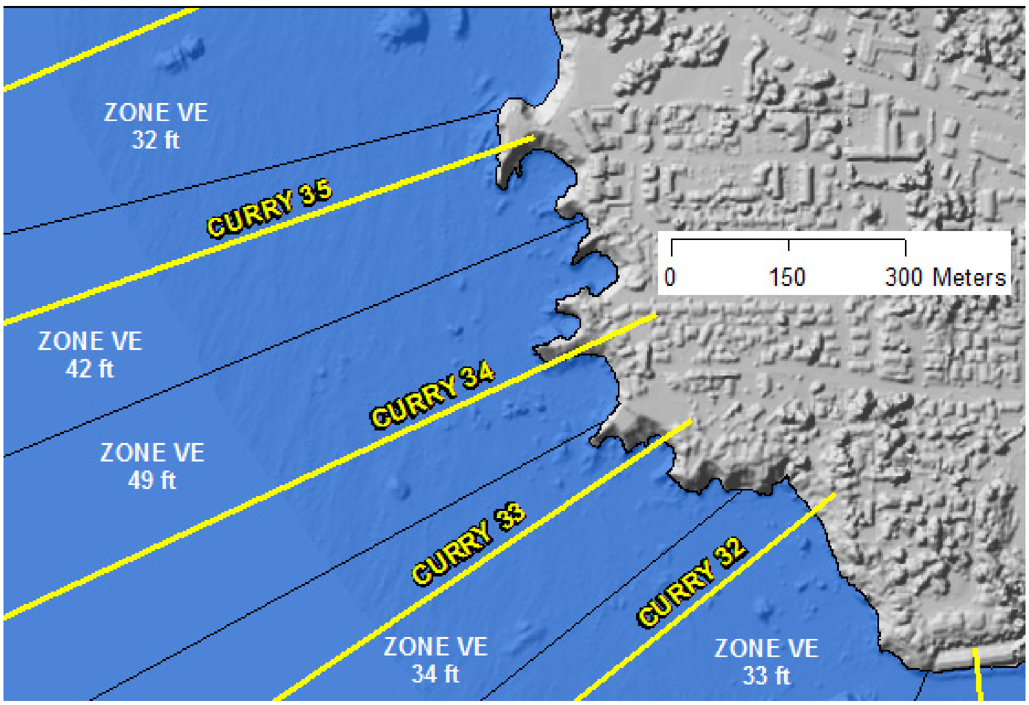

Figure 8-2. Example of along-shore zone breaks and their relationship to geomorphic barriers and surveyed transects. Surveyed transects are symbolized as yellow lines; zone breaks are solid black lines.

8.1.2 Dune-backed beaches

For dune-backed beaches, the VE flood zone was determined according to one or more criteria specified in the NHC (2005) guidelines. These include:

1. The ***wave runup zone***, which occurs where the TWL exceeds the (eroded) ground profile by ≥ 0.91 m (3 ft);
2. The ***wave overtopping splash zone*** is the area landward of the dune/bluff/structure crest where splashover occurs. The landward limit of the splash zone is only mapped in cases where the wave runup exceeds the crest elevation by ≥ 0.91 m (3 ft);
3. The ***high-velocity flow zone*** occurs landward of the overtopping splash zone, where the product of flow times the flow velocity squared (hV^2) is ≥ 5.7 m^3/s^2 (or 200 ft^3/s^2);
4. The ***breaking wave height zone*** occurs where wave heights ≥ 0.91 m (3 ft) could occur and is mapped when the wave crest profile is 0.64 m (2.1 ft) or more above the static water elevation; and
5. The ***primary frontal dune (PFD) zone*** as defined in Part 44 of the U.S. Code of Federal Regulations, Section 59.1; FEMA Coastal Hazard Bulletin, No. 15.

Table 6-3 lists the overtopping calculations for those transects where overtopping occurs, including the calculated splashdown distances ($Y_{G\ outer}$), bore height associated with wave overtopping (h_o) and the landward extent of the high-velocity flow (hV^2) where the flows approach 5.7 m^3/s^2 (or 200 ft^3/s^2). As noted above, hV^2 reflects the furthest point landward of the dune/bluff/structure crest that experiences coastal flooding due to overtopping and is ultimately controlled by the extent of the landward flow where it approaches 5.7 m^3/s^2 (or 200 ft^3/s^2); values greater than 5.7 m^3/s^2 (or 200 ft^3/s^2) are located within the high-velocity flow (VE) zone while lower values are located within the passive overland flooding (AE) zone. Included in **Table 6-3** is the transition zones in which the calculated bore decreases in height, which have been defined accordingly:

- Dist_3 identifies the landward extent of flood zones where the bore height (h_o) was determined to be ≥ 0.91 m (3 ft) and were ultimately rounded up to the nearest whole foot (i.e., having an elevation of 0.91 m (3 ft) above the land surface);
- Dist_2 identifies the landward extent of flood zones where the bore height (h_o) was determined to be between 0.61 and 0.91 m (2 and 3 ft high) and were ultimately rounded up to the nearest whole foot above the ground surface; and
- "Dist_1" marks the seaward extent of flood zones where the bore height falls below 0.3 m (1 ft) above the ground surface; these values were again rounded up to the nearest whole foot.

Areas where flood zones exhibited bore height elevations of 0.61 m (2 ft) above the land surface were inferred as existing in the area between the two previously described regions (i.e., between "Distance from 'x' Where Bore > 2 < 3 ft" and "Distance from 'x' Where Bore < 1").

Similar to the bluff-backed beaches, professional judgment was once again used to establish appropriate zone breaks between the detailed transects. This was achieved through a combination of having detailed topographic information of the backshore and from knowledge of the local geomorphology. Some interpretation was required to produce flood zones appropriate for the printed map scale. Elevations were identified from the 1-m resolution bare-earth lidar DEM to aid in establishing zone breaks due to changes in flood depth landward of the dune crest (**Figure 8-3**). Slope and hillshade derivatives of the lidar DEM, as well as 1-m orthophotos, provided base reference.

In overtopping splash situations, the flood zone was determined by adding the splashdown distances ($Y_{G\ outer}$) to the D_{high} distance. For all overtopping splash situations on the Curry coast, the splash distance was very short and not distinguishable at a mapping scale. Therefore, it was added to the VE zone extent (**Figure 8-4**).

For flood zones seaward of the dune crest, the calculated TWL values were used. As with the bluff-backed beaches, along-shore geomorphic barriers were identified within which the transect TWL value is valid. In all cases, an effort was made to orient zone breaks perpendicular to the beach at the location of the geomorphic barrier. The seaward extent of the flood zones were inherited from the preliminary DFIRM (2011) whenever possible.

The PFD is defined as "a continuous or nearly continuous mound or ridge of sand with relatively steep seaward and landward slopes immediately landward and adjacent to the beach and subject to erosion and overtopping from high tides and waves during major coastal storms. The landward limit of the primary frontal dune, also known as the toe or heel of the dune, occurs at a point where there is a distinct change from a relatively steep slope to a relatively mild slope. The primary frontal dune toe represents the landward extension of the Zone VE coastal high hazard velocity zone" (Part 44 of the U.S. Code of Federal Regulations, Section 59.1, as modified in FEMA Coastal Hazard Bulletin, No. 15, https://www.floodmaps.fema.gov/listserv/ch_jul02.shtml).

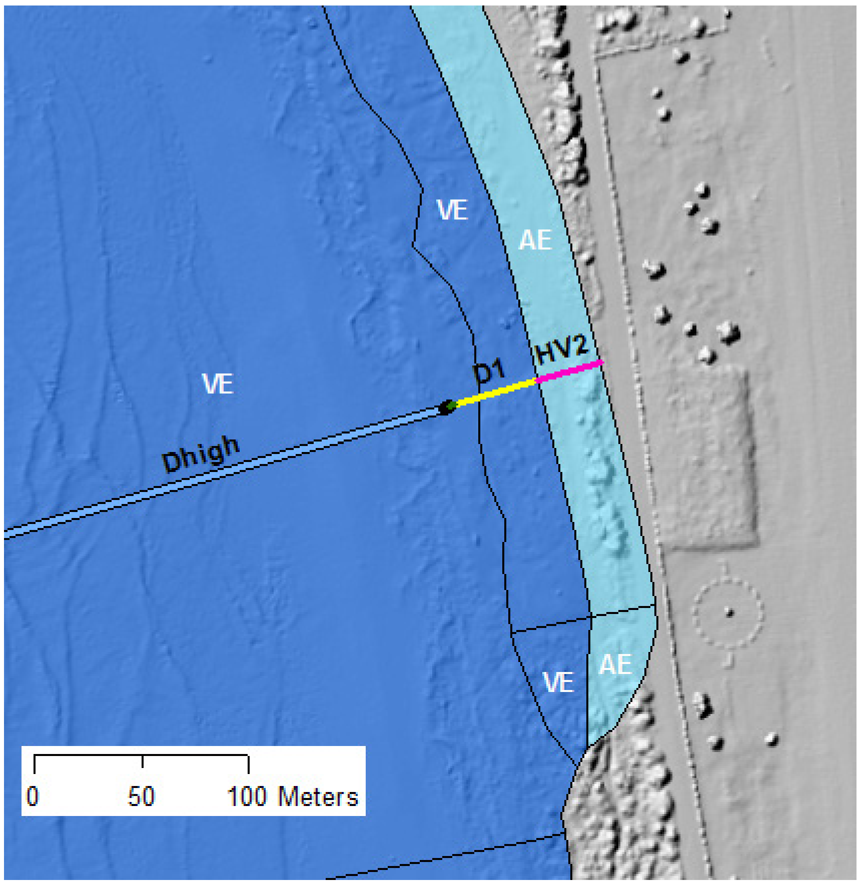

Figure 8-3. Overtopping along the CURRY 61 transect (south of the Rogue River entrance), where Dhigh is the area seaward of Dhigh distance, Splash is the splashdown distance, D1 is depth ≤ 0.31 m, HV2 is flow < 5.7 m^3/s^2 (or 200 ft^3/s^2) . Zone breaks are solid black lines. Dark blue flood zones are VE zones; light blue are AE zones.

The approach developed by DOGAMI to define the morphology of the beach and dune system, including the location of the PFD, follows procedures developed in our Coos Bay study (Allan and others, 2012). The procedure was based on detailed analyses of light detection and ranging (lidar) data measured by the USGS/NASA/NOAA in 1998 and 2002, by DOGAMI in 2009, and by the USACE in 2010. However, because the lidar data flown by the USGS/NASA/NOAA and by the USACE are of relatively poor resolution (~1 point/m²) and reflect a single return (i.e., include vegetation where present), while the lidar data flown by DOGAMI have a higher resolution (8 points/m²) and were characterized by multiple returns enabling the development of a bare-earth DEM, determination of the PFD was based entirely on analysis of the 2008 lidar data.

Lidar data flown in 1998, 2002, and 2010 were downloaded from NOAA's Coastal Service Center (http://coast.noaa.gov/dataregistry/search/collection/info/coastallidar), and gridded in ArcGIS using a triangulated irregular network (TIN) algorithm (Allan and Harris, 2012). Transects spaced 10 m apart were cast for the full length of the county coastline using the Digital Shoreline Analysis System (DSAS) developed by the USGS (Thieler and others, 2009); this process yielded 13,489 individual transects throughout Curry County. For each transect, xyz values for the 1998, 2002, 2008, and 2010 lidar data were extracted at 1-m intervals along each transect line and saved as a text file using a customized ArcGIS script.

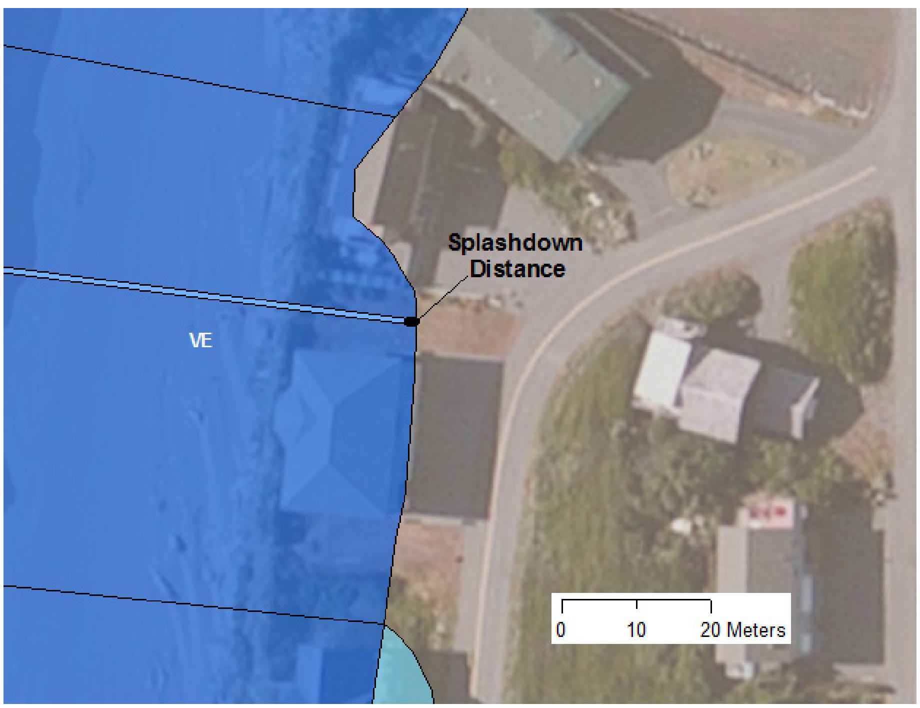

Figure 8-4. CURRY 68 transect (north of the Rogue River entrance) with overtopping Splash zone . The short splash zone distance (black) was added to the extent of Zone VE.

Processing of the lidar data was undertaken in MATLAB using a beach profile analysis script developed by DOGAMI. This script requires the user to interactively define various morphological features including the dune/bluff/structure crest/top, bluff/structure slope, landward edge of the PFD(s), beach-dune juncture elevations for various years, and the slopes of the beach foreshore [Allan and Harris, 2012]. Although we extracted topographic data for all 13,489 transects, not all transects were processed. Instead, we identified discrete sections of the coast characterized as dune-backed and processed just those transects (we eventually used transects spaced 20 m apart) located within each dune-backed section.

Figure 8-5 provides an example from Curry #6424 located north of the Rogue River near the CURRY73 transect site. The profile data reveal the presence of a primary and secondary dune that have formed seaward of a marine terrace. The primary dune is identified as the most seaward of the two dunes and has a crest elevation (2008) of 8.8 m (28.9 ft), while the location of the PFD has been identified for both dunes. Because the 1998, 2002, and 2010 lidar are not bareearth, deviations from the 2009 bare-earth Digital Elevation Model (DEM) highlight the effect of vegetation. As can be seen from **Figure 8-5**, the foredune has prograded seaward by about 7 m (23 ft) since 2002.

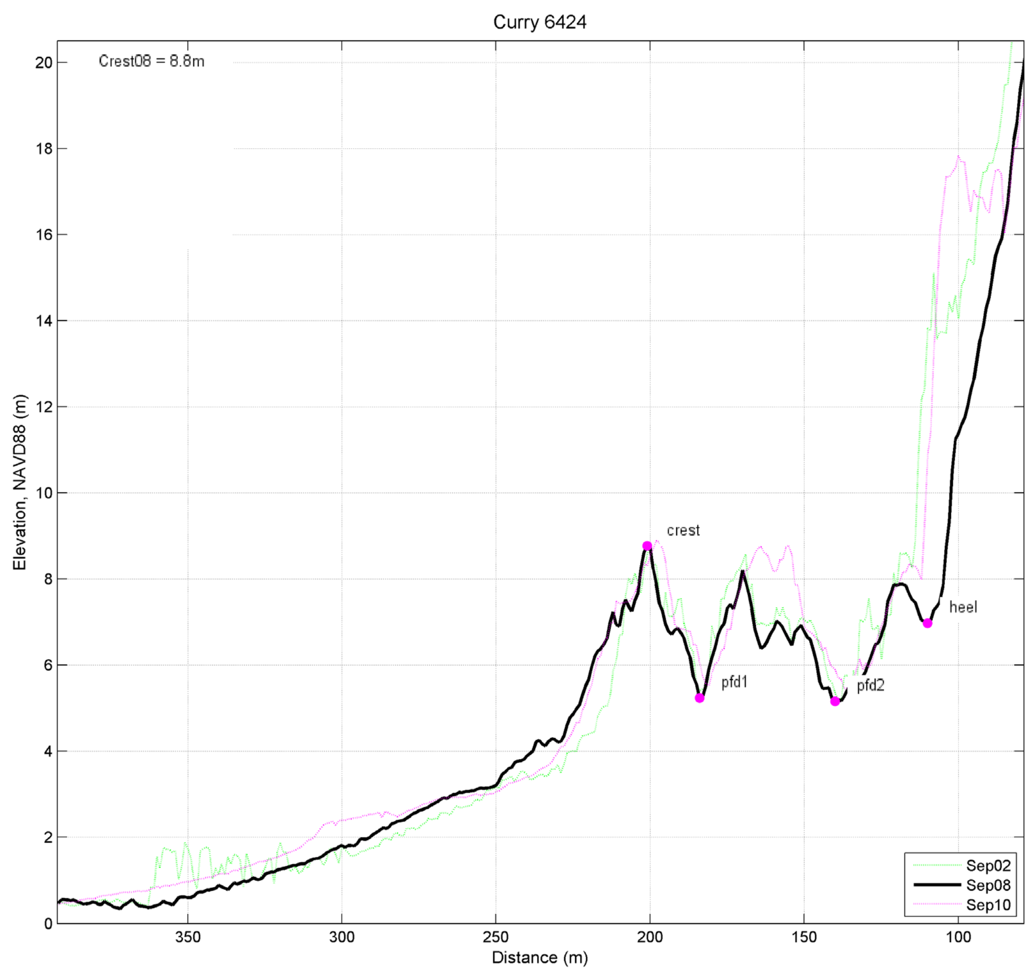

Figure 8-5. Example beach profile (#6424) located near the CURRY73 transect (Rogue Shores area) and derived from 2008 lidar data.

After the lidar transect data had been interpolated to define various morphological parameters, the actual locations of the PFDs were plotted in ArcGIS and overlaid on both current and historical aerial photos of the county and on shaded relief imagery derived from the 2008 lidar. In many cases, multiple PFD locations were defined along a single transect. In a number of locations the PFD was found to be located either farther landward or seaward relative to adjacent PFD locations. This response is entirely a function of the degree to which the morphology of foredunes vary along a coast, and further the ambiguity of defining the PFD as defined above in the FEMA definition. Our observations of the PFD approach highlighted a number of uncertainties, including:

1. There were numerous examples of smaller dune features that have begun to develop in front of a main dune (or are the product of erosion of the dune), but have not yet attained dimensions and volumes where they would be considered an established dune or may continue to erode and could disappear entirely. However, the PFD approach does not adequately account for such features. In this example, the smaller dunes are almost certainly subject to erosion and periodic over-topping, and have morphologies that resemble the FEMA PFD definition. However, because they are subject to short-term erosion responses they are more ephemeral in nature and thus it is debatable whether they should be defined as PFDs. Furthermore, over the life of a typical map (~10 years) these dunes could be eroded and removed entirely leaving a "gap" between the original polygon boundary and the eroding dune. For example, from repeated observations of beach profile transects on the northern Oregon coast, storms have been documented to remove as much as 9–25 m (30–82 ft) of the dune (Allan and Hart, 2007, 2008);
2. The PFD does not adequately account for a large established foredune, where the dune may have attained heights of 10-15 m (33–49 ft), with cross-shore dimensions on the order of 100-200 m (328–656 ft) wide due to prolonged aggradation and progradation of the beach. In this example, although there may be a clear landward heel located well inland away from the beach (e.g., profile #840 in **Figure 8-6**, which was derived from our Clatsop County study), the PFD is clearly not subject to "frequent" wave over-topping due to its height and erosion (because of its large volume of sand). Defining the PFD at the location of the heel is consistent within the definition provided by FEMA, but would almost certainly generate a very conservative V-zone.
3. Although numerous transects exhibited clear examples of single PFD locations, many others were characterized by more than one PFD (e.g., **Figure 8-5**).

To account for these variations and uncertainties, the PFD shown on the profile plots (e.g., **Figure 8-5**) were re-examined and adjustments were made where necessary in order to define a single PFD line. For example, in a few locations the PFD extent for a particular transect was physically moved so that it was more in keeping with the adjacent PFD locations to its immediate north and south and the lidar bare-earth DEM. As can be seen in **Figure 8-7**, the final PFD designation varied somewhat from the initial mapping, often representing the clearest signal determined from all available data and adhering best to the FEMA definition

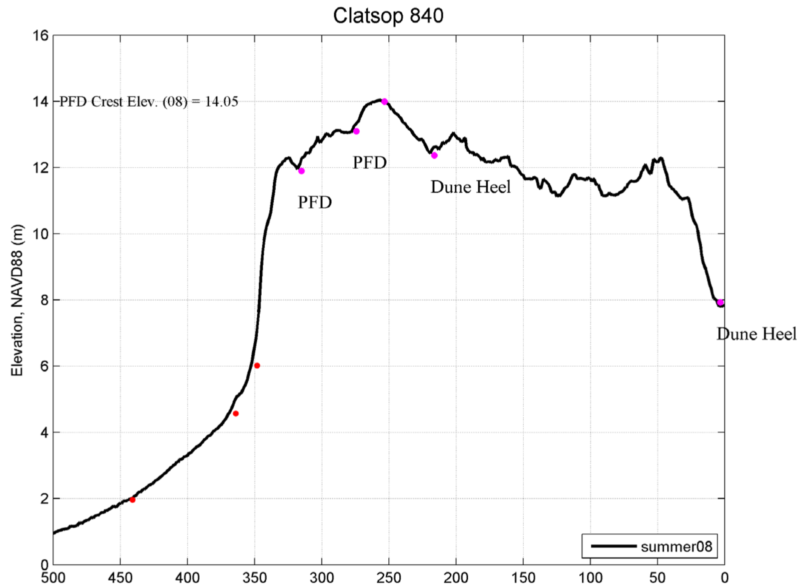

Figure 8-6. Example profile from the Clatsop Plains where considerable aggradation and progradation of the dune has occurred. In this example, the PFD could conceivably be drawn at a variety of locations and meet the FEMA definition.

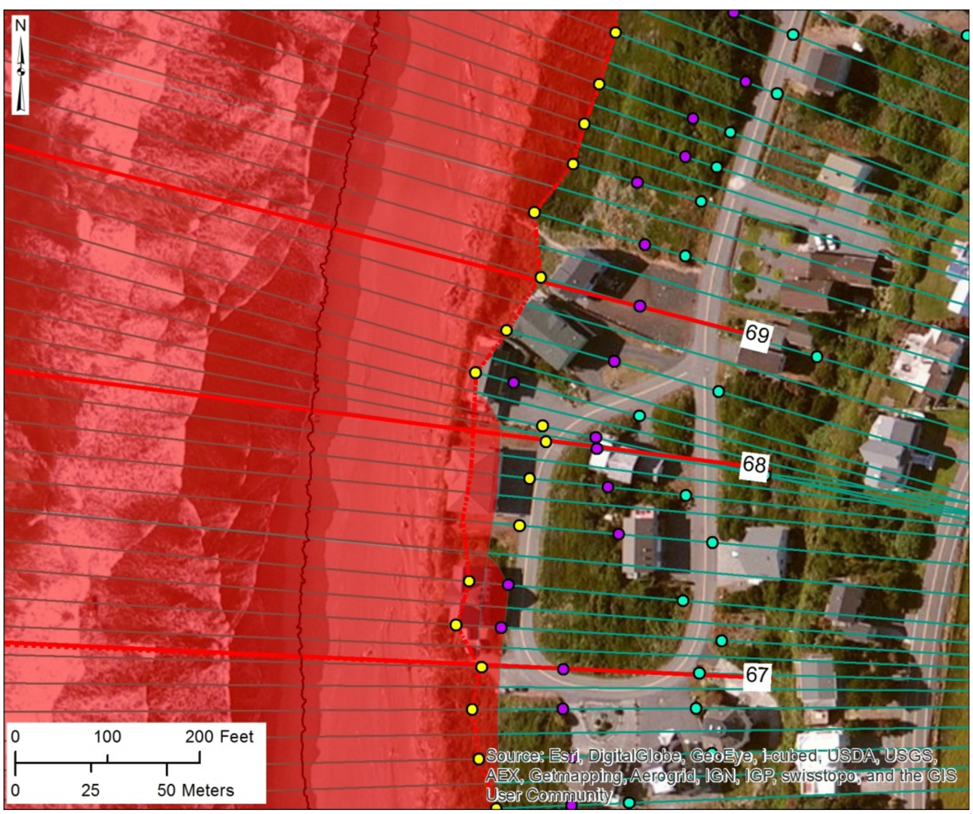

Figure 8-7. Plot showing identified PFD locations (yellow and magenta dots) along each transect, landward most dune heel (cyan dots), and derived PFD line (red dashed line) in the Rogue Shores area. Red zone depicts the VE zone having accounted for all possible criteria. Green lines depict the locations of the lidar transects, which were spaced 10 m (33 ft) apart.

8.1.3 Mapping of estuarine flooding

Curry County does not possess significant estuaries where the still water level (SWL) could be used for large areas of mapping. The SWL was used to map only two small areas: at the mouths of the Pistol River and the Elk River (**Figure 8-8**). The 1% SWL value for the Curry coast is 3.39 m (11.1 ft, NAVD88) and 0.2% SWL is estimated to be 3.56 m (11.7 ft, NAVD88). The area between the jetties at the mouth of the Rogue River was redelineated to the previously effective BFE (**Figure 8-9**). On the Chetco River mouth DOGAMI delineated an Approximate zone to replace the 2009 A zone. This flood zone has coastal influence because the 11.1ft SWL was used at the bottom of the reach, while the known water surface elevation of 15.9 ft from the detailed riverine study was used at the upstream end of the reach. This A zone is a gradual transition between the SWL elevation and the Chetco detailed riverine elevation upstream (**Figure 8-10**).

8.2 Coastal V-Zone Mapping along the Curry County Shoreline

8.2.1 Dune-backed beaches

The FEMA guidelines provide little direct guidance for mapping approximate coastal velocity zones (Zone V) in areas where no detailed studies have occurred, other than by defining the location of the PFD, using the methodology described above. In the case of Curry County, many dune-backed areas were very remote and did require detailed mapping. The PFD in these areas defined the landward limit of the approximate V zone.

8.2.2 V-zone mapping on coastal bluffs and headlands

Coastal bluffs and cliffs of varying heights characterize much of the Curry County coastline. For these areas, the approach adopted by DOGAMI was to map the top of the active bluff (**Figure 8-11**) that is most likely subject to wave erosion, which is a readily identifiable feature that can be used to constrain the landward extent of the Zone V. **Figure 8-11** depicts the derived bluff top line based on a synthesis of all available information, including the analyses of lidar contours, hillshades, and orthophotos. On large bluffs where no clear bluff top could be defined within a reasonable distance of the source of flooding, the 51ft contour was used as the landward extent of the V zone. The V zone mapping approach was used for the shorelines between the northern boundary of Brookings and the southern boundary of Gold Beach, between Euchre Creek and the southern boundary of the of Port Orford, Port Orford Heads State Park, and between Garrison Lake and the northern boundary of Curry County.

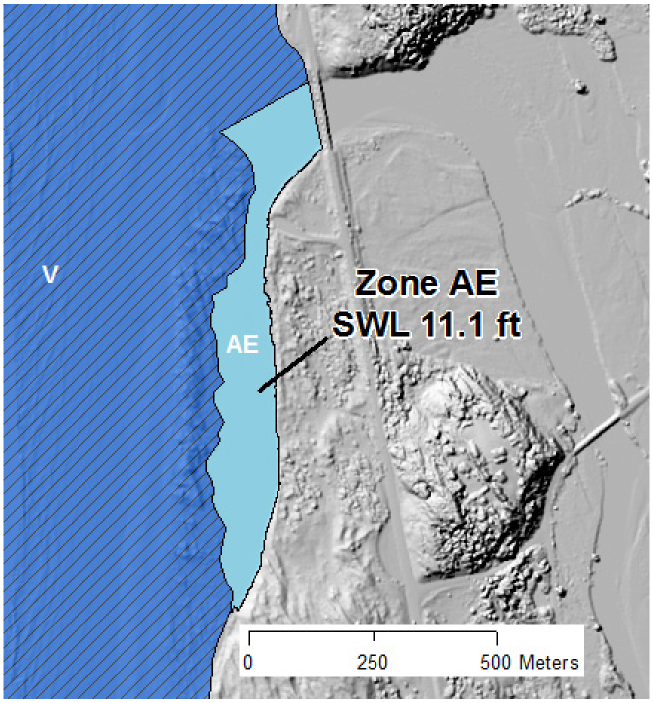

Figure 8-8. Coastal SWL near the mouth of the Pistol River. The 0.2% chance flooding is too small to map.

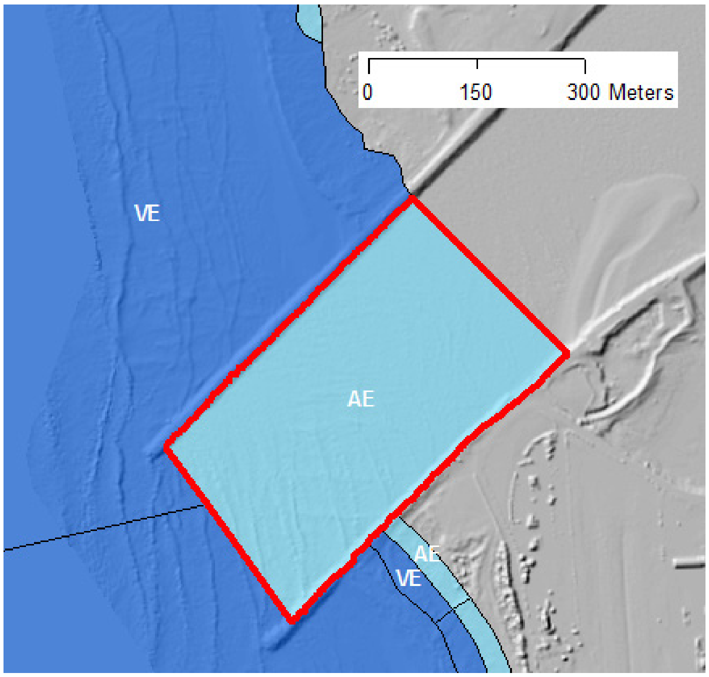

Figure 8-9. Redelineation at the mouth of the Rogue River. The red line outlines the redelineation.

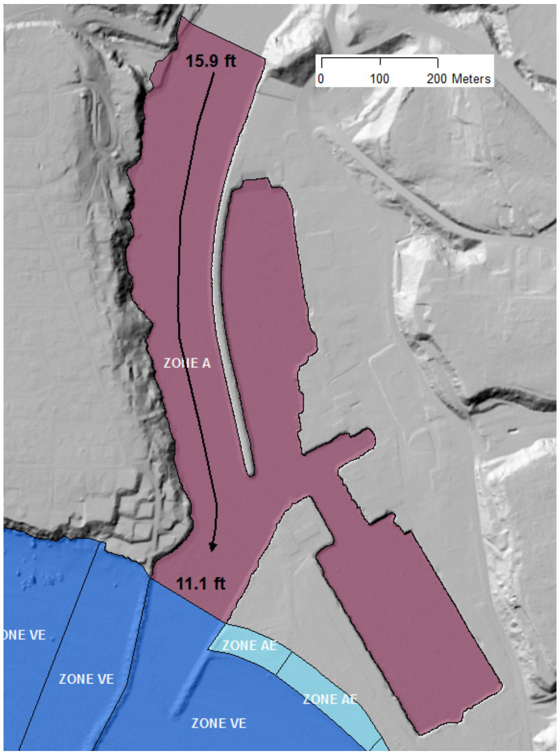

Figure 8-10. Revised A zone on the mouth of the Chetco River. The zone transitions from the SWL at the downstream end to meet the detailed riverine redelineation upstream.

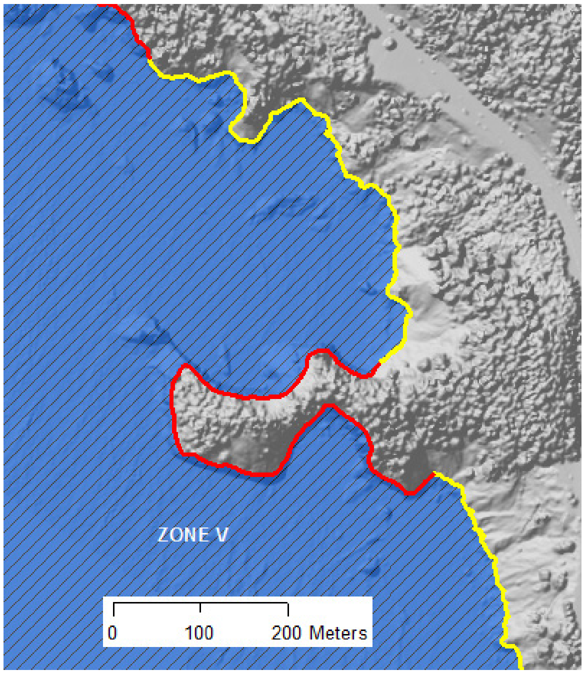

Figure 8-11. Zone V mapping example showing a section of V between Brookings and Gold Beach . The red line represents the defined top of the bluff and the yellow line represents the 51-ft contour. The 51-ft contour was used on large bluffs where no bluff top could be defined within a reasonable distance of the ocean.

9.0 ACKNOWLEDGMENTS

Funding for this study was provided by the Federal Emergency Management Agency as part of the Flood Map Modernization program under Cooperating Technical Partner award EMS-2011-GR-0013. We are grateful to Dr. Bill McDougal for his technical advice throughout this project. We would especially like to acknowledge Nicole Walker from Atkins Global and Dr. Paul Komar for their insightful reviews of the report.

10.0 REFERENCES

Aguilar-Tunon, N.A., and Komar, P.D., 1978, The annual cycle of profile changes of two Oregon beaches: Ore Bin, v. 40, no. 2, p. 25-39.

Allan, J.C., and Komar, P.D., 2002, Extreme storms on the Pacific Northwest Coast during the 1997-98 El Niño and 1998-99 La Niña: Journal of Coastal Research, v. 18, no. 1, p. 175-193.

Allan, J.C., Komar, P.D., and Priest, G.R., 2003, Shoreline variability on the high-energy Oregon coast and its usefulness in erosion-hazard assessments, *in* Byrnes, M.R., Crowell, M., and Fowler, C., eds., Shoreline mapping and change analysis: Technical considerations and management implications: Journal of Coastal Research, Special Issue No. 38, p. 83-105.

Allan, J.C., 2005, Evaluation of coastal change and the potential for erosion during extreme storms at Crissey Field, southern Oregon coast: Oregon Department of Geology and Mineral Industries Open-File Report O-05-12.

Allan, J.C., Hart, R., and Geitgey, R., 2005, Dynamic revetments for coastal erosion stabilization: A feasibility analysis for application on the Oregon Coast: Oregon Department of Geology and Mineral Industries Special Paper 37, 71 p.

Allan, J.C., and Komar, P.D., 2006, Climate controls on U.S. West Coast erosion processes: Journal of Coastal Research, v. 22, no. 3, p. 511-529.

Allan, J.C., and Hart, R., 2007, Assessing the temporal and spatial variability of coastal change in the Neskowin littoral cell: Developing a comprehensive monitoring program for Oregon beaches: Oregon Department of Geology and Mineral Industries Open-File Report O-07-01, 27 p.

Allan, J.C., and Hart, R., 2008, Oregon beach and shoreline mapping and analysis program: 2007-2008 beach monitoring report: Oregon Department of Geology and Mineral Industries Open-File Report O-08-15, 60 p.

Allan, J.C., Komar, P.D., and Ruggiero, P., 2011, Storm surge magnitudes and frequenciy on the central Oregon coast, *in* Solutions to Coastal Disasters 2011, Anchorage, Alaska, American Society of Civil Engineers, p. 53-64.

Allan, J.C., and Harris, E.L., 2012, An "expanded" geospatial database of beach and bluff morphology determined from LIDAR data collected on the northern Oregon coast; Tillamook to Clatsop County: Oregon Department of Geology and Mineral Industries Open-File Report O-12-08, 23 p.

Allan, J.C., Komar, P.D., Ruggiero, P., and Witter, R.C., 2012a, The March 2011 Tōhoku tsunami and its impacts along the U.S. West Coast: Journal of Coastal Research, v. 28, no. 5, p. 1142-1153.

Allan, J.C., Ruggiero, P., and Roberts, J.T., 2012b, Coastal flood insurance study, Coos County, Oregon: Oregon Department of Geology and Mineral Industries Special Paper 44, 132 p.

Allan, J.C., and Stimely, L., 2013, Oregon Beach Shoreline Mapping and Analysis Program: Quantifying short to long-term beach and shoreline changes in the Gold Beach, Nesika, and Netarts littoral cells: Oregon Department of Geology and Mineral Industries Open-File Report O-13-07, 46 p.

Atwater, B.F., Satoko, M.-R., Satake, K., Yoshinobu, T., Kazue, U., and Yamaguchi, D.K., 2005, The orphan tsunami of 1700—Japanese clues to a parent earthquake in North America: U.S. Geological Survey Professional Paper 1707, 144 p.

Baird & Associates, 2005, Pacific Ocean wave information study: Validation of wave model results against satellite altimeter data. Prepared for U.S. Army Corp of Engineers, Engineering Research and Development Center, Vicksburg, Miss.: Madison, Wisconsin, 13 p.

Beaulieu, J.D., and Hughes, P.W., 1976, Land use geology of western Curry County, Oregon: Oregon Department of Geology and Mineral Industries, 148 p. [Bulletin 90].

Bernstein, D.J., Freeman, C., Forte, M.F., Park, J.-Y., Gayes, P.T., and Mitasova, H., 2003, Survey design analysis for three-dimensional mapping of beach and nearshore morphology, *in* Fifth International Symposium on Coastal Engineering and Science of Coastal Sediment Processes (Coastal Sediments '03), Clearwater Beach, Fla., American Society of Civil Engineers, p. 12.

Booij, N., Ris, R.C., and Holthuijsen, L.H., 1999, A third-generation wave model for coastal regions, Part I: Model description and validation: Journal of Geophysical Research, v. 104, no. C4, p. 7649-7666.

Boon, J.D., 2004, Secrets of the tide: Tide and tidal current analysis and predictions, storm surges and sea level trends: Cambridge, U.K., Woodhead Publishing, 224 p.

Bruun, P., 1962, Sea level rise as a cause of shore erosion: Journal of Waterways, Harbors Division, Amer. Soc. Civil Engrs., v. 88, p. 117-130.

Carignan, K.S., Taylor, L.A., Eakins, B.W., Warnken, R.R., Sazonova, T., and Schoolcraft, D.C., 2009, Digital elevation model of Port Orford, Oregon: Procedures, data sources and analysis NOAA Technical Memorandum NESDIS NGDC-21, 38 p.

Clemens, K.E., and Komar, P.D., 1988, Oregon beach-sands compositions produced by the mixing of sediments under a transgressing sea: Journal of Sedimentary Petrology, v. 58, no. 3, p. 519-529.

Coles, S., 2001, An introduction to statistical modeling of extreme values: London, Springer-Verlag, 208 p.

Davis, R.E., and Dolan, R., 1993, Nor'easters: American Scientist, v. 81, p. 428-439.

Dean, R.G., 1977, Equilibrium beach profiles: U.S. Atlantic and Gulf Coasts; Ocean Engineering Technical Report No. 12: Newark, Del., University of Delaware, Department of Civil Engineering and College of Marine Studies, 45 p.

Goldfinger, C., Nelson, C.H., and Johnson, J.G., 2003, Holocene earthquake records from the Cascadia Subduction Zone and Northern San Andreas fault based on precise dating of offshore turbidites: Annual Review of Earth and Planetary Sciences, v. 31, p. 555-577.

Goldfinger, C., 2009, Paleoseismically derived probabilities for Cascadia great earthquakes [abs.]: Geological Society of America Abstracts with Programs, v. 41, no. 7, p. 520.

Goldfinger, C., and others, 2009, Turbidite event history: methods and implications for Holocene paleoseismicity of the Cascadia subduction zone Professional Paper 1661-F.

Grothe, P.R., Taylor, L.A., Eakins, B.W., Carignan, K.S., Caldwell, R.J., Lim, E., and Friday, D.Z., 2011, Digital Elevation Models of Crescent City, California: Procedures, Data Sources and Analysis: Department of Commerce NOAA Technical Memorandum NESDIS NGDC-51, 31 p.

Hedges, T.S., and Mase, H., 2004, Modified Hunt's equation incorporating wave setup: Journal of Waterway, Port, Coastal, and Ocean Engineering, v. 130, no. 3, p. 109-113.

Jennings, R., and Shulmeister, J., 2002, A field based classification scheme for gravel beaches: Marine Geology, v. 186, p. 211-228.

Kelsey, H.M., Nelson, A.R., Hemphill-Haley, E., and Witter, R.C., 2005, Tsunami history of an Oregon coastal lake reveals a 4600 yr record of great earthquakes on the Cascadia subduction zone: Geological Society of America Bulletin, v. 117, no. 7/8, p. 1009-1032.

Komar, P.D., Torstenson, R.W., and Shih, S.-M., 1991, Bandon, Oregon: Coastal development and the potential for extreme ocean hazards: Shore & Beach, v. 59, no. 4, p. 14-22.

Komar, P.D., 1997, The Pacific Northwest Coast: Living with the shores of Oregon and Washington:

Durham and London, Duke University Press, 195 p.

Komar, P.D., 1998a, Beach processes and sedimentation (2nd ed.): Englewood Cliffs, New Jersey, Prentice Hall, Inc., 544 p.

Komar, P.D., 1998b, The 1997-98 El Niño and erosion on the Oregon coast: Shore & Beach, v. 66, no. 3, p. 33-41.

Komar, P.D., McDougal, W.G., Marra, J.J., and Ruggiero, P., 1999, The rational analysis of setback distances: Applications to the Oregon coast: Shore & Beach, v. 67, p. 41-49.

Komar, P.D., Allan, J.C., and Ruggiero, P., 2011, Sea level variations along the U.S. Pacific Northwest Coast: Tectonic and climate controls: Journal of Coastal Research, v. 27, no. 5, p. 808-823.

Mori, N., Takahashi, T., Yasuda, T., and Yanagisawa, H., 2011, Survey of 2011 Tohoku Earthquake Tsunami Inundation and Run-up: Geophysical Research Letters, v. 38, no. L00G14, p. 6.

Morton, R.A., Leach, M.P., Paine, J.G., and Cardoza, M.A., 1993, Monitoring beach changes using GPS surveying techniques: Journal of Coastal Research, v. 9, no. 3, p. 702-720.

Northwest Hydraulic Consultants, Inc. (NHC), 2005, Final draft guidelines for coastal flood hazard analysis and mapping for the Pacific Coast of the United States, report prepared for FEMA: West Sacramento, Calif., Northwest Hydraulic Consultants, Inc., 344 p.

Oceanweather Inc., 2010, Global Reanalysis of Ocean Waves Fine Northeast Pacific Hindcast (GROW-FINE NEPAC): Oceanweather Inc., 39 p.

Ozkan-Haller, H.T., Allan, J.C., Barth, J.A., Haller, M.C., Holman, R.A., and Ruggiero, P., 2009, Baseline observations and modeling for the Reedsport wave energy site: Oregon State University and the Oregon Department of Geology and Mineral Industries on behalf of Oregon Wave Energy Trust, 35 p.

Peterson, C.D., Darienzo, M.E., Hamilton, D., Pettit, D.J., Yeager, R.K., Jackson, P.L., Rosenfeld, C.L., and Terich, T.A., 1994, Beach-shoreline database, Pacific Northwest Region, USA: Oregon Department of Geology and Mineral Industries Open-File Report O-94-2, 29 p.

Priest, G.R., Allan, J.C., and Sonnevil, R., 2004, Evaluation of coastal erosion hazard zones from Sisters Rocks to North Gold Beach, Curry County, Oregon: Technical report to Curry County: Oregon Department of Geology and Mineral Industries Open file report O-04-20 [Technical report to Curry County].

Priest, G.R., Goldfinger, C., Wang, K., Witter, R.C., Zhang, Y., and Baptista, A.M., 2010, Confidence levels for tsunami-inundation limits in northern Oregon inferred from a 10,000-year history of great earthquakes at the Cascadia subduction zone: Natural Hazards, v. 54, p. 27-73.

Pullen, T.A., Allsop, N.W.H., Bruce, T., Kortenhaus, A., Schuttrümpf, H., and van der Meer, J.W., 2007, EurOtop - wave overtopping of sea defences and related structures: Assessment manual, 193 p.

Ris, R.C., Booij, N., and Holthuijsen, L.H., 1999, A third-generation wave model for coastal regions, Part II: Verification: Journal of Geophysical Research, v. 104, no. C4, p. 7667-7681.

Ruggiero, P., Komar, P.D., McDougal, W.G., and Beach, R.A., 1996, Extreme water levels, wave runup and coastal erosion, *in* Proceedings of the 25th International Conference on Coastal Engineering, Sept. 2-6, 1996, Orlando, Fla., American Society of Civil Engineers, p. 2793-2805.

Ruggiero, P., and Voigt, B., 2000, Beach monitoring in the Columbia River littoral cell, 1997-2000: Coastal Monitoring & Analysis Program, Washington Department of Ecology Publication No. 00-06-026, 113 p.

Ruggiero, P., Komar, P.D., McDougal, W.G., Marra, J.J., and Beach, R.A., 2001, Wave runup, extreme water levels and the erosion of properties backing beaches: Journal of Coastal Research, v. 17, no. 2, p. 407-419.

Ruggiero, P., Holman, R.A., and Beach, R.A., 2004, Wave run-up on a high-energy dissipative beach: Journal of Geophysical Research, v. 109, p. C06025.

Ruggiero, P., Kaminsky, G.M., Gelfenbaum, G., and Voight, B., 2005, Seasonal to interannual morphodynamics along a high-energy dissipative littoral cell: Journal of Coastal Research, v. 21, no. 3, p. 553-578.

Ruggiero, P., Buijsman, M.C., Kaminsky, G.M., and Gelfenbaum, G., 2010a, Modeling the effects of wave climate and sediment supply variability on large-scale shoreline change: Marine Geology, v. 273, p. 127-140.

Ruggiero, P., Komar, P.D., and Allan, J.C., 2010b, Increasing wave heights and extreme value projections: The wave climate of the U.S. Pacific Northwest: Coastal Engineering, v. 57, no. 5, p. 539-552.

Ruggiero, P., Kratzmann, M.G., Himmelstoss, E.A., Reid, D., Allan, J., and Kaminsky, G., 2013, National Assessment of Shoreline Change: Historical Shoreline Change along the Pacific Northwest coast (Oregon and Washington): U.S. Geological Survey Open-File Report 2012-1007, 62 p.

Satake, K., Shemazaki, K., Yoshinobu, T., and Ueda, K., 1996, Time and size of a giant earthquake in Cascadia inferred from Japanese tsunami records of January 1700: Nature, v. 379, no. 6562, p. 246-249.

Smith, J.M., Sherlock, A.R., and Resio, D.T., 2001, STWAVE: Steady-state spectral wave model user's manual for STWAVE, Version 3.0: U.S. Army Engineer Research and Development Center, Coastal and Hydraulics Laboratory Technical Report ERDC/CHL SR-01-1, 81 p.

Soler, T., Weston, N.D., and Foote, R.H., 2011, The "Online Positioning User Service" suite (OPUS-S, OPUS-RS, OPUS-DB), *in* Soler, T., ed., CORS and OPUS for Engineers: Tools for Surveying and Mapping Applications Reston, Va., American Society of Civil Engineers, p. 17-26.

Stockdon, H.F., Holman, R.A., Howd, P.A., and Sallenger, A.H., 2006, Empirical parameterization of setup, swash, and runup: Coastal Engineering, v. 53, no. 7, p. 573-588.

Thieler, E.R., Himmelstoss, E.A., Zichichi, J.L., and Ayhan, E., 2009, Digital Shoreline Analysis System (DSAS) version 4.0—An ArcGIS extension for calculating shoreline change: U.S. Geological Survey Open-File Report 2008-1278.

Tillotson, K., and Komar, P.D., 1997, The wave climate of the Pacific Northwest (Oregon and Washington): A comparison of data sources: Journal of Coastal Research, v. 13, no. 2, p. 440-452.

Trimble, 2005, Trimble 5700 GPS system datasheet: Dayton, Ohio, Trimble Navigation Limited, Engineering & Construction Group, p. 2.

van der Meer, J.W., 2002, Technical report wave run-up and wave overtopping at dikes: Deflt, Netherlands, Technical Advisory Committee on Flood Defence, Road and Hydraulic Engineering Institute, 50 p.

Witter, R.C., Kelsey, H.M., and Hemphill-Haley, E., 2003, Great Cascadia earthquakes and tsunamis of the past 6700 years, Coquille River estuary, southern coastal Oregon: Geological Society of America Bulletin, v. 115, p. 1289-1306.

Witter, R.C., 2008, Prehistoric Cascadia tsunami inundation and runup at Cannon Beach, Clatsop County, Oregon: Oregon Department of Geology and Mineral Industries Open-File Report O-08-12, 36 p.

Witter, R.C., Zhang, Y.J., Goldfinger, C., Priest, G.R., and Wang, K., 2010, Validating numerical tsunami simulations in southern Oregon using late Holocene records of great Cascadia earthquakes and tsunamis [abs.]: Seismological Research Letters, v. 81, no. 2, p. 290.

Wright, L.D., and Short, A.D., 1984, Morphodynamic Variability of Surfzones and Beaches: A Synthesis.: Marine Geology, v. 56, p. 93-118.

Yamamoto, M., 2011, Tōhoku Tsunami March 11, 2011 as of 30 March 2011: United Nations Educational, Scientific and Cultural Organization, Intergovernmental Oceanographic Comission IOC/UNESCO Bulletin No. 13.

Zhang, K., Douglas, B.C., and Leatherman, S., 2001, Beach erosion potential for severe nor'easters: Journal of Coastal Research, v. 17, no. 2, p. 309-321.

11.0 APPENDICES

Appendix A: Ground Survey Accuracy Assessment Protocols

Appendix B: Curry County Beach and Bluff Profiles

11.1 Appendix A: Ground Survey Accuracy Assessment Protocols

See report by Watershed Sciences, Inc., dated May 27, 2009.

11.2 Appendix B: Curry County Beach and Bluff Profiles

11.2.1 Brookings

fm_curry 1

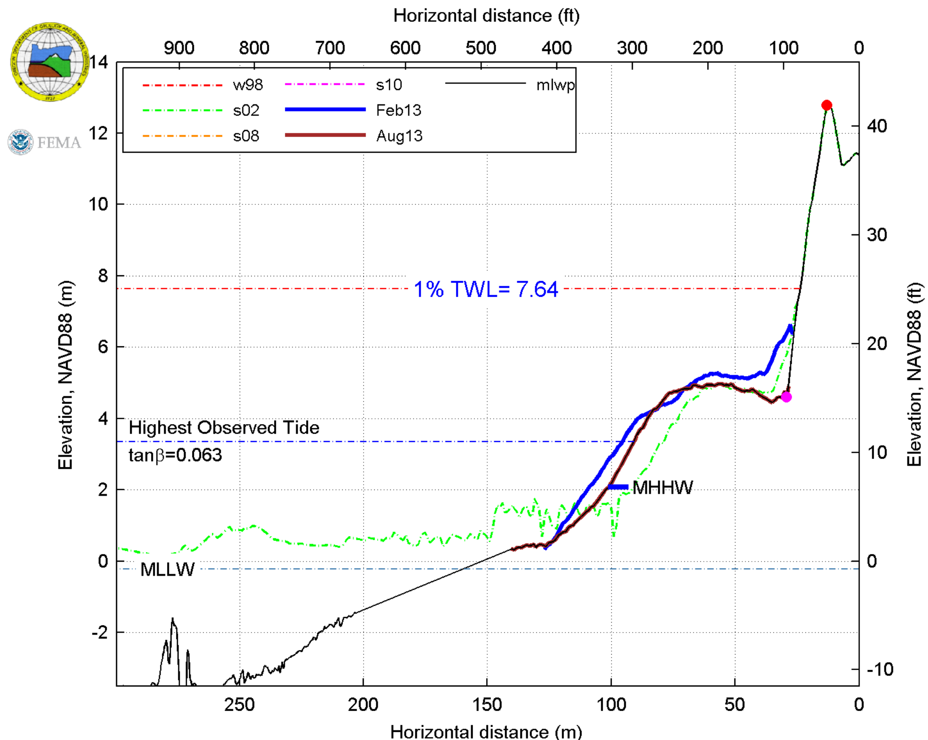

fm_curry1

fm_curry 2

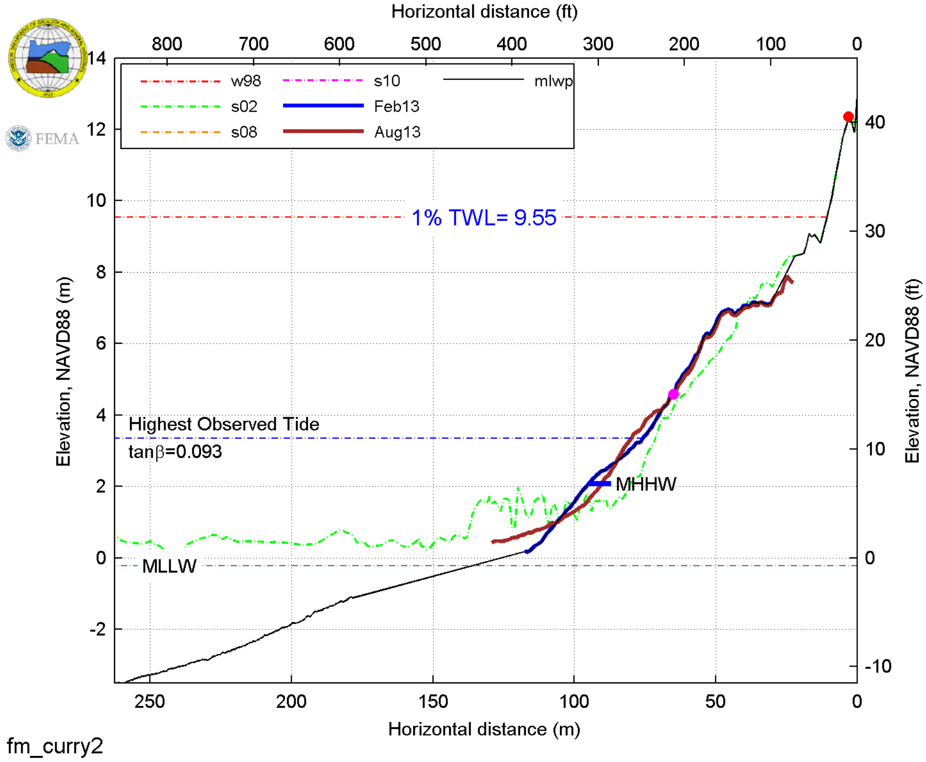

fm_curry 3

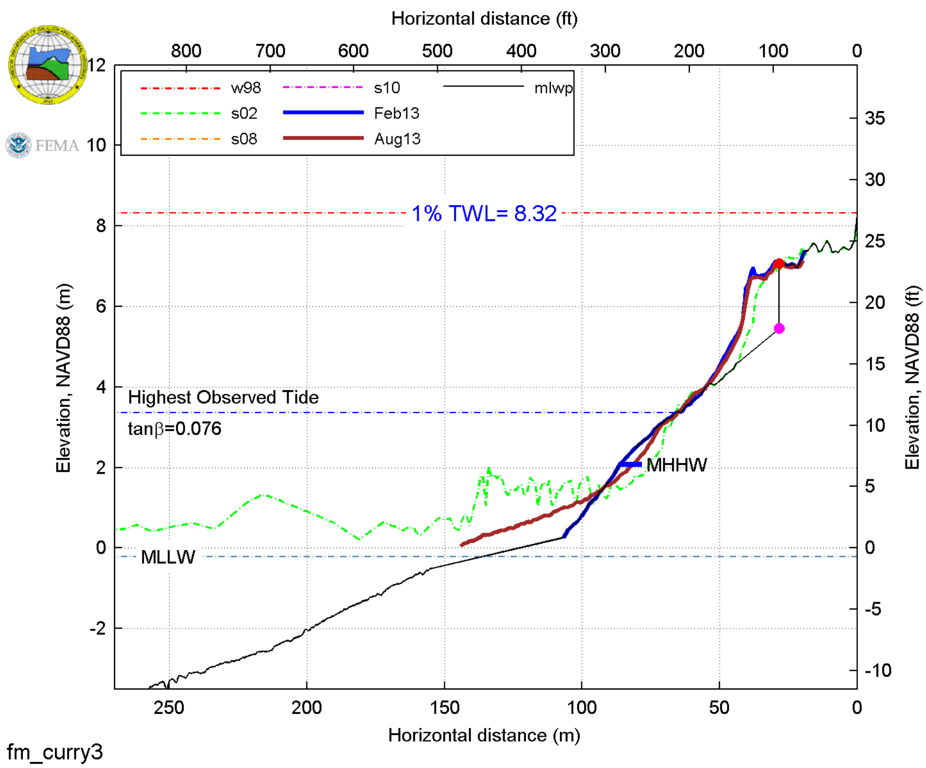

fm_curry 4

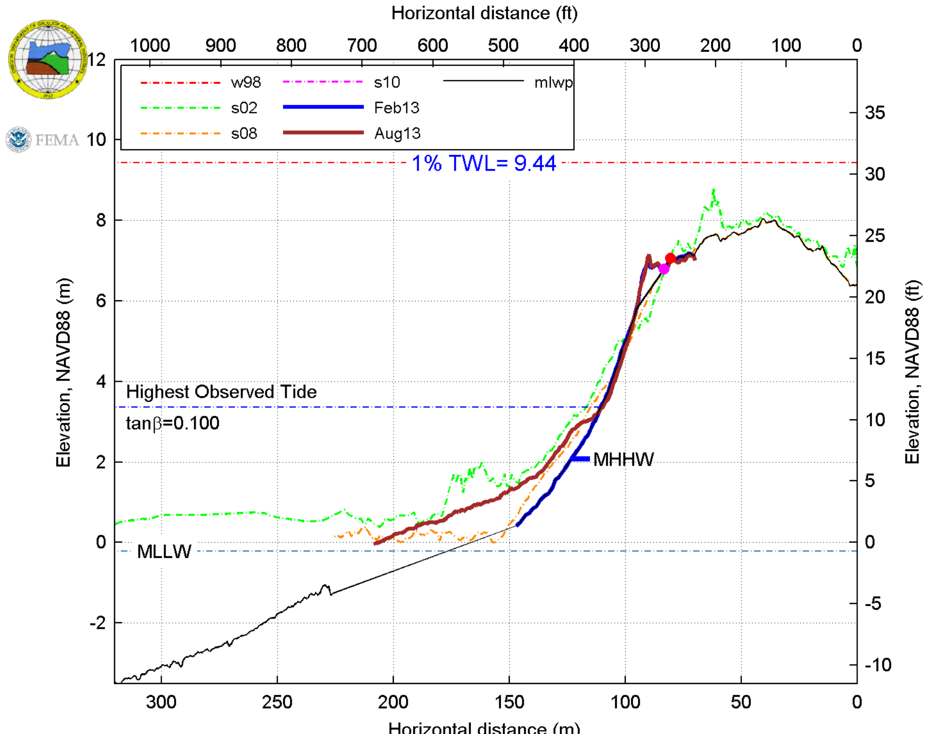

fm_curry4

fm_curry 5

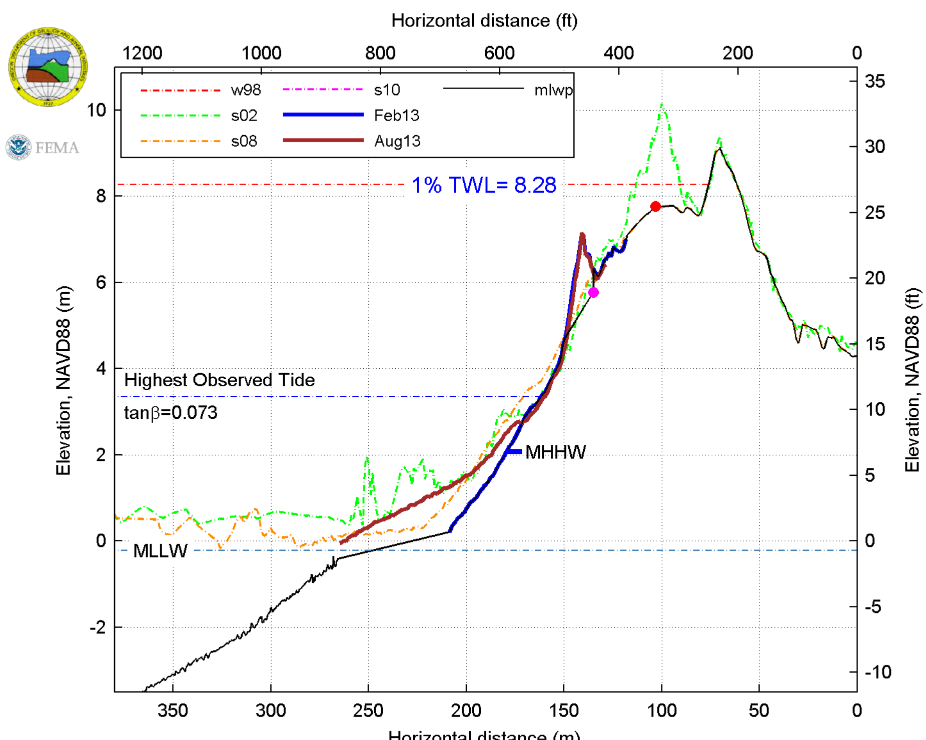

fm_curry5

fm_curry 6

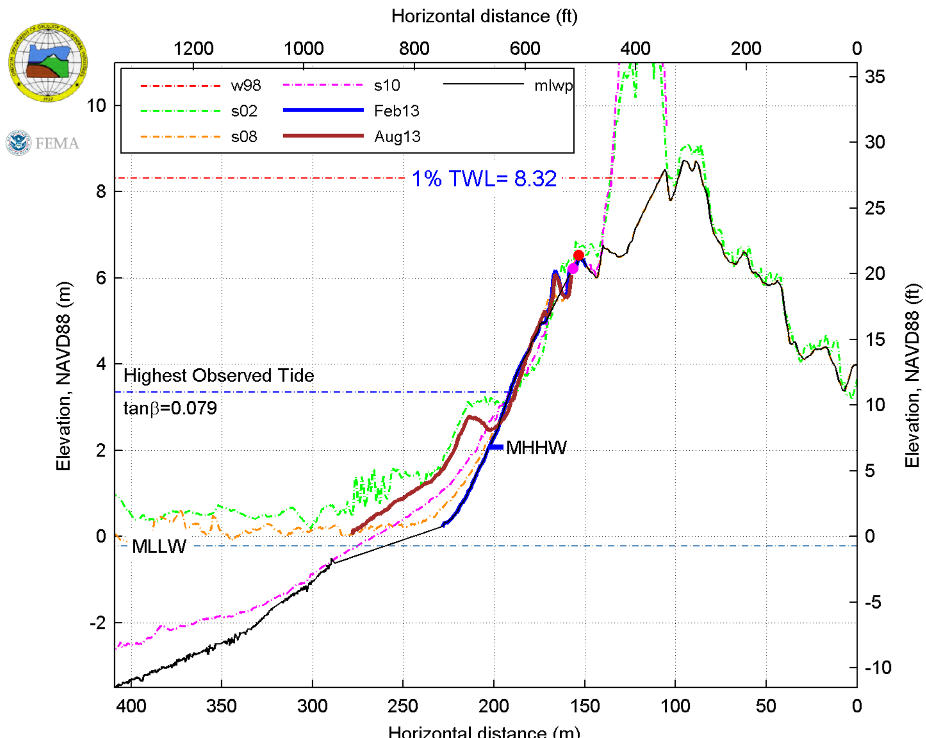

fm_curry6

fm_curry 7

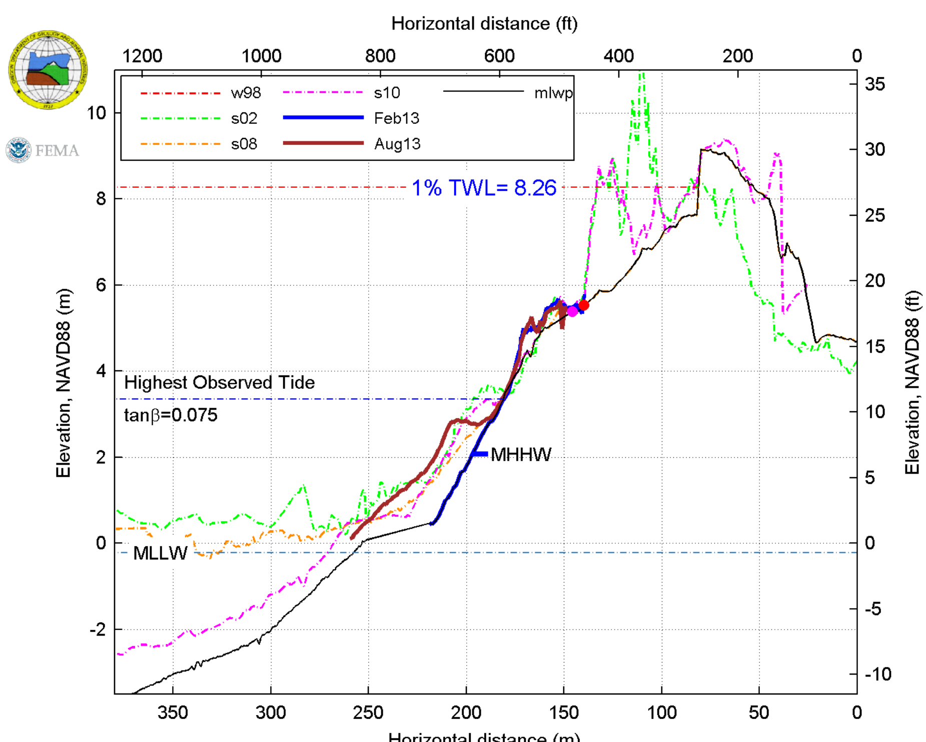

fm_curry7

fm_curry 8

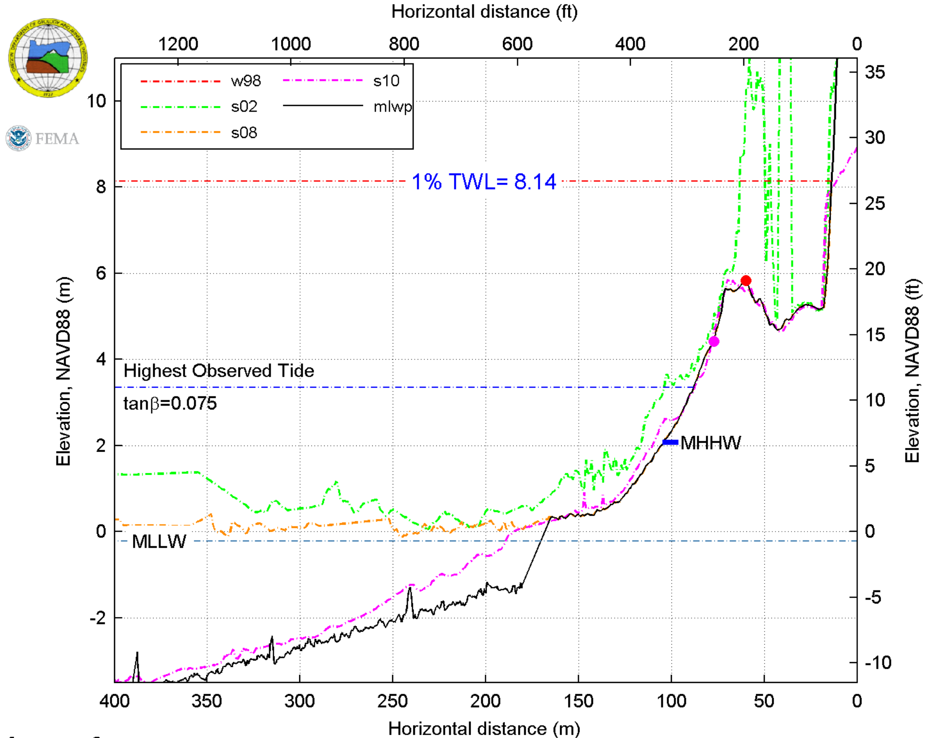

fm_curry8

fm_curry 9

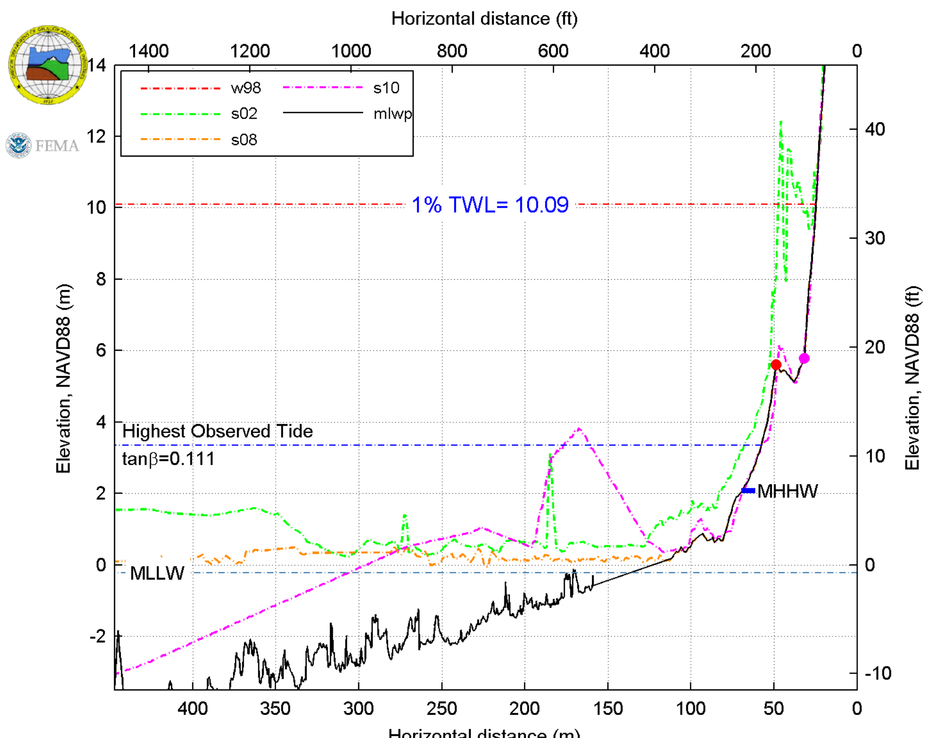

fm_curry9

fm_curry 10

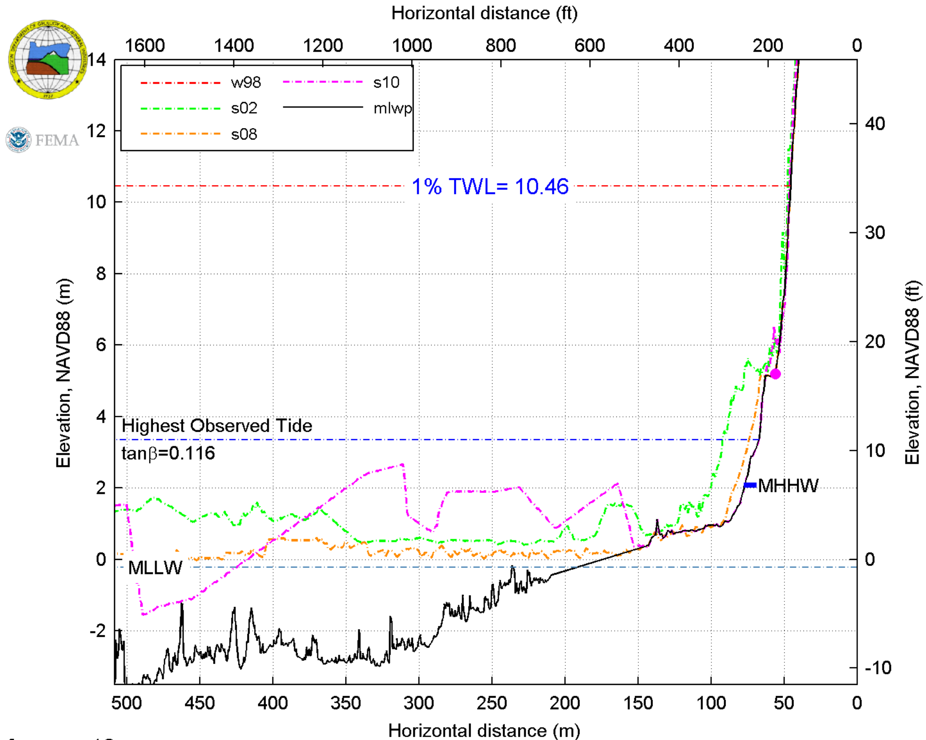

fm_curry10

fm_curry 11

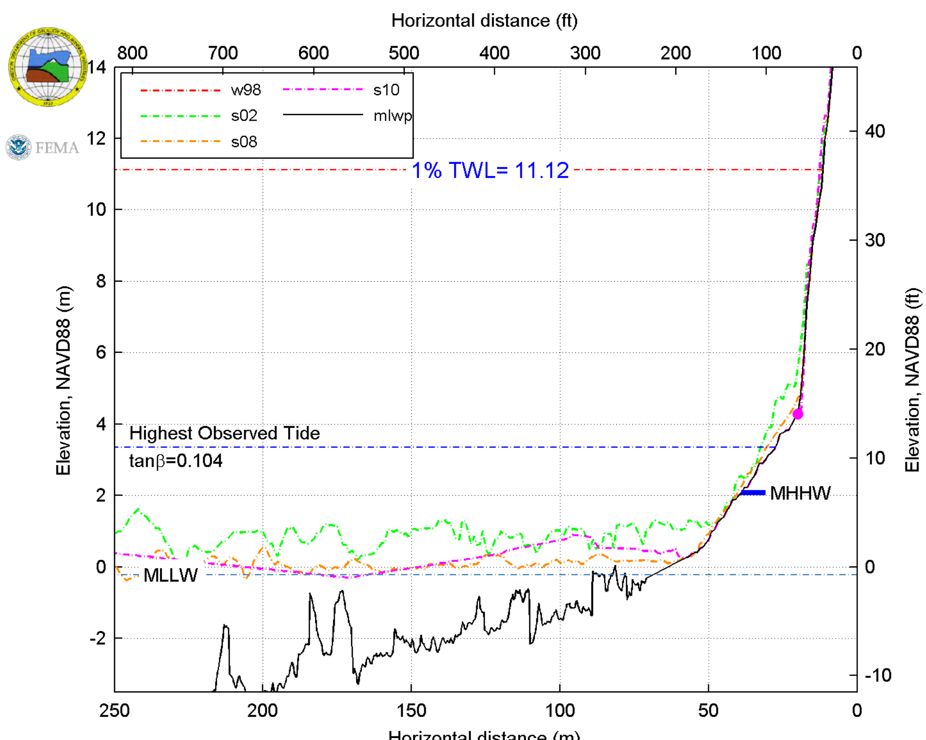

fm_curry11

fm_curry 12

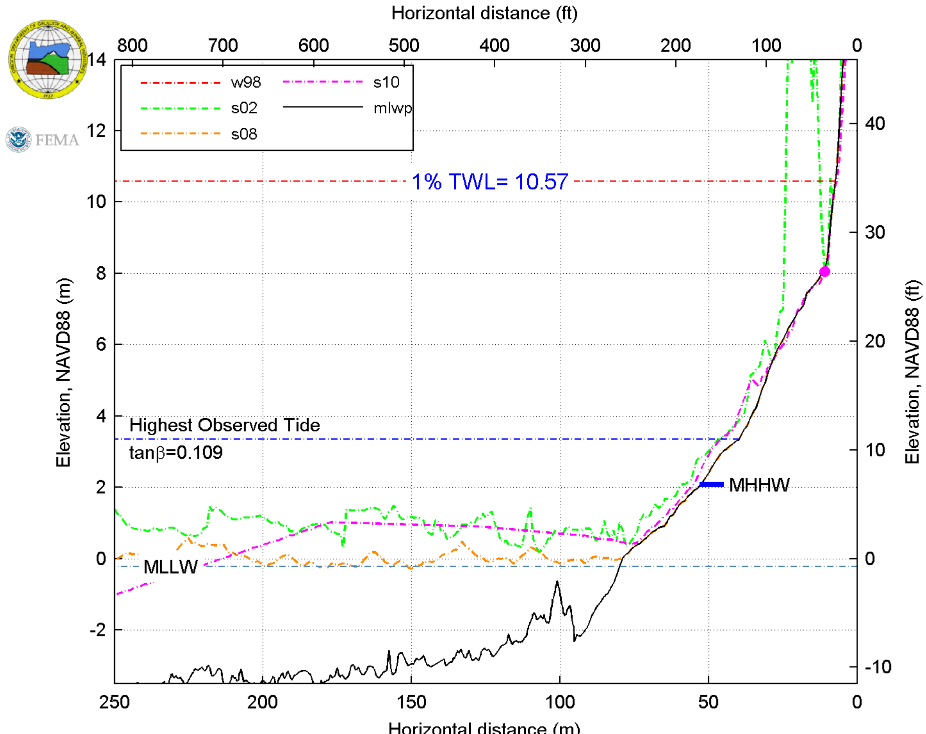

fm_curry12

fm_curry 13

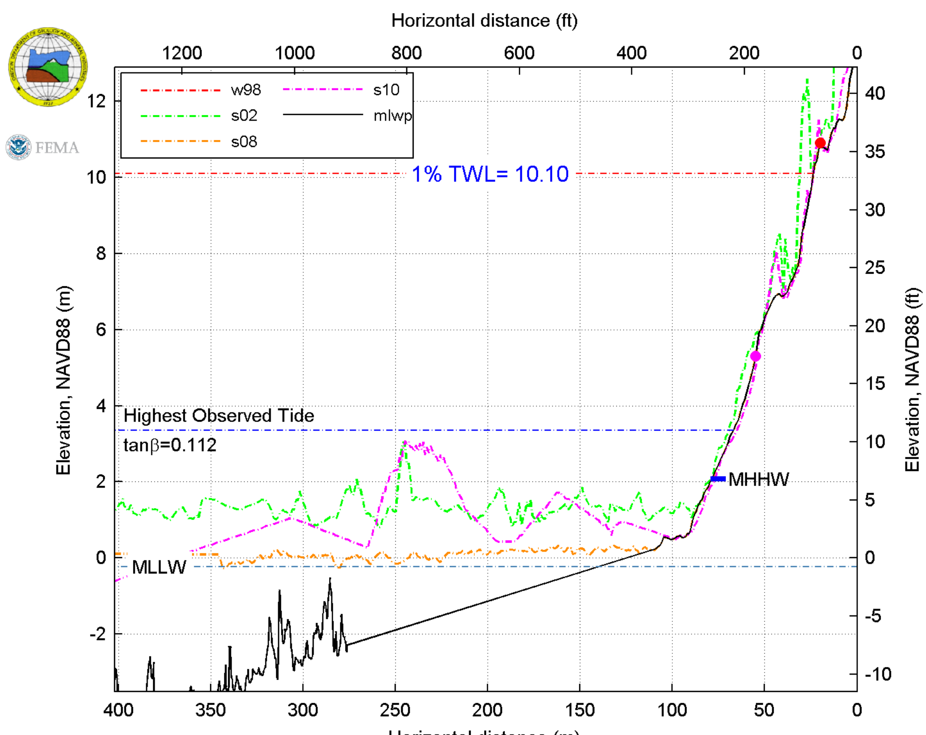

fm_curry13

fm_curry 14

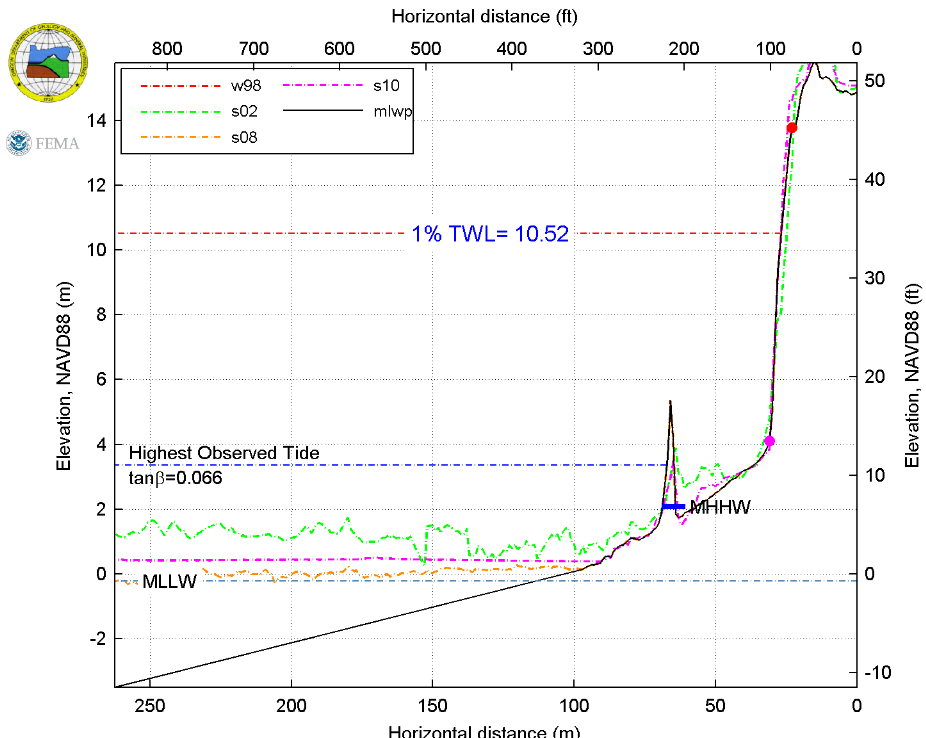

fm_curry14

fm_curry 15

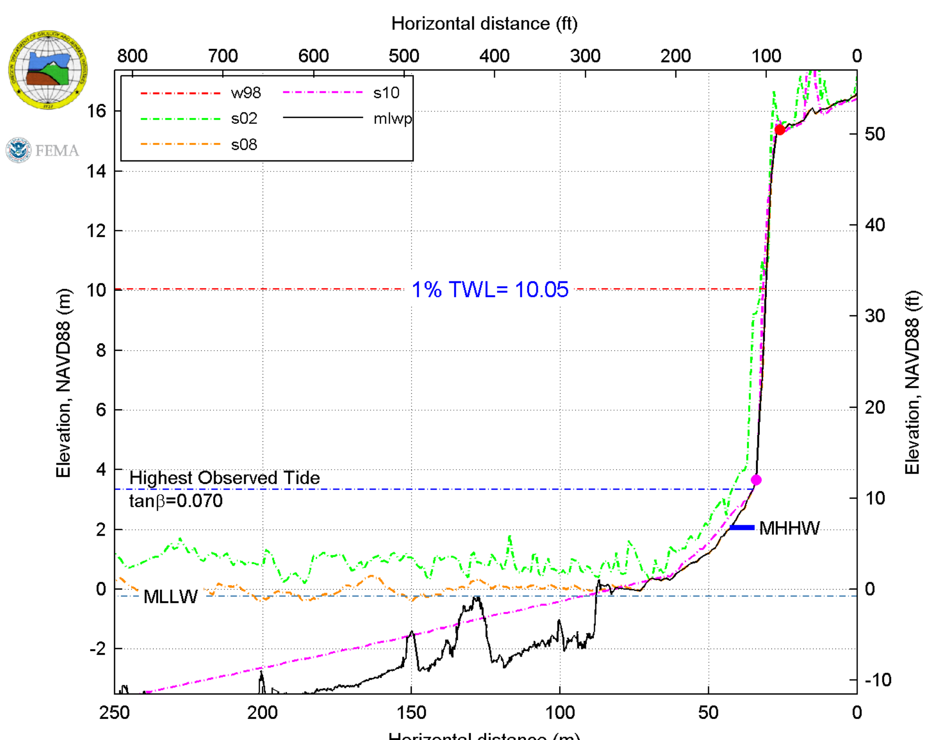

fm_curry15

fm_curry 16

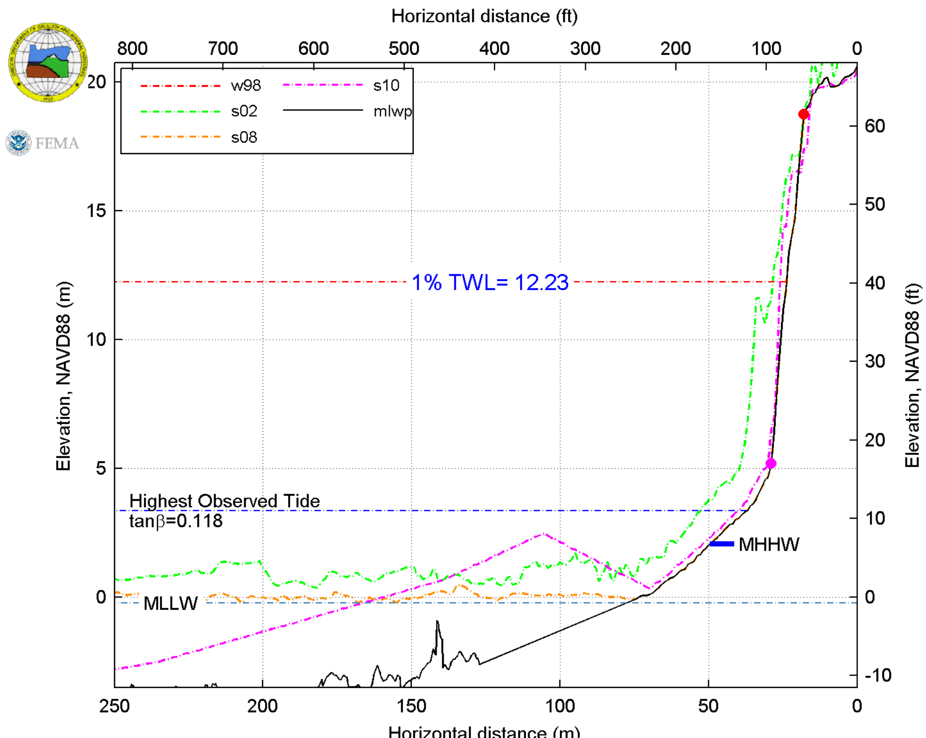

fm_curry16

fm_curry 17

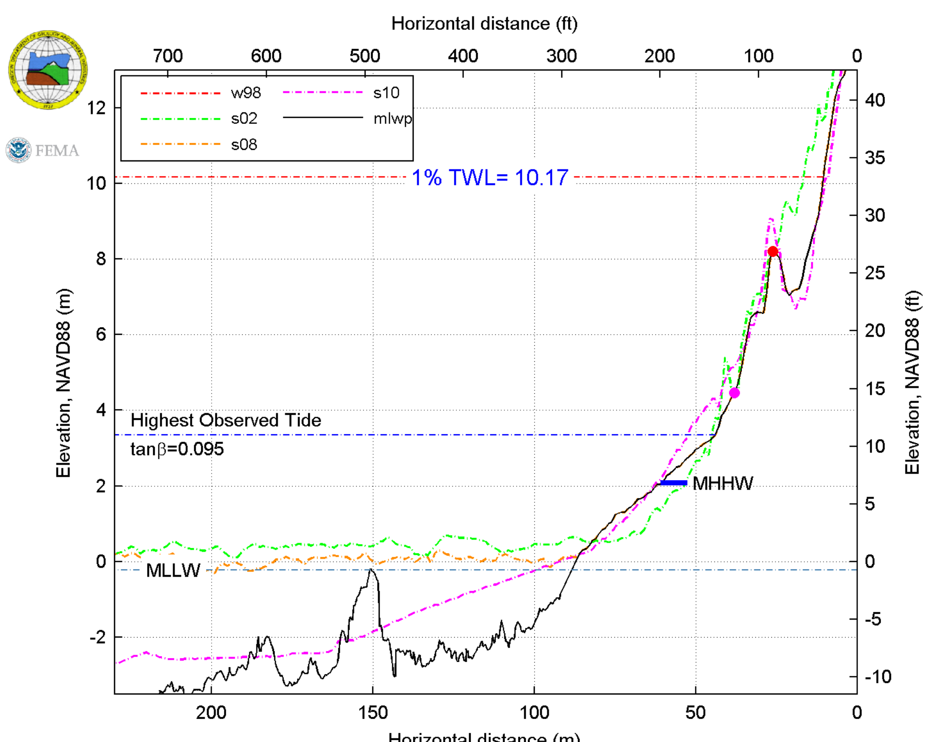

fm_curry17

fm_curry 18

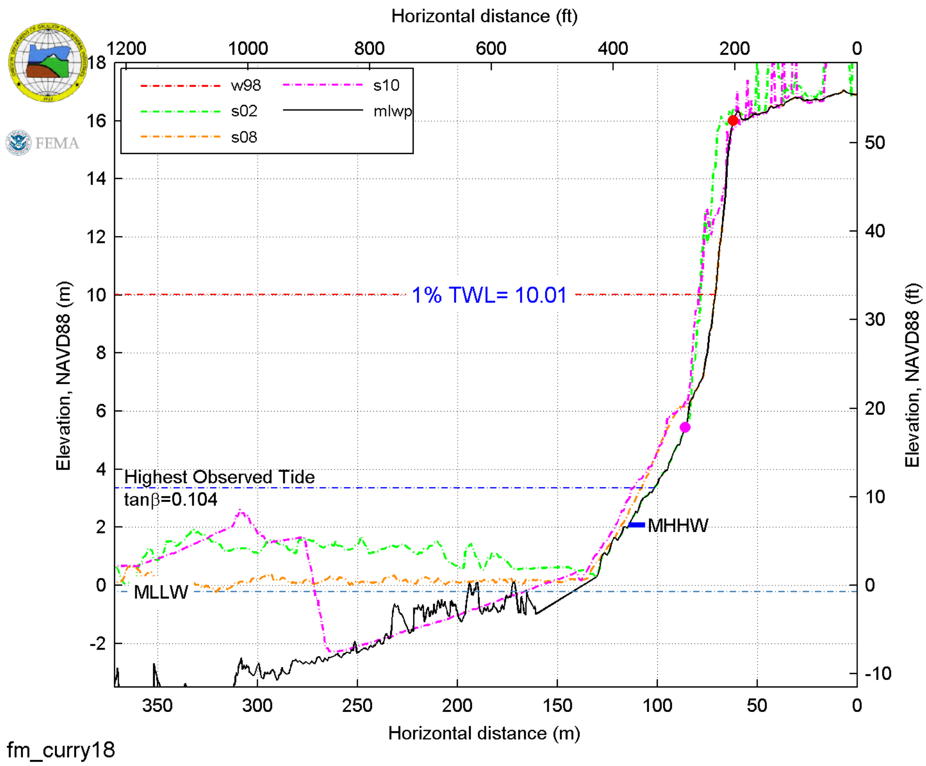

fm_curry 19

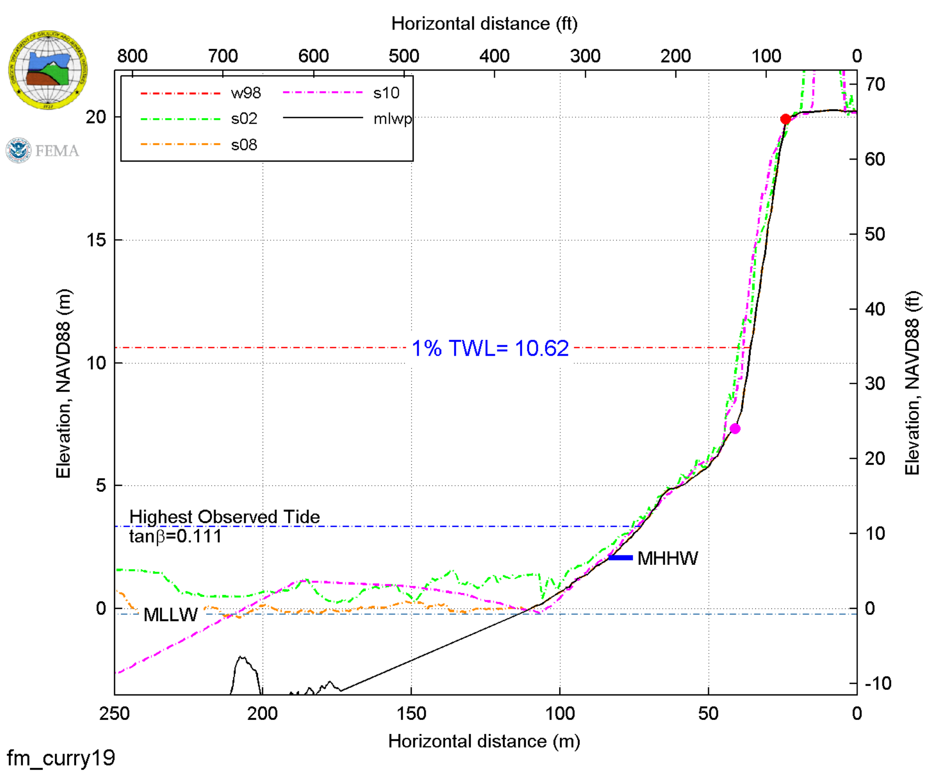

fm_curry 20

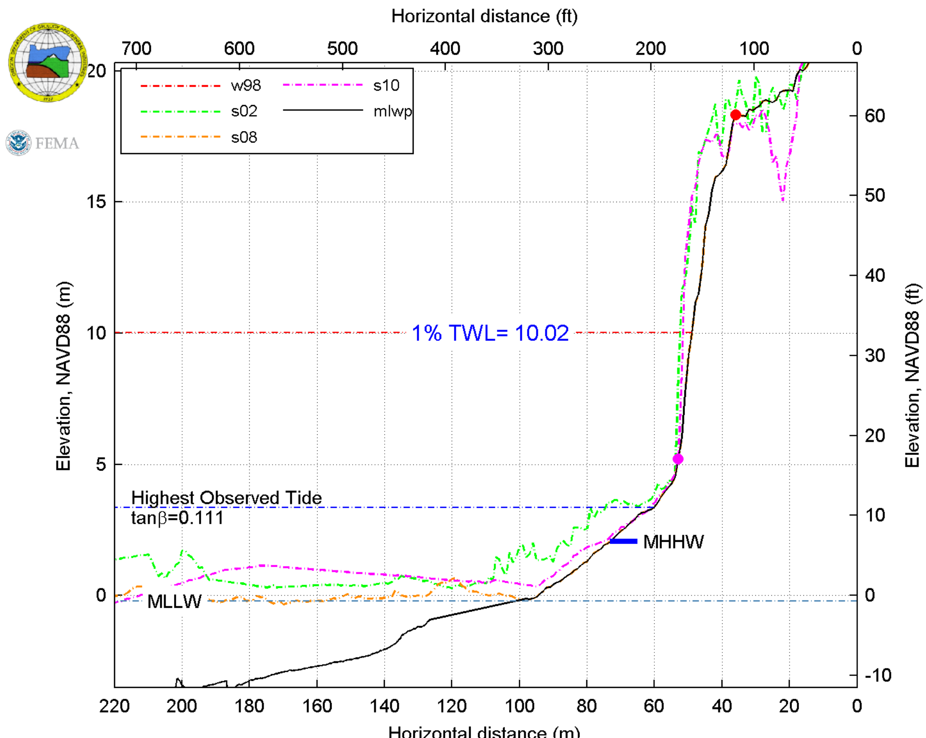

fm_curry20

fm_curry 21

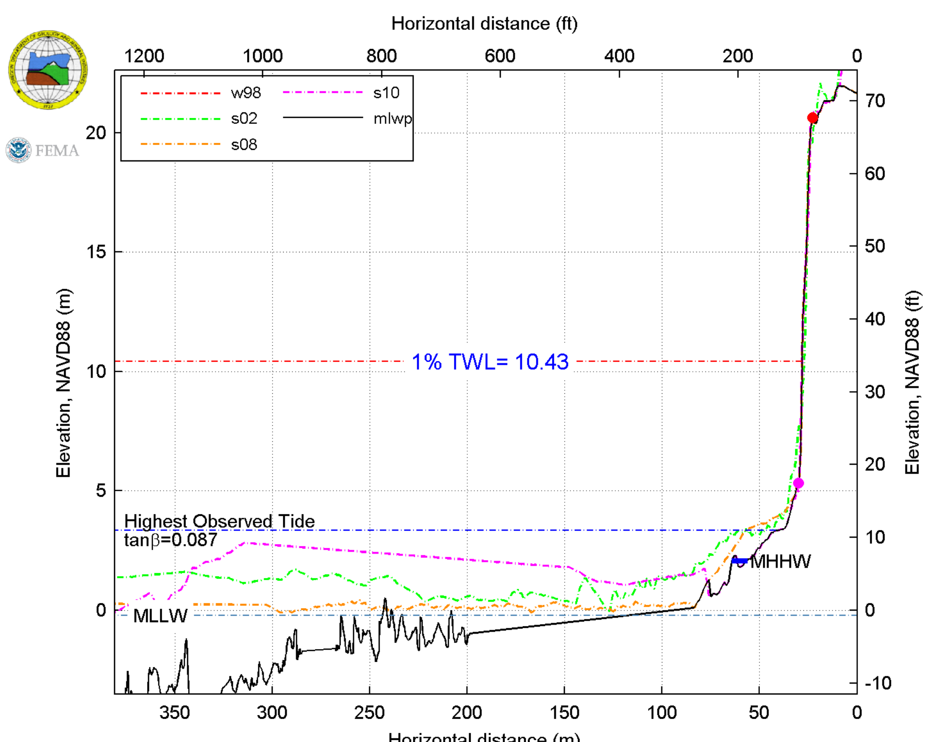

fm_curry21

fm_curry 22

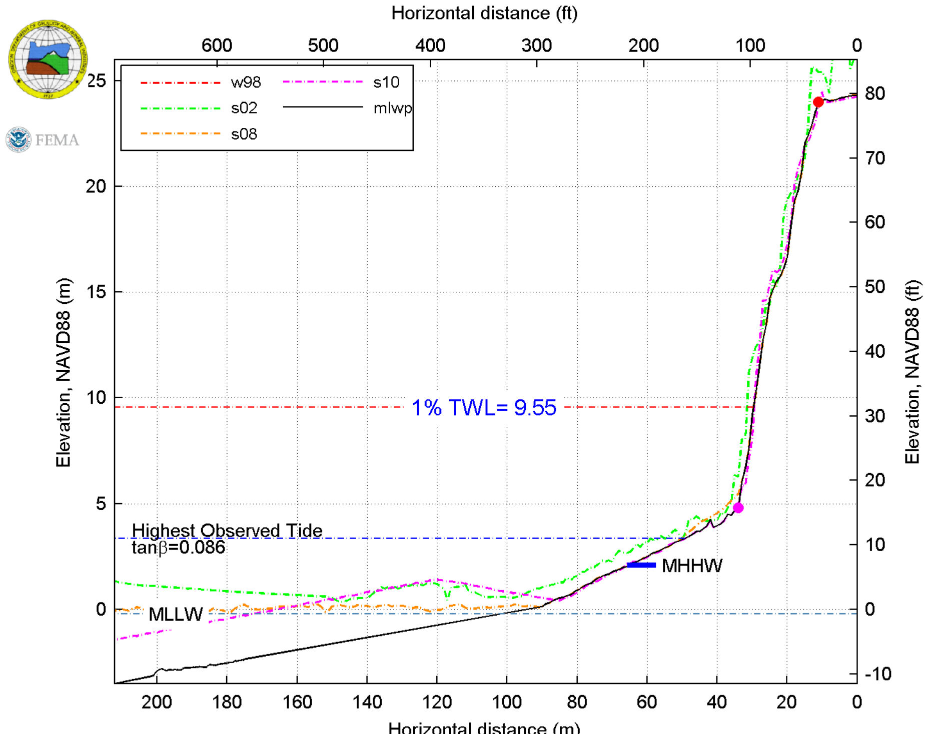

fm_curry22

fm_curry 23

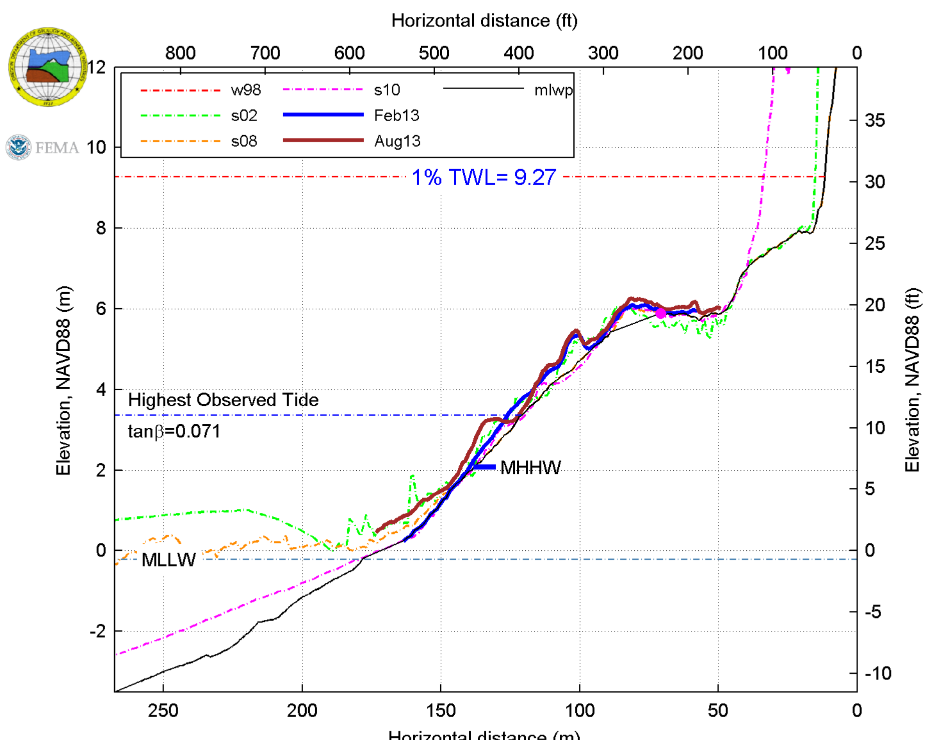

fm_curry23

fm_curry 24

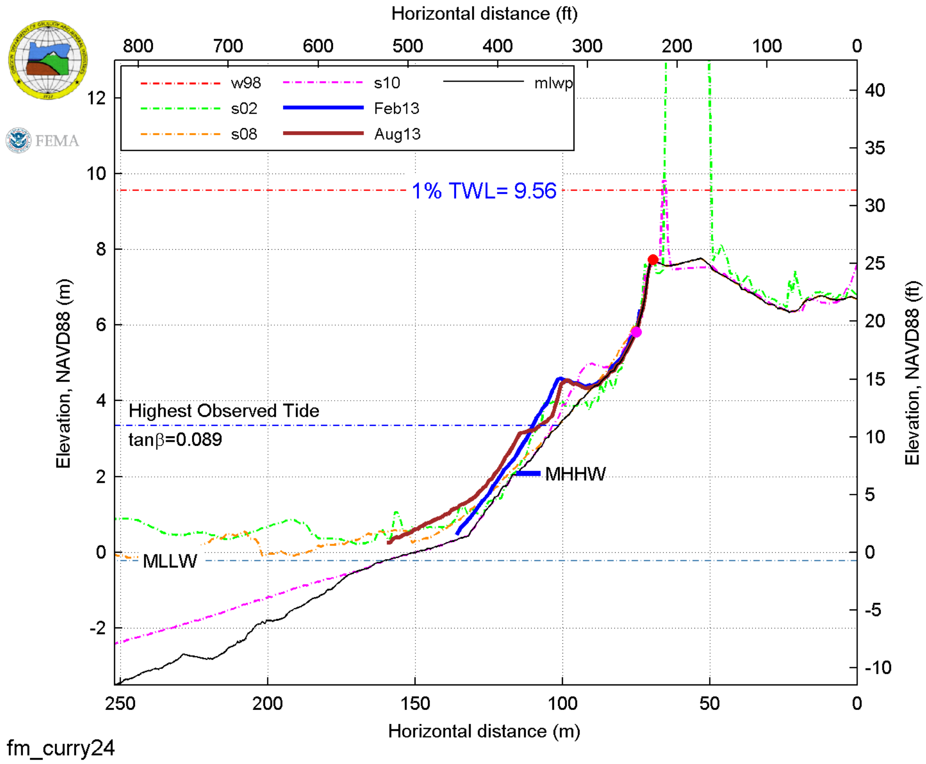

fm_curry 25

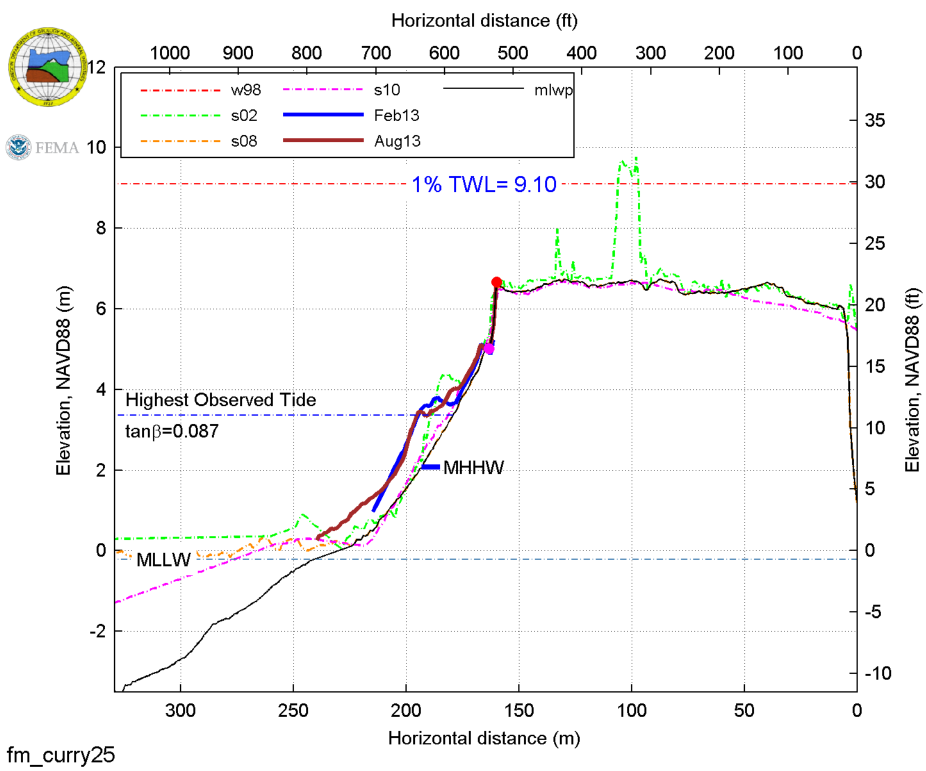

fm_curry 26

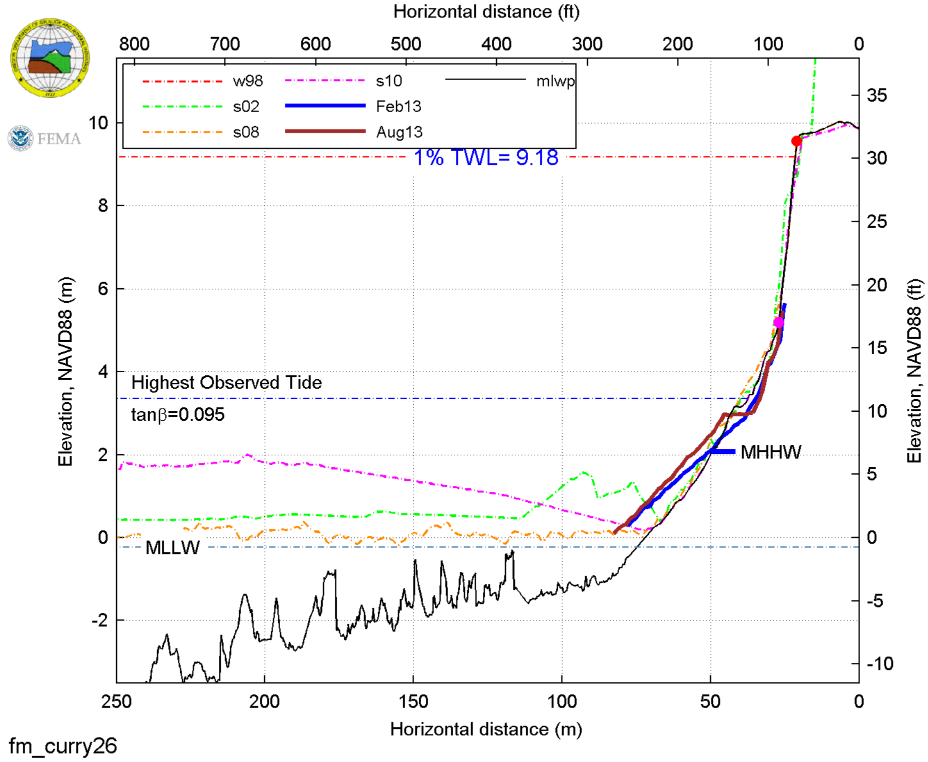

fm_curry 27

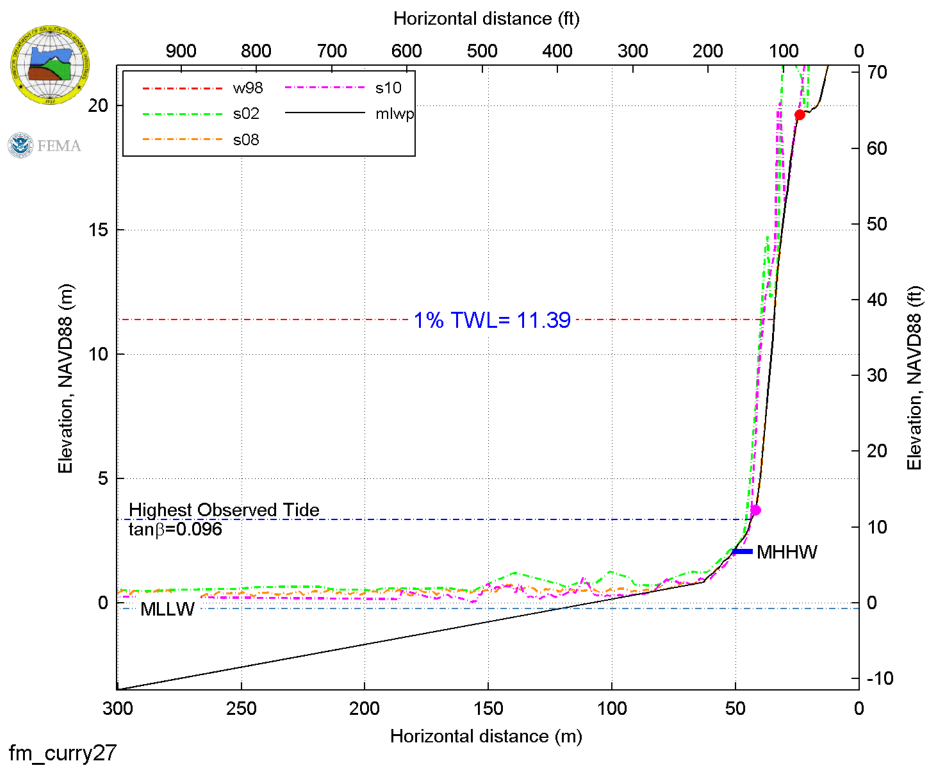

fm_curry 28

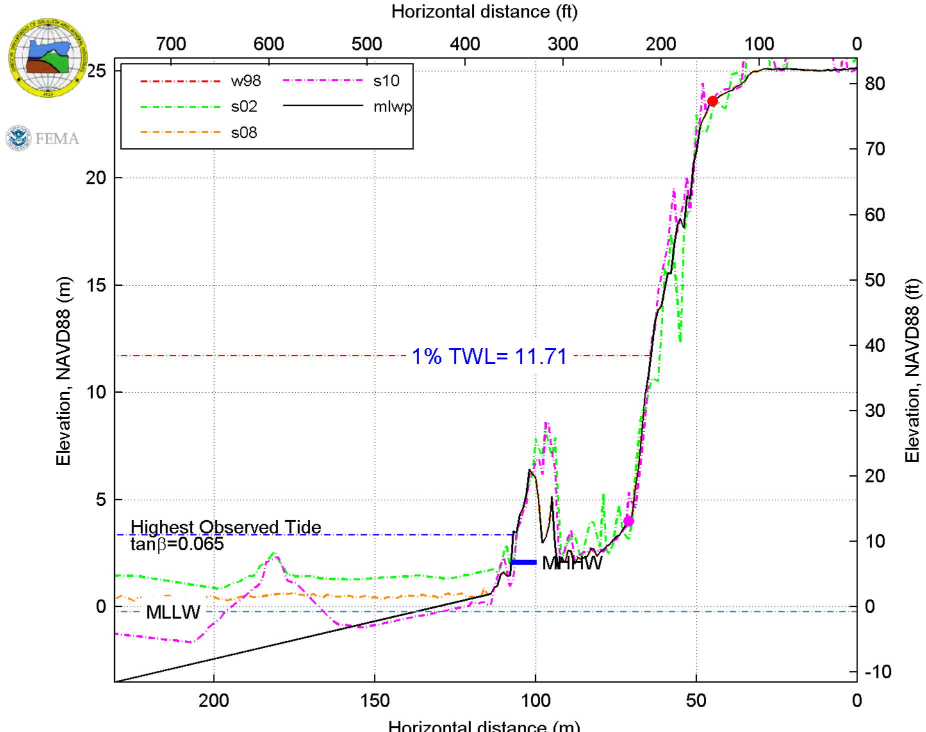

fm_curry28

fm_curry 29

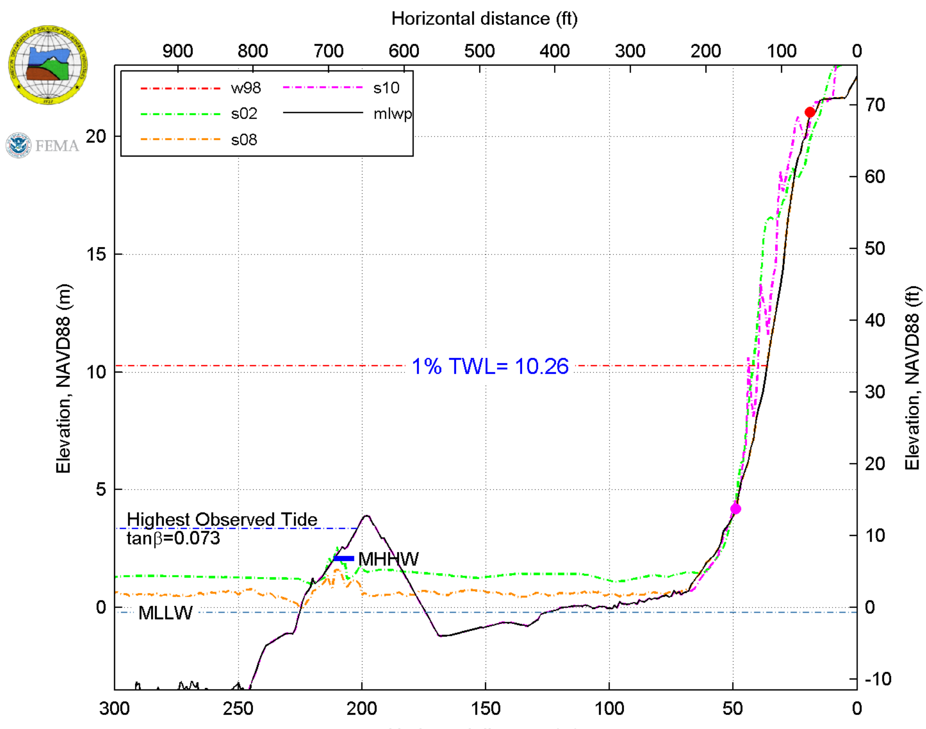

fm_curry29

fm_curry 30

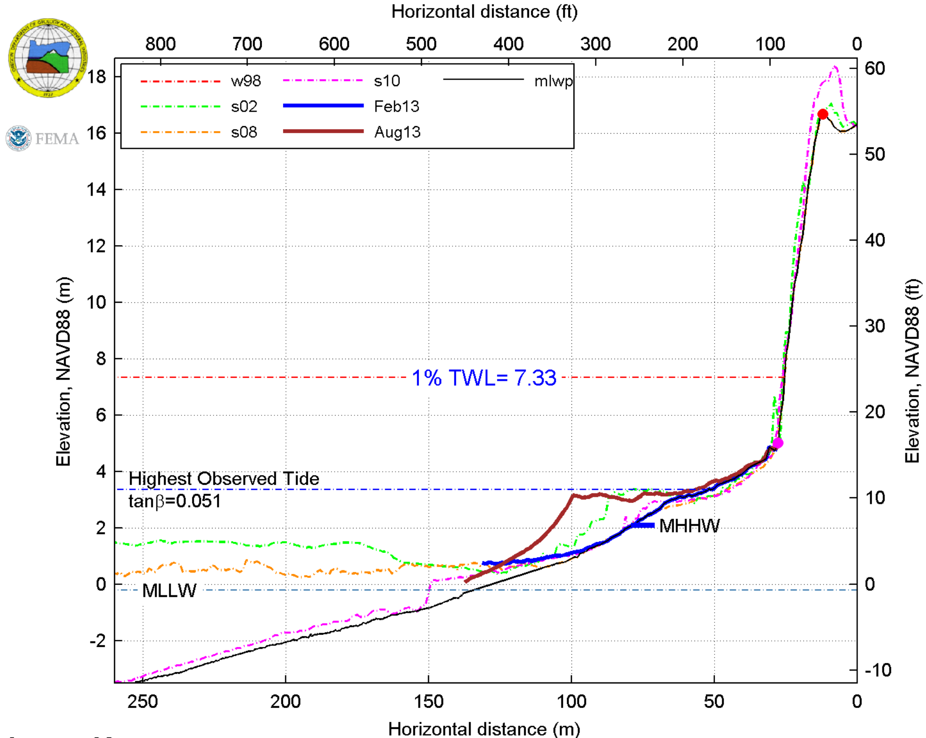

fm_curry30

fm_curry 31

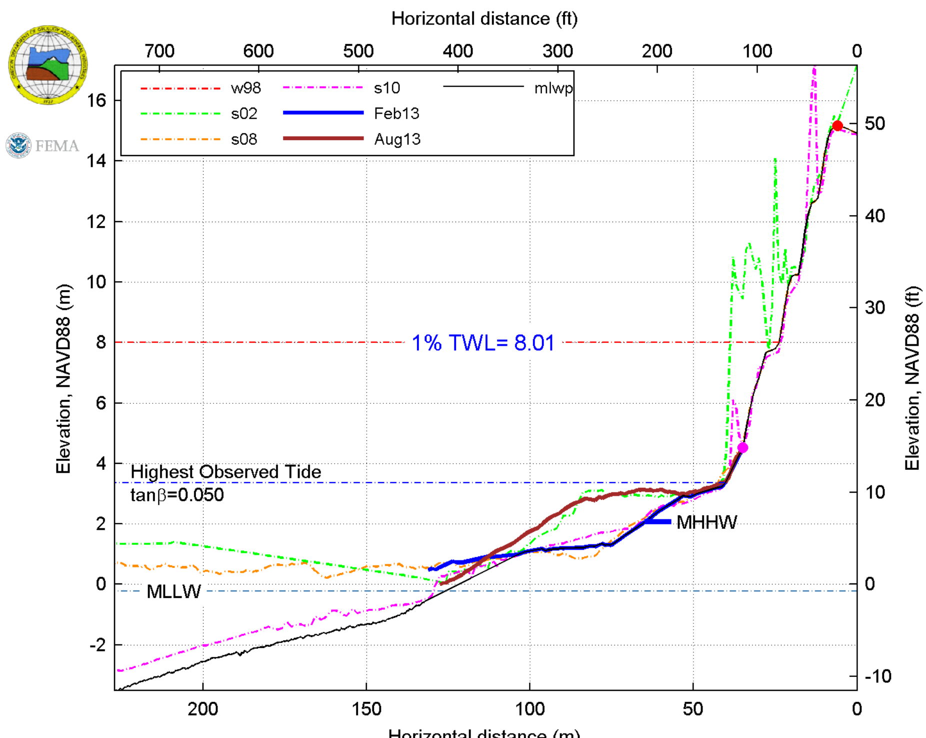

fm_curry31

fm_curry 32

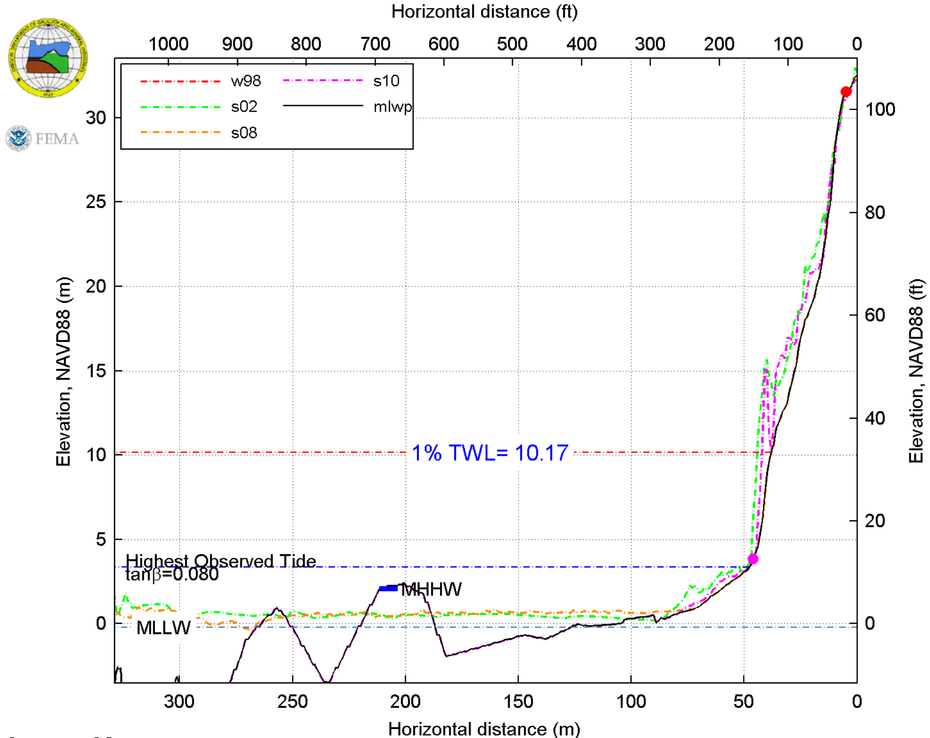

fm_curry32

fm_curry 33

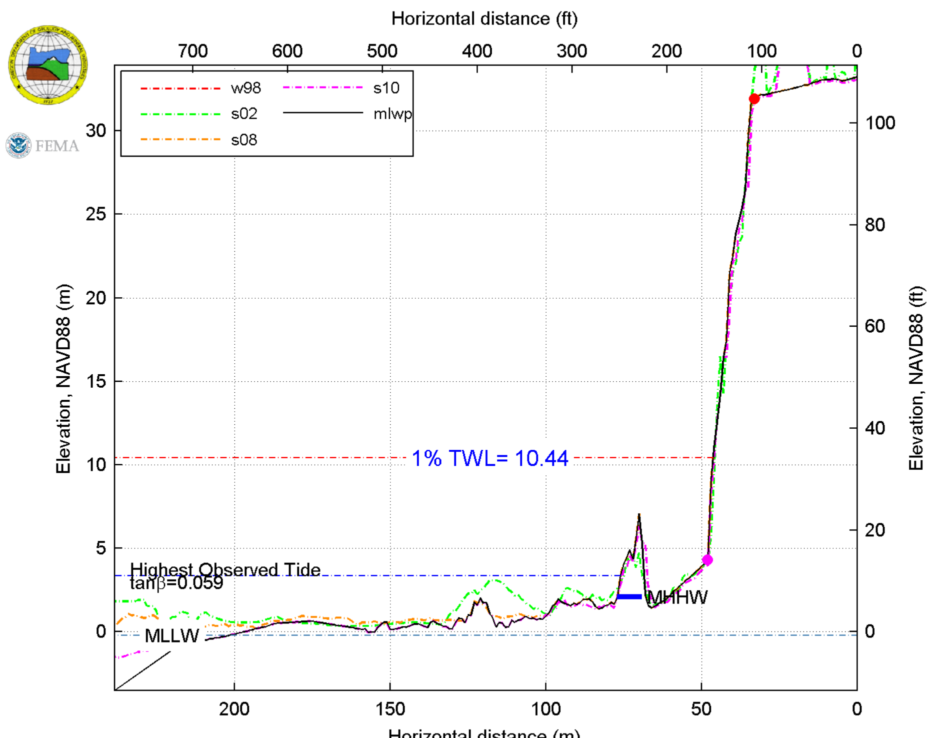

fm_curry33

fm_curry 34

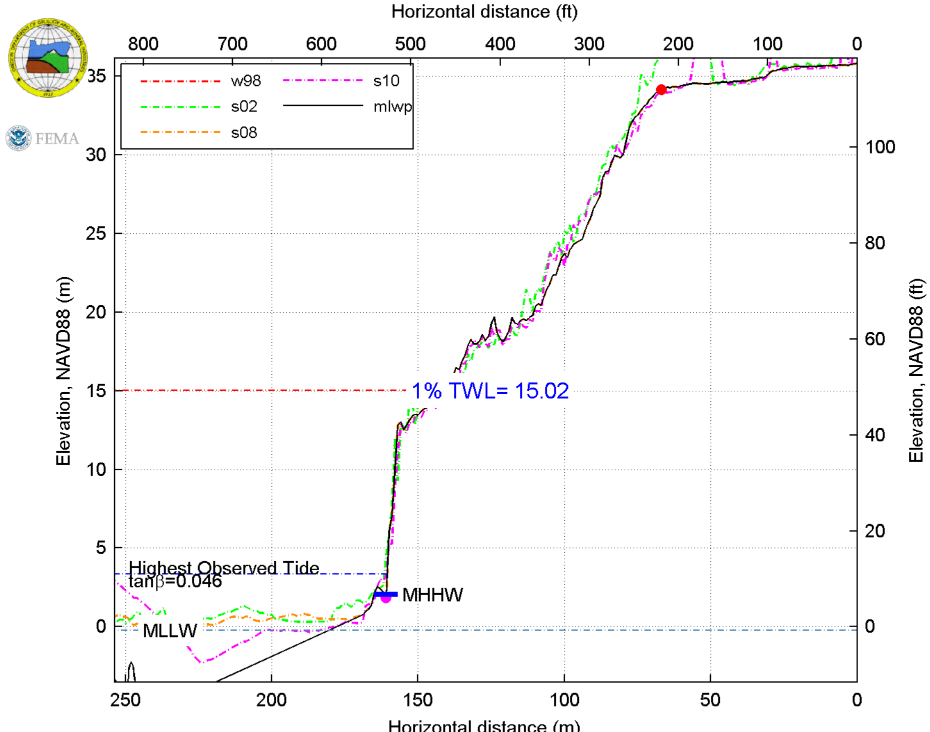

fm_curry34

fm_curry 35

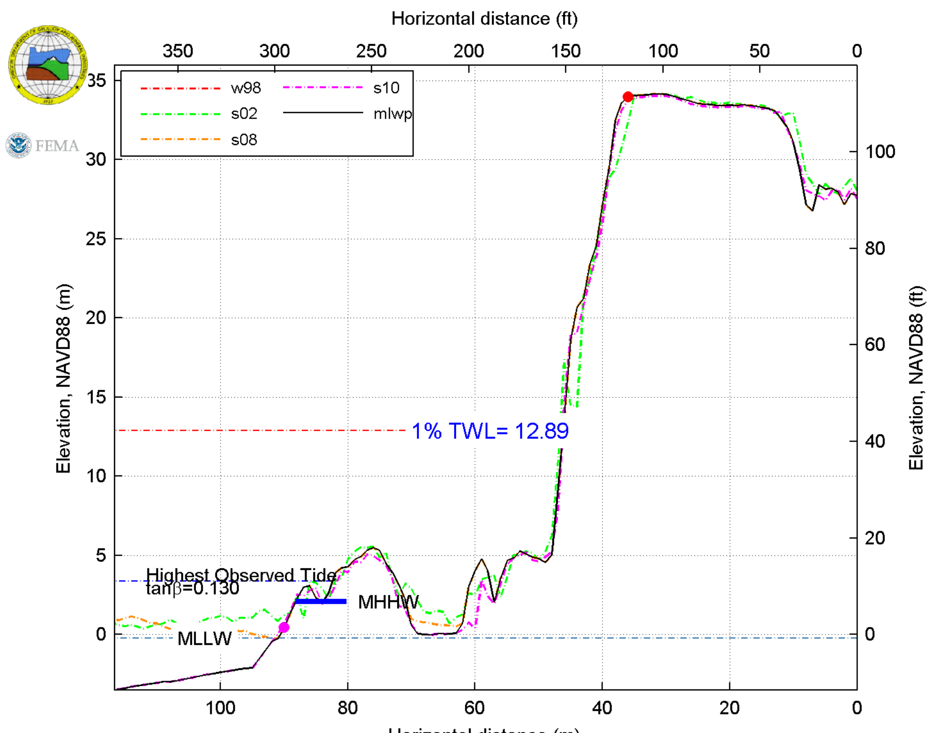

fm_curry35

fm_curry 36

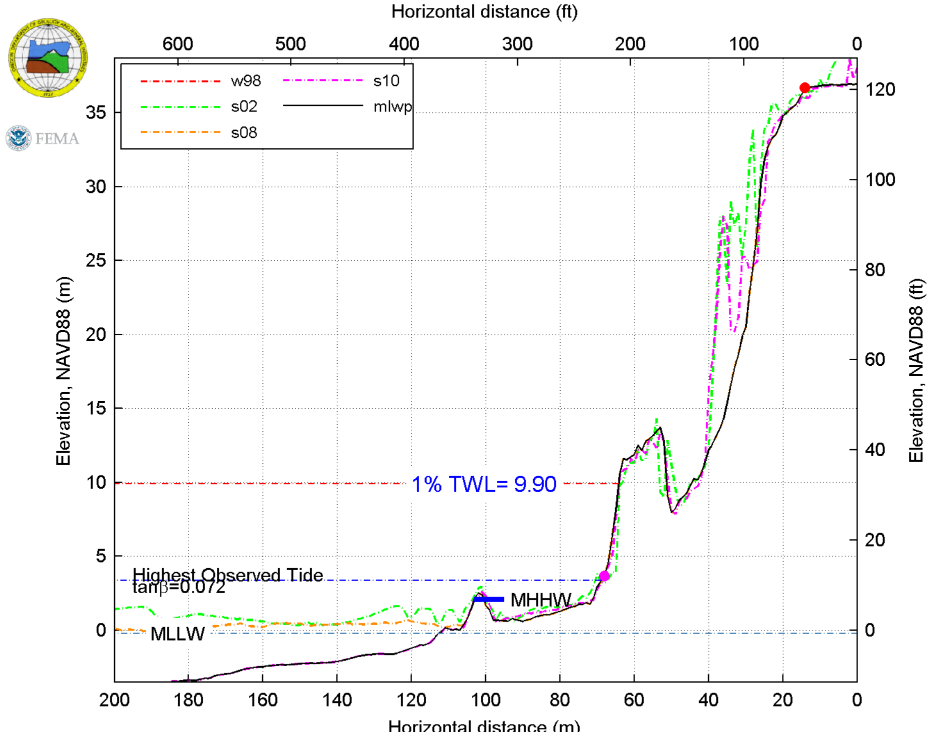

fm_curry36

fm_curry 37

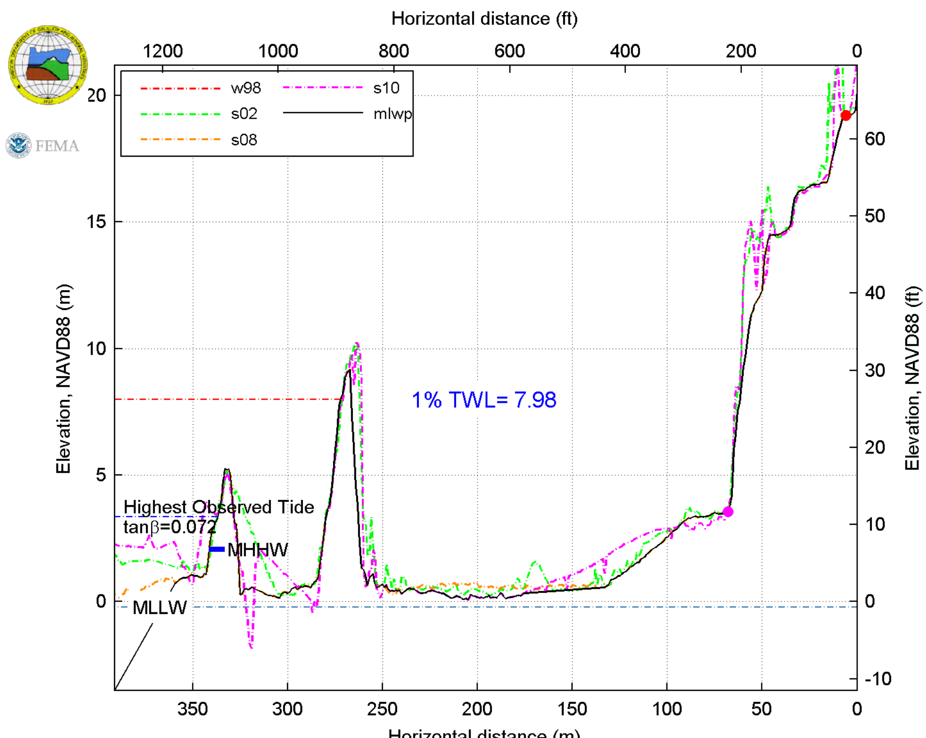

fm_curry37

fm_curry 38

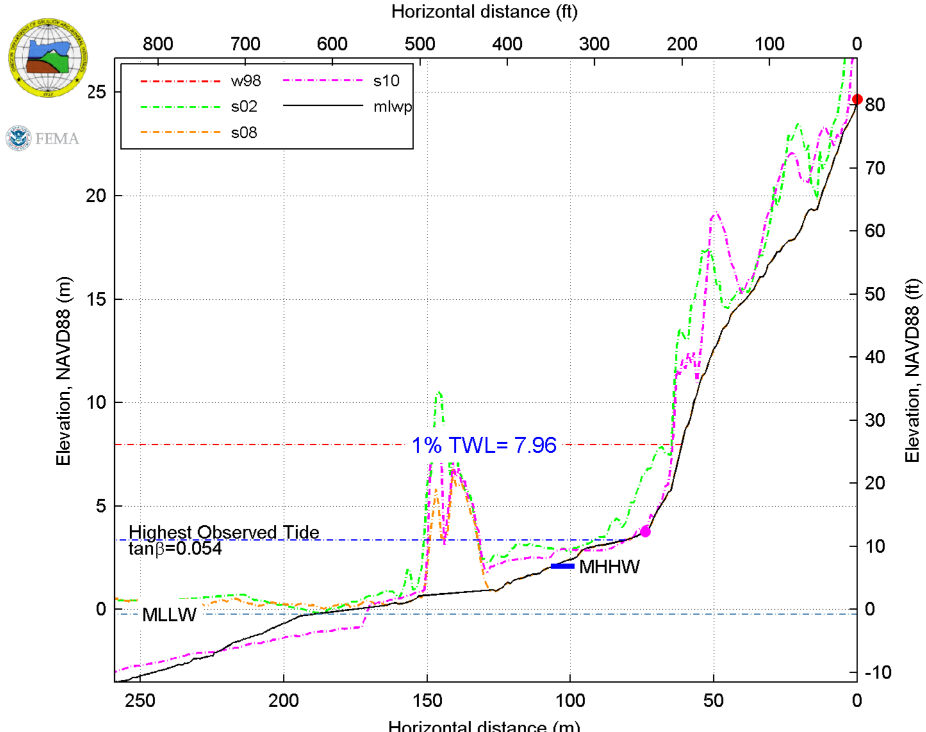

fm_curry38

fm_curry 39

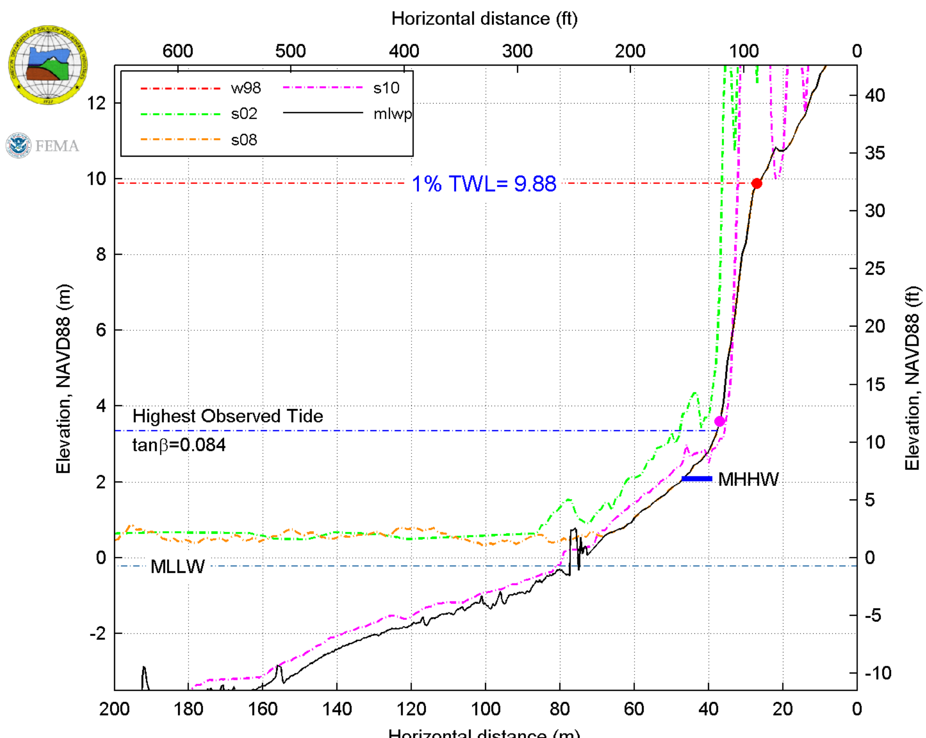

fm_curry39

fm_curry 40

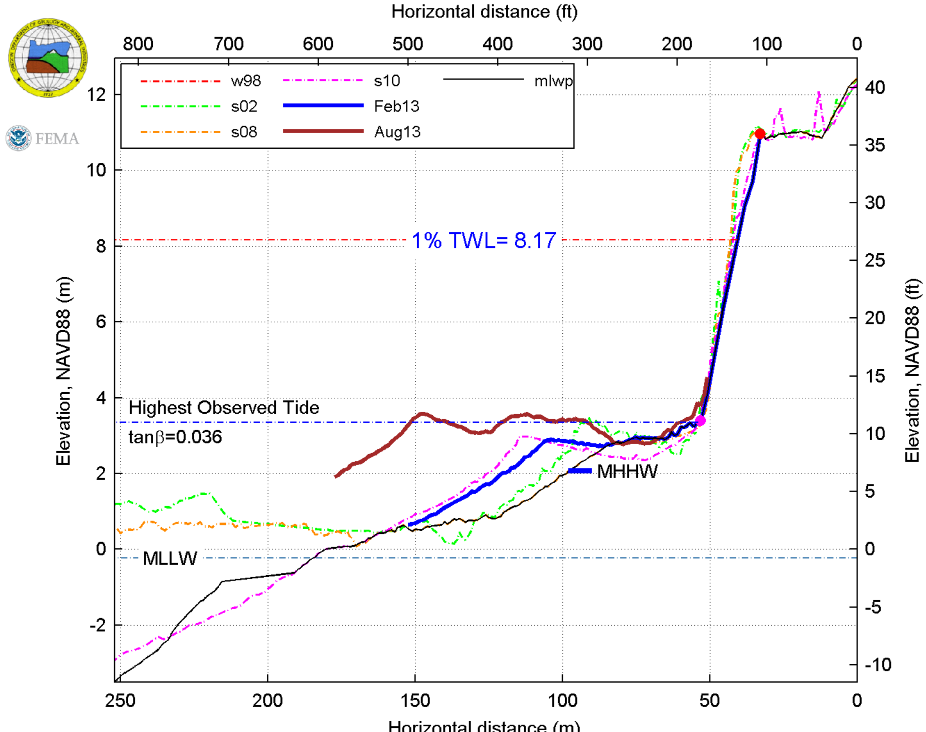

fm_curry40

fm_curry 41

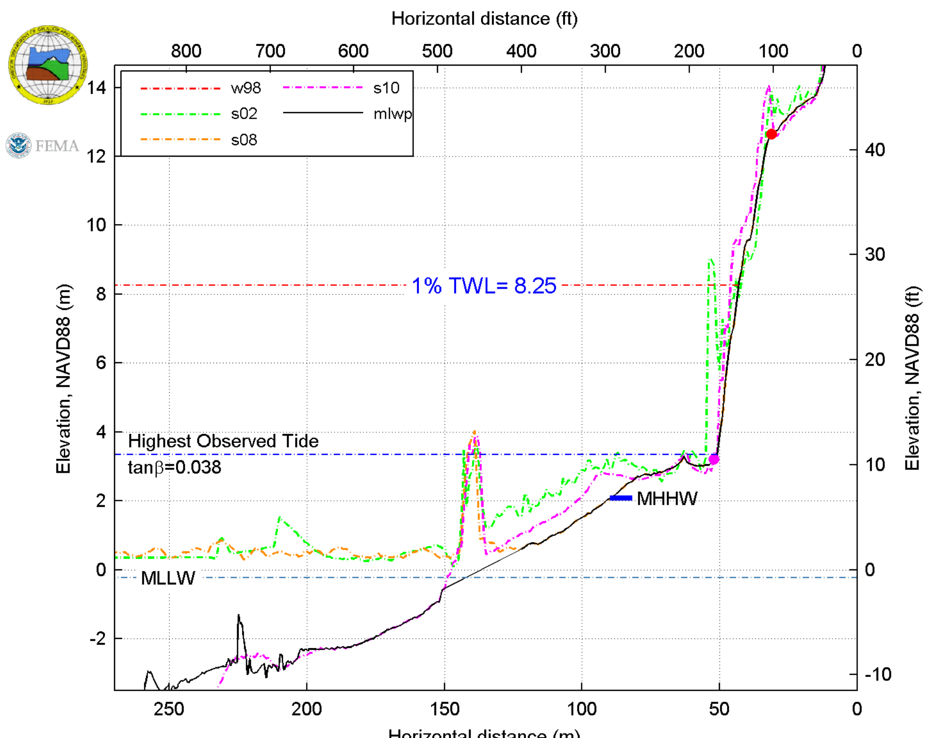

fm_curry41

fm_curry 42

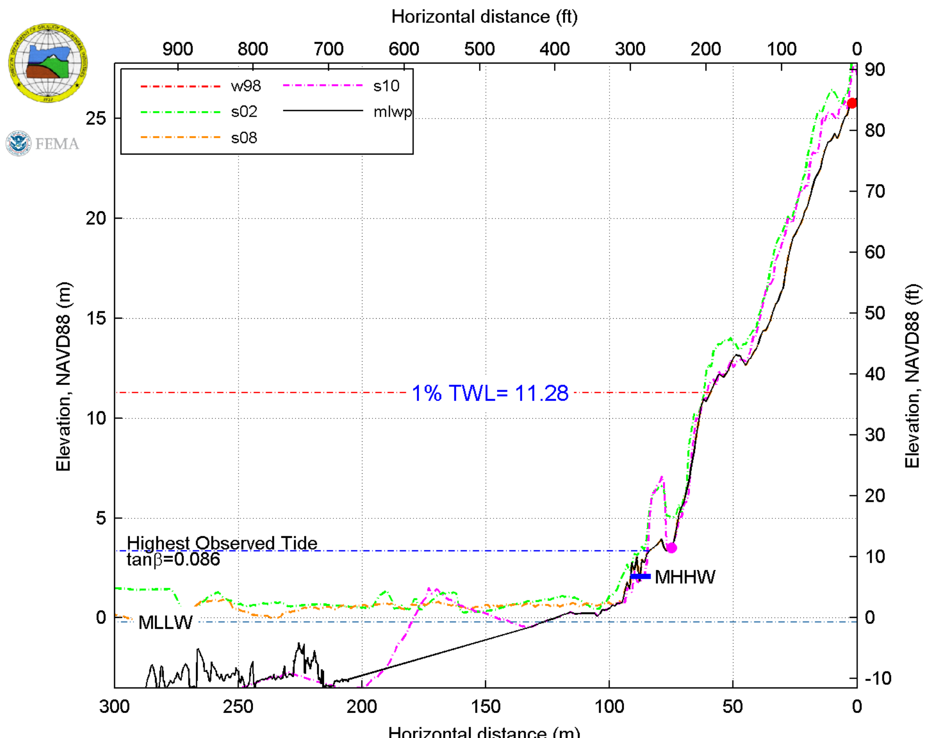

fm_curry42

fm_curry 43

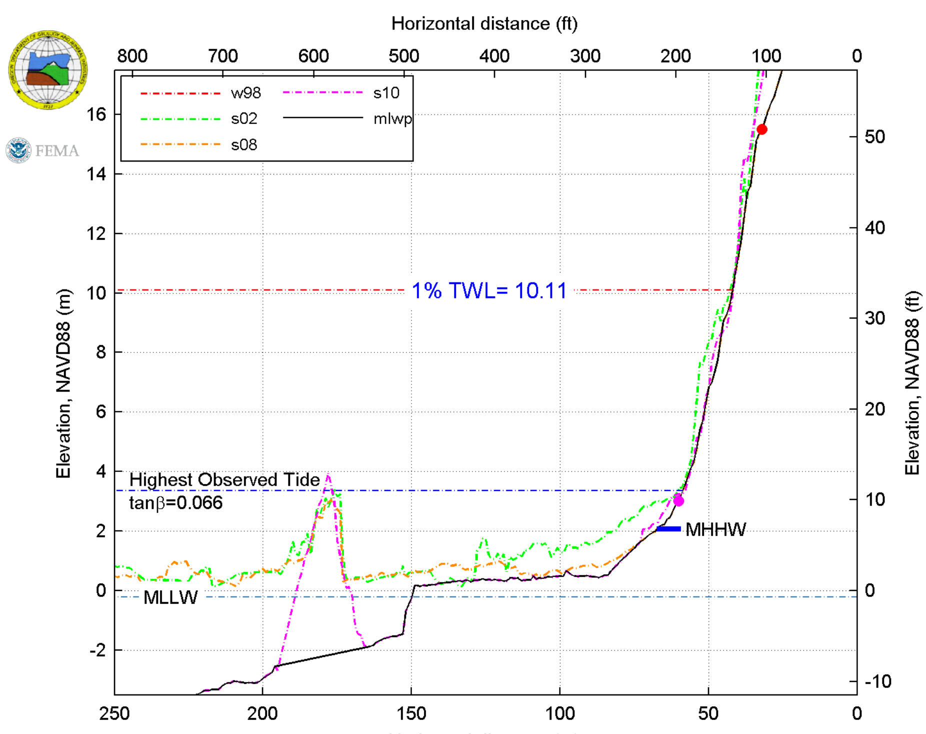

fm_curry43

fm_curry 44

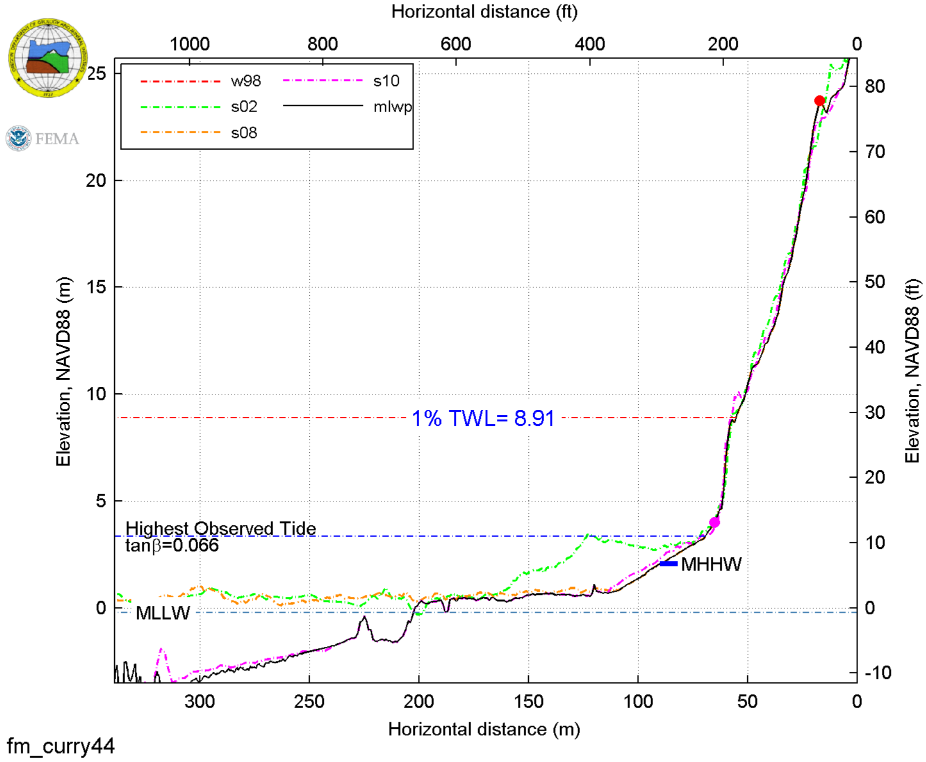

fm_curry 45

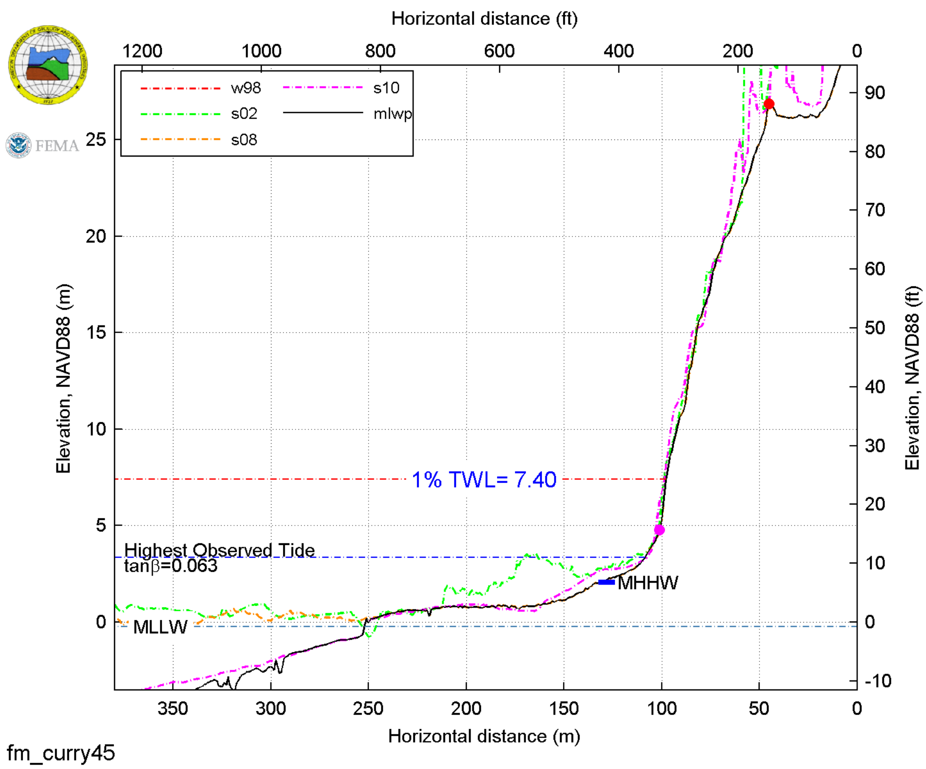

fm_curry 46

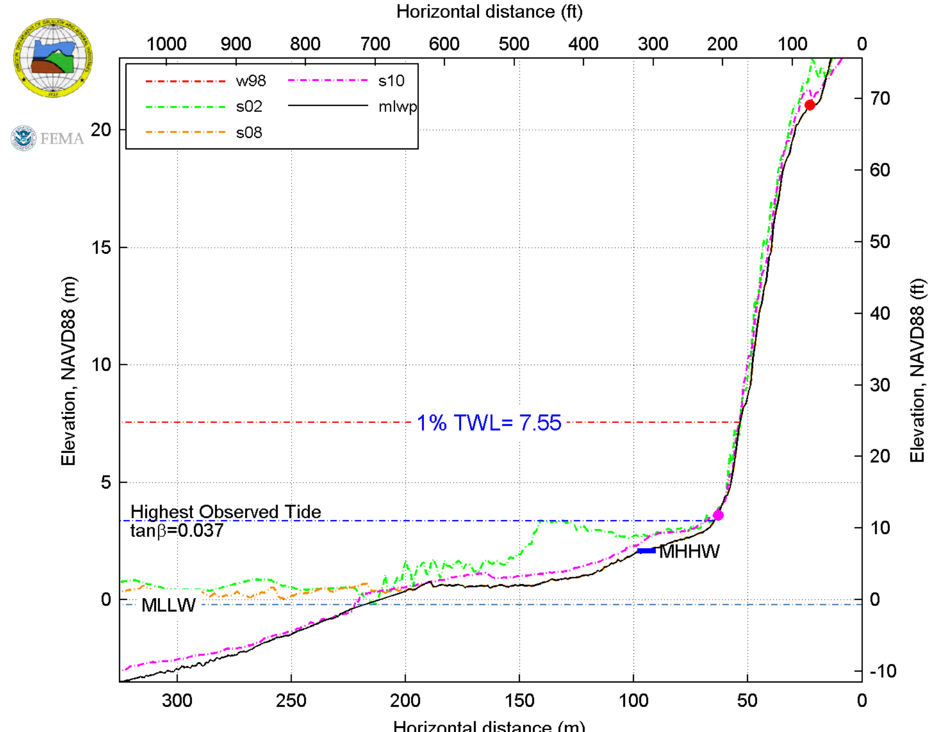

fm_curry46

fm_curry 47

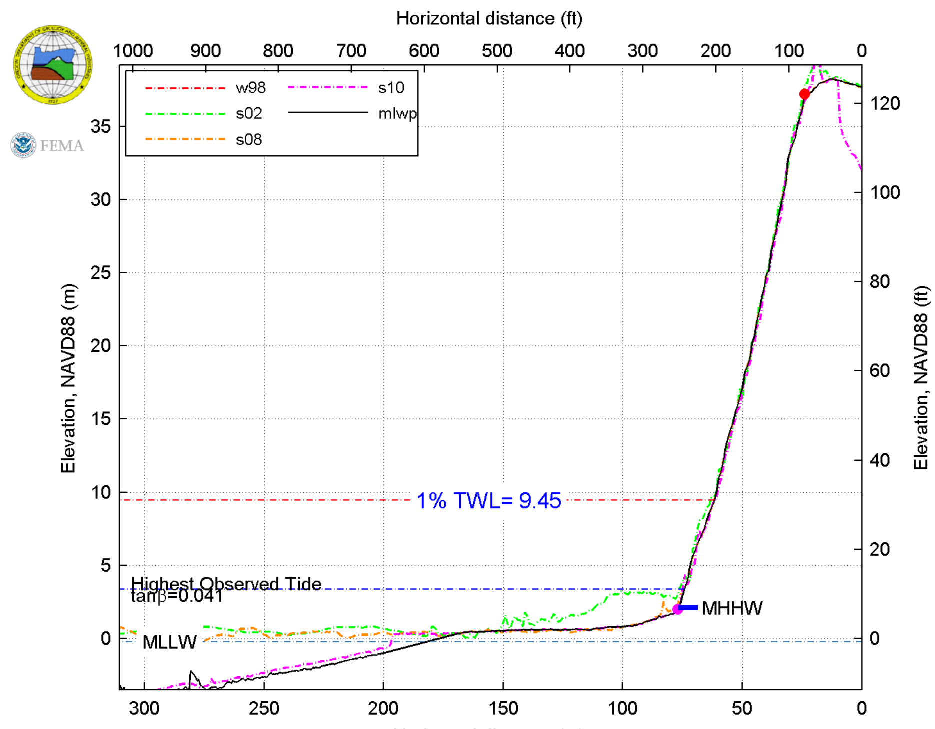

fm_curry47

11.2.2 Gold Beach

fm_curry 48

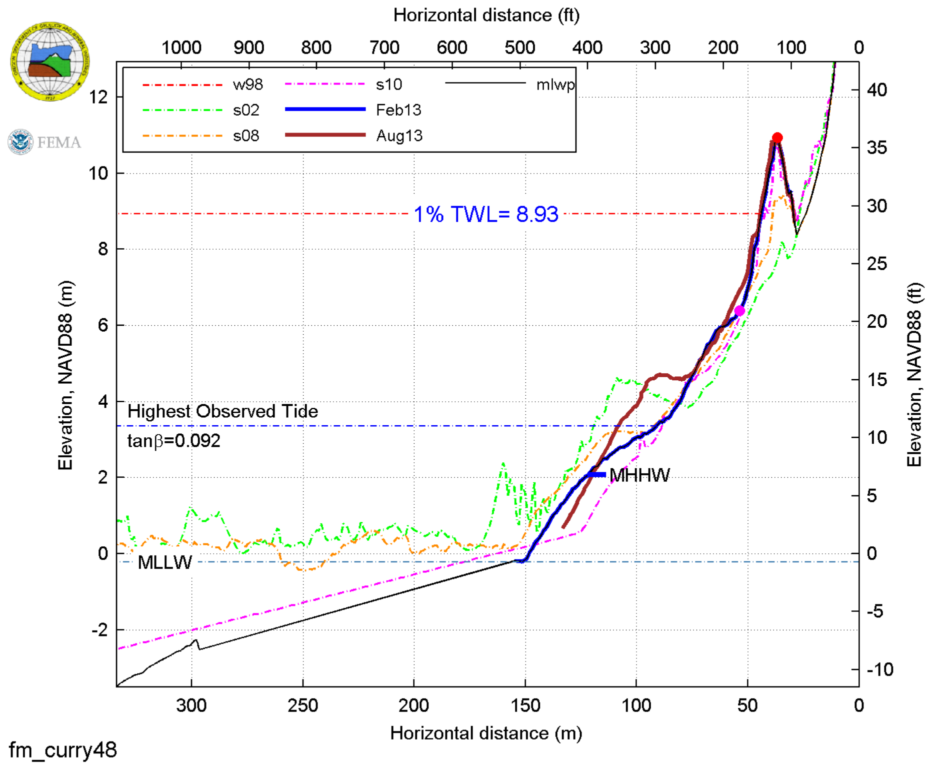

fm_curry 49

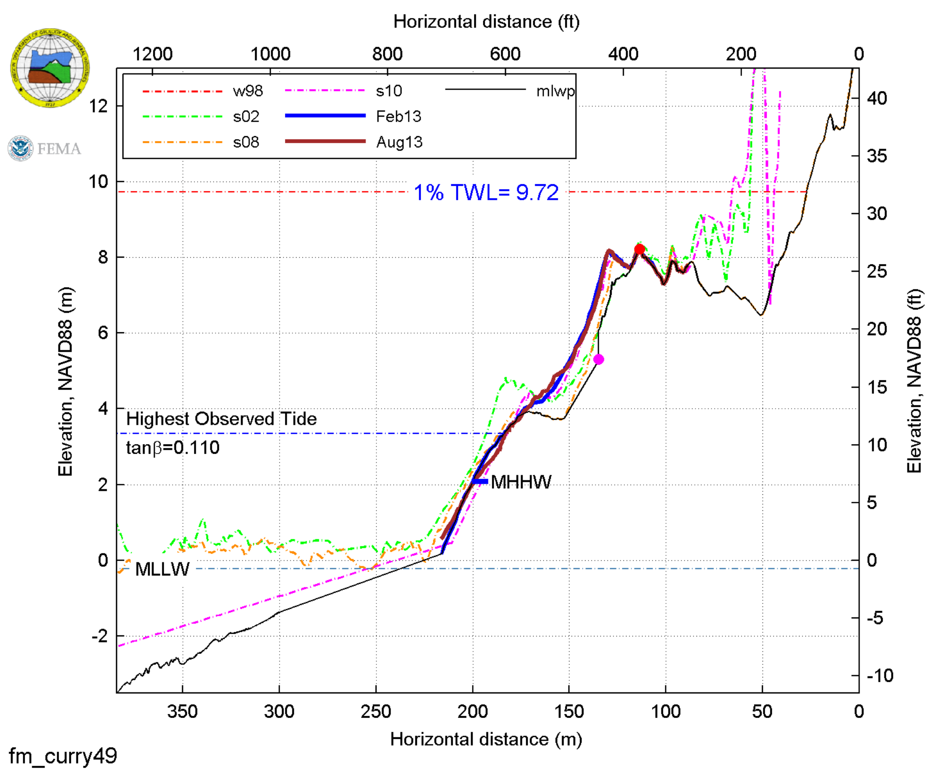

fm_curry 50

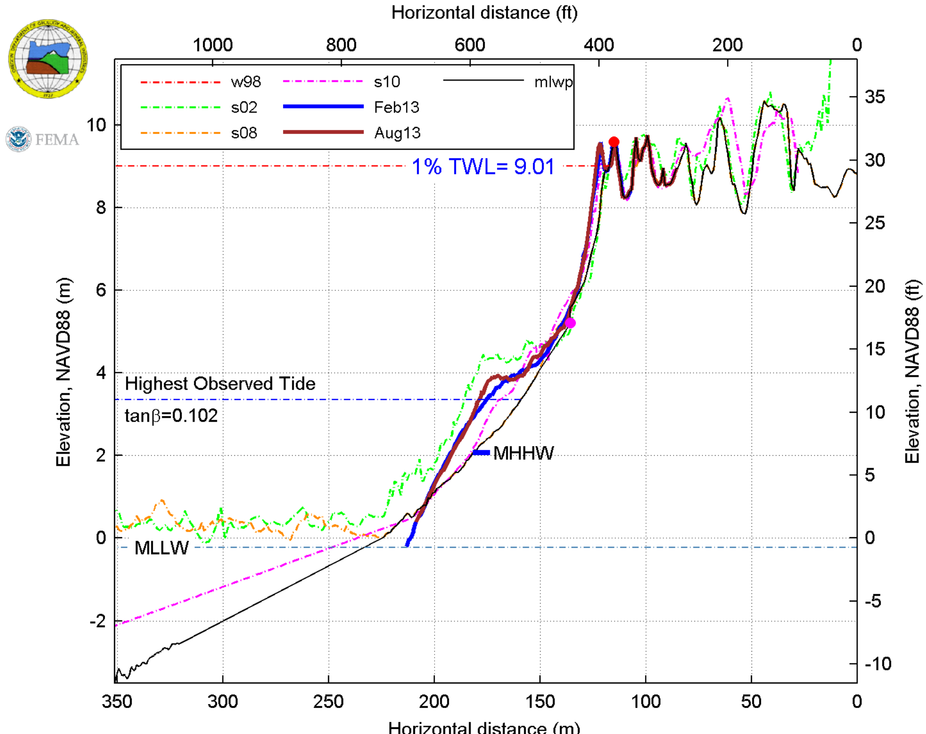

fm_curry50

fm_curry 51

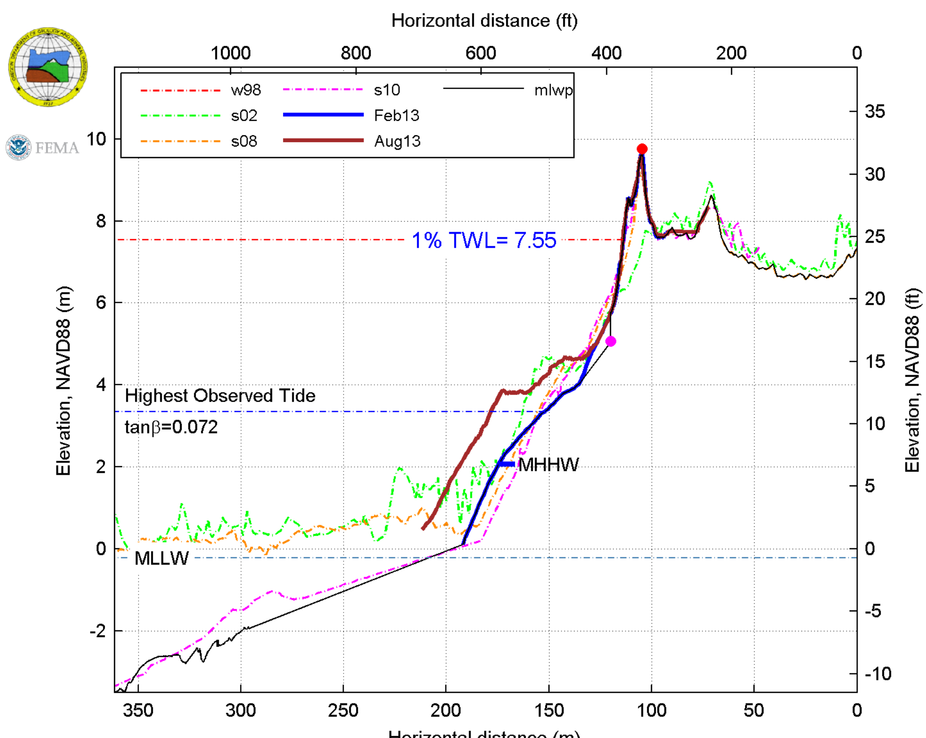

fm_curry51

fm_curry 52

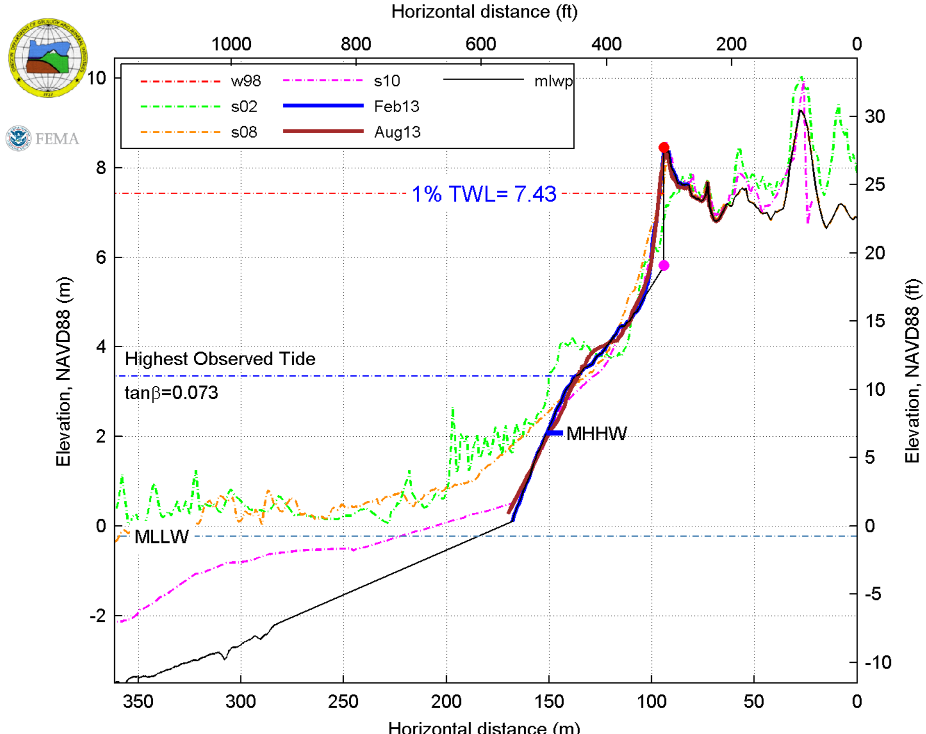

fm_curry52

fm_curry 53

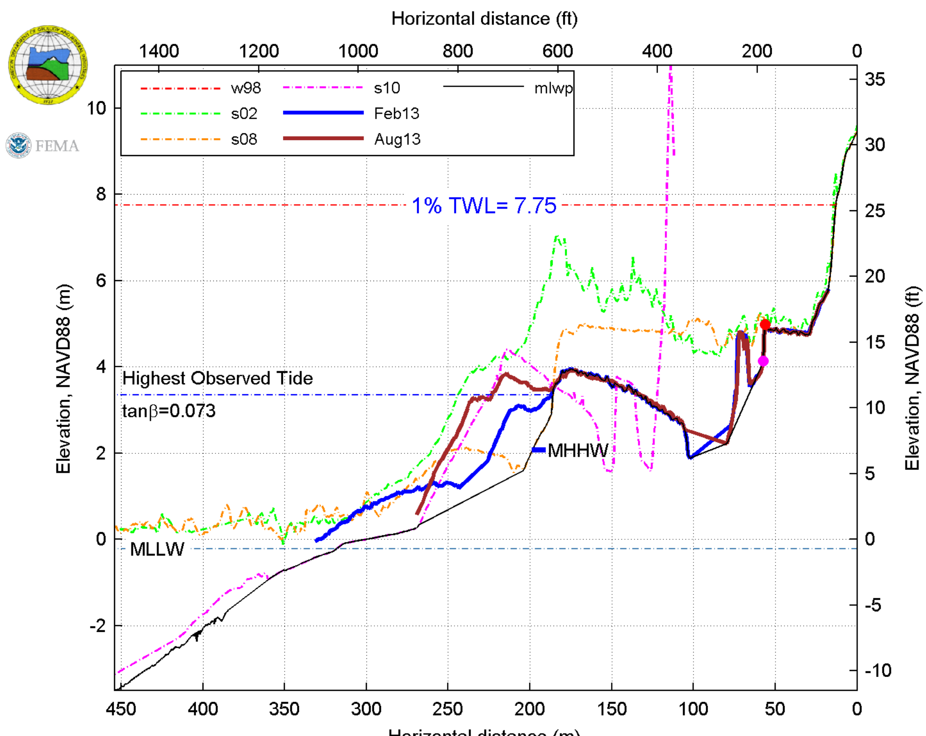

fm_curry53

fm_curry 54

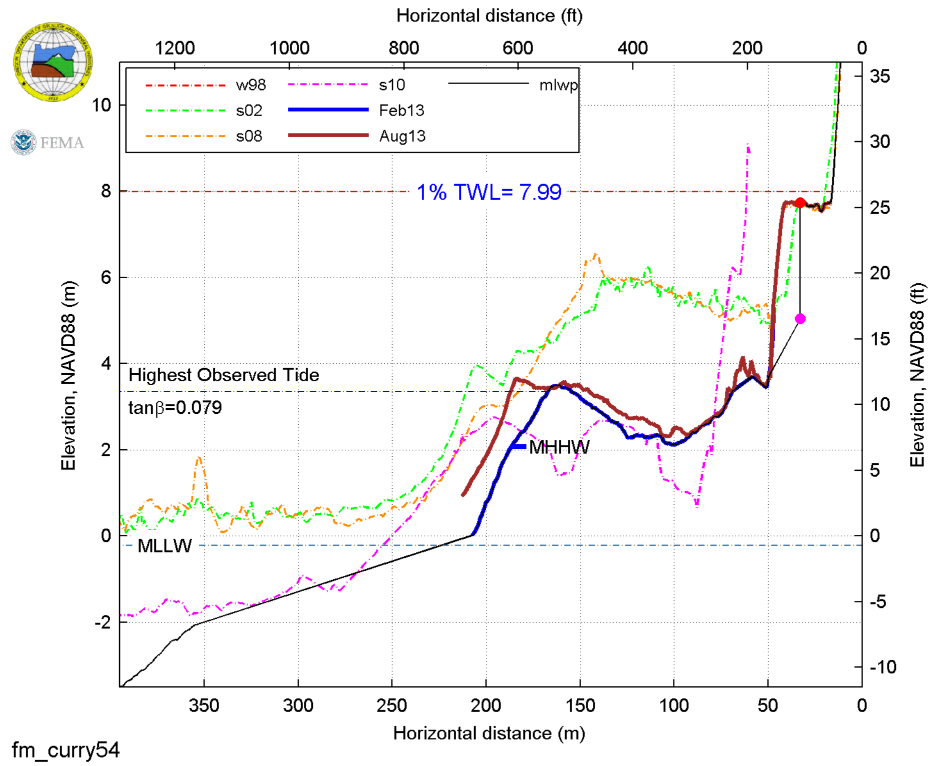

fm_curry 55

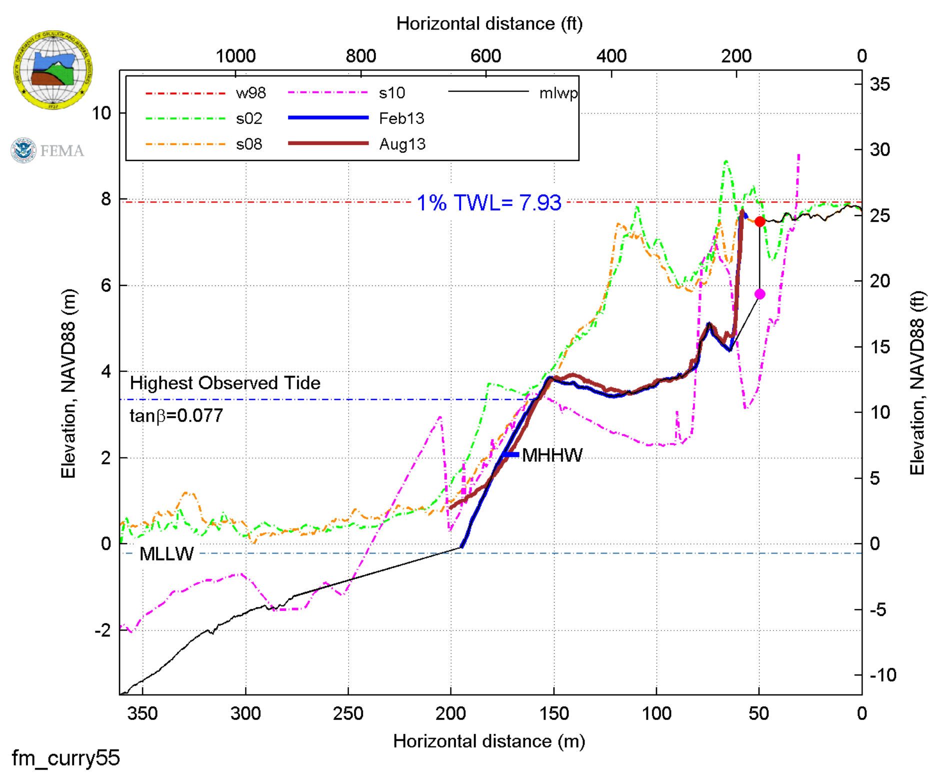

fm_curry 56

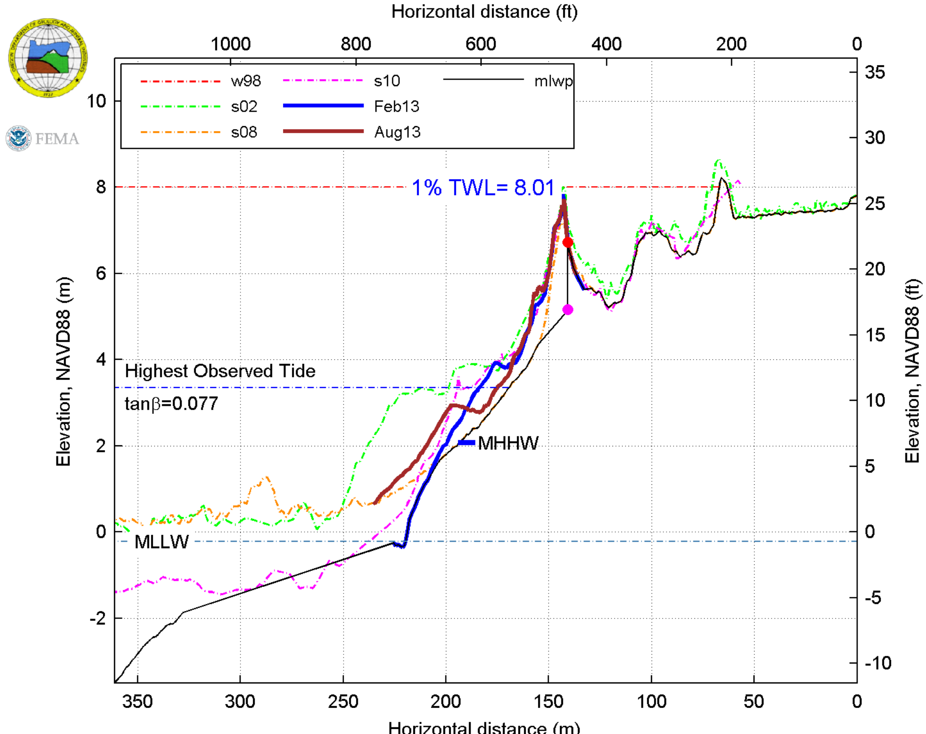

fm_curry56

fm_curry 57

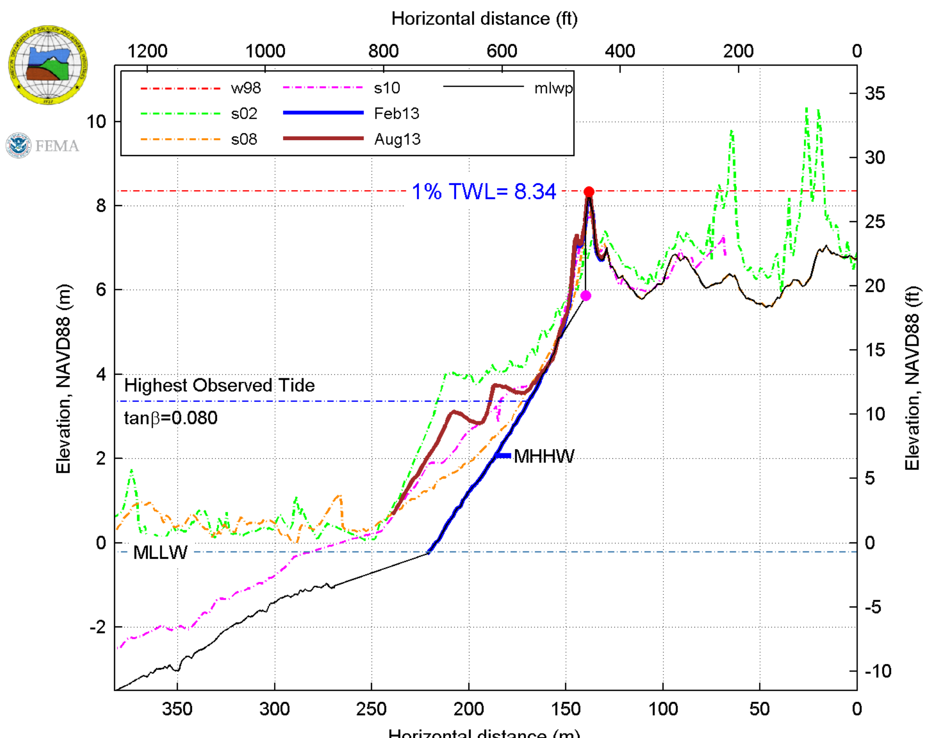

fm_curry57

fm_curry 58

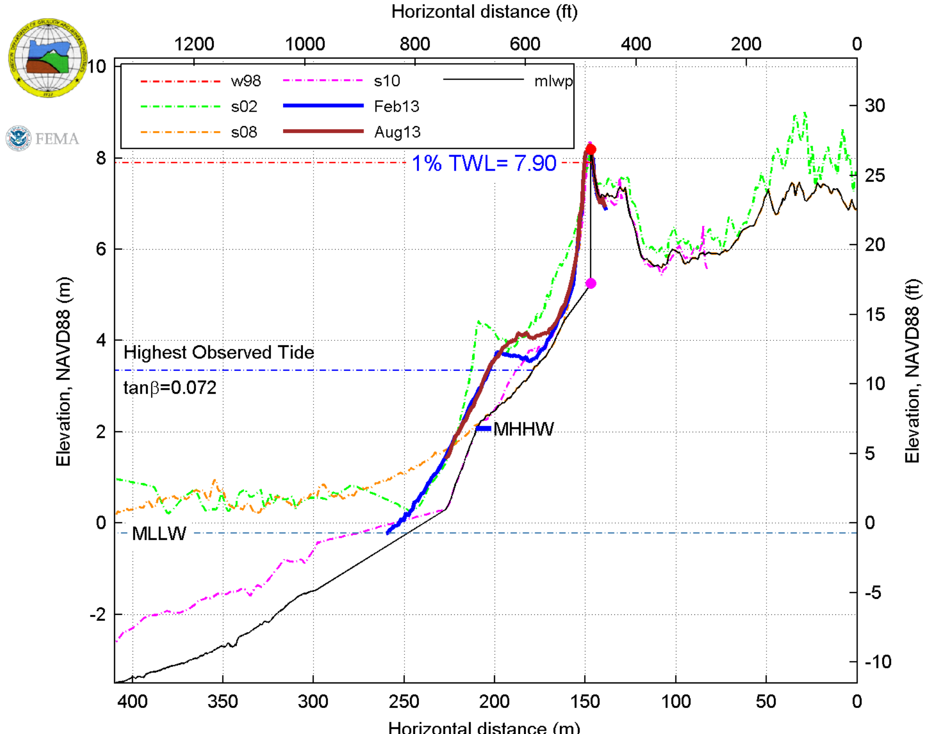

fm_curry 59

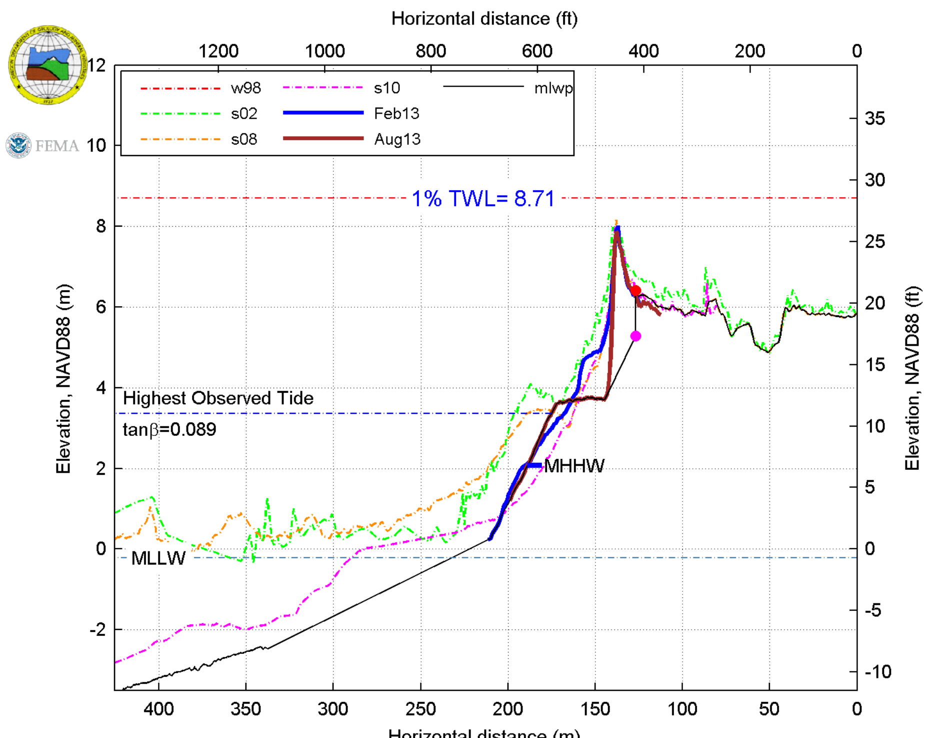

fm_curry 60

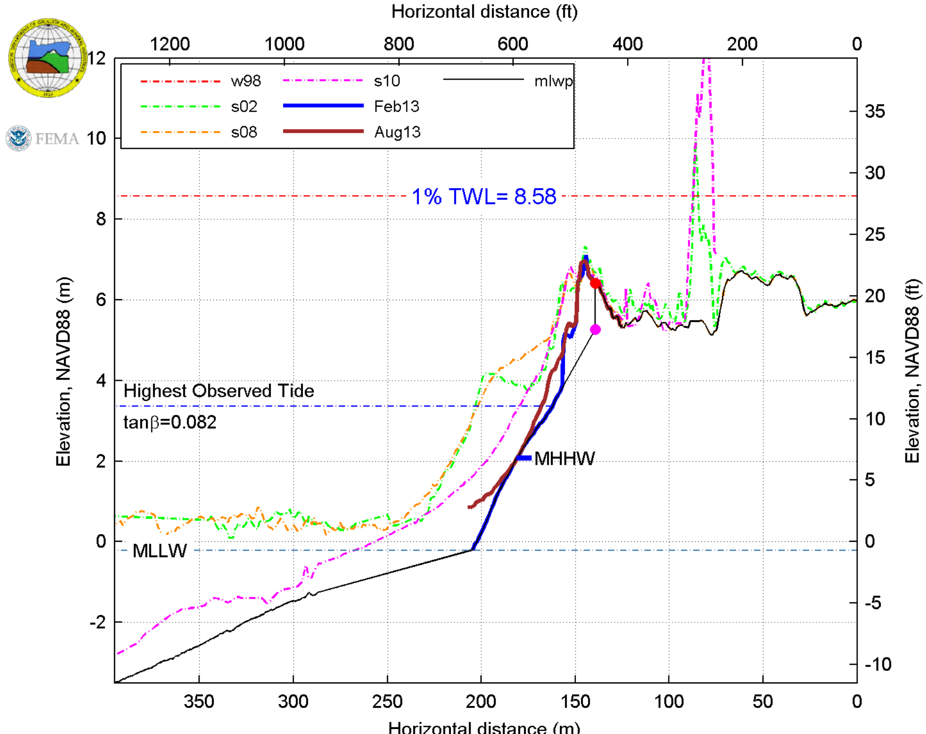

fm_curry60

fm_curry 61

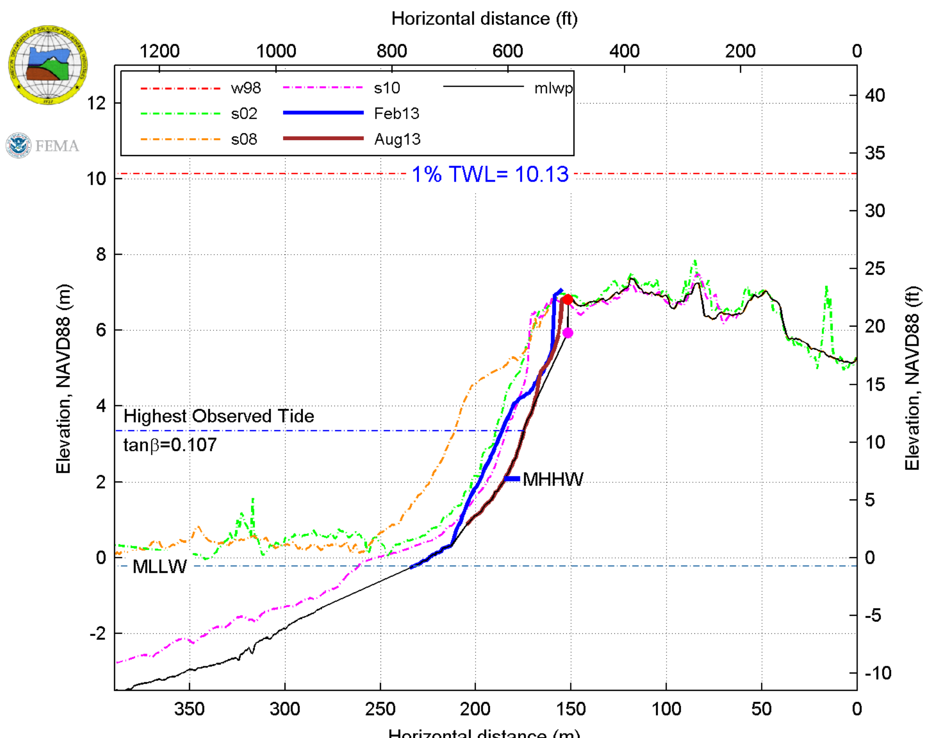

fm_curry61

11.2.3 Rogue Shores

fm_curry 62

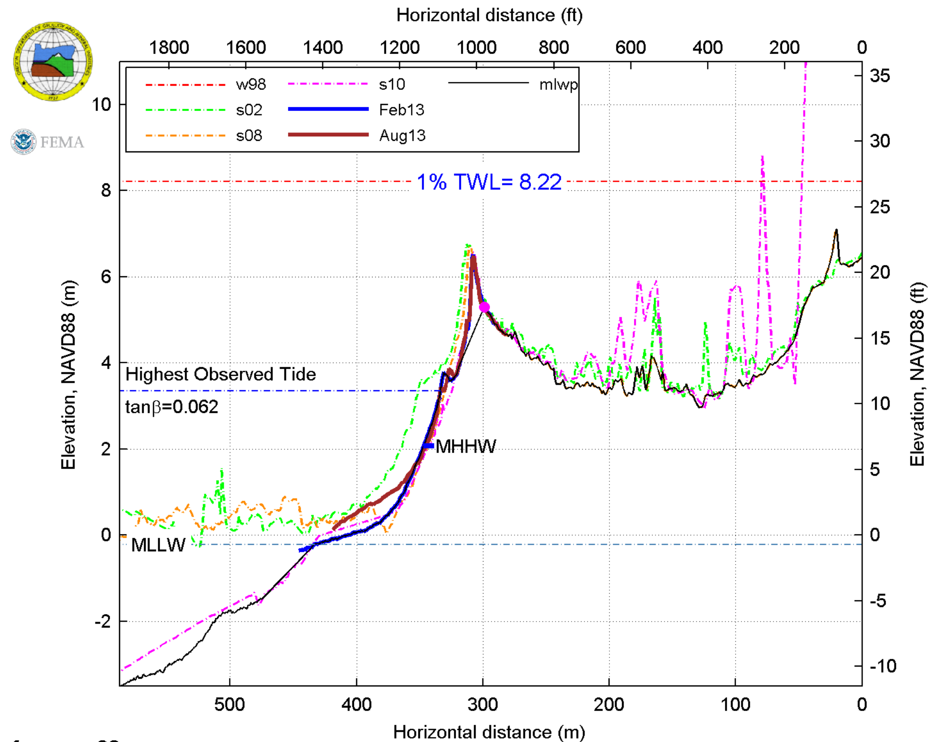

fm_curry62

fm_curry 63

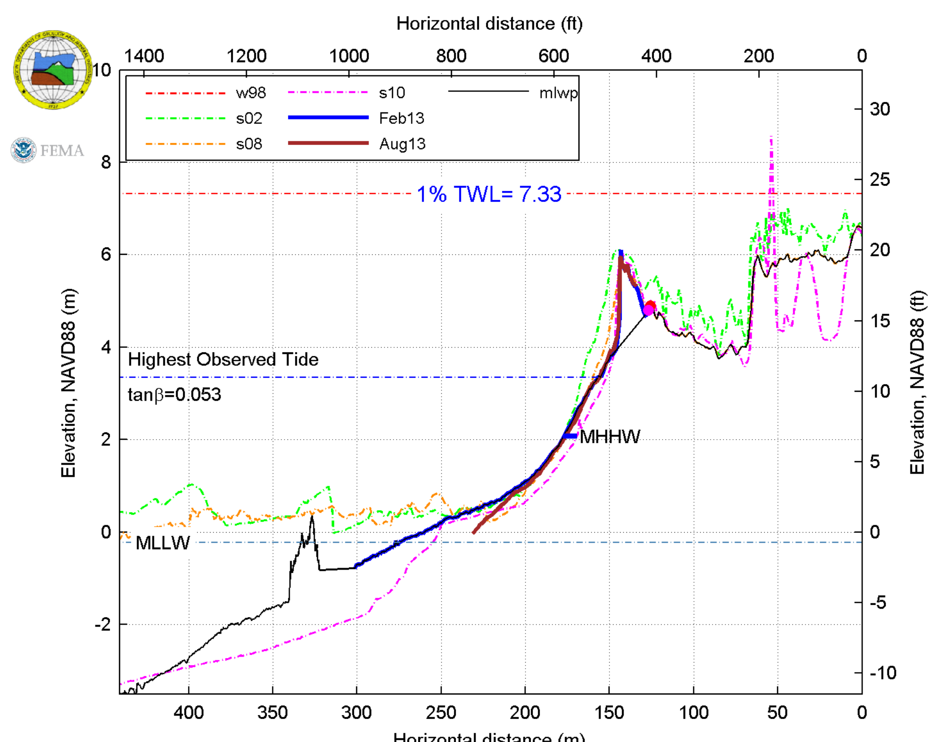

fm_curry63

fm_curry 64

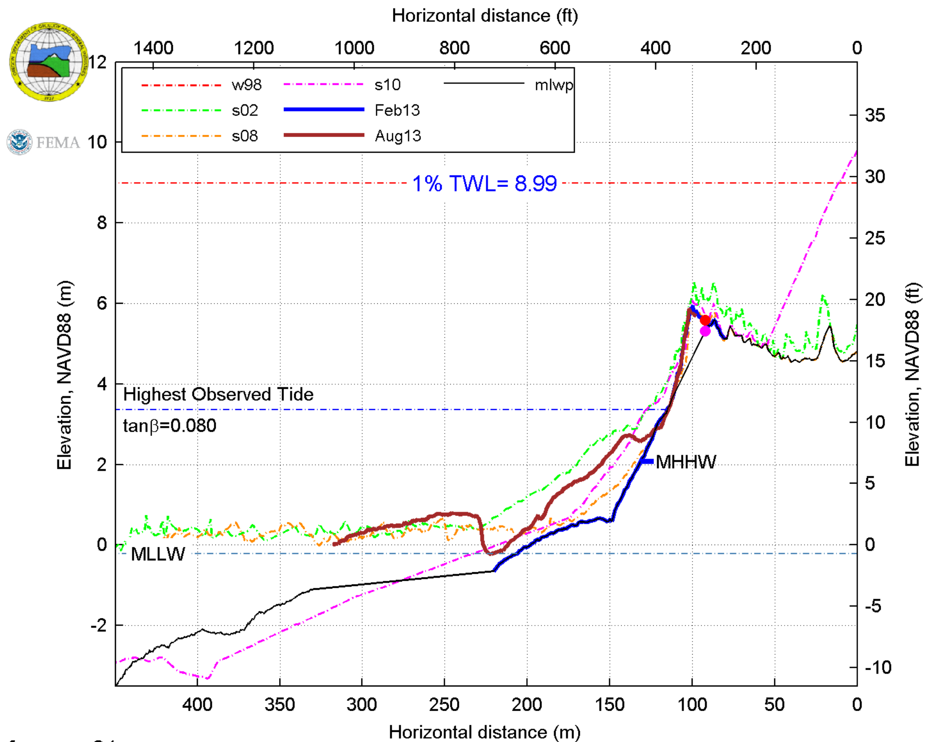

fm_curry64

fm_curry 65

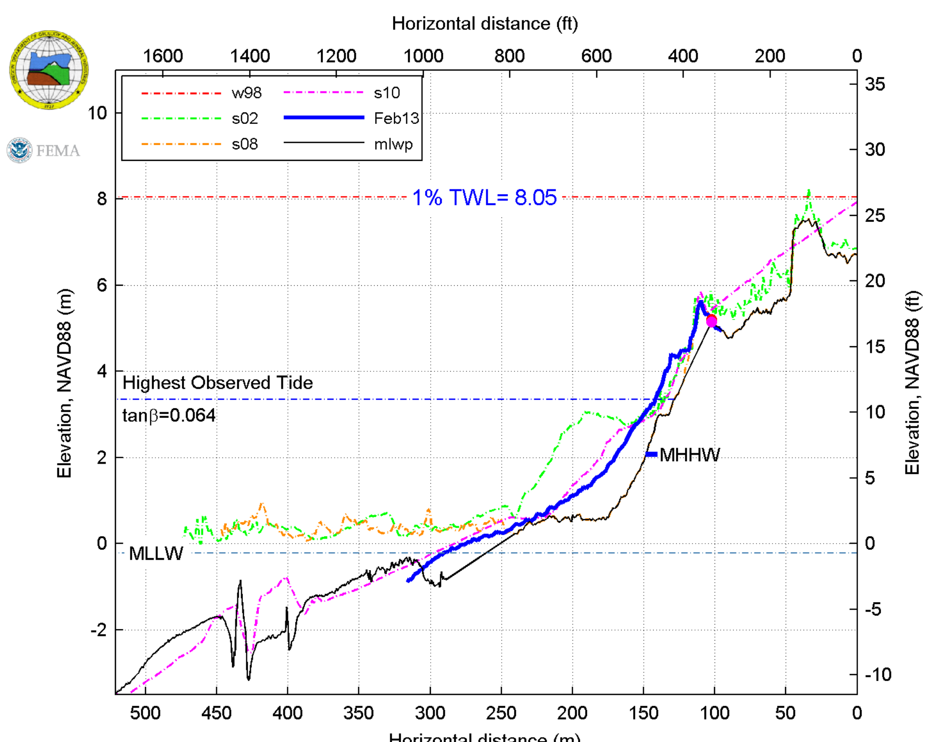

fm_curry65

fm_curry 66

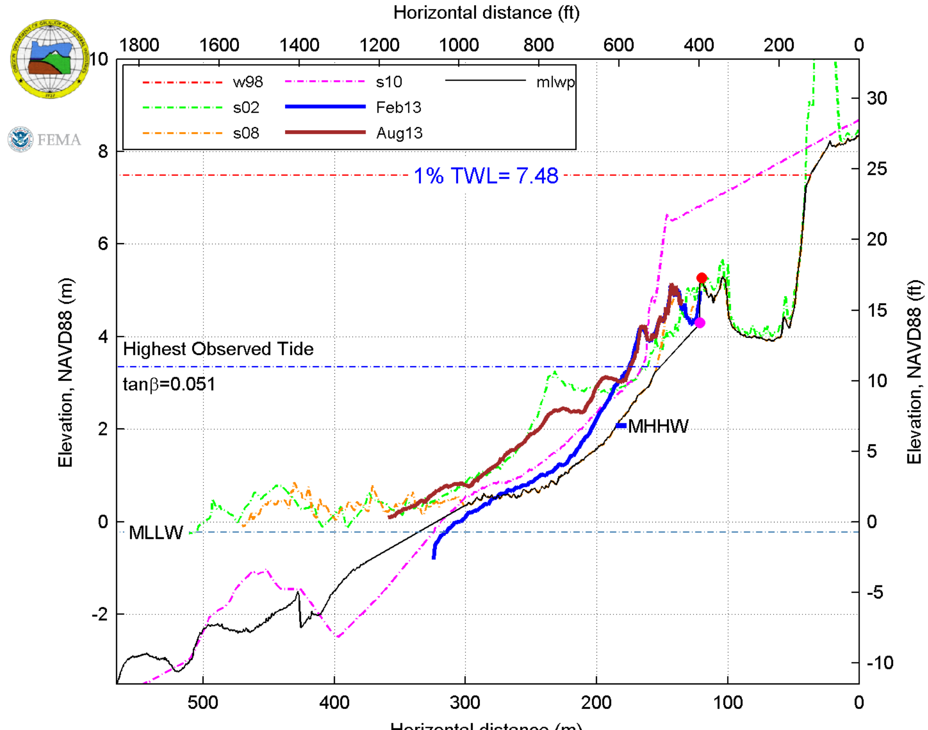

fm_curry66

fm_curry 67

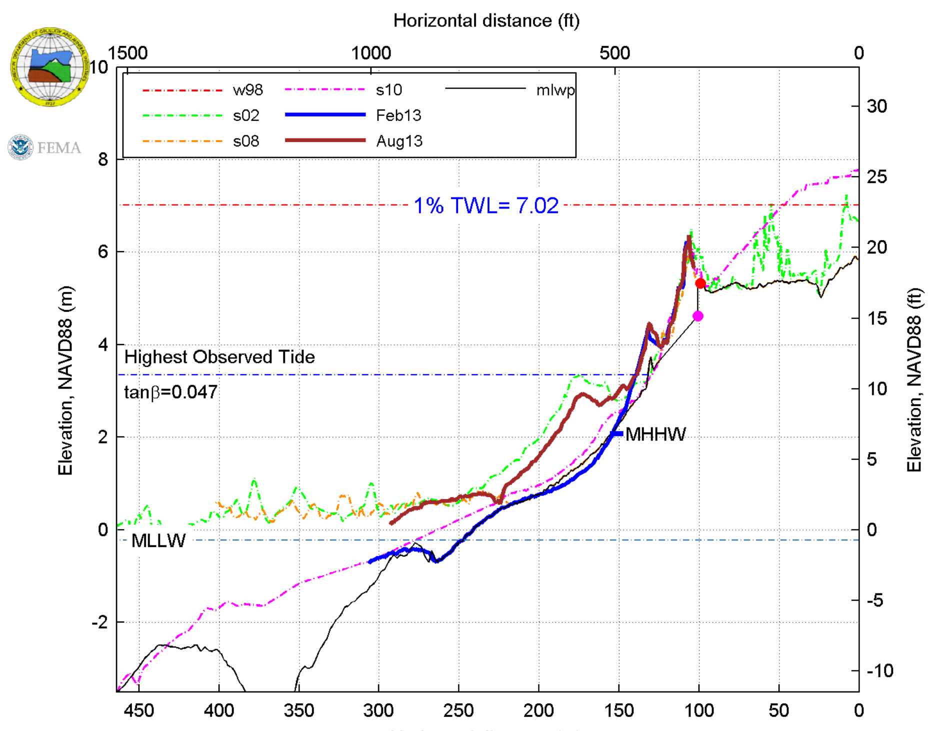

fm_curry67

fm_curry 68

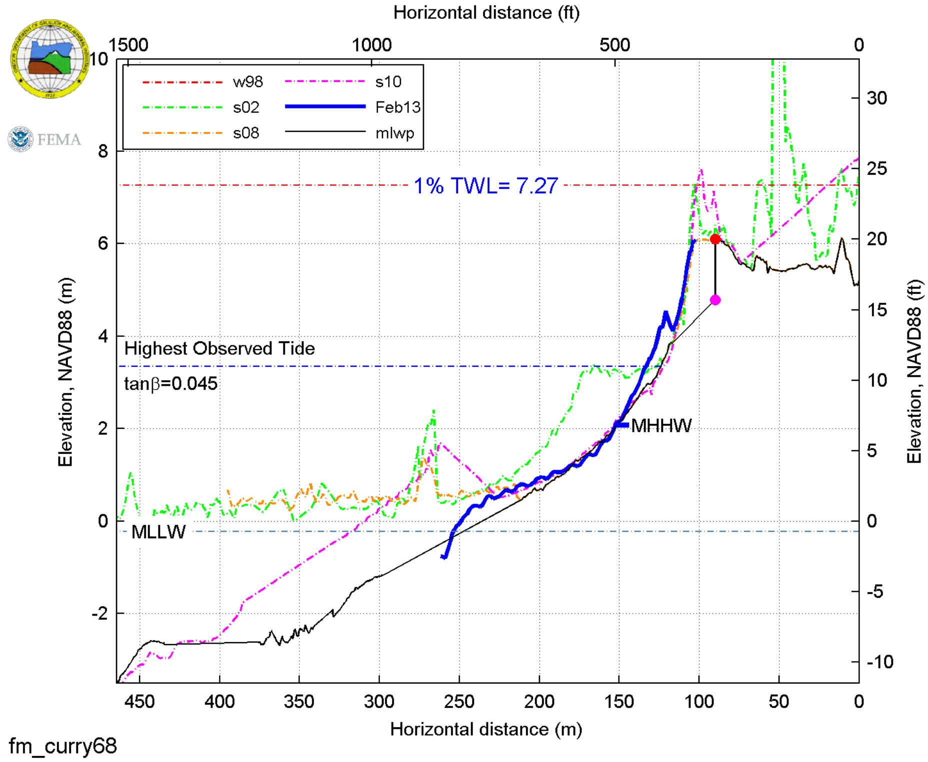

fm_curry 69

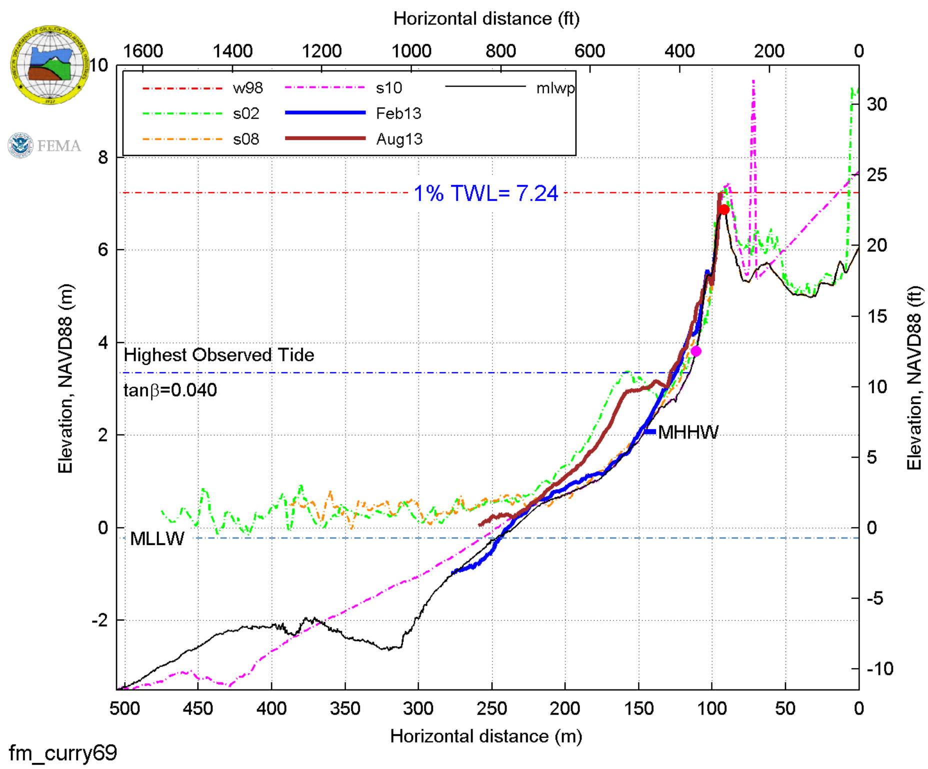

fm_curry 70

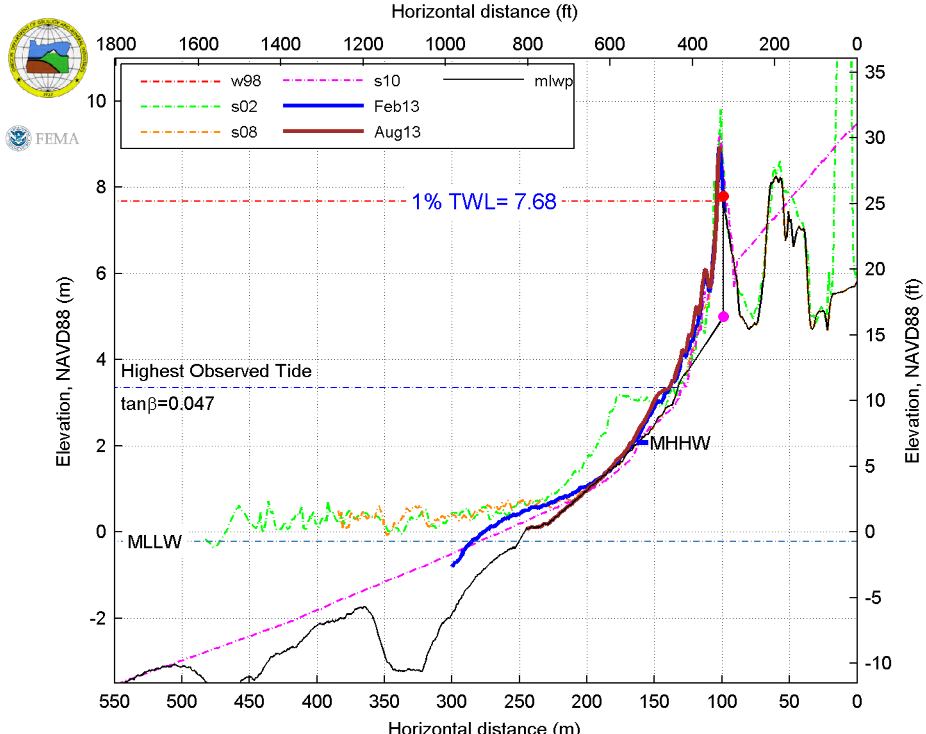

fm_curry70

fm_curry 71

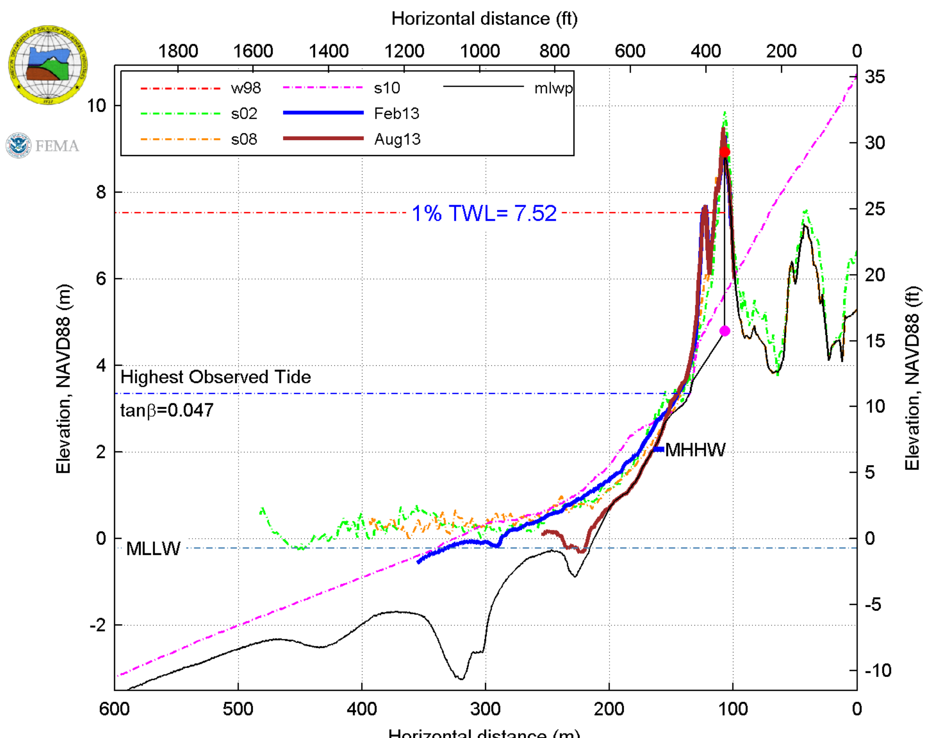

fm_curry71

fm_curry 72

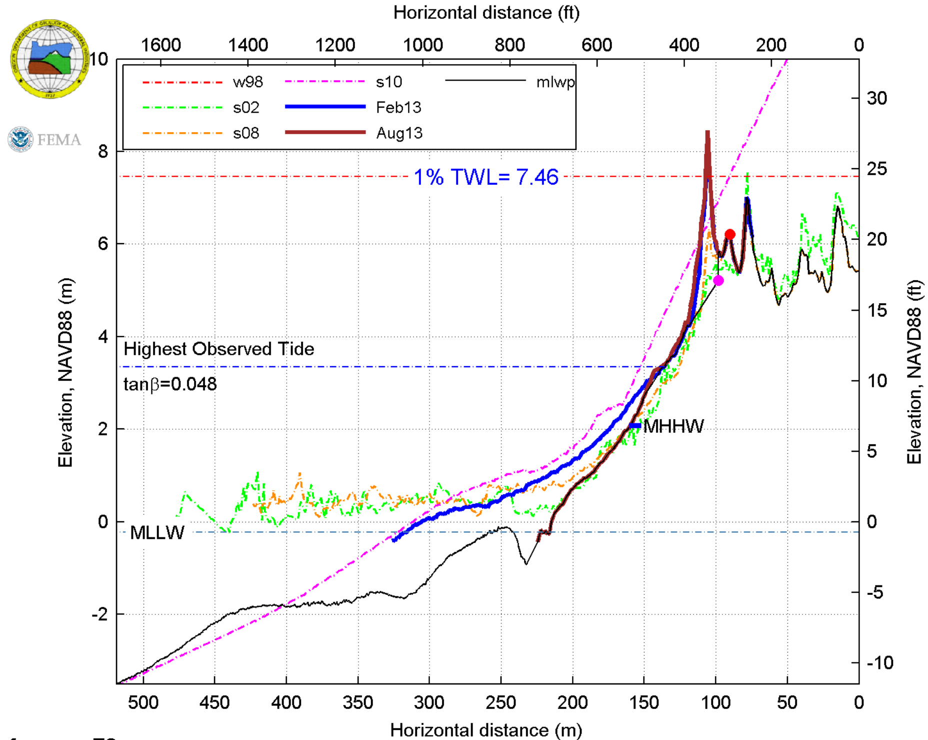

fm_curry72

fm_curry 73

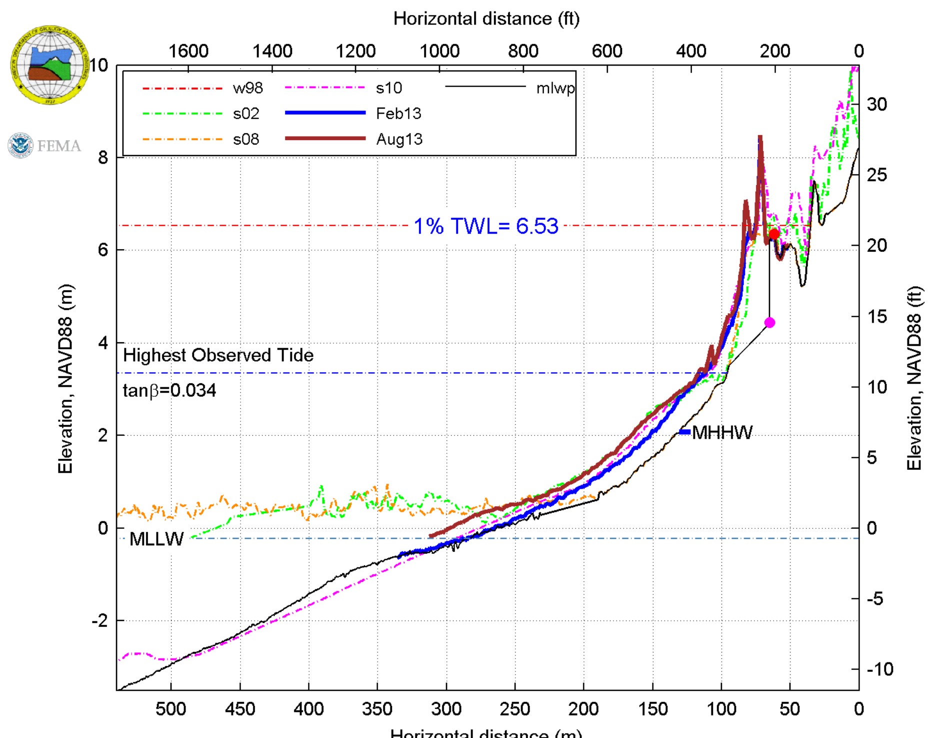

fm_curry73

fm_curry 74

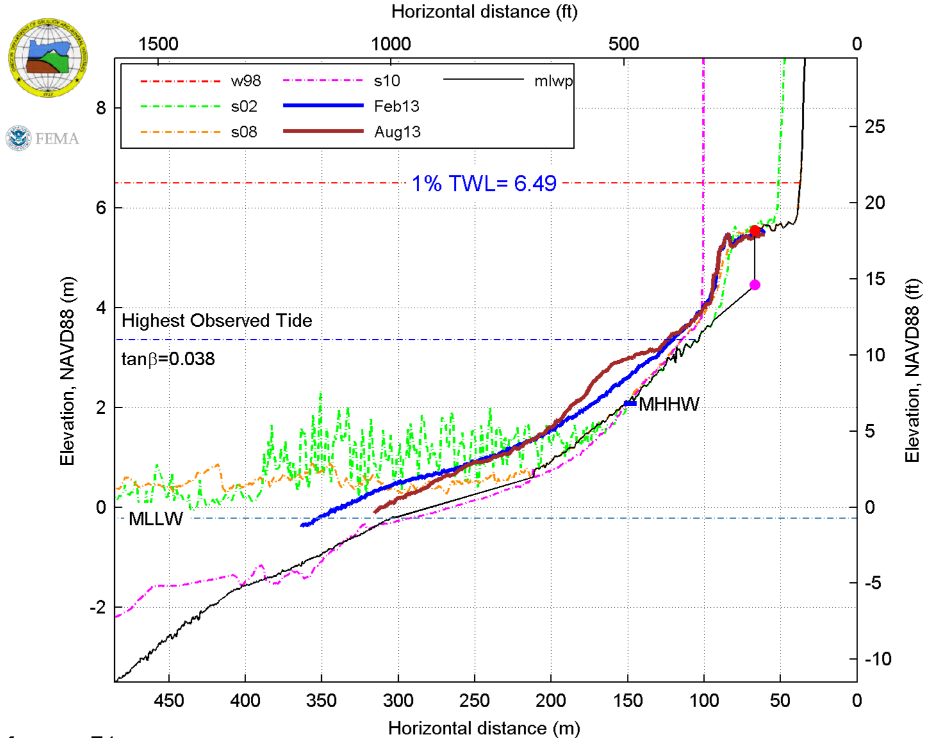

fm_curry74

11.2.4 Nesika Beach

fm_curry 75

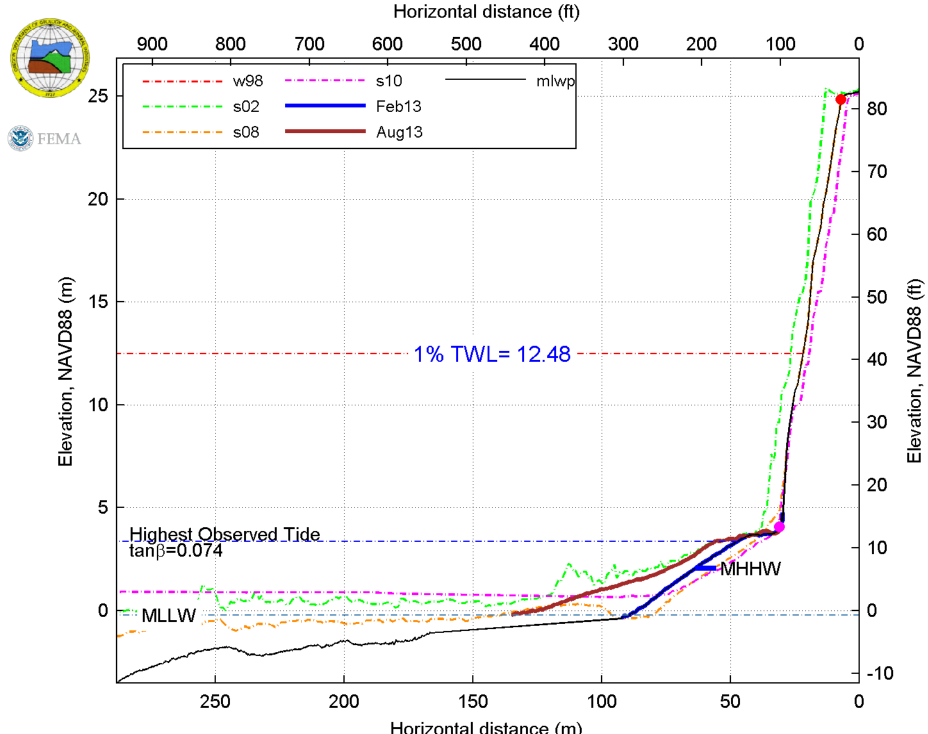

fm_curry75

fm_curry 76

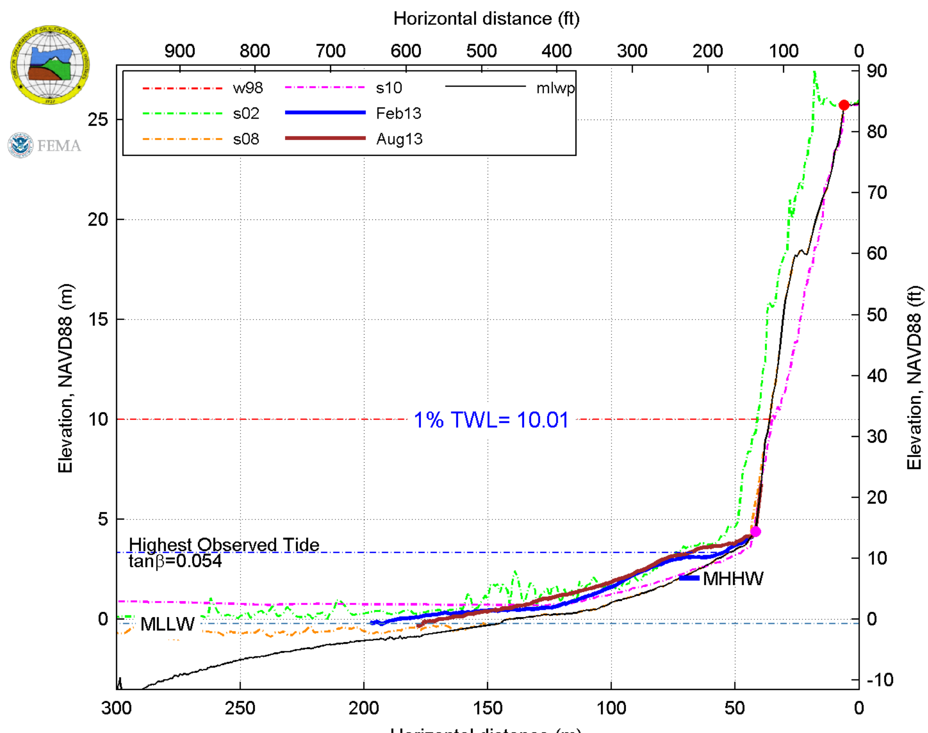

fm_curry76

fm_curry 77

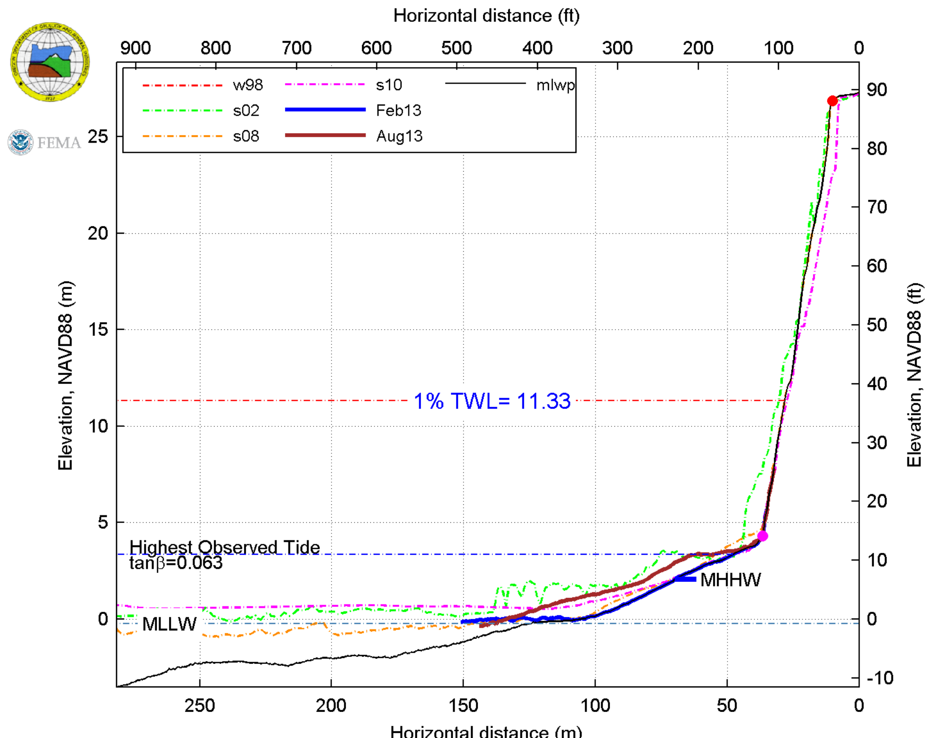

fm_curry77

fm_curry 78

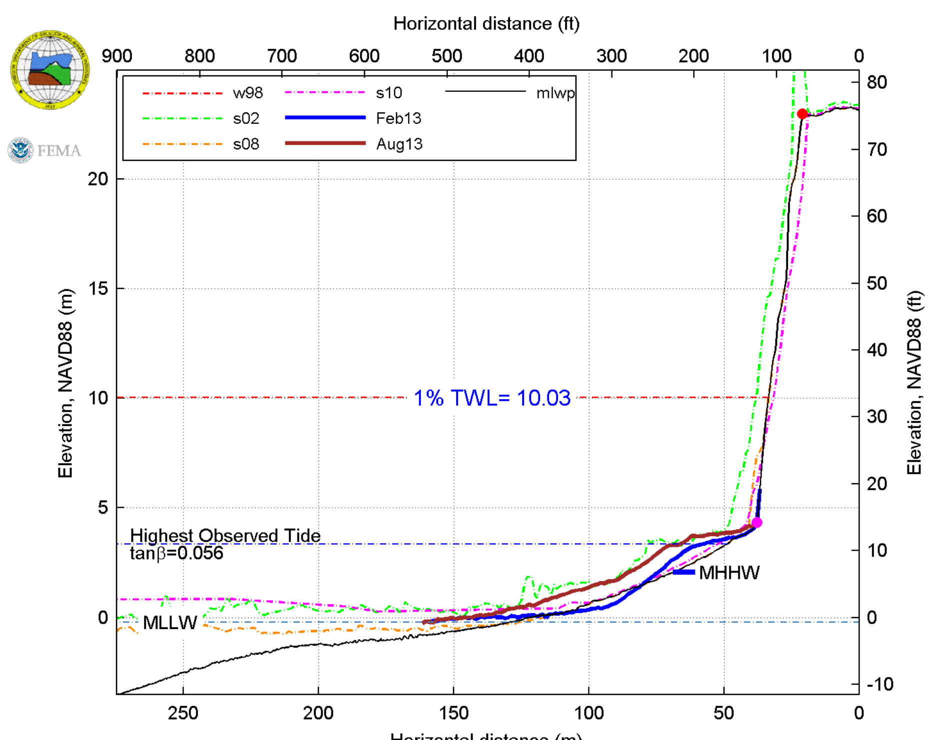

fm_curry78

fm_curry 79

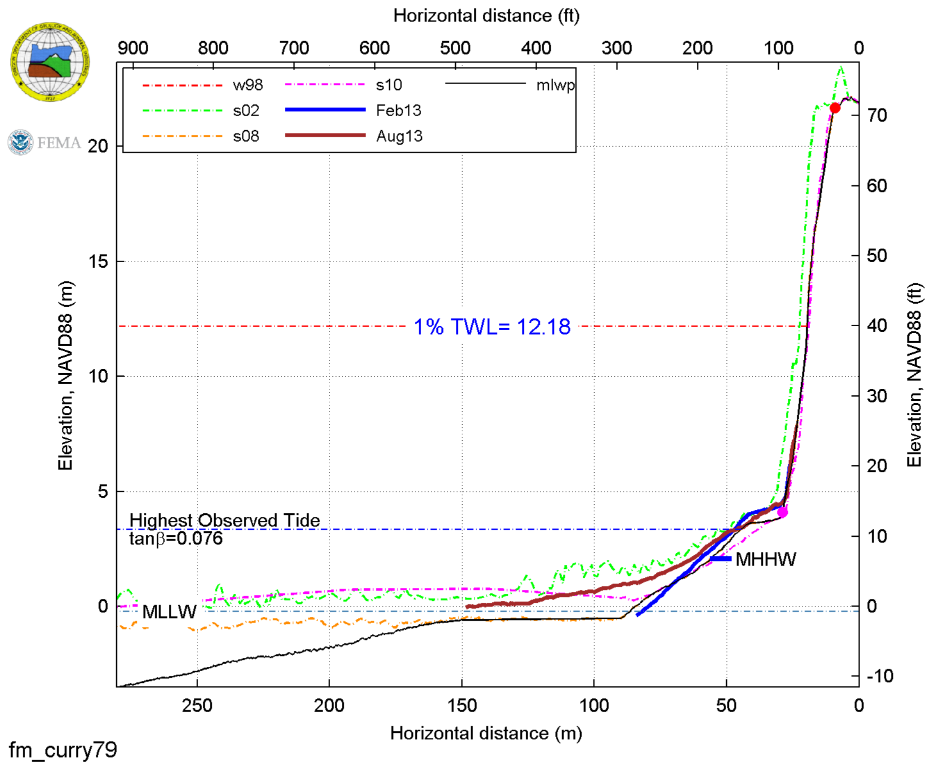

fm_curry 80

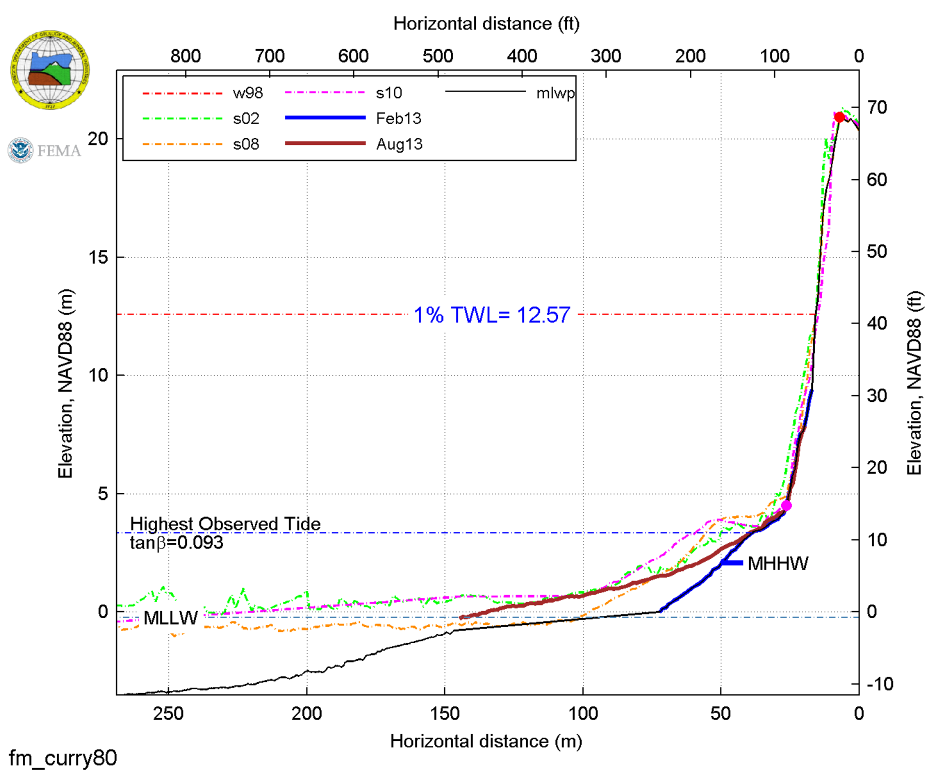

fm_curry 81

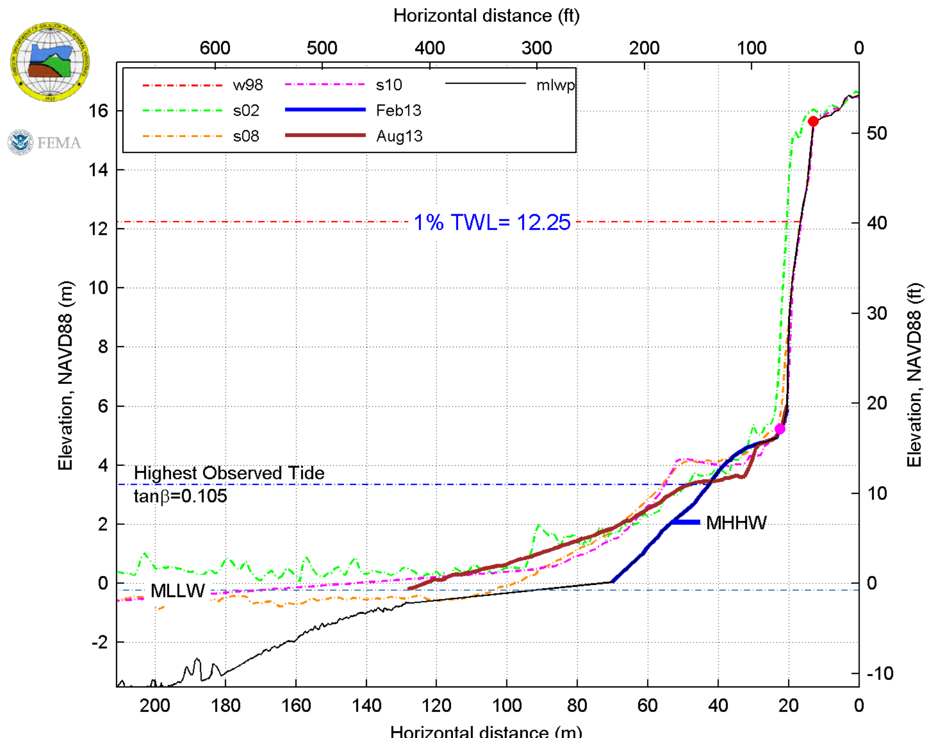

fm_curry81

fm_curry 82

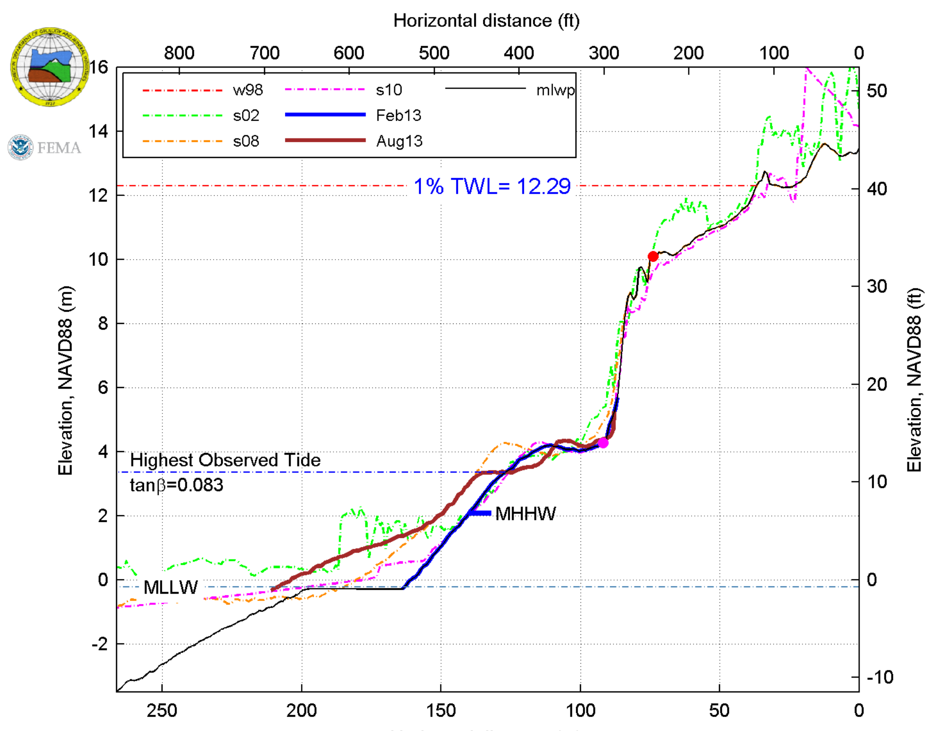

fm_curry82

fm_curry 83

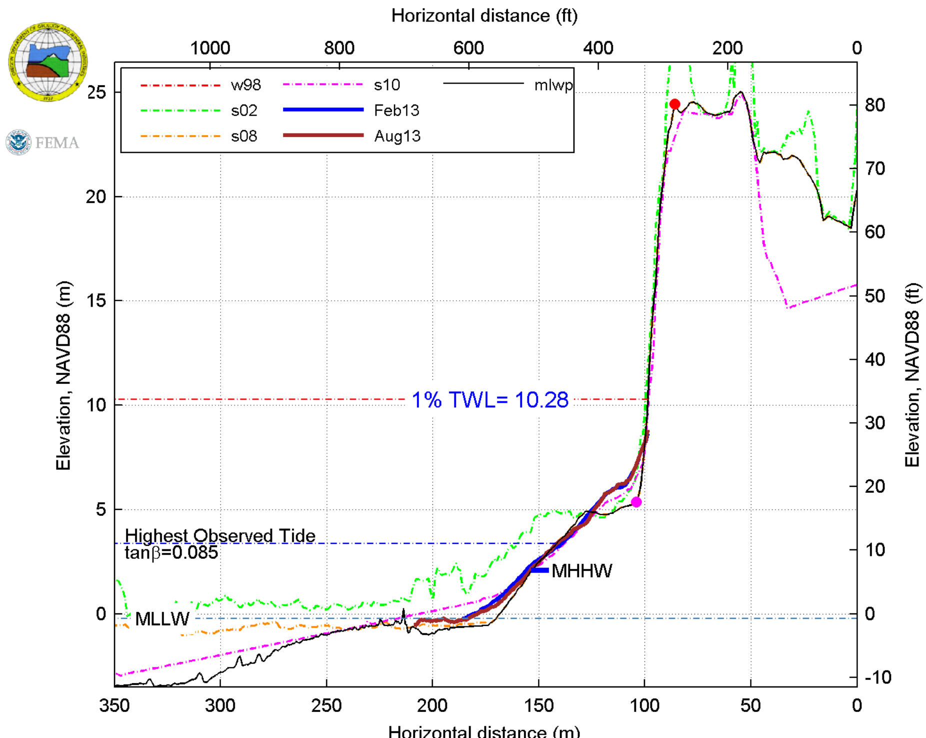

fm_curry83

fm_curry 84

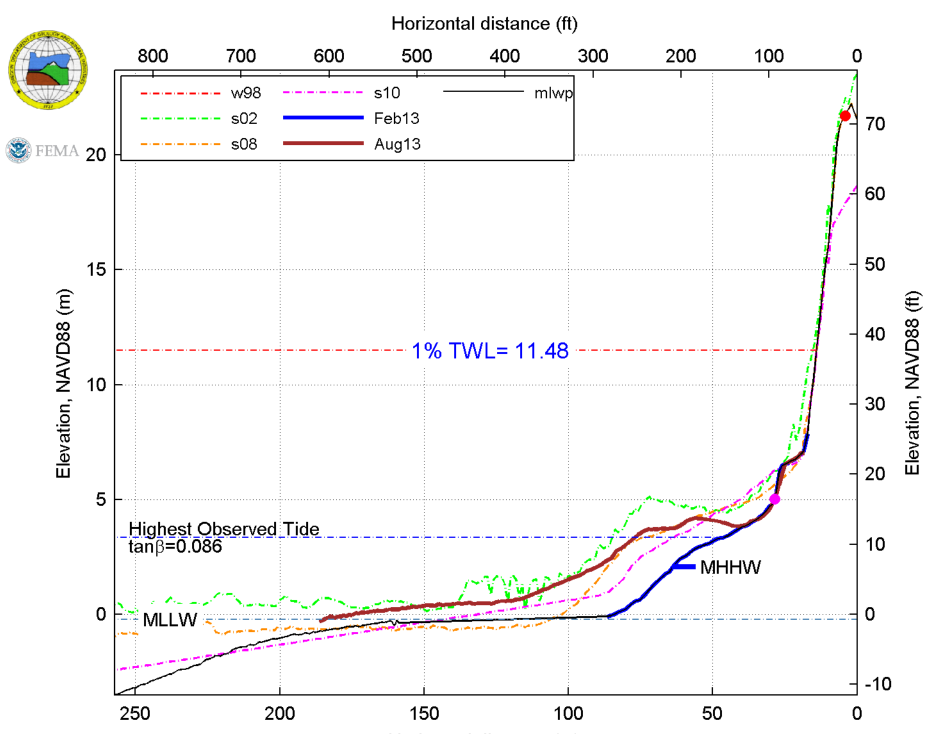

fm_curry84

fm_curry 85

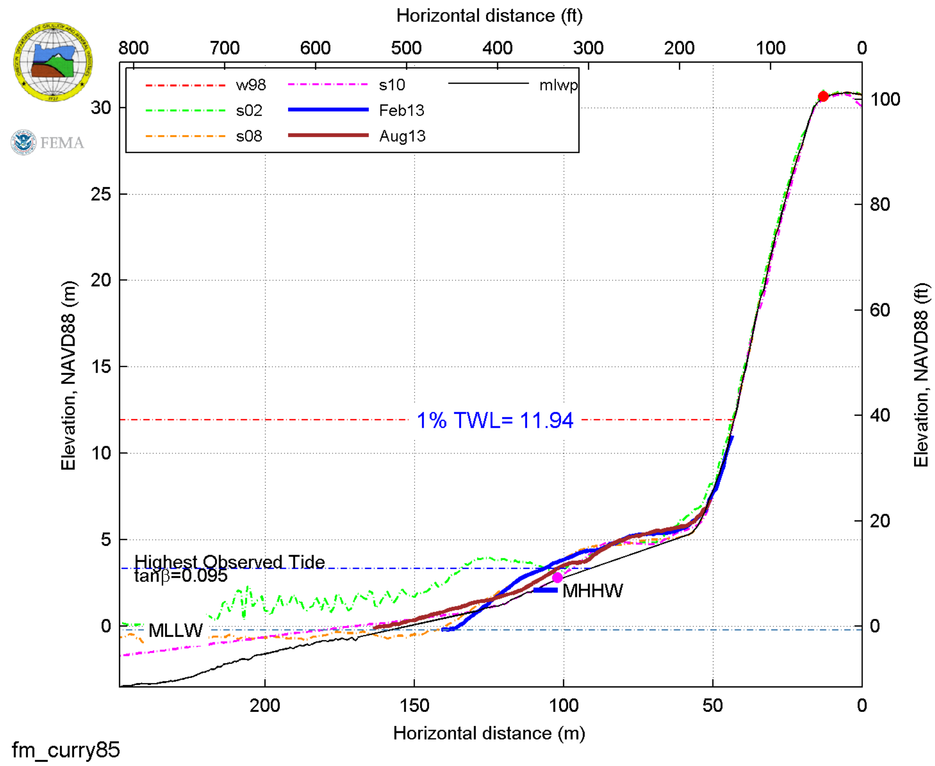

fm_curry 86

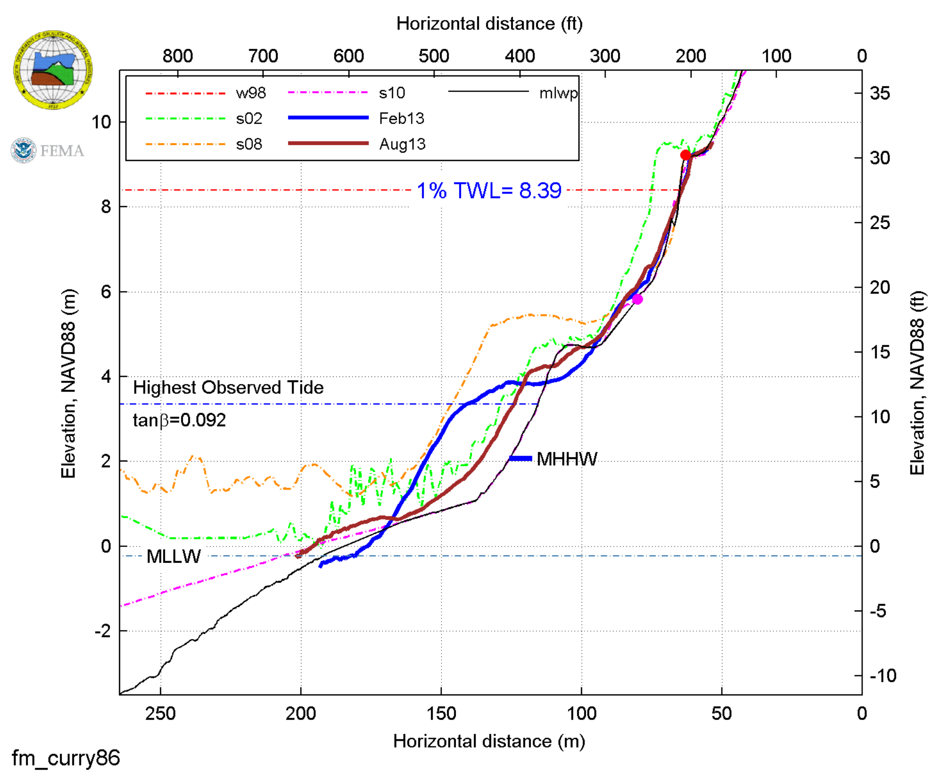

fm_curry 87

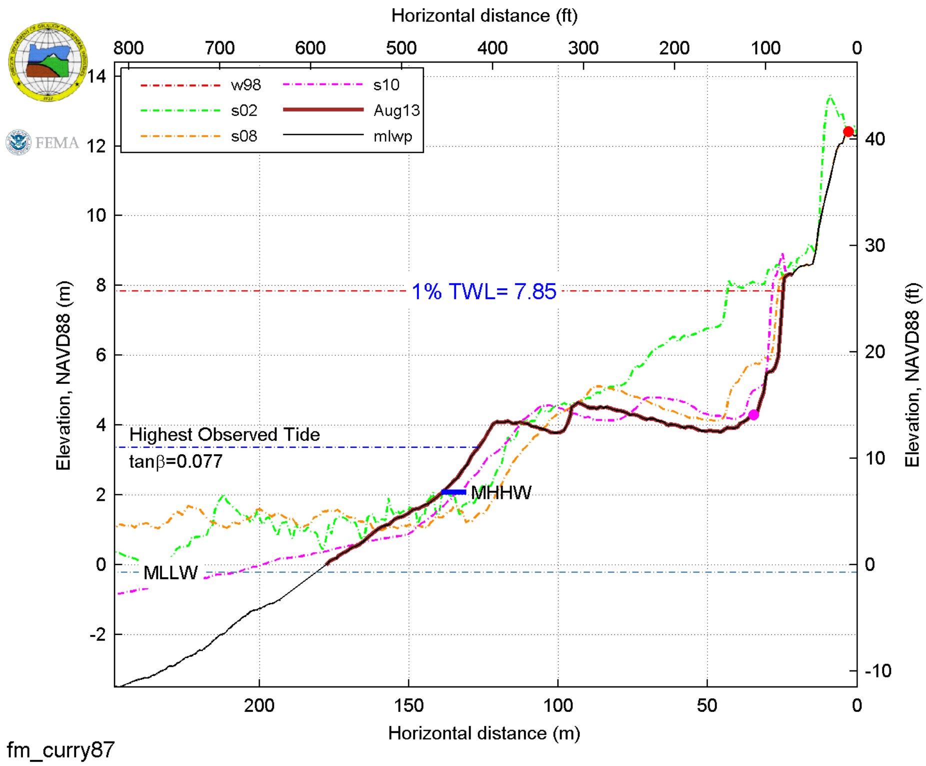

fm_curry 88

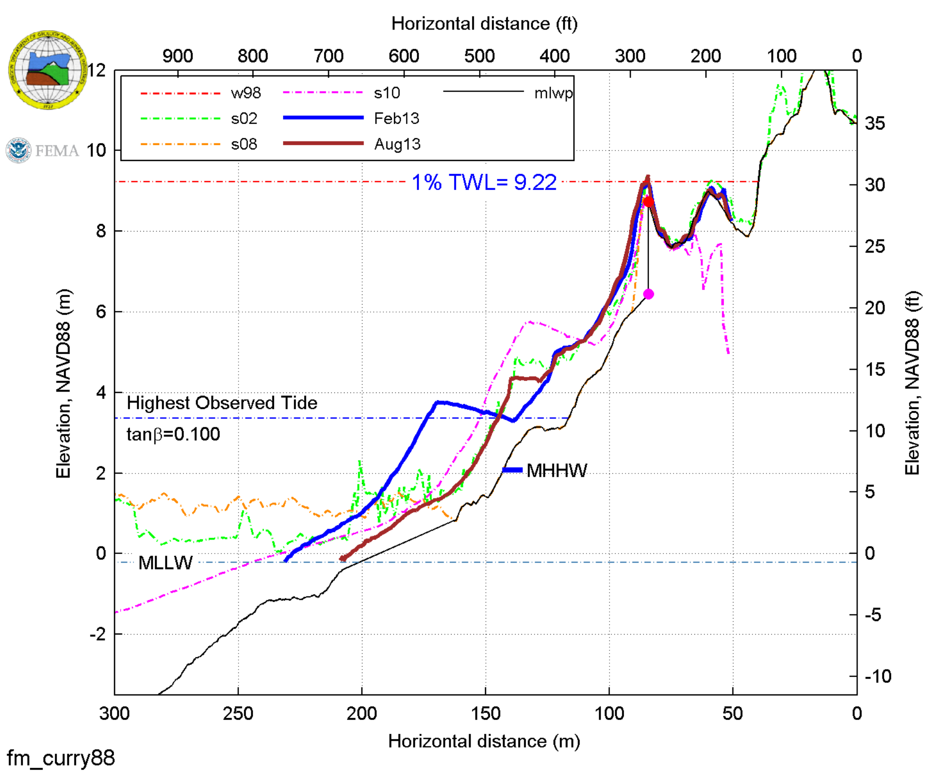

fm_curry 89

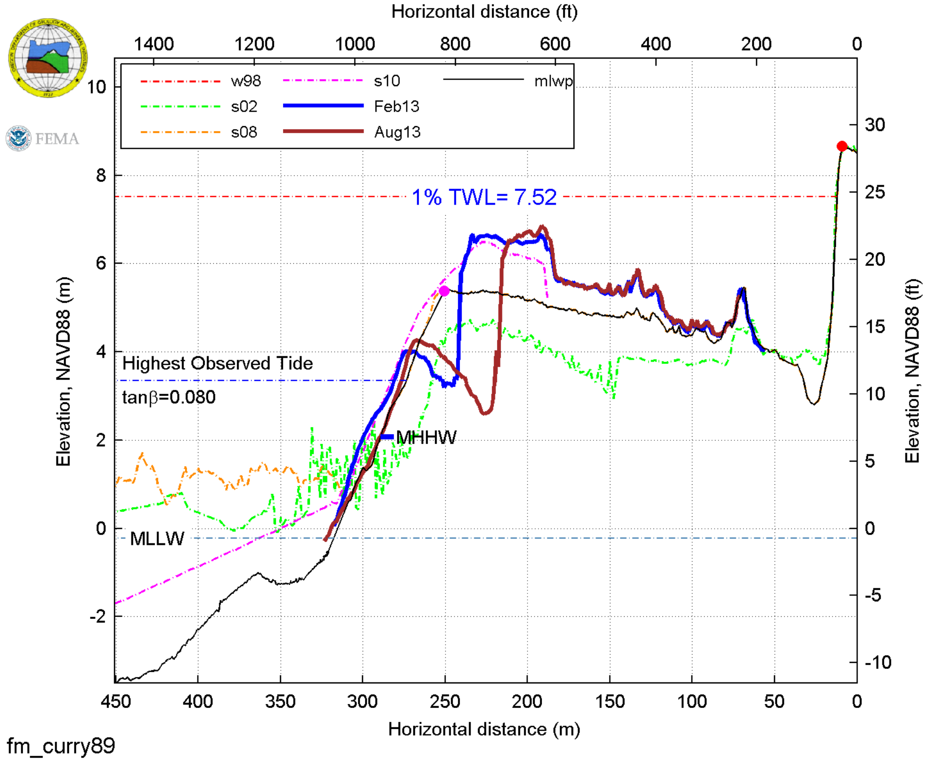

fm_curry 90

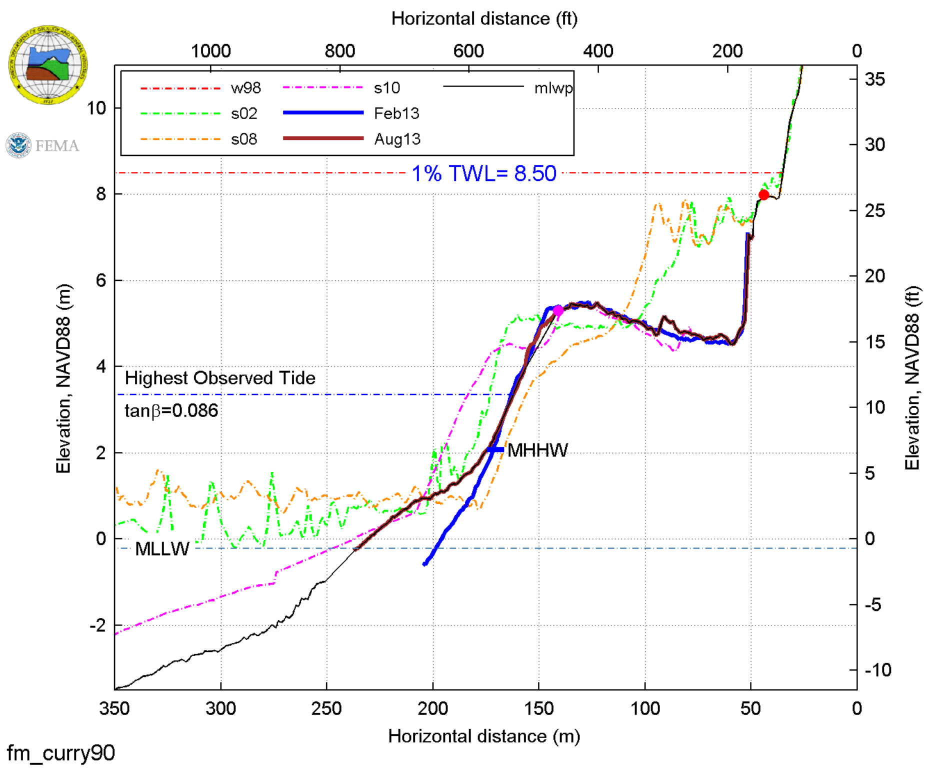

fm_curry 91

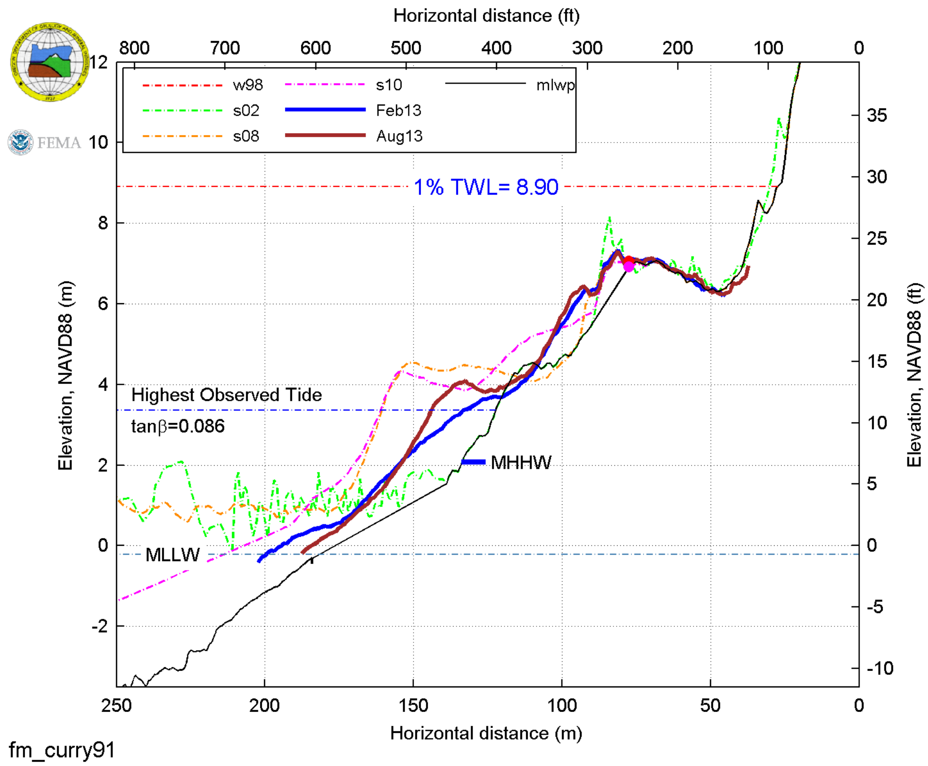

fm_curry 92

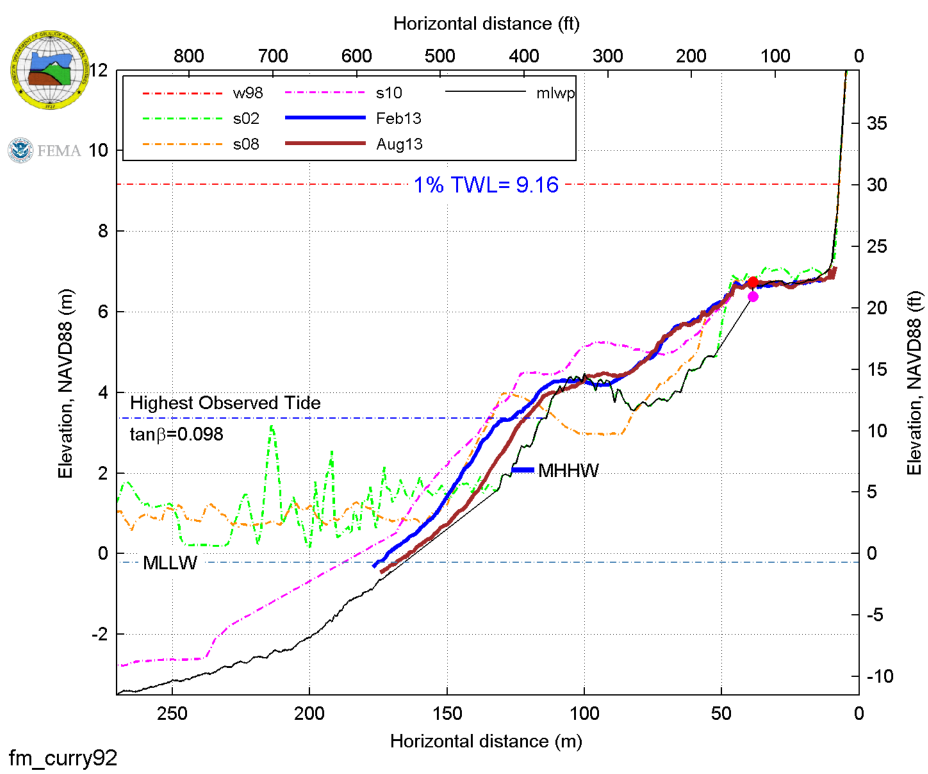

fm_curry 93

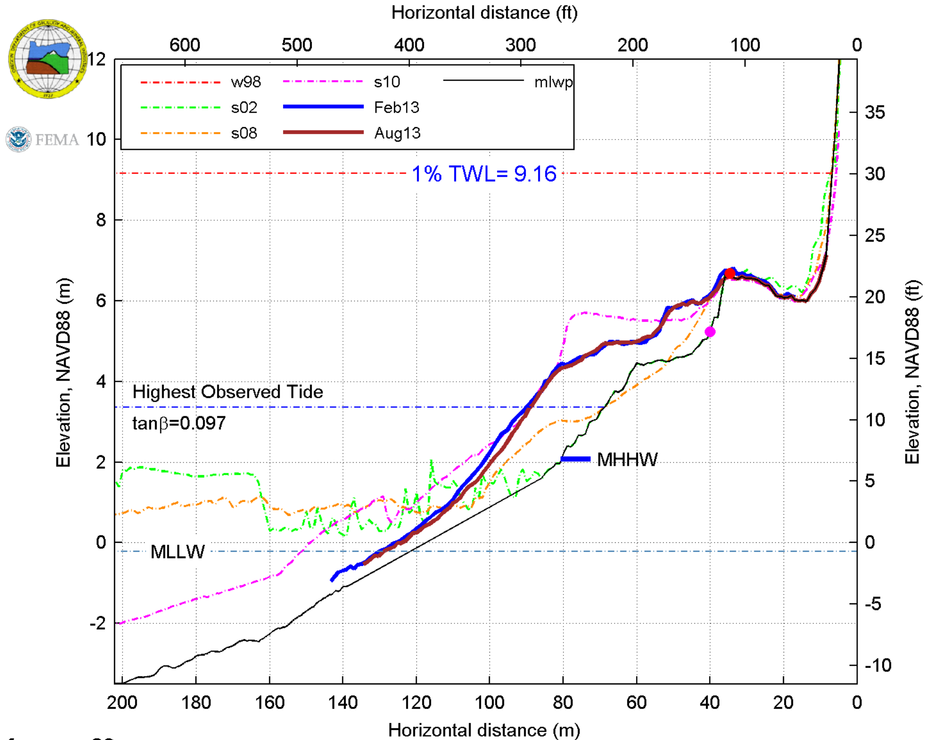

fm_curry93

11.2.5 Port Orford

fm_curry 94

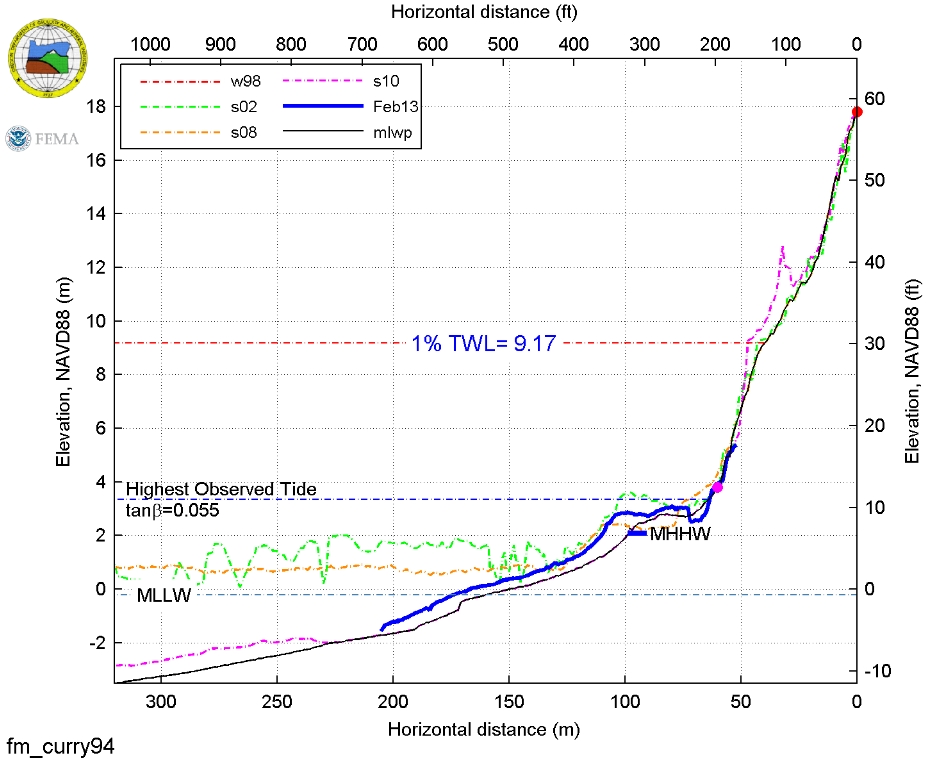

fm_curry 95

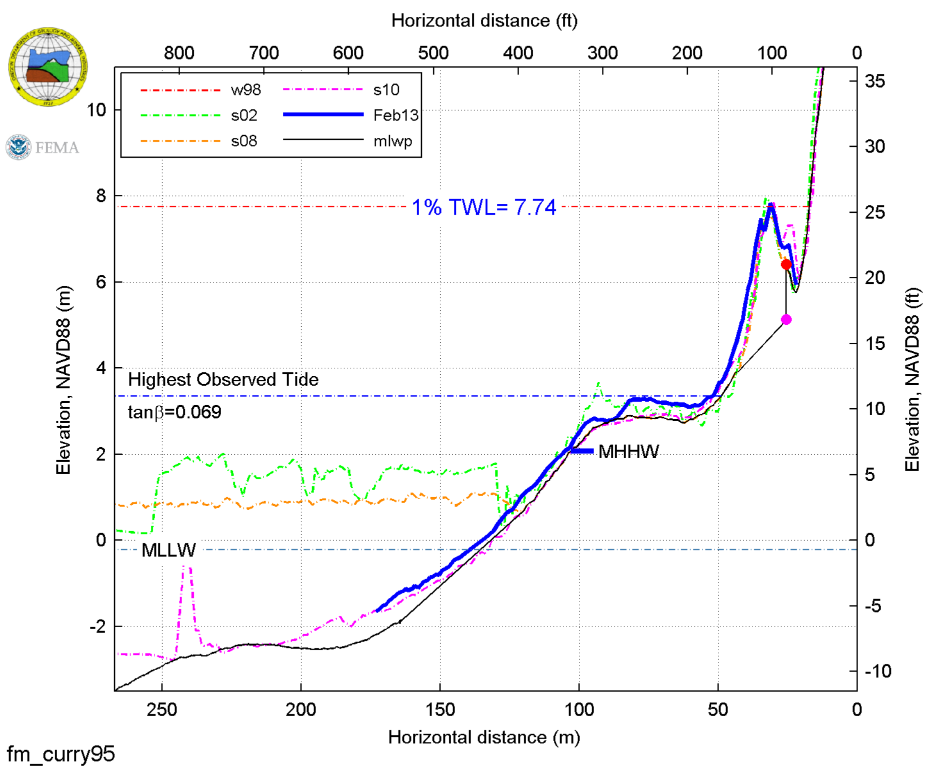

fm_curry 96

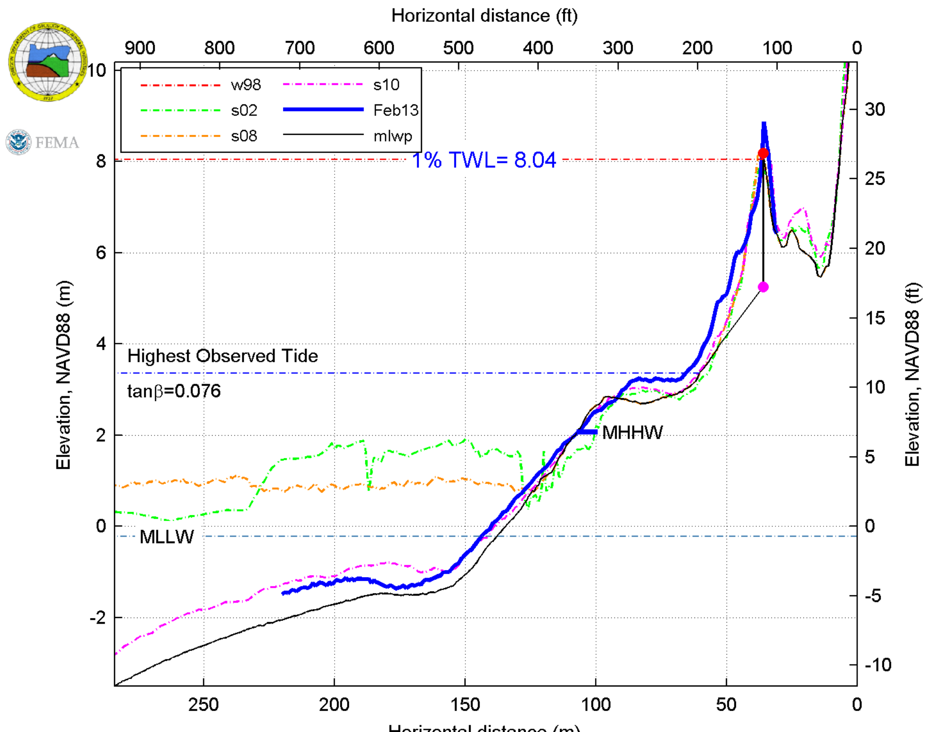

fm_curry96

fm_curry 97

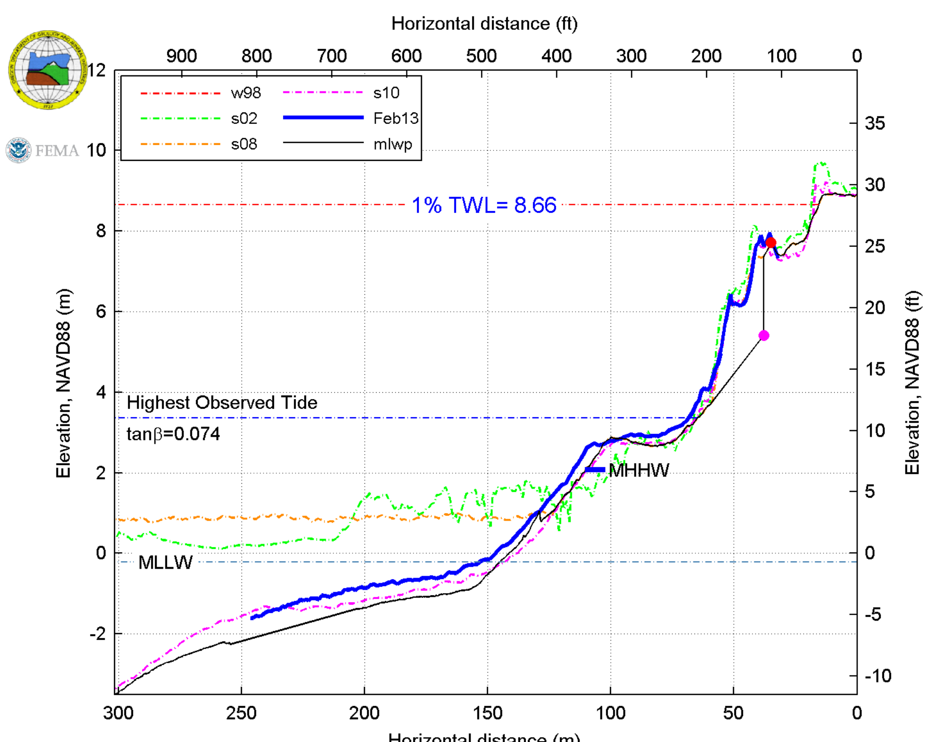

fm_curry97

fm_curry 98

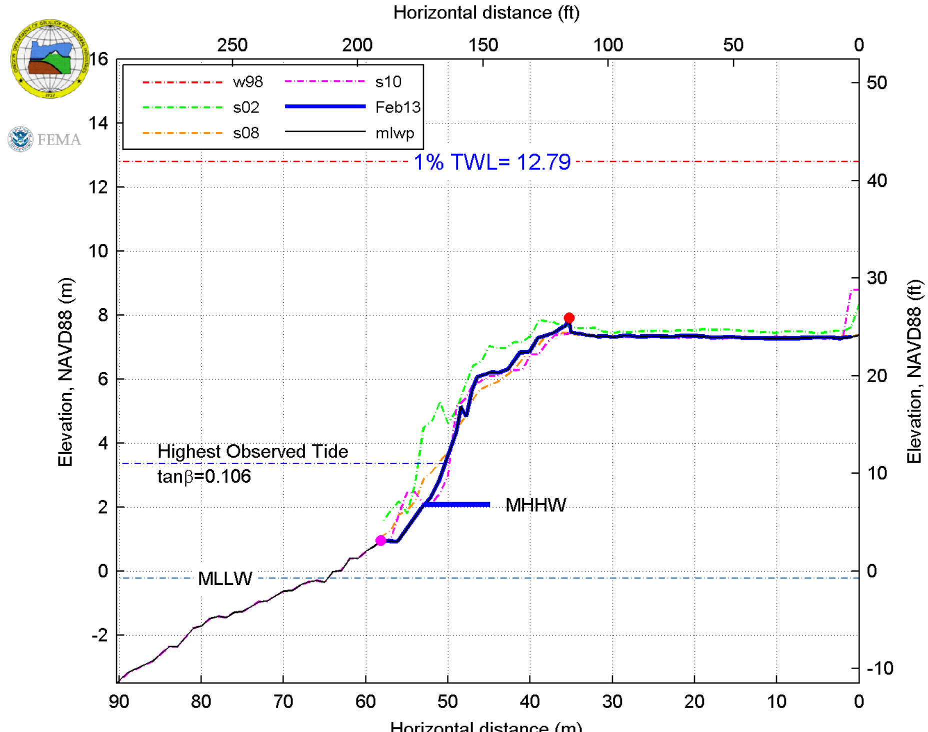

fm_curry98

fm_curry 99

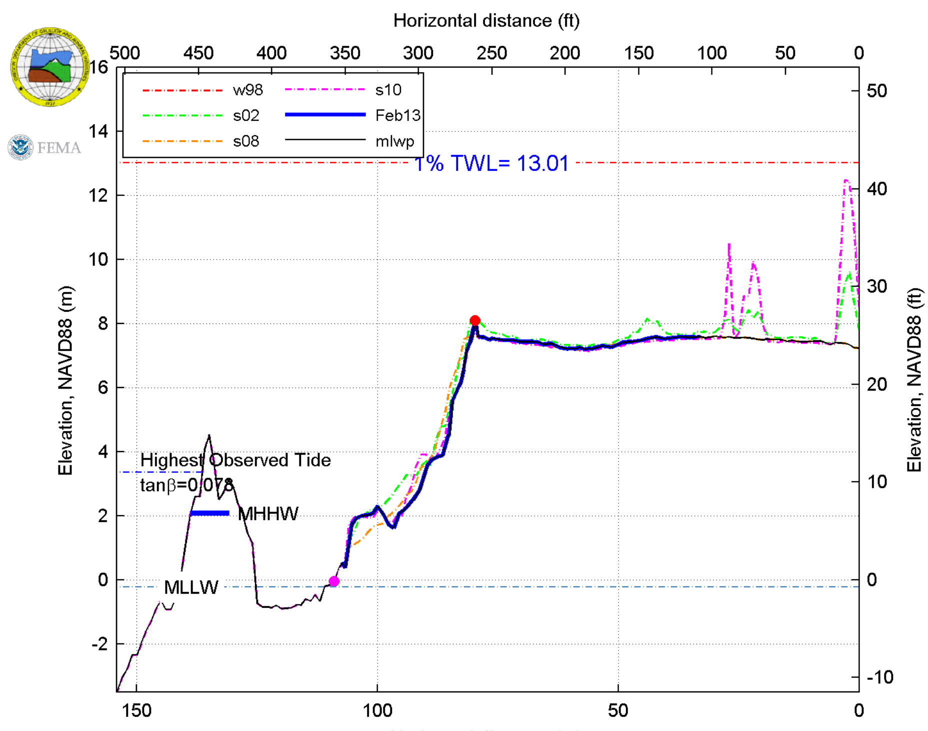

fm_curry99

fm_curry 100

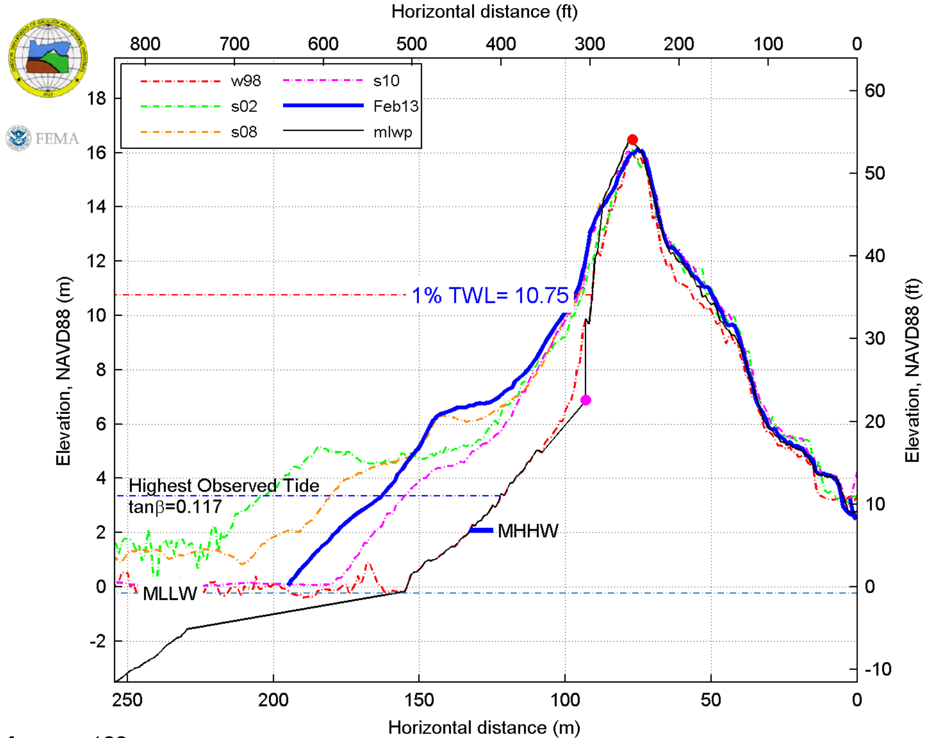

fm_curry100

fm_curry 101

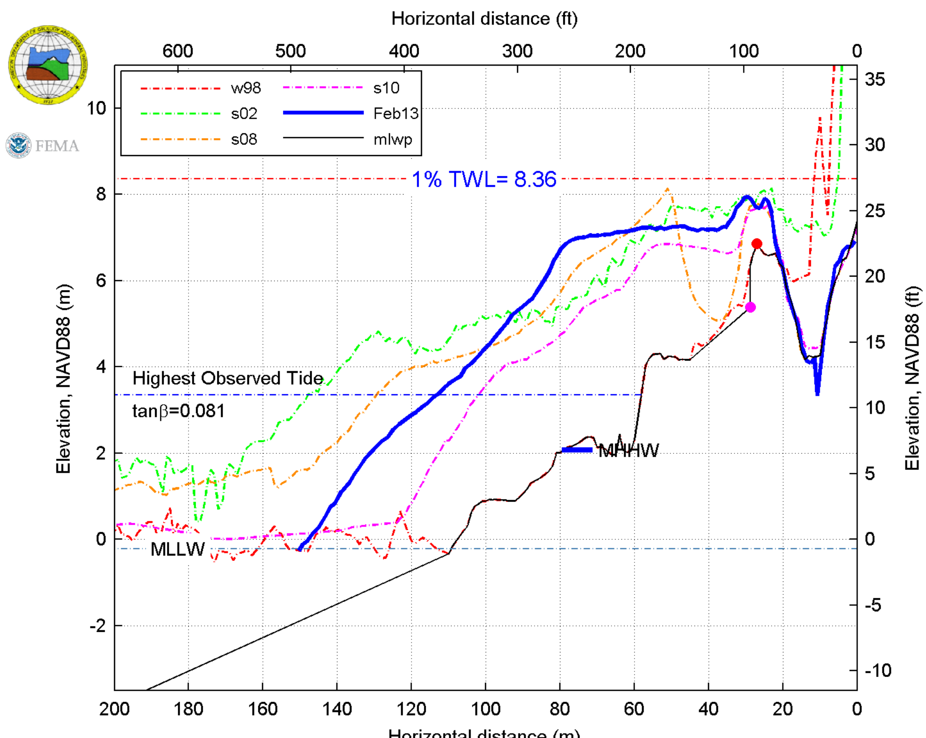

fm_curry101

fm_curry 102

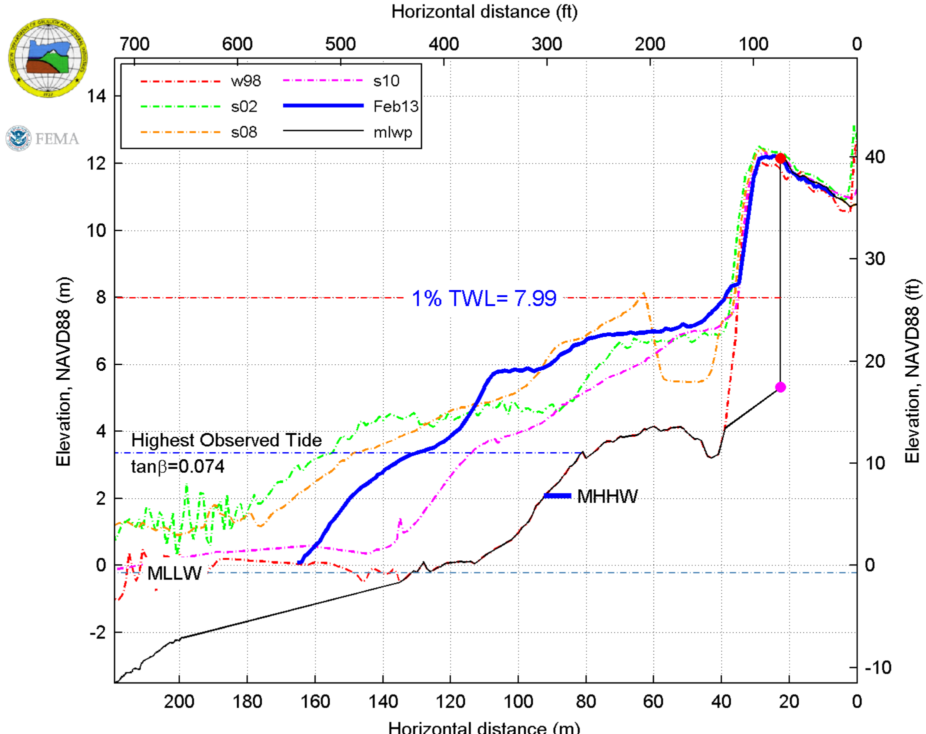

fm_curry102

fm_curry 103

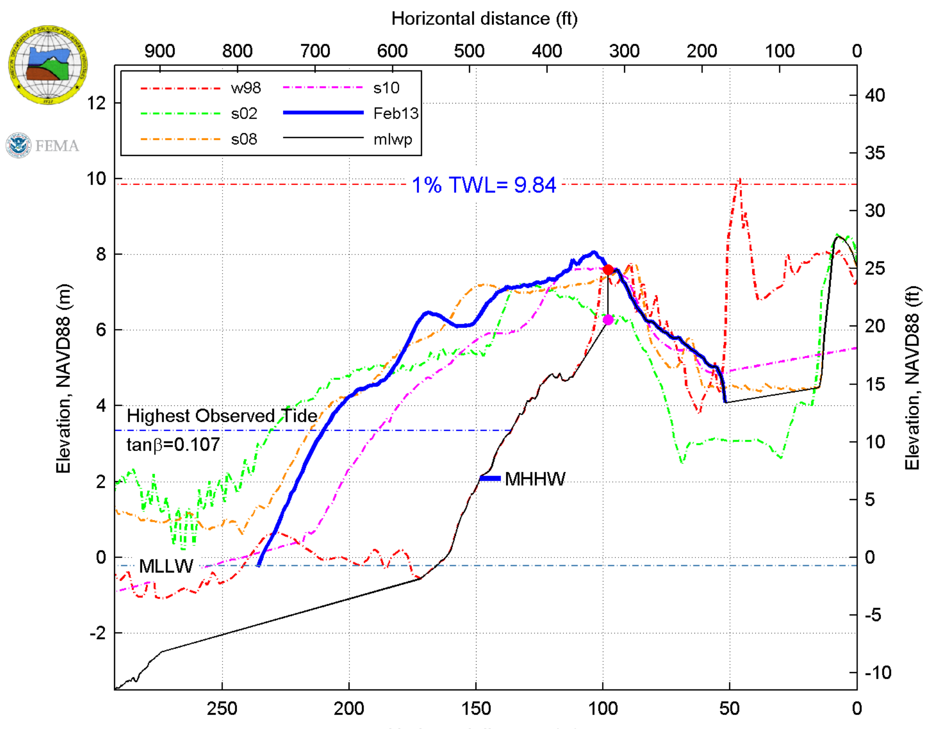

fm_curry103

fm_curry 104

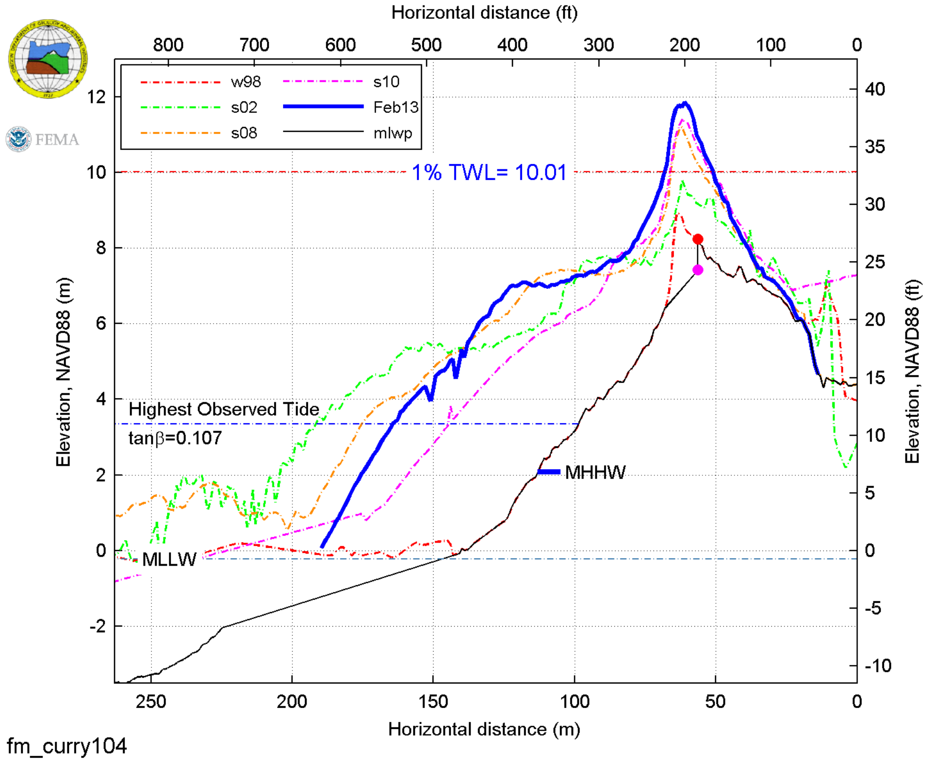

fm_curry 105

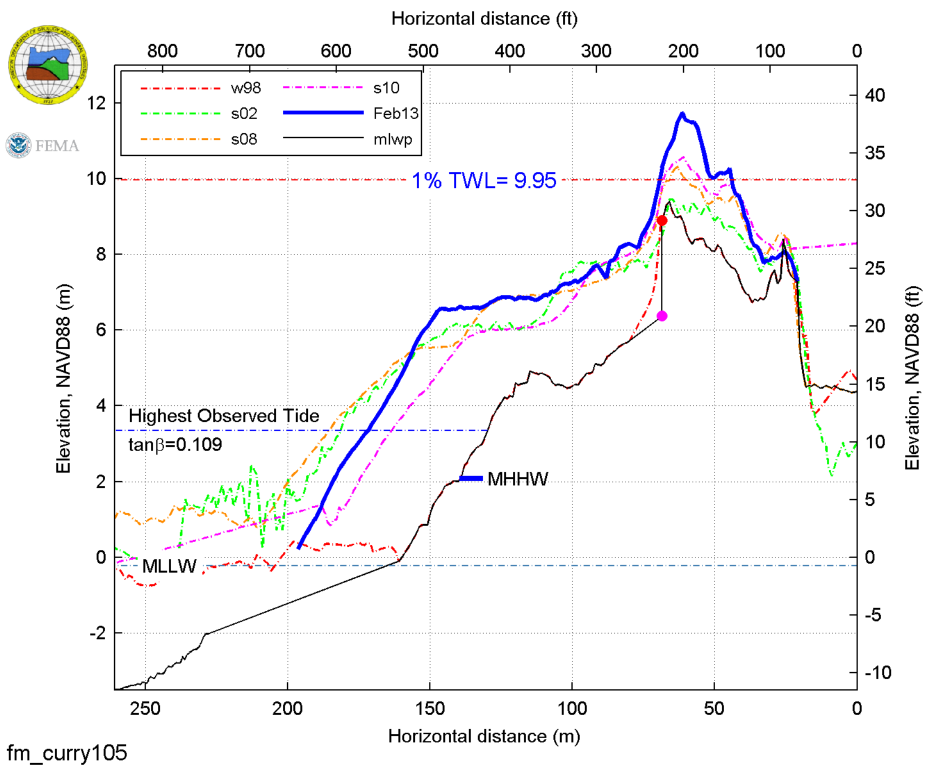

fm_curry 106

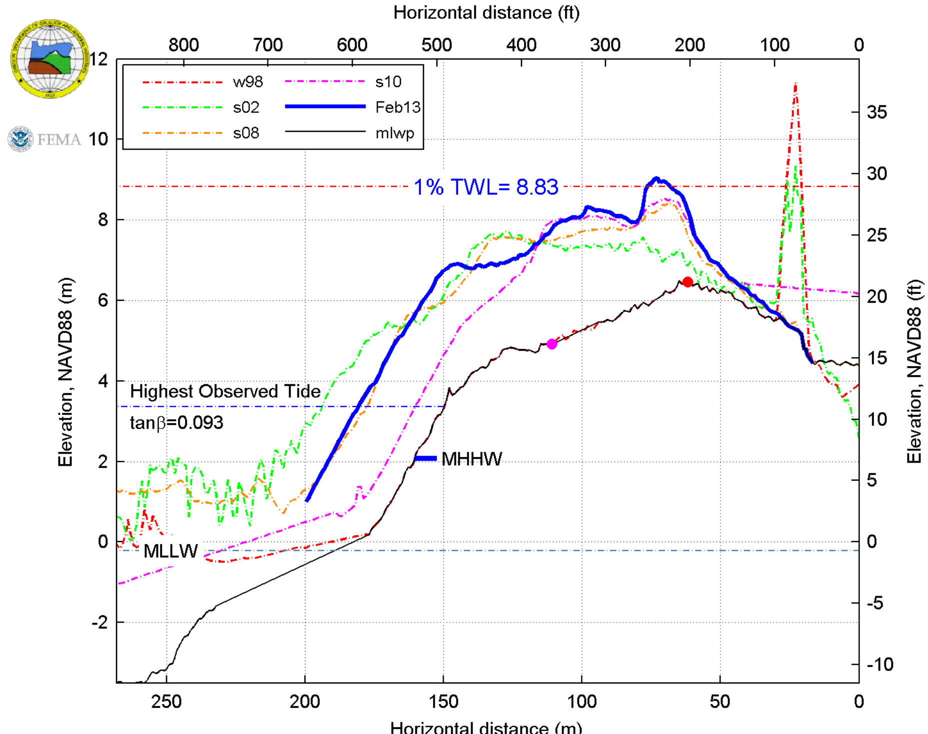

fm_curry106

fm_curry 107

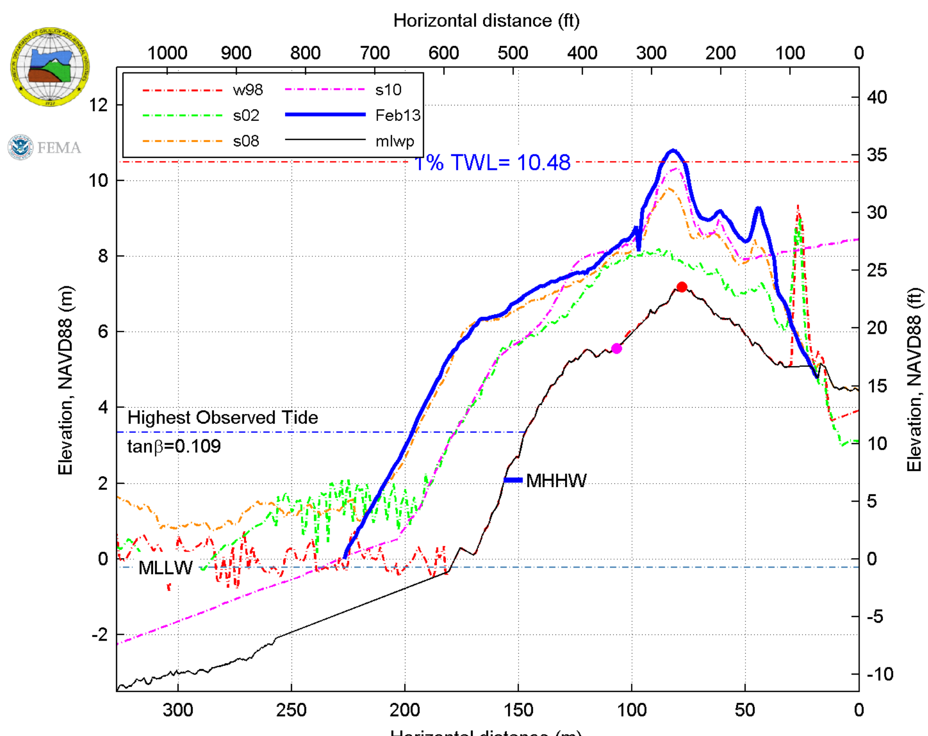

fm_curry107

fm_curry 108

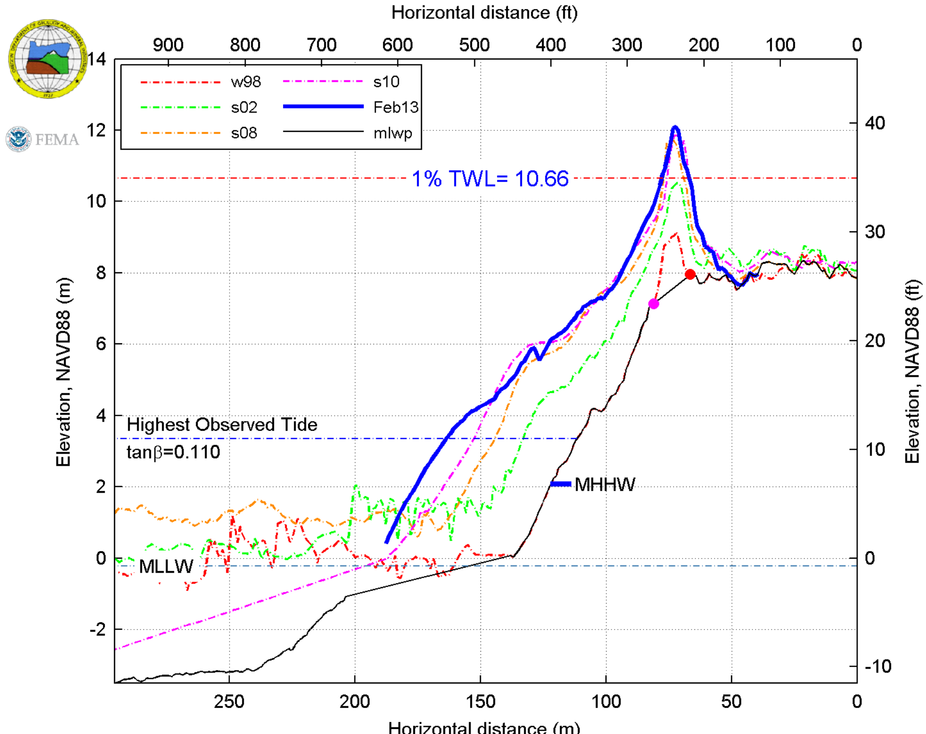

fm_curry108

fm_curry 109

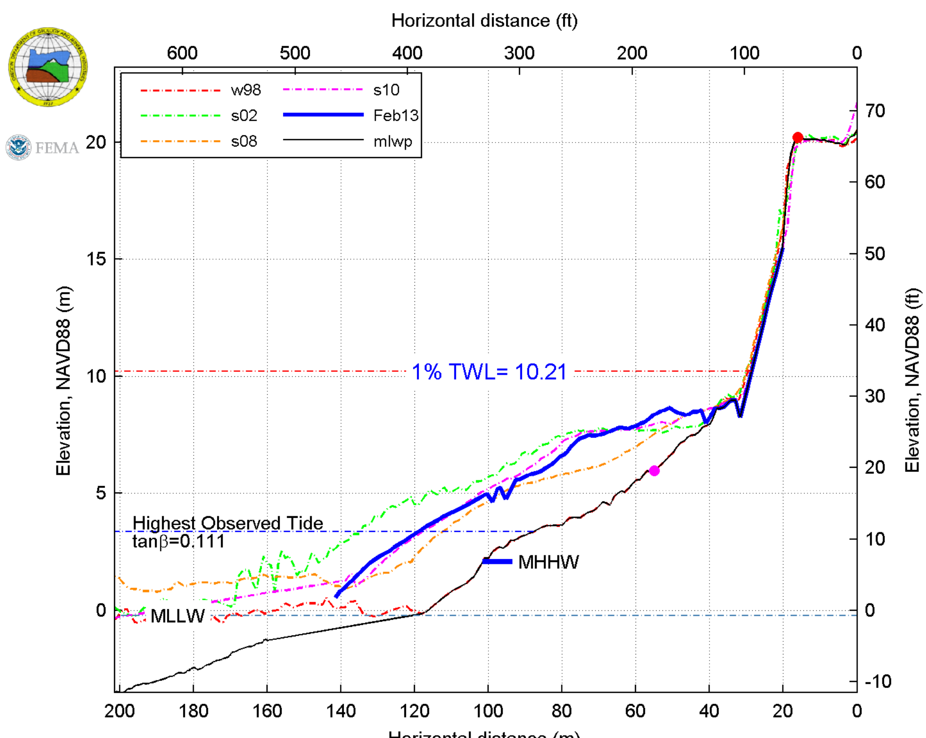

fm_curry109

11.2.6 Brookings – Supplemental Transect

7_13401

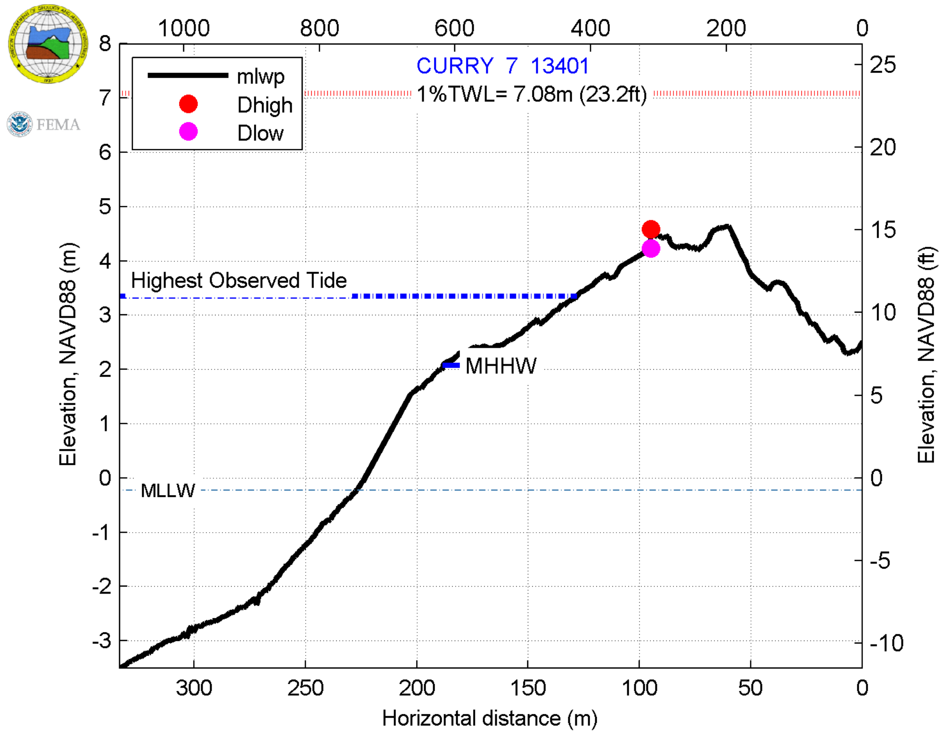

Oregon Department of Geology and Mineral Industries
Ian P. Madin, Interim Director
www.oregongeology.org

ERRATA SHEET for

DOGAMI Open-File Report O-15-07, Coastal Flood Hazard Study, Curry County, Oregon

Last update: 7/31/2015

This sheet identifies any errors identified after release of the publication. These errors have been corrected in the electronic version of the report available on the website.

#	Description	Location	Date Error Corrected
1	Coauthors Fletcher E. O'Brien and Katherine Serafin were omitted from original author list; author list has been corrected.	page 1	7/31/12015